LE COPY

④

Report No. 115

𝔆𝔬𝔩𝔲𝔪𝔟𝔦𝔞 𝔘𝔫𝔦𝔳𝔢𝔯𝔰𝔦𝔱𝔶
𝔦𝔫 𝔱𝔥𝔢 𝔆𝔦𝔱𝔶 𝔬𝔣 𝔑𝔢𝔴 𝔜𝔬𝔯𝔨

Theoretical and Experimental Research on a Millimeter-Wavelength Free-Electron Laser

Thomas C. Marshall

1989

DTIC
ELECTE
OCT 11 1989
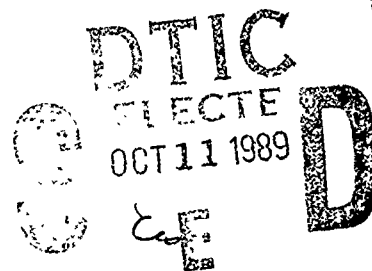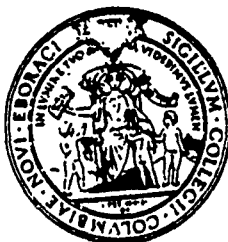D

has been approved
for public l.
ed.

Report No. 115

Columbia University
in the City of New York

Theoretical and Experimental Research on a Millimeter-Wavelength Free-Electron Laser

Thomas C. Marshall

1989

Accession For

NTIS GRA&I	X
DTIC TAB	☐
Unannounced	☐
Justification	

By

Distribution/

Availability Codes

Dist	Avail and/or Special

A-1

DTIC
COPY
INSPECTED
4

REPORT DOCUMENTATION PAGE

1a. REPORT SECURITY CLASSIFICATION	1b. RESTRICTIVE MARKINGS
Unclassified	

2a. SECURITY CLASSIFICATION AUTHORITY	3. DISTRIBUTION/AVAILABILITY OF REPORT
	Approved for public release - distribution
2b. DECLASSIFICATION/DOWNGRADING SCHEDULE	unlimited

4. PERFORMING ORGANIZATION REPORT NUMBER(S)	5. MONITORING ORGANIZATION REPORT NUMBER(S)
Columbia Plasma Lab Report	

6a. NAME OF PERFORMING ORGANIZATION	6b. OFFICE SYMBOL (If applicable)	7a. NAME OF MONITORING ORGANIZATION
Columbia University		

6c. ADDRESS (City, State, and ZIP Code)	7b. ADDRESS (City, State, and ZIP Code)
New York . New York 10027	

8a. NAME OF FUNDING/SPONSORING ORGANIZATION	8b. OFFICE SYMBOL (If applicable)	9. PROCUREMENT INSTRUMENT IDENTIFICATION NUMBER
Office of Naval Research		

8c. ADDRESS (City, State, and ZIP Code)	10 SOURCE OF FUNDING NUMBERS			
	PROGRAM ELEMENT NO.	PROJECT NO.	TASK NO.	WORK UNIT ACCESSION NO.
Arlington, VA 22217				

11. TITLE (Include Security Classification) Theoretical and Experimental Research on a Millimeter-Wavelength . Free Electron Laser

12. PERSONAL AUTHOR(S) T. C. Marshall

13a. TYPE OF REPORT	13b. TIME COVERED	14. DATE OF REPORT (Year, Month, Day)	15. PAGE COUNT
Final	FROM 1979 TO 1988	September 1989	

16. SUPPLEMENTARY NOTATION

17.	COSATI CODES		18. SUBJECT TERMS (Continue on reverse if necessary and identify by block number)
FIELD	GROUP	SUB-GROUP	

19. ABSTRACT (Continue on reverse if necessary and identify by block number)

Ten years' research on the Columbia Free Electron Laser are summarized with a selection of key reprints. Topics include: gain and wavelength studies, Thomson-scattering diagnostics for electron beam momentum-spread, efficiency-enhancement experiments, theory and experiments on optical guiding and sidebands. —> next page

20. DISTRIBUTION/AVAILABILITY OF ABSTRACT	21. ABSTRACT SECURITY CLASSIFICATION
☒ UNCLASSIFIED/UNLIMITED ☐ SAME AS RPT. ☐ DTIC USERS	Unclassified

22a. NAME OF RESPONSIBLE INDIVIDUAL	22b. TELEPHONE (Include Area Code)	22c. OFFICE SYMBOL
T. C. Marshall	(212) 854-3116	

DD FORM 1473, 84 MAR 83 APR edition may be used until exhausted. SECURITY CLASSIFICATION OF THIS PAGE
All other editions are obsolete.

INTRODUCTION

This report is a summary of the principal research completed under contract N0014-79C-0769 on experimental and theoretical research relating to Free Electron Lasers, in particular the millimeter-wavelength Raman FEL at Columbia University. The research spans a period of approximately ten years.

Following this introduction, the remainder of the report consists of a compilation of published research papers. These comprise a representative sample (not complete) of the major research findings. The remainder of this section is an overview of these findings.

Section I consists of two papers published in the first IEEE FEL review issue, one describing the first results from our new FEL facility and the other being a theory of beam-temperature effects upon the gain of an FEL (one of the first of several such studies that have been made by several groups). Section II and III is a pair of papers discussing results from a type of FEL which has since become known as a *CARM*; the principles were the subject of a patent recently issued. Sections IV-VI are the results of a CO_2 laser - Thomson backscattering experiment which determined the momentum spread of the electron beam in our FEL. Sections VII-IX describe gain and dispersion studies of our 2mm FEL and X,XI report the sideband spectrum of this FEL configured as an oscillator as well as a demonstration that the sideband frequency depends on the group velocity of the carrier wave. Sections XII and XIII report the operation of the FEL oscillator operating with a tapered undulator, in which not only efficiency enhancement but also sideband power reduction was obtained. Concluding, section XIV deals with the theory of optical guiding in our Raman FEL and XV presents experimental evidence that the optical power profile is

modified by optical guiding as it occurs in our overmoded waveguide system.

Further studies of optical guiding, including new results on the effects of guiding on the sidebands, are to be published in Physical Review A this year, and represent a follow-on of the above research continued under further ONR and additional NSF sponsorship.

A Submillimeter Free-Electron Laser Experiment

DAVID S. BIRKETT, T. C. MARSHALL, S. P. SCHLESINGER, SENIOR MEMBER, IEEE,
AND DAVID B. MC DERMOTT

Abstract—A free-electron laser (FEL) Raman-backscattering oscillator, using a $\frac{1}{2}$-1 MeV, 20 kA electron beam pumped with a weak (~250 g) periodic (8 mm) transverse magnetic field, is operated as a source of high power millimeter and submillimeter radiation, with lasing developing during the 150 ns beam pulse. Measurements of lasing operation are described at 1.0 and 0.6 mm. The temporal behavior of cavity radiation is considered and effective gain is measured and compared with theory.

I. INTRODUCTION

WE report recent results from the new Columbia free-electron laser (FEL) facility, which is a source of millimeter and submillimeter radiation operating in the stimulated Raman backscattering regime [1], [2]. Signal growth occurs when an intense, relativistic electron beam, propagating parallel to and near the walls of a cylindrical drift tube, interacts with a periodic magnetic field produced by a pulsed undulator. Magnetic profiling of the beam permits introduction of mirrors on the optical ray path of the electron beam; this allows signal feedback and lasing. A pulsed electron beam of 150 ns duration permits as much as 15 transits of radiation to accumulate in the cavity. We have confirmed previous observa-

tion of lasing in a similar system [1], extended the duration of laser pulses, thus making possible a detailed study of signal growth, and examined a range of tuneable wavelengths in the near millimeter and submillimeter regimes. The reader is referred to review papers [3]-[5] on the Raman FEL for additional theoretical details and an overview of past relevant research.

II. APPARATUS

The Columbia FEL and its electron accelerator are shown schematically in Figs. 1 and 2. The accelerator (Fig. 1) is a Physics International Pulserad 220, consisting of a 20 stage Marx Bank and a four meter coaxial transmission line serving as a pulse forming cavity. The Marx, storing 20 kJ, is erected to 2 MV and charges the transmission line. The electron beam is formed after breakdown of a spark gap switch, when ~1 MV is applied to the graphite cathode of a foilless diode. Electrons are field emitted from the cathode in a region of high magnetic field, and then follow the magnetic field lines into the interaction region (L ~50 cm), where a weak (B_1 ~200 g) periodic (λ_0 ~8 mm), perpendicular magnetic field (provided by the undulator) is superposed on the guide magnetic field (B_0 ~10 kg).

An essential feature of the guide field for the FEL oscillator is a gradual 2:1 step in field strength (Fig. 2), located about
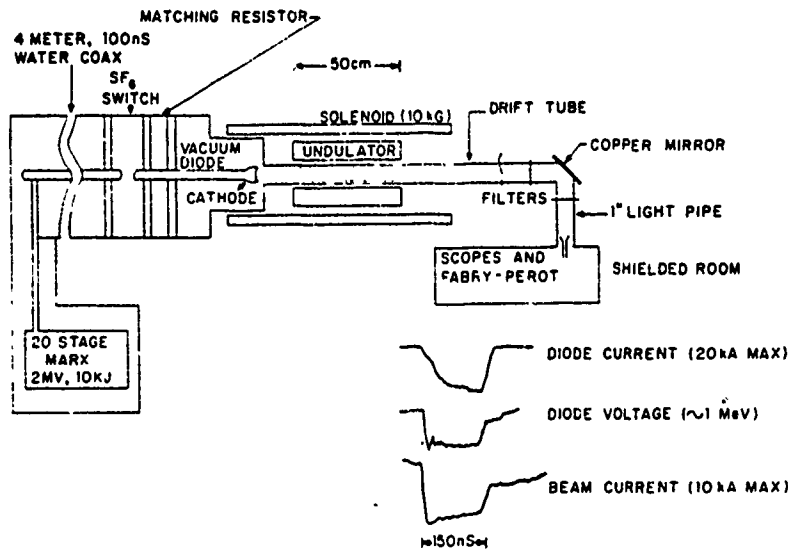
Fig. 1. The Columbia FEL facility. The laser is shown in the super-radiant configuration.
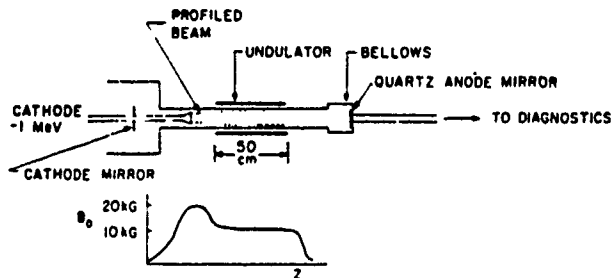

Fig. 2. The FEL oscillator cavity and requisite tapered magnetic field.

7.5 cm downstream from the cathode. This step expands the 1 mm thick annular beam to within 1 mm of the drift tube (5 cm diameter) wall, and locates the beam within the periodic field of the undulator, thus removing the cathode from the ray path of the beam. Other desirable features of this beam profiling include a cooling of beam perpendicular temperature due to conservation of the adiabatic invariant $\gamma T_{\perp}/B_0$, and the elimination of hot electrons emitted from the cathode shank. As the beam gradually expands toward the wall, it traverses a region of increasing pump field, over a zone of several 8 mm periods.

Typical diode voltage and current waveforms are presented in Fig. 1. The diode voltage is measured with a divider circuit mounted on the dump resistor; the latter is used for impedance matching to the 20 Ω line. The diode current is measured with a small loop linking the B_{θ} of the diode current and an integrator. The beam current is measured with a Faraday cup mounted in the drift tube intersecting the beam.

The cathode mirror (Fig. 2) is a stainless-steel flat mounted directly on the cathode stalk, and is electrostatically shielded to prevent breakdown to the diode walls. The anode mirror, an aluminum coating deposited on z-cut quartz, is mounted in an adjustable bellows. Both mirrors can be aligned precisely for parallelism under vacuum with an external red laser. The mirrors are set perpendicular to the drift tube, which is aligned

parallel to the lines of guide magnetic field with the aid of witness plates. Both the high field zone of the guide magnetic field near the cathode and the undulator field are produced by discharging separate capacitor banks. These fields penetrate the walls of the drift tube via a longitudinal slot in the drift tube. The undulator is wound as a bifilar helix. About 10 percent of radiation in the cavity is coupled out through a 2 cm hole in the center of the anode mirror, and then transmitted along 7 m of light pipe to a shielded screen room. A microwave filter and two separated screen meshes (mesh spacing 0.8 mm) are used to filter low frequency beam radiation. Schottky barrier diodes are used for detection and an external adjustable Fabry-Perot cavity is used for spectroscopy.

III. PRINCIPLES

Before considering experimental results, we present in this section a qualitative discussion of certain basic features of FEL operation. The mechanism of signal growth in the FEL is stimulated Raman backscattering [2]-[4]: this is a three-wave process in which an idler, a longitudinal plasma wave ($\omega_p = (4\pi n e^2/\gamma m)^{1/2} \sim 8$ GHz), and scattered electromagnetic wave grow parametrically as a convective instability depleting a "pump" transverse wave. For our case of a relativistic beam, a periodic magnetostatic undulation in the guiding axial magnetic field serves as the electromagnetic pump wave in the beam frame. If K is the beam kinetic energy (somewhat less than the diode voltage due to beam space charge), the relativistic γ of the beam is given by $(K + mc^2)/mc^2$, and the backscattered wavelength is given approximately by

$$\lambda_s \sim \frac{c}{2\gamma^2} \left(\frac{\beta_z c}{\lambda_0} - \frac{\omega_p}{2\pi\gamma} \right)^{-1} \tag{1}$$

where $\beta_z = v_z/c$, v_z = longitudinal velocity, and λ_0 is the undulator period. In our experiment, since electrons have a rest energy of 0.51 MeV, we can vary the beam γ between 2 and 3.
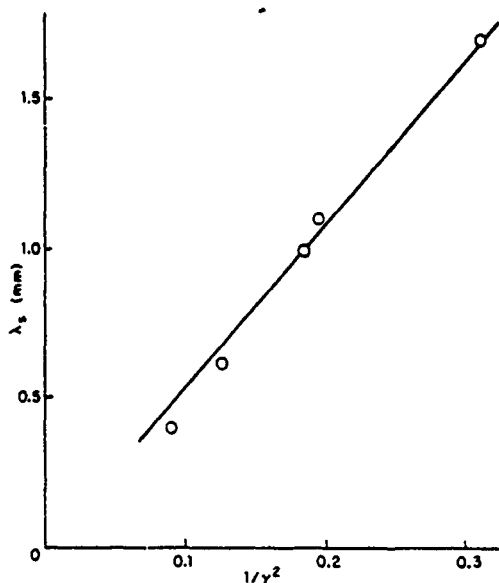
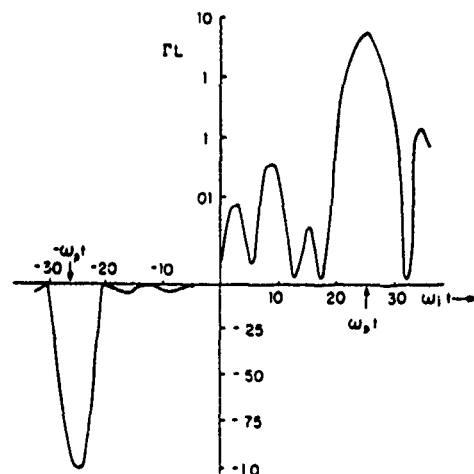Fig. 3. Scattered wavelength as a function of beam γ.

Fig. 4. Dependence of total gain upon pump signal mismatch: $f = 1$, $\omega_s t = 250$, $(eB_\perp/mc)t = 10$. Note that this pump amplitude is about twice that actually used in the experiment.

For $\lambda_0 = 8$ mm, the pump frequency is $\beta c/\lambda_0 \sim 30$ GHz, well above the electron gyrofrequency of $(1/2\pi)(eB_0/\gamma mc) \sim 10$ GHz. Thus, we avoid magnetoresonant interaction of the electrons with the undulator field.

Stimulated Raman backscattering has been observed over a range of beam energies, in both laser and superradiant (single-pass) configurations. Fig. 3 summarizes experimental confirmation of scattered frequency dependence on γ^2 for several experiments on three different machines using $\lambda_0 = 8$ mm. The two longer wavelength points were measured in superradiant configurations, one of which used a less energetic, less intense ($\omega_p \sim 4$ GHz) beam of 10 ns duration [6]. The shortest wavelength point was measured on the first collective FEL [1], which used the 50 ns 1.2 MV Naval Research Laboratory veba accelerator. Points at $\lambda_s \sim 0.6$ mm and $\lambda_s \sim 1.0$ mm, taken on the new Columbia facility, show the inherent tunability of the FEL. For the point $\lambda_s \sim 1$ mm and $\gamma \sim 2.3$, the diode voltage was -700 kV while for $\lambda_s \sim 0.6$ mm, $\gamma \sim 2.9$, the diode voltage was -950 kV.

Since the scattered radiation is one component of a three-wave coupling instability, the introduction of mirrors provides regenerative feedback with the associated benefit of narrowed bandwidth and increased power. We may estimate the bandwidth of this FEL oscillator to be the spread of unstable frequencies in the three-wave interaction, which, for our system, yields $\Delta\omega_s/\omega_s \sim \frac{1}{2}$ percent [1], [2]. Decreased pump amplitude reduces the spread of unstable frequencies [6] and narrows the bandwidth, while feedback permits power to grow over many bounce times of the cavity radiation. Low pump amplitude is also desirable because of the possibility of an absolute instability disrupting the beam. This instability has been predicted theoretically [7] to occur for our experimental parameters when $B_\perp$ exceeds ~ 1 kG, more than twice the value of the $B_\perp$ attainable by us. In the case of the weak pump, cold beam collective regime [4] of our experiment, conditions given by

respectively, backscattered radiation will grow exponentially along the beam with growth coefficient predicted to be

$$\Gamma_{eff} = \left\{ \left(\frac{eB_\perp}{mc}\right)^2 \frac{\omega_p f \lambda_0}{8\pi\gamma c^3} \right\}^{1/2} \tag{4}$$

where f is the cavity filling factor, the fraction of cavity radiation that interacts with the beam. Equation (4) applies when ω_l given by

$$\omega_l = \frac{\omega_s}{2\gamma} - \frac{2\pi\gamma c}{\lambda_0} \tag{5}$$

is equal to ω_p of the beam, i.e., to resonance between the frequency of the plasma oscillation and the beat disturbance produced by the nonlinear mixing of the pump and scattered waves. A finite mismatch will reduce this quantity. Fig. 4 shows a calculation [2] of single-pass gain for a system with parameters similar to our system for arbitrary frequency mismatch. The calculation is done in the beam frame where $t = L/c\gamma$. Notice that both stimulated emission and absorption can occur with relatively small changes of order ω_p in the beat frequency ω_l. This fact imposes stringent conditions on variations of γ in time ($\tilde{\Delta}\gamma$), since ω_l is a sensitive function of γ. Note that it is the pump frequency which varies during the FEL pulse; the scattered frequency is established by ambient cavity radiation. We see from Fig. 4 that exponentially growing power in time would require $\tilde{\Delta}\gamma/\gamma < 1$ percent throughout the pulse, a requirement not met by the high voltage technology of our accelerator. Thus, we cannot expect power to grow exponentially with constant coefficient for the duration of the pulse.

In the FEL system, γ must be nearly constant in time; it must also be nearly uniform in space. A spread of particle
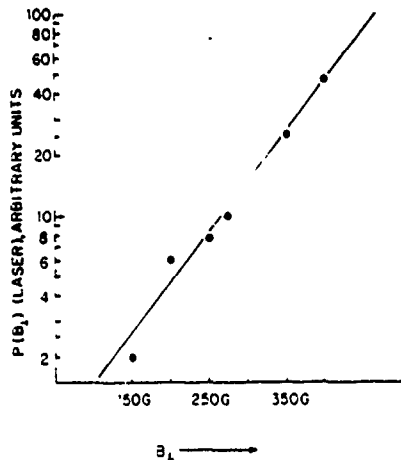
$$\frac{eB_\perp}{mc} \ll \left(\omega_p \frac{2\pi c}{\lambda_0}\right)^{1/2} \tag{2}$$

$$\frac{\Delta\gamma}{\gamma} < \frac{\lambda_0}{2\gamma} \frac{\omega_p}{2\pi c} \sim 3 \text{ percent} \tag{3}$$

Fig. 5. Scattered power as function of undulator pump amplitude $\gamma =$ 2.9. The system begins to lase at $B_\perp \sim 200$–250 g.
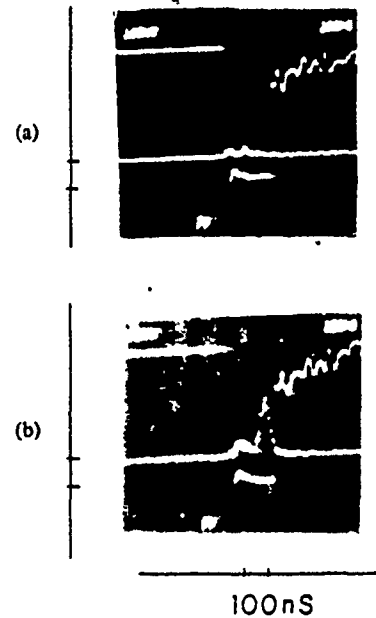

100 nS

Fig. 6. Dual-beam oscilloscope traces of filtered radiation at $\lambda \sim 1$ mm: (a) no mirrors (100 mV/div); and (b) laser, 50 mV/div. Diode voltage waveform is the negative pulse in each case.

energies within the electron beam, characterized by $(\Delta\gamma)$ in (3), may be considered as a temperature effect which causes a reduced growth rate due to Landau damping of the plasma wave [3], [8]. Beam temperature is due to several effects, all of which may remove the beam from the cold beam, high gain regime. For example, if the beam current is large, a beam space charge potential drop develops across the beam radius [9], leading to a shear in longitudinal electron energy. Other effects causing beam energy spread are finite beam emittance [10], radial inhomogeneity of the undulator field, and coupling of particle motion in the undulator field to the electron cyclotron frequency of the guide field [11]. All these effects are aggravated by increased pump amplitude. Direct measurement of beam energy spread has not been undertaken, but, in lieu of such measurements successful lasing, must be taken as evidence of a sufficiently cold beam.

The laser will oscillate when beam gain exceeds the cavity losses. We present estimates of these cavity parameters, obtained from the data, in the next section.

IV. OPERATION OF THE FEL

As shown in Fig. 5, increased pump amplitude $(B_\perp)$ was observed to increase scattered power exponentially. However, multipass operation should yield exponentiating power in time, which is not always observed (see Fig. 6). One obstacle here appears to be the requirement of constant γ, not met by our system. While increased $B_\perp$ relaxes this requirement, it also should broaden the oscillator bandwidth and increase the beam energy spread. We found similar temporal behavior at various pump amplitudes, and no evidence of saturation.

The resonator cavity used in this experiment is neither in the free space or guided wave limiting regimes. Even though its transverse dimensions are roughly forty times that of the scattered wavelength, the cavity is not optical. This is because diffraction is very large near the cathode and cathode mirror, which form sharp discontinuities in the cavity lateral dimensions. Also, the beam propagates only ~ 1–2 wavelengths from the drift tube walls. Radiated power was not observed to depend critically on precise mirror alignment. However, there is

evidence that decreasing λ_s will put the system in a quasi-optical regime: a similar experiment [1] showed more critical dependence on mirror alignment for 400 μm radiation.

When we operated the equipment with mirrors removed, we found beam noise radiation [Fig. 6(a)], a small portion of which is superradiant. Analysis of the spectral content, using a Fabry–Perot interferometer, showed a spectral width $\Delta\lambda/\lambda \sim$ 10 percent at $\lambda \sim \lambda_s \sim 1$ mm. Addition of mirrors to the beam system extended the duration of the radiation to an appreciable fraction of the pulse, and enhanced the total power output by roughly an order of magnitude [Fig. 6(b)]. The spectral width of the radiation decreased to ~ 1–2 percent with mirrors in place, as was the case in a previous experiment [1]. Thus, quasi-optical feedback permits the development of a relatively strong, coherent component from the broad-band beam noise.

For a quantitative understanding of the system, we have analyzed laser signals in terms of the reflection coefficients of the mirrors, diffraction and coupling losses, effective gain along the beam, and filling factor (see Figs. 7 and 8). The wavelength in Fig. 7(b) is $\lambda_s \sim 0.6$ mm, while that of Fig. 8(b) is $\lambda_s \sim 1.0$ mm due to lower beam γ. We propose that the power $P(t)$ be given by the equation

$$P(t) = fqP(t - 10 \text{ ns}) \cosh^2 (\Gamma_{eff}L) + (1 - f)qP(t - 10 \text{ ns})$$

$$(6)$$

where f is the filling factor, q is the fraction of radiation surviving a roundtrip in the cavity, and $\cosh(\Gamma_{eff}L)$ is the single pass amplification of signal in the cavity. Radiation trapped between the mirrors is thus expressed in terms of radiation present one bounce time (10 ns) earlier. The second term in the equation represents radiation which does not interact with the beam. In both cases, Figs. 7 and 8, we may distinguish several
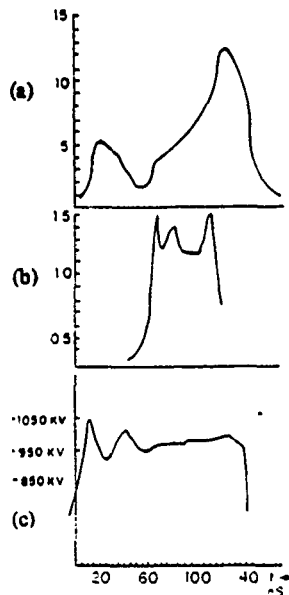
Fig. 7. Calculation of $\Gamma_{eff}L$ for $\gamma = 2.9$, $\lambda_s = 0.6$ mm: (a) power amplitude, (b) $\Gamma_{eff}L$ from (6), and (c) diode voltage.

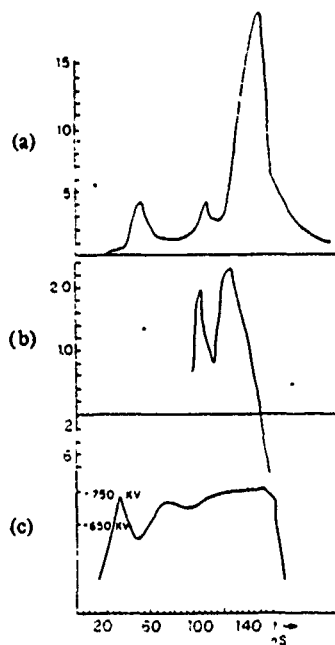Fig. 8. Calculation of $\Gamma_{eff}L$ for $\gamma = 2.3$, $\lambda_s = 1.0$ mm: (a) power amplitude, (b) $\Gamma_{eff}L$ from (6), and (c) diode voltage.

features of the cavity radiation, including erratic low level signals during the initial diode voltage ringing, periods of stimulated emission and absorption, and the decay of radiation emitted from the cavity after the electron beam terminates. The latter permits a calculation of q, the radiation survival fraction, which is 0.6. Because of diffraction, we assume that radiation fills the cavity cross section in the annular interaction region between the cathode and the wall of the drift tube. Geometrically, f is the ratio of the area filled by the beam to the annular cross section, about $\frac{1}{4}$. However, the rms scattered field amplitude is not radially uniform, even in a highly overmoded cavity, so that this estimate of f could be low. We begin by taking $f \sim \frac{1}{3}$.

With these values q and f, we have solved (6) for $\Gamma_{eff}L$. This yields the two time dependent gain curves shown in Figs. 7(b) and 8(b). We find that $\Gamma_{eff}L$ is a somewhat erratic function of time, even during periods of apparent relative smoothness in diode voltage. In Fig. 8(c) we find a 5 ns interval of stimulated absorption ($\Gamma_{eff}L < 0$), which corresponds to an abrupt drop in power as the diode voltage falls. We also note that, on the average, $\Gamma_{eff}L$ is somewhat larger for the case of lower γ.

In both cases, we find rough agreement between calculation of $\Gamma_{eff}L$ and theory. Equation (4) predicts $\Gamma_{eff}L$ to be 1.0 for $\gamma = 2.9$, and 1.1 for $\gamma = 2.3$, which compare with the average respective values of 1.3 and 1.5 computed from experiment. Equation (4) also shows that the gain per pass of the FEL should be linear in pump amplitude. Analysis of signals similar to those shown in Figs. 7 and 8, but at reduced pump amplitude, shows that a reduction in pump amplitude by a factor of 0.7 causes an experimental reduction in gain by a corresponding factor.

Taking our experimental estimate of single-pass gain during lasing ($\Gamma_{eff}L \sim 1.5$), and scaling this down by reducing the pump amplitude to the point where the system can just sustain a constant power level built up during a prior interval ($\Gamma_{eff}L \sim 1$), we can check our estimate of f using (6). We take $P(t)/P(t - 10$ ns$) \sim 1$ and q in the range of 0.6-0.7, and find $f \sim 0.3-0.5$, confirming our original estimate. To summarize, we have found that our FEL oscillator is operating for at least five or more passes of radiation with a single-pass gain near the threshold value ($\Gamma_{eff}L \gtrsim 1$) needed for sustained oscillation, taking reasonable values for the cavity parameters f and q. Lasing is observed during the diode pulse interval where the beam energy fluctuation is a minimum.

In order to make an absolute measurement of radiated power, we used a CH_3F 497 μm laser source to measure the insertion losses of the various elements of our diagnostic system. The detectors were calibrated against a Molectron P-300 pyroelectric element (this was calibrated with a Carcinotron source at 1 mm). We estimate the power radiated from the cavity to be $\sim 10^6$ W, corresponding to an intercavity power of $\sim 10^7$ W. We have not been able to drive the laser power to saturation owing to limitations imposed by electrical insulation and structural strength of the undulator so we do not quote an efficiency of this device.

Note Added in Proof: In connection with our observation that $\Gamma_{eff}L \sim 1$ is the oscillation threshold of this FEL, it is interesting to consider the coupled equations describing this system:

$$\frac{dE_s}{dz} = \frac{-j\Gamma}{2} E_i^* - \frac{1}{2}\alpha_s E_s$$

$$\frac{dE_i^*}{dz} = +\frac{j\Gamma}{2} E_s - \frac{1}{2}\alpha_i E_i^*$$

where E_s and E_i are proportional to the wave amplitudes of the signal and idler, and α_s and α_i are the corresponding damping terms. The threshold for parametric oscillation occurs when $d/dz \rightarrow 0$, or

$$\Gamma_T = \sqrt{\alpha_s \alpha_i} .$$

We estimate α_s from the cavity radiation loss time $(\tau_c \simeq 15\text{-}20$ ns) using $\alpha_s \sim 1/c\tau_c$; α_t is related to the Landau damping time (τ_L) by $\alpha_t = 1/c\tau_L$. If the space charge wave wavelength is twice the Debye wavelength ($\Delta K/K \sim 4$ percent), the plasma wave should damp in about ten plasma periods $(2\pi/\omega_p)$, or $\tau_L \sim 1$ ns. Taking $L \sim 50$ cm, we find $(\Gamma L)_T \sim \frac{1}{2}$.

REFERENCES

[1] D. B. McDermott, T. C. Marshall, S. P. Schlesinger, R. K. Parker, and V. L. Granatstein, "High power free electron laser based on stimulated Raman backscattering," *Phys. Rev. Lett.*, vol. 41, pp. 1368-1371, 1978.

[2] D. B. McDermott and T. C. Marshall, "The collective free electron laser," in *Physics of Quantum Electronics*, vol. 7, Jacobs, Pilloff, Sargent, Scully, and Spitzer, Eds. Reading, MA: Addison-Wesley, 1980, p. 509-522.

[3] A. Hasegawa, "The free electron laser," *Bell Syst. Tech. J.*, vol. 57, pp. 3069-3089, 1978.

[4] P. Sprangle, R. A. Smith, and V. L. Granatstein, "Free electron lasers and stimulated scattering from relativistic electron beams, in *Infrared and Millimeter Waves*, vol. 1, K. J. Button, Ed. New York: Academic. 1979, pp. 279-327.

[5] T. C. Marshall, S. P. Schlesinger, and D. B. McDermott, "The free electron laser: A high power submillimeter radiation source," in *Advances in Electronics and Electron Physics*, vol. 53, C. Marton, Ed. New York: Academic, 1980, pp. 47-84.

[6] R. M. Gilgenbach, T. C. Marshall, and S. P. Schlesinger, "Spectral properties of stimulated Raman radiation from an intense relativistic electron beam," *Phys. Fluids*, vol. 22, pp. 971-977, 1979.

[7] T. J. Kwan and J. R. Cary, "Absolute and convective instabilities in a two dimensional free electron laser," Los Alamos Rep. LA-UR-80-2775.

[8] R. C. Davidson and H. S. Uhm, "Self-consistent Vlasov description of the free electron laser instability," *Phys. Fluids*, vol. 23, pp. 2076-2084, 1980.

[9] R. C. Davidson, *Theory of Non-Neutral Plasmas*. Reading, MA: Benjamin, 1974.

[10] V. L. Granatstein, R. K. Parker, and P. A. Sprangle, "Free electron lasers-millimeter and submillimeter lasers," *CRC Handbook of Lasers*, to be published.

[11] A. Grossman and T. C. Marshall, "Orbits of a test electron in a wiggler," *Bull. Amer. Phys. Soc.*, vol. 25, p. 989, 1980.

T. C. Marshall was born in Cleveland, OH, on January 29, 1935. He received the Ph.D. degree in physics from the University of Illinois, Urbana, in 1960.

He is currently a Professor of Applied Physics at Columbia University, New York, NY. In addition to research in free-electron lasers, he has undertaken research in intense relativistic beam phenomena, plasma-wave scattering and instabilities, trapped-particle effects in plasmas, and the formation and heating of plasmas in high beta equilibrium.

Prof. Marshall is a Fellow of the American Physical Society.

S. P. Schlesinger (M'55-SM'64) was born in New York, NY, on October 9, 1918. He received the B.A. degree from Michigan State University, East Lansing, in 1941, the M.S. degree from Union College, Schenectady, NY, in 1950, and the Doctor of Engineering degree from The Johns Hopkins University, Baltimore, MD, in 1957.

In 1946, following war service in the U.S. Navy, he joined the General Electric Company, Schenectady, NY. He subsequently served on the faculties of Union College and the U.S. Naval Academy, Annapolis, MD. From 1953 to 1956 he was a member of the research staff at the Radiation Laboratory of Johns Hopkins University. and worked on scattering problems, millimeter techniques, and surface wave studies including the dielectric image line. He joined the faculty of Columbia University, New York, NY, in 1956, where he now serves as Chairman and Professor of the Department of Electrical Engineering, as well as Professor in the Department of Applied Physics and Nuclear Engineering. In addition to teaching and consulting, he has conducted research on a range of problems in the general area of microwaves, electromagnetic theory, and related phases of plasma physics, the latter as a member of the Plasma Physics Laboratory at Columbia. Concentrating on electromagnetic wave-plasma interactions since 1963, he has, for the past several years, been studying novel methods for the generation of high power microwave and millimeter waves utilizing intense relativistic electron beams, in particular, most recently the Raman or collective free-electron laser.

Dr. Schlesinger is a member of the American Physical Society, Sigma Xi, Phi Kappa Phi, and Eta Kappa Nu.

David S. Birkett received the B.S.E.E. degree from Michigan State University, East Lansing, in 1977, and the M.S.E.E. degree from Columbia University, NY, in 1979. He is presently working towards the Ph.D. degree at Columbia University.

He has worked on the development of the RF system of the Michigan State superconducting cyclotron. He is interested in microwave sources and computer modeling of resonant cavities.

David B. McDermott received the B.S. degree in 1976 from the University of California, Davis, and the Ph.D. degree from Columbia University, New York, NY, in 1979.

At the Naval Research Laboratory, Washington, DC, he investigated the effect of feedback on the stimulated Raman scattering process in an intense relativistic electron beam. As a Postdoctoral Research Associate at Columbia University, he is currently studying the IREB SRS process in the amplifier mode.

Finite-Temperature Effects in Free-Electron Lasers

LUIS F. IBANEZ AND SHAYNE JOHNSTON

Abstract—The effect of energy spread on the gain of a dense-beam free-electron laser amplifier is analyzed. The formalism includes collective effects and allows for the use of an arbitrary distribution function. The dispersion relation is solved numerically. Besides broadening of the spectrum and decrease in gain, lowering of the central emission frequency with energy spread is observed.

An initial-value problem is formulated and numerically solved, with power computed as a function of distance. The relative contributions of the different modes when temperature changes are analyzed. In particular, the competing effects of a decrease in coupling loss with temperature together with Landau damping are investigated.

I. INTRODUCTION

BEAM quality is a critical parameter in the Raman operation of a dense-beam free-electron laser. If the mediating space-charge wave is Landau damped, the gain is severely reduced. Initial theoretical formulations distinguished between the Raman and Compton regimes of free-electron lasers by expanding the potentials in the pump parameter and considering limiting cases. In [1], a formalism which incorporated potentials which were valid to all orders of the pump was developed, although transverse inhomogeneities [2] and thermal effects were not considered. Within this framework, the Raman regime would arise whenever two of the roots of the dispersion relation have imaginary parts, and the Compton regime mechanism would be represented by spatial interference of the different modes. In practice, both situations may arise and compete with each other. There are beam qualities for which the spatial interference could compete with a Landau damped growth.

The formalism developed in [1] allows one in principle to study this intermediate regime.

Our analysis starts by introducing a distribution function in the perturbed current from [1]. The beam is assumed to be infinite in cross section and a wiggler with no radial dependence is considered. This approximation is justified for small wiggler parameters [2]. The momentum integrals are analytically continued by adding Landau type resonant terms. The distribution function alters the coupling of the slow space-charge mode to one of the electromagnetic modes. The numerical results show a mismatch between the coupled waves which causes a decrease in the gain, together with a broadening of the spectrum which shifts towards lower frequencies. The modes are tracked at higher frequencies to search for other possible growth mechanisms.

We then examine the propagation of the radiation field and radiation power with distance. To this end, the differential equations governing the fields are solved numerically by Laplace transformation. By keeping the thermal terms, the dependence of the mode coefficients on energy spread can be studied. Only one mode grows while the other two are Landau damped. Besides this mechanism, the power sharing of the growing mode is a function of temperature. There is a gradual transition from a three-mode into a two-mode situation as temperature increases. This mechanism can alleviate the decrease in gain due to the mismatch between the two coupled waves caused by the width of the distribution function.

II. THEORY

Consider a beam of electrons described by a distribution function $f(\vec{r}, \vec{u}, t)$ satisfying the relativistic Vlasov equation

$$\frac{\partial f}{\partial t} + \frac{c}{\gamma} \vec{u} \cdot \frac{\partial f}{\partial \vec{r}} - \frac{|e|}{m} \left(\vec{E} + \frac{c}{\gamma} \vec{u} \times \vec{B} \right) \cdot \frac{\partial f}{\partial \vec{u}} = 0 \qquad (1)$$

where $\vec{u} = \gamma \vec{v}/c$ denotes dimensionless momentum, $\gamma = (1 + u^2)^{1/2}$ the usual relativistic factor, and m the electron rest mass. Consider next an electromagnetic field depending only on coordinates z and t; such a field can be described by vector and scalar potentials of the form

$$\vec{A} = \vec{A}_\perp(z, t), \quad \Phi = \Phi(z, t). \tag{2}$$

It follows that the two components of perpendicular canonical momentum

$$\vec{\alpha}_\perp = \vec{u}_\perp - \frac{|e| \vec{A}_\perp}{mc^2} \tag{3}$$

are constants of the motion which we shall employ as new coordinates to facilitate solution of the Vlasov equation (1). Under the transformation $(\vec{u}_\perp, u_z, z, t) \to (\vec{\alpha}_\perp, u, z, t)$, (1) simplifies to

$$\frac{\partial f}{\partial t} + \frac{cu_z}{\gamma} \frac{\partial f}{\partial z} - \frac{|e|}{mc} \vec{E} \cdot \frac{\vec{u}}{u} \frac{\partial f}{\partial u} = 0 \tag{4}$$

where

$$u_z = \{u^2 - [\vec{\alpha}_\perp - \vec{\xi}_\perp(z, t)]^2\}^{1/2}, \tag{5}$$

$$\vec{u} = \hat{z} u_z + [\vec{\alpha}_\perp - \vec{\xi}_\perp(z, t)], \tag{6}$$

and we have defined

$$\vec{\xi}_\perp(z, t) = -\frac{|e|}{mc^2} \vec{A}_\perp(z, t). \tag{7}$$

In terms of these new variables, the current density $\vec{J}$ can be written

$$\vec{J}(z, t) = -|e|c \int du \int d^2\alpha_\perp \frac{u}{u_z} \frac{\vec{u}}{\gamma} f \tag{8}$$

where account has been taken of the Jacobian of the transformation in the integrand.

The equilibrium will now be specified more precisely as time independent with zero electric field. We adopt the standard form for the helical wiggler field, neglecting any radial dependence [2]. Thus, we consider the equilibrium potentials $\Phi_o = 0$ and

$$\vec{A}_o = -\frac{mc^2}{|e|} \xi_o (\hat{x} \cos k_o z + \hat{y} \sin k_o z). \tag{9}$$

Finally, we assume that the electron beam is uniform in the transverse plane and that the electrons execute helical orbits with energy-dependent amplitude a and constant axial velocity v_{oz} in accordance with the relations

$$k_o a = \frac{v_{o\perp}}{v_{oz}} = \frac{\xi_o}{u_{oz}}, \tag{10}$$

$$\vec{u}_o = \hat{z} u_{oz} - \xi_o [\hat{x} \cos (k_o v_{oz} t + \phi_o) + \hat{y} \sin (k_o v_{oz} t + \phi_o)]. \tag{11}$$

We seek now to analyze the spatial evolution of small perturbations of this equilibrium state.

Upon linearization, the Vlasov equation (4) can be written

$$\frac{\partial f^{(1)}}{\partial t} + \frac{cu_{oz}}{\gamma} \frac{\partial f^{(1)}}{\partial z} = \frac{n_o |e|}{mc} \vec{E}^{(1)} \cdot \frac{\vec{u}_o}{u} \frac{\partial g_o}{\partial u} \tag{12}$$

where a superscript (1) denotes a perturbed quantity and we have introduced the unperturbed density n_o by writing

$$f_o = n_o \delta(\vec{\alpha}_\perp) g_o(u). \tag{13}$$

Following Bernstein and Hirshfeld [1], we introduce a new set of basis vectors which track the wiggler field,

$$\hat{e}_1(z) = -\hat{x} \sin k_o z + \hat{y} \cos k_o z, \tag{14}$$

$$\hat{e}_2(z) = -\hat{x} \cos k_o z - \hat{y} \sin k_o z, \tag{15}$$

$$\hat{e}_3 = \hat{z}, \tag{16}$$

and seek monochromatic solutions of the linearized Vlasov-Maxwell equations corresponding to a perturbed electric field of the form

$$\vec{E}^{(1)}(z, t) = \text{Re}\, \vec{a}(z) \exp(-i\omega t). \tag{17}$$

The solution of the linearized Vlasov equation (12) can then be written

$$g^{(1)}(z, t) = g^{(1)}(o, t - z/v_{oz})$$

$$+ \exp[-i\omega(t - z/v_{oz})] \frac{|e|}{mcv_{oz}} \frac{u_{oz}}{u} \frac{\partial g_o}{\partial u}$$

$$\times \int_0^z dz' \exp\left(-\frac{i\omega z'}{v_{oz}}\right) \left[a_3(z') + \frac{v_{o\perp}}{v_{oz}} a_2(z')\right]. \tag{18}$$

The perturbed current density $\vec{J}^{(1)}$ can be written, upon linearization of (8) and for distribution functions of the form (13), as

$$\vec{J}^{(1)} = -n_o |e|c \int du \frac{u}{\gamma} \left[\left(\hat{z} + \frac{v_{o\perp}}{v_{oz}} \hat{e}_2\right) g^{(1)}\right.$$

$$\left. + \left(\frac{\vec{u}_\perp^{(1)}}{u_{oz}} - \frac{u_z^{(1)}}{u_{oz}^2} \vec{u}_{o\perp}\right) g_o\right] \tag{19}$$

where

$$\vec{u}_\perp^{(1)} = -\frac{i |e|}{mc\omega} \vec{a}(z), \tag{20}$$

$$u_z^{(1)} = -\frac{v_{o\perp}}{v_{oz}} \hat{e}_2 \cdot \vec{u}_\perp^{(1)}. \tag{21}$$

Expression (19), with $g^{(1)}$ replaced by (18), is now to be inserted into Maxwell's equations which take the form [1]

$$\frac{d^2 \vec{a}_\perp}{dz^2} + \frac{\omega^2}{c^2} \vec{a}_\perp = -\frac{4\pi i\omega}{c^2} \vec{J}_\perp^{(1)}, \tag{22}$$

$$a_z = -\frac{4\pi i}{\omega} J_z^{(1)}. \tag{23}$$

The $\hat{e}_1$, $\hat{e}_2$, $\hat{e}_3$ components of these equations then yield, respectively,

$$\frac{d^2 a_1}{dz^2} + \left(\frac{\omega^2}{c^2} - k_o^2\right) a_1 - 2k_o \frac{da_2}{dz}$$

$$= a_1 \frac{\omega_p^2}{c^2} \int du \, \frac{u}{\gamma u_{oz}} g_o, \tag{24}$$

$$\frac{d^2 a_2}{dz^2} + \left(\frac{\omega^2}{c^2} - k_o^2\right) a_2 + 2k_o \frac{da_1}{dz}$$

$$= a_2 \frac{\omega_p^2}{c^2} \int du \, \frac{u}{\gamma u_{oz}} \left(1 + \frac{v_{o\perp}^2}{v_{oz}^2}\right) g_o$$

$$+ \frac{i\omega}{c} \frac{\omega_p^2}{c^2} \int du \, \frac{v_{o\perp}}{v_{oz}} \frac{dg_o}{du} \int_0^z dz'$$

$$\cdot \exp\left[\frac{i\omega}{v_{oz}}(z - z')\right] \left[a_3(z') + \frac{v_{o\perp}}{v_{oz}} a_2(z')\right]$$

$$+ \frac{i\omega}{c} 4\pi n_o |e| \int du \, \frac{u}{\gamma} \frac{v_{o\perp}}{v_{oz}} \exp\left[\frac{i\omega}{v_{oz}} z\right] g^{(1)}(z = 0), \tag{25}$$

$$a_3 = \frac{i\omega}{c} \frac{\omega_p^2}{\omega^2} \int du \, \frac{dg_o}{du} \int_0^z dz' \exp\left[\frac{i\omega}{v_{oz}}(z - z')\right]$$

$$\times \left[a_3(z') + \frac{v_{o\perp}}{v_{oz}} a_2(z')\right] \tag{26}$$

where $\omega_p^2 = 4\pi n_o e^2/m$ denotes the plasma frequency of the beam.

In the chosen helical coordinate system, the set of integro-differential equations (24)–(26) has constant coefficients and multiple integrals of convolution type, and so can be conveniently solved by the Laplace transformation in z:

$$\tilde{a}(k) = \int_0^\infty dz \, e^{-ikz} \, \vec{a}(z). \tag{27}$$

The Laplace transformed versions of (24)–(26) are as follows:

$$-k^2 \tilde{a}_1 + \left(\frac{\omega^2}{c^2} - k_o^2\right) \tilde{a}_1 - 2ikk_o \tilde{a}_2 - \tilde{a}_1 \frac{\omega_p^2}{c^2} \int du \, \frac{u}{\gamma u_{oz}} g_o$$

$$= a_1'(0) + ika_1(0) - 2k_o a_2(0), \tag{28}$$

$$-k^2 \tilde{a}_2 + \left(\frac{\omega^2}{c^2} - k_o^2\right) \tilde{a}_2 + 2ikk_o \tilde{a}_1 - \tilde{a}_2 \frac{\omega_p^2}{c^2} \int du \, \frac{u}{\gamma u_{oz}}$$

$$\cdot \left(1 + \frac{v_{o\perp}^2}{v_{oz}^2}\right) g_o - \frac{\omega}{c} \frac{\omega_p^2}{\omega^2} \int du \, \frac{v_{o\perp}}{v_{oz}} \frac{dg_o}{du} \frac{v_{oz}}{(kv_{oz} - \omega)}$$

$$\cdot \left(\tilde{a}_3 + \frac{v_{o\perp}}{v_{oz}} \tilde{a}_2\right)$$

$$= \frac{\omega}{c} 4\pi n_o |e| \int du \, \frac{u}{\gamma} \frac{v_{o\perp}}{v_{oz}} \frac{v_{oz}}{(kv_{oz} - \omega)} g^{(1)}(z = 0)$$

$$+ a_2'(0) + ika_2(0) + 2k_o a_1(0), \tag{29}$$

$$\tilde{a}_3 - \frac{\omega}{c} \frac{\omega_p^2}{\omega^2} \int du \, \frac{dg_o}{du} \frac{v_{oz}}{(kv_{oz} - \omega)} \left(\tilde{a}_3 + \frac{v_{o\perp}}{v_{oz}} \tilde{a}_2\right)$$

$$= \frac{c}{\omega} 4\pi n_o |e| \int du \, \frac{u}{\gamma} \frac{v_{oz}}{(kv_{oz} - \omega)} g^{(1)}(z = 0). \tag{30}$$

This system can be written symbolically in the form

$$\overleftrightarrow{\epsilon}(k) \cdot \vec{a}(k) = \vec{I}(k) \tag{31}$$

where $\overleftrightarrow{\epsilon}(k)$ represents the 3×3 dispersion tensor of the equilibrium configuration and $\vec{I}(k)$ the initial perturbations at $z = 0$.

The entries in the dispersion tensor $\overleftrightarrow{\epsilon}(k)$ can be identified directly from the transformed equations (28)–(30). With the normalizations

$$x = \frac{kc}{\omega}, \quad x_o = \frac{k_o c}{\omega}, \quad p = \frac{\omega_p}{\omega}, \tag{32}$$

we find the following:

$$\epsilon_{11} = 1 - (x_o^2 + x^2) - p^2 \int_{\xi_o}^\infty du \, \frac{u}{\gamma u_{oz}} g_o, \tag{33}$$

$$\epsilon_{22} = 1 - (x_o^2 + x^2) - p^2 \int_{\xi_o}^\infty du \, \frac{u}{\gamma u_{oz}} \left(1 + \frac{\xi_o^2}{u_{oz}^2}\right) g_o$$

$$+ p^2 \int_{\xi_o}^\infty du \, \frac{\xi_o^2}{u_{oz}^2} \frac{dg_o}{du} \frac{u_{oz}}{(\gamma - xu_{oz})}, \tag{34}$$

$$\epsilon_{33} = 1 + p^2 \int_{\xi_o}^\infty du \, \frac{u_{oz}}{(\gamma - xu_{oz})} \frac{dg_o}{du}, \tag{35}$$

$$\epsilon_{12} = -\epsilon_{21} = -2ix_o x, \tag{36}$$

$$\epsilon_{23} = \epsilon_{32} = p^2 \xi_o \int_{\xi_o}^\infty du \, \frac{1}{(\gamma - xu_{oz})} \frac{dg_o}{du}, \tag{37}$$

$$\epsilon_{13} = \epsilon_{31} = 0 \tag{38}$$

where $u_{oz} = (u^2 - \xi_o^2)^{1/2}$ and $\gamma = (1 + u^2)^{1/2}$. Note that the off-diagonal elements occur in pairs since the dispersion tensor $\overleftrightarrow{\epsilon}$ must be Hermitian for (ω, k) real and in the absence of dissipation to resonant particles.

Finally, the entries in the inital perturbation vector are as follows:

$$I_1(k) = \frac{c^2}{\omega^2} [ika_1(0) + a_1'(0) - 2k_o a_2(0)], \tag{39}$$

$$I_2(k) = \frac{c^2}{\omega^2} [ika_2(0) + a_2'(0) + 2k_o a_1(0)]$$

$$+ \frac{4\pi n_o |e| c^2}{\omega} \xi_o \int_{\xi_o}^\infty du \, \frac{u}{\gamma^2} \frac{\omega}{(kv_{oz} - \omega)} g^{(1)}(z = 0), \tag{40}$$

$$I_3(k) = \frac{4\pi n_o |e| c}{\omega} \int_{\xi_o}^\infty du \, \frac{u}{\gamma} \frac{v_{oz}}{(kv_{oz} - \omega)} g^{(1)}(z = 0). \tag{41}$$

III. The Dispersion Relation

The dispersion relation $det\ \tilde{\epsilon}(k) = 0$ can be written

$$\epsilon_{33}Q(x) = \epsilon_{23}^2 \epsilon_{11} \qquad (42)$$

where

$$Q(x) = \epsilon_{11}\epsilon_{22} + \epsilon_{12}^2. \qquad (43)$$

There are six roots which, when uncoupled, correspond to two space-charge waves ($\epsilon_{33} = 0$) and to two backward and two forward propagating electromagnetic waves ($Q = 0$). $Q(x)$, save terms proportional to p^2, can be approximated by

$$Q(x) \approx [1 - (x_o^2 + x^2)]^2 - 4x_o^2 x^2, \qquad (44)$$

which has the four roots

$$x = -1 \pm x_o, \qquad x = 1 \pm x_o. \qquad (45)$$

The longitudinal factor ϵ_{33} can be written $\epsilon_{33} = (1 + p^2\chi)$, where χ denotes the susceptibility function

$$\chi(x) = \int_{\xi_o}^{\infty} du \, \frac{u_{oz}}{(\gamma - xu_{oz})} \frac{dg_o}{du}. \qquad (46)$$

For a Gaussian distribution, χ is shown in Figs. 1 and 2, where Δ denotes the standard deviation of $g_o(u)$. Qualitatively, χ has features similar to those of the usual plasma dispersion function.

The dispersion relation (42) was solved numerically for the following parameters: $\omega_P = 5.026 \times 10^{10}$ rad/s, $\xi_o = 0.058$, $k_o = 5.027$ cm^{-1}, $\gamma = 2.5$, and several values of the energy spread Δ. An initial frequency ω was given as an input and the real and imaginary parts of the wave vector k were calculated. The energy integrals appearing in $\tilde{\epsilon}(k)$ were analytically continued in the sense of Landau whenever Im $k > 0$. For x real and $x > 1$, we have

$$\mathrm{Re}\,\chi(x) = \frac{1}{2u_{res}(x^2 - 1)} \left[\int_{\xi_o}^{\infty} du \, \frac{dg_o}{du} \frac{(\gamma + xu_{oz})}{(u - u_{res})} \right.$$

$$\left. - \int_{\xi_o}^{\infty} du \, \frac{dg_o}{du} \frac{(\gamma + xu_{oz})}{(u + u_{res})} \right], \qquad (47)$$

$$\mathrm{Im}\,\chi(x) = \frac{\pi}{2u_{res}(x^2 - 1)} \frac{dg_o}{du}\bigg|_{u=u_{res}} (\gamma + xu_{oz})\bigg|_{u=u_{res}} \qquad (48)$$

where

$$u_{res} = \left[\frac{(1 + \xi_o^2 x^2)}{(x^2 - 1)} \right]^{1/2}. \qquad (49)$$

The first term on the right-hand side of (49) is the dominant one.

It is illustrative to compare solutions to the dispersion relation for the thermal and cold beam cases. In both cases, there are six roots. The significant difference between them is that the space-charge wave roots become more separated and Landau damped. The indexes of refraction for both waves satisfy,
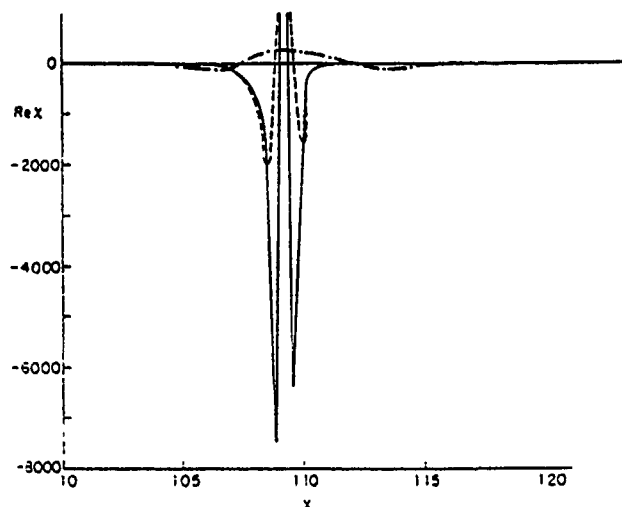

Fig. 1. Real part of longitudinal susceptibility (Re χ) versus index of refraction (x). $\omega_p = 5.027 \times 10^{10}$ rad/s, $k_o = 5.027$ cm^{-1}, $\xi_o = 0.058$, $\gamma = 2.5$, $B_z = 0$. —— $\Delta = 1$ percent, - - - $\Delta = 2$ percent, -·-· $\Delta = 10$ percent.
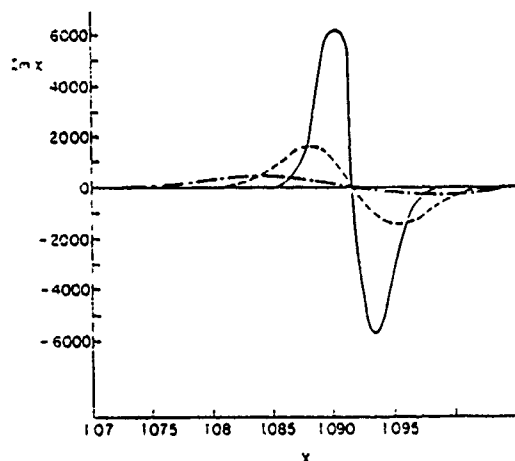

Fig. 2. Imaginary part of longitudinal susceptibility (Im χ) versus index of refraction (x). —— $\Delta = 1$ percent, - - - $\Delta = 2$ percent, -·-· $\Delta = 5$ percent.

when uncoupled, the dispersion relation

$$X_{p1, p2} = \frac{c}{v_{zo}} \left(1 \pm \frac{P}{\gamma_o^{3/2}} \right) \pm f(\Delta) \qquad (50)$$

where f is an increasing function of momentum spread which goes to zero at $\Delta = 0$ and v_{zo} is the central parallel velocity. From (45), the uncoupled forward electromagnetic waves satisfy approximately

$$X_{em\pm} = 1 \pm X_o. \qquad (51)$$

Therefore, the coupling occurs at lower frequency and the spectrum broadens as Δ increases.

When the slow space-charge wave couples to $em+$, we note the following:

1) The roots corresponding to the two coupled waves are no longer complex conjugates since the dispersion relation is no longer a sixth order polynomial.

2) The real parts of the coupled roots are shifted and the growth rate is diminished due to Landau damping.
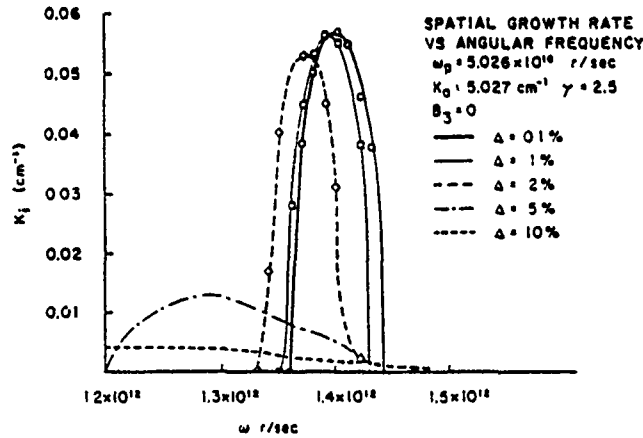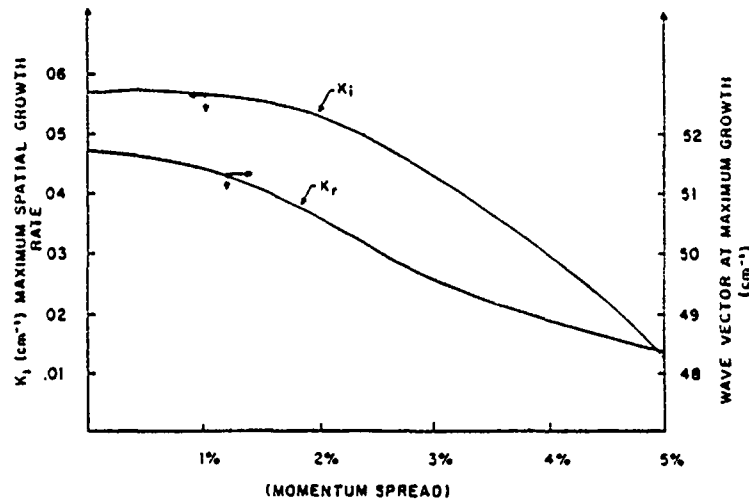
Fig. 3. Spatial growth rate versus angular frequency.

Fig. 4. Maximum spatial growth rate (left axis) and wave vector at central frequency (right axis) versus momentum spread Δ.

3) The shift of the real parts is minimum at the frequency corresponding to the highest growth rate.

The spatial growth rate as a function of frequency is shown in Fig. 3. The spectrum shifts towards lower frequencies when Δ increases. At about a 2 percent spread, it starts to develop a tail. Both the maximum growth rate and its corresponding wave vector decrease with Δ (Fig. 4); for a spread of 5 percent, k_r at maximum decreases by about 10 percent.

It is instructive to track how the two space-charge waves and the two electromagnetic waves interact with the distribution function. One electromagnetic wave couples to the negative-energy space-charge wave while they interact with electrons in the region of positive slope of the distribution function. However, the growth rate diminishes due to the fact that the slow space-charge wave has negative energy. This can be observed numerically since

$$\frac{dx}{d\omega} \simeq \frac{c}{\omega} \frac{(v_{ph} - v_g)}{v_{ph}v_g}, \qquad (52)$$

and so sign $(\Delta x/\Delta \omega) = $ sign $(v_{ph} - v_g)$.

At larger frequencies, once the $em+$ wave and the negative-energy slow space-charge wave have coupled, both space-charge
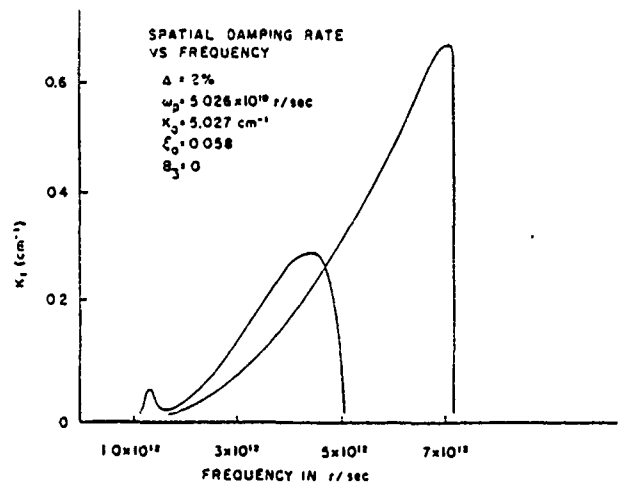
Fig. 5. Spatial damping rate of one coupled mode (curve with two maxima) and the fast space-charge mode (curve with only one maximum) versus angular frequency. $\Delta = 2$ percent.

waves are Landau damped (Fig. 5). At a spread of about 2 percent, there is a small bump in the damping rate for the damped coupled mode. For frequencies for which there is a tail in the growth rate in one of the modes, the damping of

the other mode does not go monotonically to zero, but instead it goes through a local minimum and then continues growing. There is no other region of coupling; at larger frequencies the em+ wave crosses over the positive energy space-charge wave without coupling.

IV. INITIAL-VALUE PROBLEM

Consider next the inversion of the Laplace transformation according to the relation

$$\vec{a}(z) = \frac{1}{2\pi} \int_C dk \, e^{ikz} \, \vec{a}(k) \tag{53}$$

where C denotes the usual Bromwich contour below all the singularities of $\vec{a}(k)$. Now from (31), we have

$$\vec{a}(k) = [\vec{\epsilon}(k)]^{-1} \cdot \vec{I}(k) \tag{54}$$

where we can write

$$[\vec{\epsilon}(k)]^{-1} = \frac{\vec{Q}(k)}{D(k)}, \tag{55}$$

with $\vec{Q}(k)$ the cofactor tensor for $\vec{\epsilon}^T$ and $D(k) = det \, \vec{\epsilon}(k)$. Employing the Residue Theorem to evaluate the integral (53), we find the superposition of modes

$$\vec{a}(z) = i \sum_{j=1}^{6} \frac{\vec{Q}(k_j) \cdot \vec{I}(k_j)}{\frac{dD}{dk}\Big|_{k_j}} e^{ik_j z} \tag{56}$$

where $(k_1, \cdots, k_6)$ denote the six zeros of $D(k)$. In particular, we have

$$a_2(z) = i \sum_{j=1}^{6} B_j e^{ik_j z} \tag{57}$$

where

$$B_j = \sum_{l=1}^{3} \frac{Q_{2l}(k_j) I_l(k_j)}{\frac{dD}{dk}\Big|_{k_j}}. \tag{58}$$

Recall that expressions for the initial perturbations $\vec{I}(k)$ at $z = 0$ are given by (39)-(41).

In order to model an amplifier experiment, it is assumed that the two backward-propagating electromagnetic modes have zero amplitude. As pointed out by Bernstein and Hirshfield, these conditions $(B_1 = 0$ and $B_2 = 0)$ can serve to determine $a_1'(0)$ and $a_2'(0)$ in terms of $a_1(0)$ and $a_2(0)$. In this work, the polarization of the incident wave was chosen as $a_1(0) = 0$ and $a_2(0) = 1$. We assume here that the amplitude of the incident radiation field dominates any fluctuation fields present at $z = 0$ although such effects can readily be accommodated in the formalism.

The expression (57) was evaluated numerically for different momentum spreads Δ and for the same set of parameter values employed in the solution of the dispersion relation. For the root with an imaginary part greater than zero, the momentum integral was analytically continued by adding the residue at the pole. The formalism allows for the use of an arbitrary perturbation function at the entrance of the interaction region
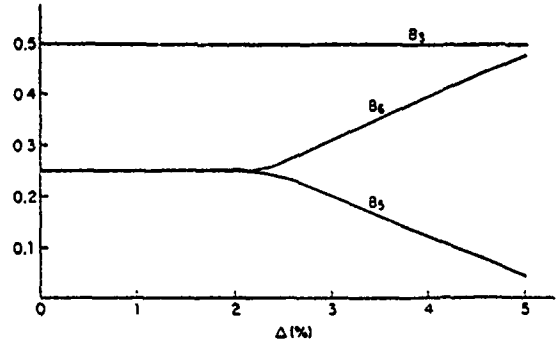

Fig. 6. Mode coefficients versus momentum spread at central emission frequency. B_3 uncoupled electromagnetic modes, B_5, B_6 coupled modes.

$g^{(1)}(z = 0)$. It is assumed in this work that $g^{(1)}(z = 0) = 0$. It is possible, however, to treat some design features by means of this perturbation, such as the extra perpendicular energy spread due to nonadiabaticity at the entrance to the wiggler region.

The fast space-charge wave has negligible amplitude $(B_4 \approx 0)$. When temperature increases, B_3 (uncoupled electromagnetic mode) remains close to 0.5, but B_6 progressively increases, approaching 0.5, whereas B_5 approaches zero (see Fig. 6).

From (58), we have

$$B_j = \frac{i\epsilon_{33}(\epsilon_{12}I_1 + \epsilon_{11}I_2)}{dD/dk}\Bigg|_{k_j} \tag{59}$$

where

$$\frac{dD}{dk} = \frac{d\epsilon_{33}}{dk} Q + \epsilon_{33} \frac{dQ}{dk} + O(\xi_0^2) \tag{60}$$

for small pump parameters ξ_0. Thus, for the fast space-charge wave x_4, $\epsilon_{33}(x_4) \approx 0$ and so

$$B_4 \approx \frac{i\epsilon_{33}(\epsilon_{12}I_1 + \epsilon_{11}I_2)}{Q d\epsilon_{33}/dk}\Bigg|_{k_4} \approx 0. \tag{61}$$

For x_3, eliminating $a_1'(0)$ and $a_2'(0)$ and substituting, we find

$$B_3 \approx \frac{i(\epsilon_{12}I_1 + \epsilon_{11}I_2)}{dQ/dk}\Bigg|_{k_3} \approx \frac{1}{2}, \tag{62}$$

save terms of order p^2.

In the cold beam limit in the complex roots regime, B_5 and B_6 are complex conjugates; then, $Re \, B_5 = Re \, B_6 = 0.25$. For both roots, $\epsilon_{33} \approx 0$ but also $Q \approx 0$ and so B_5 and B_6 remain finite. In a thermal beam, there is a mismatch between the roots and one tends to satisfy $\epsilon_{33} \approx 0$ but not $Q \approx 0$ and vice versa. Consequently, one amplitude approaches zero and the other 0.5 (Fig. 6).

Fig. 6 shows how the situation evolves from a three-mode process into a two-mode one when the temperature increases. It is not that both space-charge waves become Landau damped, but rather that they start with a very small amplitude at the entrance of the interaction region when the temperature is significant. Fig. 7 shows the inverse of the coupling loss as function of momentum spread. For values of Δ less than 2 percent, there is a small increase when the roots become slightly more separated. For values greater than 2 percent, it
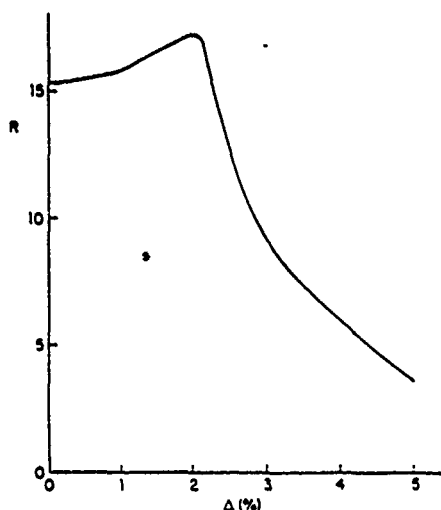
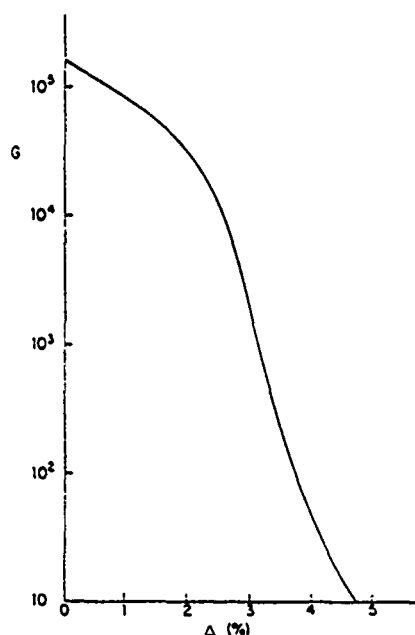Fig. 7. Inverse of the coupling loss versus momentum spread.

Fig. 9. Power gain versus distance.

Fig. 8. Power gain versus momentum spread at 100 wiggler wavelengths. The power gain is defined as the electromagnetic power at distance z, divided by the electromagnetic power at the entrance of the interaction region.

Fig. 10. Power gain versus initial frequency.

decreases monotonically. It is thus possible to extend the region of permissible temperatures for a free-electron laser by recognizing that the decrease in the coupling loss can compensate for the Landau damping. This regime would be an intermediate one between Compton and Raman operations (Fig. 8). It should be borne in mind that our linearized perturbation theory becomes invalid when the gain is sufficiently great that nonlinear effects become important. Our results for 100 wiggler lengths, for example, should be considered within the limitations of linear theory.

As was the case for the cold beam analyzed in [1], the longitudinal component of the electric field is orders of magnitude lower than the transverse ones. Outside the frequency range for which there are complex conjugate roots, the gain due to pure spatial interference of the modes was only a factor of
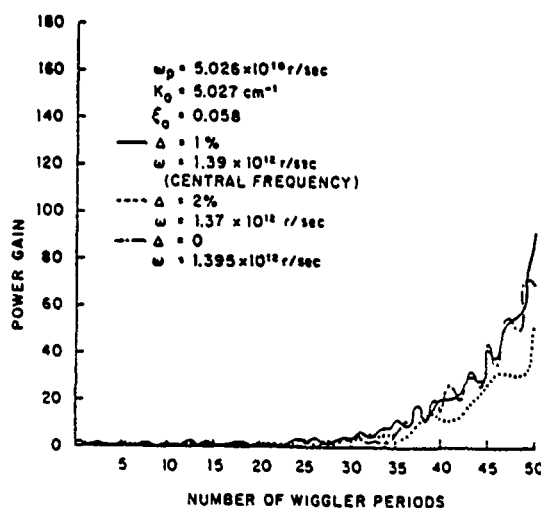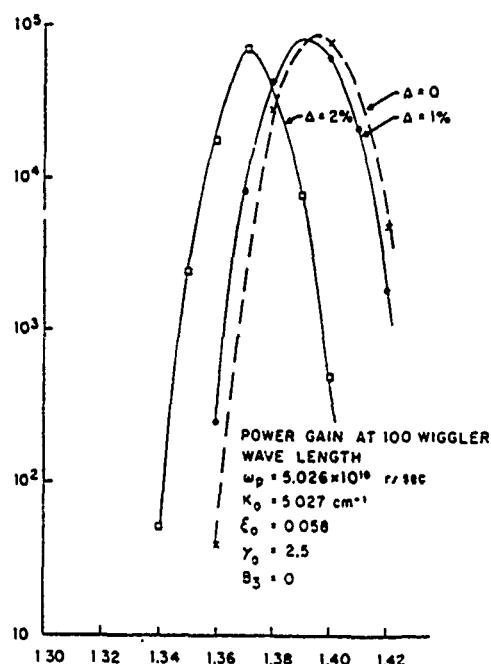
about 4–100 wiggler wavelengths for a momentum spread of 2 percent.

The radiation power oscillates as a function of distance due to spatial interference of the competing modes. At the frequency corresponding to the central emission, these oscillations become milder when the momentum spread increases (Fig. 9). There is a characteristic length at which finite temperature effects are important, it is given approximately by $1_\Delta = u_o(2\pi/k_o\Delta)$. At distances smaller than 1_Δ, the amplitude of the power oscillations is such that the cold and thermal beam cases are indistinguishable. In Fig. 9, the power at 50 wiggler wavelengths corresponding to a momentum spread of 2 percent can be distinguished from the cold beam case, but the distinction between the cold beam and the $\Delta = 1$ percent beam is not possible. However, at 100 wiggler wavelengths, the difference between the cold and the $\Delta = 2$ percent beams is clear (Fig. 10).

V. Conclusions

We have used the formalism initially developed in [1] for the free-electron laser without guide magnetic field and have extended it by considering a thermal beam and analytically continuing the momentum integrals. The momentum spread of the beam causes a mismatch between the coupling waves which, in turn, causes reduction of the growth rate, broadening of the spectrum, and lowering of the central emission frequency with momentum spread.

In the amplifier formulation, the temperature effects become noticeable at distances greater than l_Δ, and only three modes propagate for small momentum spreads. As Δ increases, there is a gradual transition from a three-mode to a two-mode situation with an intermediate region where the decrease in coupling loss can compensate for Landau damping.

References

[1] I. B. Bernstein and J. L. Hirshfield, "Amplification on a relativistic electron beam in a spatially periodic transverse magnetic field," *Phys. Rev. A*, vol. 20, p. 1661, 1979.

[2] P. Diament, "Electron orbits and stability in realizable and unrealizable wigglers of free electron lasers," *Phys. Rev. A*, vol. 23, p. 2537, 1981.

Luis F. Ibanez received the Licenciatura in physics from Univefsidad Complutense, Madrid, Spain, and the M.Sc. degree in nuclear engineering from the University of Florida, Gainesville. He is currently a doctoral candidate in plasma physics at Columbia University, New York, NY.

His current interests are free-electron lasers and MHD theory.

Shayne Johnston, for a photograph and biography, see this issue, p. 327.

A Free Electron Laser Oscillator Based on a Cyclotron–Undulator Interaction

ARTHUR A. GROSSMAN AND T. C. MARSHALL

Abstract—A free electron laser (FEL) oscillator experiment is described, in which an intense electron beam (750 kV, 20 kA) is prepared in a region of increasing guide magnetic field before injection into an undulator (60 periods, l_o = 1.25 cm). The electron motion accordingly has a substantial transverse component ($\beta_\perp \approx 0.4$), and motion at the cyclotron ($\omega_c = eB_o/\gamma mc$) and undulator ($k_o V_z$) frequencies occurs. Theory predicts, in appropriate geometry, a convectively unstable electromagnetic wave having frequency $\omega_s \approx 2\gamma_z^2 (\omega_c + k_o V_z)$, where $\gamma_z = (1 - \beta_z^2)^{-1/2}$, of the FEL type, where $k_o = 2\pi/l_o$. Megawatt level radiation at 1.7 mm, together with millimeter-harmonics and other microwave emission, is observed in a simple Fabry-Perot resonator system driven above oscillation threshold by a sufficiently large undulator field amplitude. Comparison of spectroscopic data with features of the theory permits identification of the cyclotron-undulator interaction.

I. INTRODUCTION

THE Raman free electron laser is based on stimulated backscattering of radiation from a cold intense relativistic electron beam traversing a region of superimposed uniform guide and periodic undulator fields [1]. Thermal spreads among the beam electrons can seriously degrade the performance of a Raman free electron laser because the collective electrostatic mode suffers from Landau damping.

Recently, we demonstrated that an intense beam of spiraling electrons with large initial transverse velocities can support stimulated emission as a free electron laser oscillator at millimeter wavelengths [2]. One would not expect Raman emission from this device, because the method of imparting a substantial component of velocity transverse to the predominantly axial drift of the beam also tends to impart thermal spread to the beam. This observation strongly suggests that another process besides stimulated Raman scattering is at work here. This new process involves an electromagnetic mode featuring a cyclotron-undulator interaction. Although an electromagnetic process such as cyclotron emission is best exploited with a cold beam, the requirements on the beam thermal spread are less stringent than in the Raman case.

Cyclotron emission from electrons gyrating in a uniform magnetic field alone has been the subject of intense research activities in connection with the recent development of the gyrotron or cyclotron maser, which is an impressive source of high power short wavelength microwaves. In the cyclotron maser instability, azimuthal bunching occurs as a consequence of the relativistic dependence of the cyclotron frequency.

Axial bunching from the Weibel instability, which results from velocity space anisotropy, can occur concurrently. In general, the two instabilities are strongly coupled together. However, it has been shown that azimuthal bunching dominates the fast waves, while axial bunching dominates the slow ones [3].

With the introduction of an undulator in the system, this picture of the electromagnetic emission becomes rather more complicated. This is due largely to the orbits in the combined fields, which are in general quite different from the simple helices executed in uniform fields. However, under certain limiting conditions of these combined fields, one may recover approximately helical orbits. In Section II of this paper we briefly review a theory of the cyclotron-undulator interaction which uses an especially simple orbit which appears appropriate for our experiment.

In Sections III and IV we present new experimental results with the system configured as a multipass laser oscillator. Dependences of the emission on undulator field strength and guide magnetic field are presented. We find the fast positive energy cyclotron-undulator interaction can account for the emission at millimeter wavelengths. Studies of the long wavelength emission in the X and 2 cm microwave bands are presented. An interesting correlation is found between the 2 cm band emission and the millimeter wavelength emission.

II. REVIEW OF THEORETICAL ANALYSIS

In a previous paper [2] we modeled the cyclotron-undulator instability using linear kinetic theory in parallel plate waveguide geometry, following the model of Ott and Manheimer [4]. The beam propagates along the Z-direction, with infinite conducting surfaces in the Y-Z plane, located at $x = \pm a$. Numerical solution [5] for the orbits of the electrons in the external guide and "realizable" helical undulator fields indicate the unperturbed orbits are (see Fig. 1)

$$V_x = V_\perp \cos \omega_c t + V_w \cos k_o V_z t$$

$$V_y = V_\perp \sin \omega_c t + V_w \sin k_o V_z t$$

$$V_z = V_\parallel \tag{1}$$

provided $V_w \ll V_\perp \ll V_z$ and $B_o \gg B_w$ where $k_o = 2\pi/l_o$ is the wavenumber for the undulator with periodicity l_o, and we model the quiver velocity of electrons in the undulator by $V_w = (\Omega_o V_z)/(\omega_c - k_o V_z)$ where $\omega_c = |eB_o/\gamma mc|$ is the cyclotron frequency of the guide field and $\Omega_o = |eB_w/\gamma mc|$ is the undulator cyclotron frequency. B_w is the amplitude of the undulator field transverse component measured at the location of the thin electron beam.
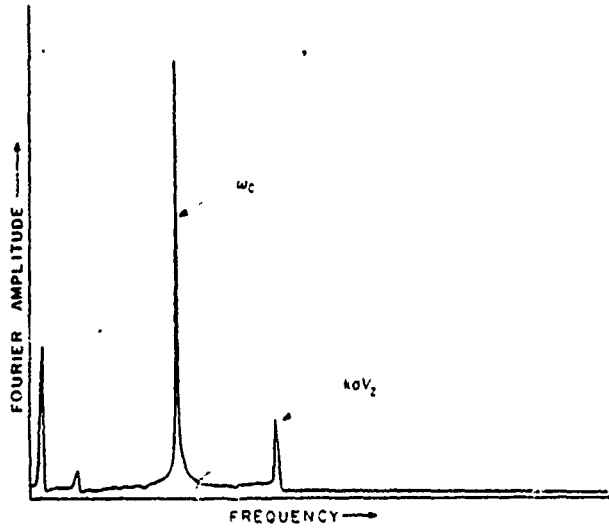
Fig. 1. Fourier amplitude of a transverse component of electron velocity computed in combined undulator and uniform magnetic fields versus frequency, showing prominent components at the cyclotron (ω_c) and undulator ($K_o V_z$) frequencies. Beam energy, 600 kV; $l_o = 12.5$ mm, $B_o = 10$ kG.

For a cold beam consisting of particles with momenta parallel (P_z) and transverse ($P_\perp$) to the guide magnetic field, the dispersion relation for the TE_{or} mode was found [2] by integrating the Vlasov-Maxwell equations along the unperturbed orbit to be

$$\omega^2 - (k^2 + k_r^2)c^2 = -\frac{\omega_p^2 m}{k_r d} \sum_{nl} \left\{ \frac{1}{R_r} \left[\left(\omega - \frac{kP_z}{\gamma m} \right) \frac{\partial B_{nl}}{\partial P_\perp} \right. \right.$$

$$\left. + \frac{kP_\perp}{\gamma m} \frac{\partial B_{nl}}{\partial P_z} \right] + \frac{B_{nl}}{(R_{nl})^2} \frac{P_\perp}{\gamma m^2}$$

$$\cdot \left[k(k + lk_o) - \frac{\omega^2}{c^2} \right] \right\} \qquad (2)$$

where $B_{nl} = d \, [\gamma \omega_c d J_n'^2(d) J_l^2(u) + \frac{1}{4} k_o (P_z/m) J_n^2(d)' u J_l^2(u)']$ and $R_{nl} = \gamma [\omega - (k + lk_o) V_z - n \omega_c]$, $d = k_r V_\perp/\omega_c$, $u = k_r V_w/$ $k_o V_z$, $k_r = r\pi/2a$, r is an integer. J_m denotes the mth order Bessel function and primes denote differentiation with respect to the argument.

For instability to occur, the resonant denominator should vanish: $R_{nl} \approx 0$. Eliminating wave number k by requiring the lowest order real part of the frequency to satisfy the vacuum relation $\omega^2 = (k^2 + k_r^2)c^2$ gives two intersections of the waveguide mode with the beam cyclotron wave for the real part of the n, lth frequency component at which growth may occur:

$$\omega_s = \gamma_z^2 (lk_o V_z + n \omega_c) [1 \pm \beta_z \alpha] \qquad (3)$$

where

$$\alpha = \left[1 - \left(\frac{k_r c}{\gamma_z (lk_o V_z + n \omega_c)} \right)^2 \right]^{1/2} .$$

Consider the Doppler upshifted, upper intersection, convective case (+ sign) of the fundamental mode $n = l = 1$ and $\alpha \approx 1$. The approximate real frequency for this mode is then simply

$$\omega_s = 2\gamma_z^2 (k_o V_z + \omega_c). \qquad (4)$$

Solving the dispersion relation for small perturbations about this frequency yields a growth rate which scales as $[\omega_p V_\perp V_w k_r]^{2/3}$ and is given by

$$\text{Im} (\delta \omega) = \pm \frac{1}{4} \sqrt{3} \left[\frac{\omega_p^2 \omega_c}{4 \gamma \omega_s} (\omega_c + k_o V_z) \left(\frac{kk_o}{k_r^2} - 1 \right) d^2 u^2 \right]^{1/3} \qquad (5)$$

provided we are much above the threshold given by

$$|du| > \frac{\omega_p^2}{\gamma \gamma_z^2} (3/2 k_o V_z)^{-3/2} \left(\left| \frac{kk_o}{k_r^2} - 1 \right| \omega_c \right)^{-1/2} . \qquad (6)$$

Since Im $(\delta \omega) \to 0$ when $k_r \to 0$, this interaction is not expected to occur for a purely transverse electromagnetic wave. However, McMullin and Bekefi [6] have found an interaction with frequency given by (4) but different growth rate that can occur with a purely transverse scattered wave, provided the undulator field is purely longitudinal.

III. EXPERIMENTAL APPARATUS

The intense relativistic electron beam used in the Columbia free electron laser experiments is generated by a Physics International 220G electron accelerator. A 10 kJ Marx generator charges a 75 ns, 20 Ω coaxial pulse-forming line to a typical peak voltage of 2 MV. A variable impedance matching radial disk resistor enables a flattop voltage to be obtained with duration between 120 and 150 ns. When the pulse-forming line is fully charged to peak voltage, an untriggered SF_6 switch is used to transfer energy directly to vacuum diode. The 20 kA, 600–800 kV annular beam (field-emitted from a graphite cathode) has a 4 cm diameter and a thickness of 1–2 mm, and propagates through a drift tube with ID = 4.7 cm. The interaction region consists of a 60 period pulsed bifilar helical undulator with adiabatic transitions (field taper) at each end; its transverse field is variable up to 1.3 kG and the spatial periodicity is fixed at 12.5 mm. This field is superimposed on a uniform guide field which can be varied independently up to 11 kG, although the beam equilibrium condition requires a minimum field of 8 kG.

The field compression technique was used to generate a beam with appreciable transverse motion. The graphite cathode with an aluminum mirror insert is located in the fringe magnetic field (Fig. 2) zone of a long solenoid. Electrons are adiabatically guided into the drift tube along convergent field lines. As B_o increases downstream, we expect the transverse velocity $\beta_\perp$ to increase and the beam radius R_B to decrease according to

$$\frac{\beta_\perp}{\beta_{\perp k}} \approx \frac{R_k}{R_B} \approx \sqrt{\frac{B_o}{B_{ok}}} \qquad (7)$$

where the subscript k denotes the value at the cathode. Since the electrons are emitted at the cathode in crossed magnetic and electric fields,

$$\beta_{\perp k} = 3.3 \cdot 10^{-6} \frac{E_{\perp k}}{B_{ok}}. \qquad (8)$$

For $E_k = 0.5$ MV/cm, $B_{ok} = 5$ kG, and $B_o = 10$ kG, we calculate $\beta_\perp = 0.4$. For $2R_k = 5.8$ cm, we calculate $2R_B = 4.0$
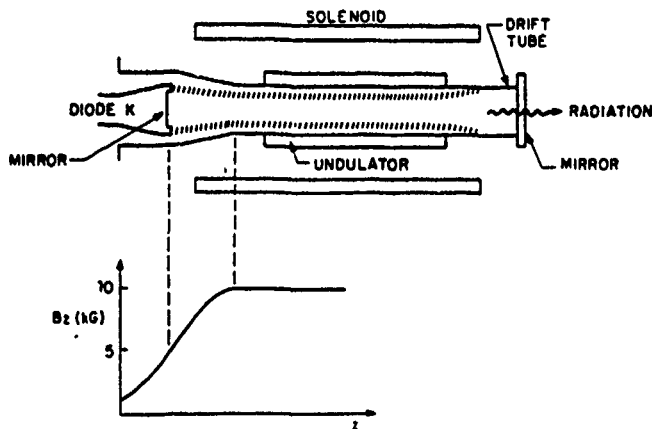
Fig. 2. The FEL oscillator system. The mirror at the cathode is a polished aluminum plate inserted into the graphite cathode (diameter 5.8 cm). The distance between the cathode and the anode mirror is about 150 cm.
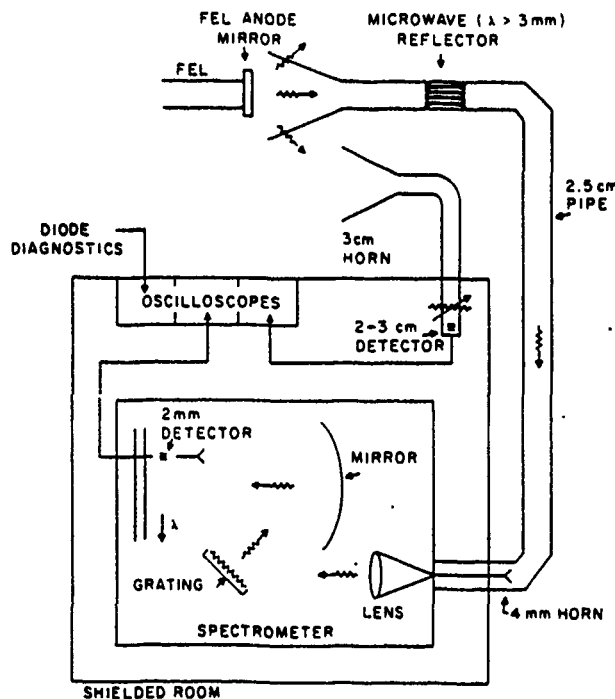

Fig. 3. Arrangement of diagnostics, showing the millimeter spectrometer.
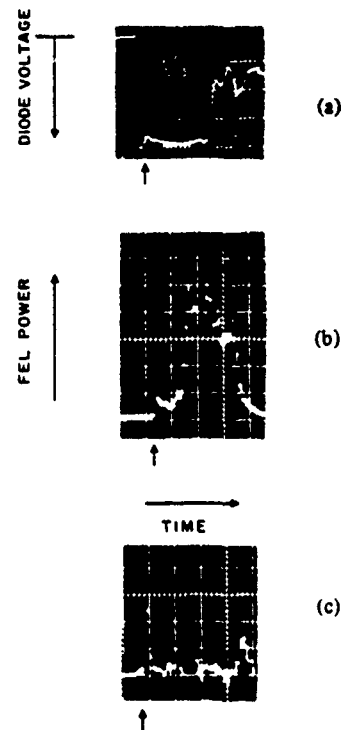

Fig. 4. (a) Diode voltage waveform (800 kV). (b) Radiation at $\lambda = 1.6$ mm when both mirrors are in place and aligned. 20 mV/div., vertical. (c) Radiation at $\lambda = 1.6$ mm when anode mirror is replaced by a thin polyethylene window; scale, 50 ns/div., arrow indicates $t = 0$ on each photo. 5 mV/div., vertical.

Spectral analysis of the scattered radiation can be performed with either a Fabry–Perot interferometer or a calibrated grating spectrometer. The detector is a point-contacted GaAs Schottky barrier diode mounted in a WR/5 waveguide.

Microwaves in the 2 cm and X bands were simultaneously detected with a completely separate detection system. An X band standard gain horn was located immediately below the quartz output coupler. Attenuation consisted of a sheet of eccosorb which completely covered the horn and a series of four standard calibrated attenuators. Either an X band diode detector or a 2 cm band diode detector and transition section could be used.

IV. EXPERIMENTAL RESULTS

Spectral analysis of the emission with wavelength in the range of 1–2.5 mm (120–300 GHz) is made with a calibrated grating spectrometer. Relatively coherent [Fig. 4(b)] narrow bandwidth emission is observed when the anode mirror is in place [2]. A relatively crude alignment of the anode and cathode mirrors is adequate at this wavelength. However, replacing the aluminized quartz anode mirror with an uncoated polyethylene window causes the coherent emission to vanish, leaving only the broad-band emission from the initial and occasionally final diode voltage transients [Fig. 4(c)]. For $\gamma = 2.4$, $\beta_\perp = 0.4$, $\beta_z = 0.8$, $k_o V_z = 2\pi(20 \text{ GHz})$, $\omega_c = 2\pi(12 \text{ GHz})$, we find from (4) that $\omega_s = 2\pi(160 \text{ GHz})$, or $\lambda_s = 1.8$ mm. As seen from Fig. 5, the theoretical frequency agrees quite well with the experimental observations. The reduction in bandwidth at the higher energy may be due to improved beam quality. Increasing the undulator strength causes the spectrum

cm, which agrees with the value determined experimentally from graphite "witness plates." The value of $\beta_\perp$ is found to be compatible with the value of β_z inferred from measurements with thermal sensitive paper, using the total beam energy inferred from the diode voltage. Numerical simulation [7] of the electron motion in this field compression geometry indicates an axial velocity spread of at least 4 percent and a transverse velocity spread of at least 10 percent.

Radiation emerging from this oscillator configuration is coupled out through a vacuum window which consists of aluminum coated z-cut quartz with a 2 cm aperture, mounted on vacuum bellows, so as to permit alignment parallel to the cathode mirror. The radiation is passed through several high-pass filters ($\lambda < 3$ mm) and is transmitted along 7 m of a 2.5 cm diameter brass pipe into a shielded room (Fig. 3).
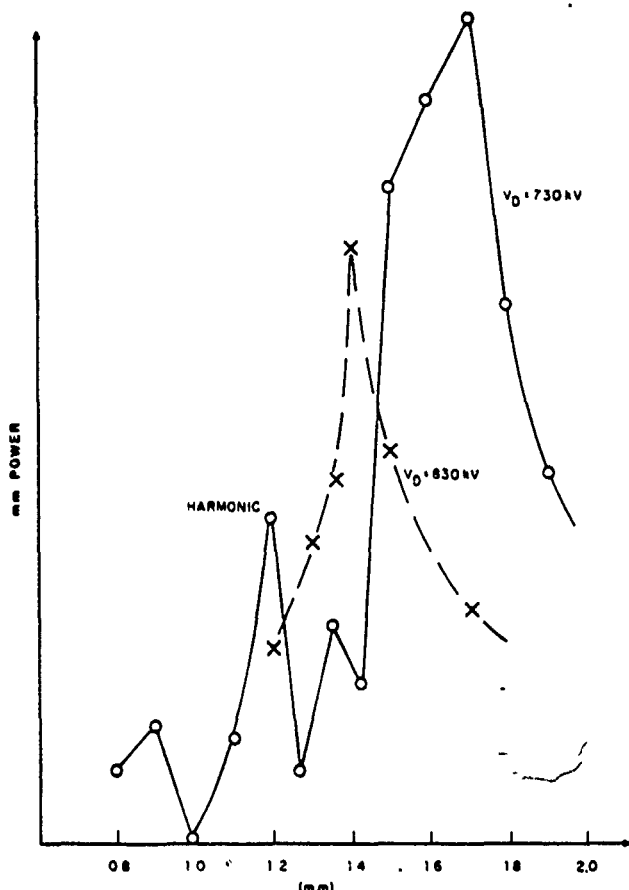
Fig. 5. FEL power versus wavelength at two values of diode voltage V_D. The point marked "harmonic" is the location of the $l = 1, n = 2$ mode from (3). Data points have been adjusted for detector response.
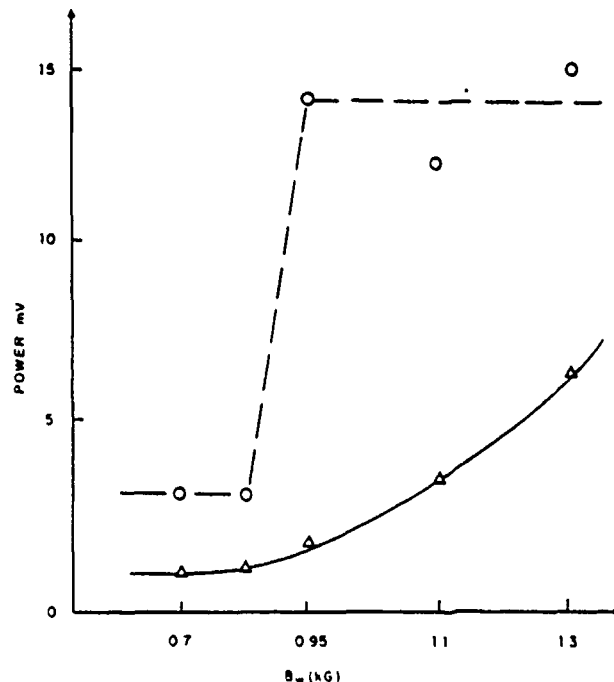

Fig. 6. Dependence of millimeter power $\lambda = 1.8$ mm upon undulator field amplitude. Upper (dashed) curve: FEL oscillator, power about 75 ns after $t = 0$ [see Fig. 4(b)]. Lower curve (solid): FEL oscillator, power shortly after $t = 0$.

to broaden and harmonics to appear, an example of which is the one at 1.2 mm shown in Fig. 5 which agrees with the $l = 1$, $n = 2$ upper frequency of (3). Increasing the beam energy, or the guiding magnetic field, causes a decrease in wavelength, as predicted by (4).

In a typical signal, such as that shown in Fig. 4, the beam noise level, Fig. 4(c), is estimated to be between 1 and 10 kW. The laser signal [Fig. 4(b)] is about 100 times larger, that is, between 100 kW and 1 MW. Since it takes about 70 ns or 7 bounces of the radiation inside the laser cavity for the laser signal to build up out of the noise, we conclude that the power gain per bounce is about 2. This should be equal to the product of the power survival per pass q, times the signal gain per pass squared:

$$q \, (\exp \Gamma_T L)^2 \approx 2 \qquad (9)$$

where L is the length of the undulator and Γ_T is the threshold spatial growth coefficient for FEL oscillation. Since it takes about 20 ns or 2 bounce times for the radiation to drain out of the cavity, we estimate $q = 0.5$, which gives

$$\Gamma_T L = \text{Im} \, (\delta \omega_T) \frac{L}{c} \approx 1. \qquad (10)$$

This estimate of the growth is close to the theoretical prediction of (5), taking $\beta_w = 0.1$ and $\beta_\perp = 0.5$.

The FEL oscillator radiation exhibits a sharp threshold in the undulator strength, as shown in Fig. 6. Below this thresh-

old very little radiation is detected. As the undulator field strength is increased above threshold, the power level jumps to a higher level, and remains relatively constant as the undulator field strength is increased still further. This saturation effect may be caused by harmonic production (Fig. 5). In constrast, radiation resulting from the initial voltage transient during the first 20 ns [see Fig. 4(b) or 4(c)] does not have a threshold, but instead grows steadily with increasing undulator strength; this radiation is incoherent [2] and occurs before the FEL oscillation is well established. For zero undulator strength, no millimeter wave signals were detected.

The FEL output power as a function of the guide magnetic field for constant undulator strength is plotted in Fig. 7. As the guide field increased, total power increases, and the coherent radiation appears earlier in the pulse. However, the threshold in the undulator field strength appears to increase with increasing guide magnetic field.

A separate waveguide system is used to detect long wavelength microwaves. Emission in the 2 cm band can arise from the lower intersection of either the $n = 1$, $l = 1$ fundamental mode or the $n = 2$, $l = 1$ harmonic. Radiation in the 2 cm band correlates with emission from the upper intersection at millimeter wavelengths (see Fig. 8). Except for the emission from the initial transient, radiation from 2 cm band wavelengths occurs after the peak emission in millimeter radiation. This observation suggests that the instabilities producing radiation at each intersection interact competitively, with the low-frequency emission disrupting the high-frequency process.

The 2 cm band emission has many of the characteristics of its millimeter wave counterpart. It exhibits a threshold effect at about the same level in the undulator strength, and similar dependences on the guide magnetic field. As with the milli-meter waves, the 2 cm band emission can be made to vanish
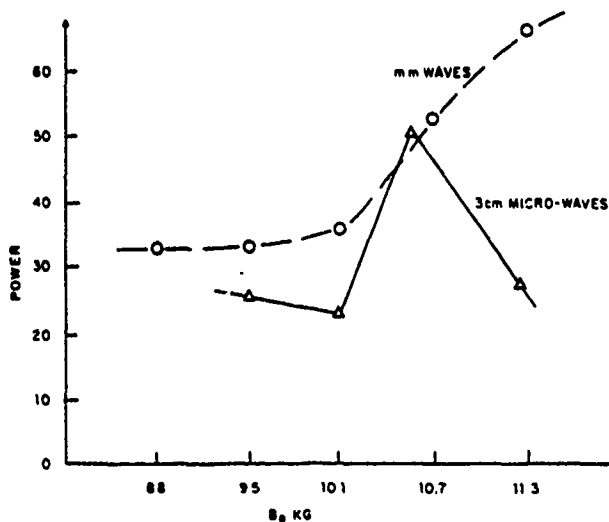
Fig. 7. Dashed line: dependence of peak millimeter power from the FEL upon guiding magnetic field strength; solid line: dependence of X band microwaves ($\lambda \approx 3$ cm) upon B_o.
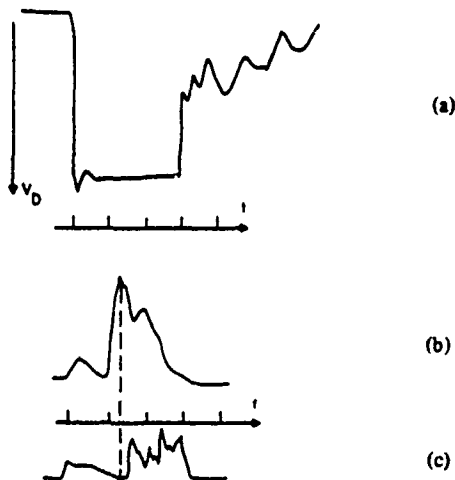

Fig. 8. (a) Diode voltage waveform, time scale 50 ns/div. (b) Millimeter wave power versus time, $\lambda \approx 1.6$ mm. (c) Microwave power versus time, $\lambda \approx 2$ cm. Signals (a), (b), and (c) are for the same shot.

whenever the anode mirror is removed or the undulator is turned off (note that microwaves are still reflected into the FEL even when the anode mirror is removed [Fig. 3]). Thus, the microwave emission mechanism is related to the high-power millimeter FEL emission.

The behavior in the microwave X band (3 cm) is rather different. X band emission can arise from the lower intersection of either the $n = 1, l = 0$ mode or the $n = 0, l = 1$ mode. X band emission is observed even with the undulator at zero field strength. Bringing up the undulator to maximum field raises the X band power level by an order of magnitude. As a function of the guide field, the emission increases considerably at $\omega_c = 12$ GHz, regardless of whether the undulator is on or off (Fig. 7); this may be due to the TE_{02} cutoff of the 5 cm drift tube. The X band emission does not appear to correlate with the $n = 1, l = 1$ millimeter emission. However, some correlation was discernible with the $l = 1, n = 0$ upper intersection emission which occurs at a wavelength of 2.5 mm.

We replaced the tapered $l_o = 12.5$ mm undulator with an untapered one of $l_o = 8.5$ mm. The maximum field obtainable

with this undulator is much smaller than the longer period undulator, and we were unable to drive the $n = 1, l = 1$ millimeter mode above threshold in the FEL oscillator. Relatively high-power broadband superradiant noise radiation extending throughout the entire millimeter wave spectrum was observed, however. We found that tapering the ripple field at the front end of this undulator substantially reduced this broadband radiation. We note that an $l_o = 8.5$ mm undulator was used to drive a Raman FEL oscillator unstable in a previous experiment [8], and so it is clear that the Raman FEL device can operate at a lower pump-field oscillation threshold, because the resonator properties [8] were very similar to those used in this experiment. This shows that the FEL radiation in this experiment is not due to the Raman mechanism.

V. SUMMARY AND CONCLUSIONS

Experiments were carried out with a free electron laser oscillator based on a cyclotron-undulator interaction; this requires a large initial transverse electron velocity before entry into an undulator. With an undulator of pitch 12.5 mm, relatively narrow-band radiation was observed at a wavelength near 1.7 mm, corresponding to the double Doppler upshifted sum of the undulator and cyclotron frequencies. Measurements of the growth rate and the radiation threshold in the undulator field strength appeared consistent with a linear kinetic theory of the cyclotron-undulator interaction. A weaker harmonic predicted by theory was observed at 1.2 mm. We also observed radiation in the 2 cm and X microwave bands which could be accounted for by the lower intersection of the modified cyclotron wave with the waveguide dispersion curve. The 2 cm band radiation correlated with the millimeter radiation from the upper intersection and appeared at a time of saturated or declining FEL millimeter emission. The appearance of many different modes of oscillation and harmonics can be expected of a device using electrons with large Larmor radius, and special resonant structures would be required to suppress undesirable modes of oscillation.

ACKNOWLEDGMENT

REFERENCES

[1] D. B. McDermott, T. C. Marshall, S. P. Schlesinger, R. K. Parker, and V. L. Granatstein, "High power free electron laser based on stimulated Raman backscattering," *Phys. Rev. Lett.*, vol. 41, pp. 1368–1371, 1978.

[2] A. Grossman, T. C. Marshall, and S. P. Schlesinger, "A new millimeter free electron laser using a relativistic beam with spiralling electrons," *Phys. Fluids*, vol. 25, pp. 337–343, 1983.

[3] K. R. Chu and J. L. Hirshfield, "Comparative study of the axial and azimuthal bunching mechanisms in electromagnetic cyclotron instabilities," *Phys. Fluids*, vol. 21, pp. 461–467, 1978.

[4] E. Ott and W. M. Manheimer, "Theory of microwave emission by velocity–space instabilities of an intense relativistic electron beam," *IEEE Trans. Plasma Sci.*, vol. PS-3, pp. 1–5, 1975.

[5] A. Grossman and T. C. Marshall, "Orbits of a test electron in a wiggler," *Bull. Amer. Phys. Soc.*, vol. 25, p. 989, 1980.

[6] W. A. McMullin and G. Bekefi, "Coherent radiation from a relativistic electron beam in a longitudinal periodic magnetic field," *Appl. Phys. Lett.*, vol. 39, pp. 845–847, 1981.

[7] S. C. Chen and R. H. Jackson, private communication.

[8] D. S. Birkett, T. C. Marshall, S. P. Schlesinger, and D. B. McDermott, "A submillimeter free-electron laser experiment," *IEEE J. Quantum Electron.*, vol. QE-17, pp. 1348–1353, 1981.

Arthur A. Grossman was born in New York, NY, on December 27, 1956. He received tne B.A. degree from Columbia College, New York, NY, and the M.A. and M.Phil. degrees in physics from Columbia University, New York, NY, in 1977, 1979, and 1980, respectively. Currently he is working towards the Ph.D. degree in physics at Columbia.

T. C. Marshall was born in Cleveland, OH on January 29, 1935. He received the Ph.D. degree in physics from the University of Illinois, Urbana, in 1960.

He is currently a Professor of Applied Physics at Columbia University, New York, NY. In addition to research in free-electron lasers, he has undertaken research in intense relativistic beam phenomena, plasma-wave scattering and instabilities, trapped-particle effects in plasmas, and the formation and heating of plasmas in high beta equilibrium.

Prof. Marshall is a Fellow of the American Physical Society.

A new millimeter free electron laser using a relativistic beam with spiraling electrons

A. Grossman, T. C. Marshall, and S. P. Schlesinger

Plasma Physics Laboratory, Columbia University, New York, New York 10027

For a dense, relativistic beam of spiraling electrons passing along a magnetic field B_0 and through an undulator, it is demonstrated theoretically and experimentally that radiation will occur at frequency ω_s given by $\omega_s \simeq (\omega_c + 2\pi V_{\parallel}/l_0)(1 - V_{\parallel}/c)^{-1}$, where $\omega_c = |eB_0/mc\gamma|$ is the electron gyrofrequency, l_0 is the undulator period, γ is the relativistic factor, $\gamma \equiv [1 - (V_{\parallel}^2/c^2) - (V_{\perp}^2/c^2)]^{-1/2}$, $V_{\parallel}$ and $V_{\perp}$ are the electron velocity components parallel and transverse to the guiding magnetic field B_0. Two experiments are described, one of which is in a practical oscillator configuration. Substantial power is emitted having wavelength 1.5 mm.

I. INTRODUCTION

In a free electron laser, (FEL) a pump wave is back-scattered via stimulated emission from the "free" electrons of a relativistic beam. A relativistic double Doppler shift permits operation at short wavelength. In the Raman free electron laser[1,2] the beam is intense and cold, so that the collective plasma mode is excited on the beam; the pump—a periodic magnetostatic undulation of the strong guiding field—and the backscattered electromagnetic wave drive the negative energy beam space charge wave, which grows for many plasma periods along the "undulator." In this paper we turn our attention to a new FEL that also involves the double Doppler shift effect and the undulator, but now the positive energy cyclotron mode is excited by a substantial component of electron transverse energy provided before the beam enters the undulator.[3]

We begin by considering electron beam systems which prepare a beam of spiraling but relatively cold electrons in the guiding magnetic field (B_0). These have been studied theoretically by Ott and Manheimer,[4] Hirshfield, Chu and Kainer[5] and recently by Vomvoridis and Sprangle.[6] In Ref. 6 it is concluded that the Doppler-shifted cyclotron mode is unstable, if $v_{\perp}/c \equiv \beta_{\perp} \gtrsim 1/\gamma$ ($v_{\perp}$ is the component of motion perpendicular to B_0), and should result in radiation with frequency given according to the relation:

$$\omega_s \simeq 2\gamma_{\parallel}^2 (\omega_c),\tag{1}$$

where $\gamma \equiv (1 - v_{\perp}^2/c^2 - v_{\parallel}^2/c^2)^{-1/2}$, $\gamma_{\parallel} \equiv (1 - v_{\parallel}^2/c^2)^{-1/2}$, $\omega_c = |eB_0/mc\gamma|$. Reference 5 presents a calculation showing that the growth rate and range of unstable frequencies is reduced as the beam energy spread is enhanced. The growth rate for this convective instability scales roughly as $\beta_{\perp}\omega_p$ and there is a threshold $\beta_{\perp}$ for growth.[4] In Ref. 6 it is proposed that the beam system should be enclosed in an open-moded resonator—a strategy adopted in the first Raman device—with one of the prime benefits being a discrimination against off-axis, higher order modes. (Note, however that we are not dealing with the mechanism of the cyclotron maser, "gyrotron.") It should also be noted that Ride and Colson[7] have considered similar techniques adapted to a very short wavelength free electron laser.

In the following, we present experimental confirmation that an intense relativistic beam of spiraling electrons will generate a band of unstable frequencies in the general range given by Eq. (1); however, more significantly, the addition of an undulator to the beam system—which operates originally below oscillation threshold—will result in a new spectrum of shorter wavelengths controlled by the undulator period (l_0) and amplitude according to a modified relation:

$$\omega_s \simeq 2\gamma_{\parallel}^2 (\omega_c + \omega_0),\tag{2}$$

where $\omega_0 = 2\pi V_{\parallel}/l_0$. In Sec. II we briefly present a calculation wherein the orbit of an electron [kinetic energy $(\gamma - 1)mc^2$] is represented in terms of the initial $\beta_{\perp}$, the guiding field, the undulator period (l_0), and amplitude (B_w). In the experimental section (Sec. IV) we present data from two distinct experimental configurations which generate the modified Doppler-shifted cyclotron radiation; one configuration operates in the superluminescent mode and the other operates as an oscillator.

II. THEORY

The stimulated emission of radiation which occurs when a spiraling relativistic electron beam traverses a region of spatially periodic magnetic field is modeled here in the framework of kinetic theory. The experimentally observable quanitites, the frequency and growth rate, are solutions of the dispersion relation obtained by solving the collisionless Boltzmann equation for the source current which appears in the Maxwell wave equation. In a linear analysis, the solution to the collisionless Boltzmann equation may be found by an integration along the single particle orbits in the externally applied magnetic field. For the free electron laser these external fields typically consist of a uniform axial guide field and a transverse helical undulator field:

$$\mathbf{B} = B_0\hat{z} + B_w(\cos k_0 z\hat{x} + \sin k_0 z\hat{y}).\tag{3}$$

Numerical solution of the equations of motion[8] for an electron in this field as well as for a similar field which includes the radial gradient associated with the actual undulator field, produces orbits which are approximately helical and contain Fourier components largely at the guide field

cyclotron frequency $\omega_c = |eB_0/mc\gamma|$ with amplitude proportional to $V_\perp$, and at the undulator frequency $k_0 V_z = (2\pi/l_0)V_z$, (l_0 = undulator spatial periodicity) with amplitude proportional to B_w, the undulator field strength. Linearizing the equation of motion in the frame which rotates with the helical undulator field gives a laboratory frame orbit which compares favorably with the numerical results:

$$V_x = V_\perp \cos \omega_c t + V_w \cos k_0 V_z t,$$
$$V_y = V_\perp \sin \omega_c t + V_w \sin k_0 V_z t, \qquad (4)$$
$$V_z = V_\parallel.$$

Here, $V_\parallel$ and $V_\perp$ are approximately constants of the motion, V_w is the undulator quiver velocity,

$$V_w = (\Omega_0 V_z)/(\omega_c - k_0 V_z) \ll c, \qquad (5)$$

and Ω_0 is the undulator cyclotron frequency given by $|eB_w/\gamma mc|$.

We are assuming the system is not magnetoresonant (i.e., $\omega_c \neq k_0 V_z$). These orbits can also be obtained from the recent work of Freund, Sprangle et al., and corresponds to Friedland's class of stable uniform V_z solutions.[9] This orbital behavior has been noted in experimentation[10] with thermally sensitive "witness paper," lining the lateral wall of the drift tube, on which periodic markings from electron contact were observed to correspond to the cyclotron period $[\lambda_c = (2\pi V_z/\omega_c)]$ and the undulator period l_0.

In our analysis of the stimulated emission from the beam–undulator interaction we assume that the Larmor precession terms in the orbit Eq. (4) are important ($V_\perp \neq 0$), and it is shown that beams with a substantial initial transverse velocity will support stimulated emission at a new band of frequencies given by the double-Doppler-shifted sum of undulator periodicity frequency and guide field cyclotron frequency, given by Eq. (2).

To keep the calculation analytically tractable we adopt parallel plate waveguide geometry as the radiation boundary condition. The radiation is assumed to be in the TE mode,

$\mathbf{E} = (0, E_y, 0)$ and $\mathbf{B} = (B_x, 0, B_z)$ with vacuum modes given for the plates at $x = \pm a$ by:

$$B_z = B_{x0} \cos k_r(x - a) \exp(-i\omega t + ikz),$$
$$B_x = (-ik/k_r)B_{x0} \sin k_r(x - a) \exp(-i\omega t + ikz), \qquad (6)$$
$$E_y = (i\omega/k_r c)B_{x0} \sin k_r(x - a) \exp(-i\omega t + ikz),$$

where $k_r = r\pi/2a$ is the waveguide eigenvalue, $\omega^2 = (k^2 + k_r^2)c^2$, and r is an integer.

Linearizing the relativistic Vlasov equation and integrating via the method of characteristics, we obtain the perturbed distribution function by performing the integration given by:

$$f_1 = -e \int_{-\infty}^{t} dt' \left(2P_y(E_y + \beta_z B_x) \frac{\partial f_0}{\partial P_\perp^2} - \beta_y B_x \frac{\partial f_0}{\partial P_z} \right) \qquad (7)$$

along the unperturbed orbit given by (4) using the TE fields given by (6); $\mathbf{P}$ is the particle momentum $\gamma m \beta c$, $\gamma^2 = (P_\perp^2 + P_z^2)/m^2 c^2 + 1$ and f_0 is the equilibrium distribution function.

The radiation source current is found by integrating the perturbed distribution function over momentum:

$$\mathbf{J} = e \int d^3\mathbf{P}(\mathbf{P}/\gamma m)f_1. \qquad (8)$$

Fourier transforming the Maxwell wave equation, discarding y dependences, and expanding about the waveguide solution, yields the dispersion relation:

$$\omega^2 - (k^2 + k_r^2)c^2 = -\frac{4\pi c}{aB_{x0}} \int_{-a}^{a} \frac{\partial J_y}{\partial x} \cos k_r(x - a)dx, \qquad (9)$$

where J_y is the y component of the source current calculated from Eqs. (7) and (8) using the standard techniques of kinetic theory. The result of this calculation is the dispersion relation given by:

$$\omega^2 - (k^2 + k_r^2)c^2 = \omega_p^2 \int_0^\infty 2\pi P_\perp \, dP_\perp \int_{-\infty}^{\infty} dP_z \left((\omega - kV_z)\frac{\partial g}{\partial P_\perp} + kV_\perp \frac{\partial g}{\partial P_z} \right)$$
$$\times \sum_{n=-\infty}^{\infty} \sum_{l=-\infty}^{\infty} \frac{m}{2} \frac{[1 + (-)^{r+n} \exp(-2k_r^2 \Delta^2)][V_\perp J_n'^2(d)J_l^2(u) + \frac{1}{2}V_w J_n^2(d)'J_l^2(u)']}{\omega - kV_z - lk_0V_z - \eta\omega_c}, \qquad (10)$$

where $u = k_r V_w/k_0 V_z$, and $d = k_r V_\perp/\omega_c$, ω_p is the plasma frequency, J_m denotes the mth-order Bessel function, primes denote differentiation with respect to the argument, g is the equilibrium momentum space distribution function, and Δ is the beam thickness.

For growth to occur, the resonant denominator must be vanishingly small:

$$\omega - kV_z - lk_0V_z - n\omega_c = 0. \qquad (11)$$

The real part of the frequency should also satisfy the vacuum waveguide dispersion relation:

$$\omega^2 = (k^2 + k_r^2)c^2. \qquad (12)$$

Eliminating k gives the two intersections for the real part of the frequencies at which growth can occur:

$$\omega_s = \gamma_\parallel^2(lk_0V_z + n\omega_c)[1 \pm \beta_z \alpha], \qquad (13)$$

where

$$\alpha = \left[1 - \left(\frac{k_r c}{\gamma_z(lk_0V_z + \eta\omega_c)} \right)^2 \right]^{1/2}.$$

For this experiment, α is close to unity. Therefore retaining only the fundamental undulator and cyclotron frequencies ($l = n = 1$) and keeping only the high-frequency intersection yields the positive energy cyclotron mode modified by the undulator as given by Eq. (2). The other frequencies which

may exhibit growth include that of Doppler-shifted cyclotron wave instability (set $l = 0$, in Eq. (13)), the undulator modified negative energy cyclotron mode ($n = -1$), the strong pump limit of the free electron laser ($n = 0$) as well as higher harmonics of both the undulator and cyclotron frequencies.

Integrating expression (10) by parts and substituting the cold beam equilibrium distribution function:

$$g(P_\perp, P_z) = (2\pi P_\perp)^{-1} \delta(P_\perp - P_{\perp 0}) \delta(P_z - P_{z0}) \qquad (14)$$

gives the dispersion relation as:

$$\omega^2 - (k^2 + k_r^2)c^2$$

$$= \frac{\omega_p^2 m}{k_r d} \sum_{nl} \left\{ \frac{1}{R_{nl}} \left[\left(\omega - \frac{kP_z}{\gamma m} \right) \frac{\partial B_{nl}}{\partial P_\perp} + \frac{kP_\perp}{\gamma m} \frac{\partial B_{nl}}{\partial P_z} \right] \right.$$

$$\left. + \frac{B_{nl}}{(R_{nl})^2} \frac{P_\perp}{\gamma m^2} \left(k(k + lk_0) - \frac{\omega^2}{c^2} \right) \right\}, \qquad (15)$$

where

$$B_{nl} = d \left[\gamma \omega_c d J_n'^2 (d) J_l^2(u) \right.$$

$$\left. + \tfrac{1}{2} k_0 (P_z/m) J_n^2(d)' u J_l^2(u)' \right],$$

and $R_{nl} = \gamma[\omega - (k + lk_0)V_z - n\omega_c]$ is the resonant denominator for the n, l harmonic.

The ω^2 term in the last term of (15) is the net result of differentiating γ with respect to momentum and is unique to a relativistic calculation. This term can describe gain from the azimuthal bunching mechanism.[11] The other terms have corresponding limits in a nonrelativistic calculation and can describe the gain arising from the axial bunching mechanism.

For the lowest-order resonance at $n = 1$, $l = 0$, in the limit of $u \to 0$, we recover the cyclotron maser dispersion relation studied by Ott and Manheimer.[4]

For the $n = l = 1$ resonance, we retain the lowest-order nonresonant terms as well as the $n = l = 1$ resonant terms and expand the frequency about the real part ω_s: $\omega = \omega_s + \delta\omega$, where ω_s satisifes (11) and (12) so $R_{11} = \gamma\delta\omega$, and the amplitude growth rate is $\text{Im}(\delta\omega)$. The resulting quartic equation in $(\delta\omega)$ can be approximated by a relatively simple cubic equation when $\omega_s, \omega_0 \gg \delta\omega \gg (\omega_c + k_0 V_z)(k_0 V_z /4\omega_c)u^2$ and $u \ll d \ll 1$, in which case we have:

$$(\delta\omega)^3 - (\omega_p^2/2\gamma\omega_s)(\omega_c + k_0 V_z)$$

$$\times \left[\frac{(\delta\omega)^2}{k_0 V_z} + \left(\frac{kk_0}{k_r^2} - 1 \right)\omega_c \frac{d^2 u^2}{16} \right] = 0. \qquad (16)$$

Two complex conjugate roots occur when the cubic discriminant is positive, which yields the threshold condition for this instability as:

$$|du| > \frac{2^{5/2}}{3^{3/2}} \frac{(\omega_p^2/\gamma\omega_s)(\omega_c + k_0 V_z)}{[|(kk_0/k_r^2) - 1|\omega_c]^{1/2}(k_0 V_z)^{3/2}}, \qquad (17)$$

above which the growth rate is given by:

$$\text{Im}(\delta\omega)$$

$$= \pm \frac{1}{4}\sqrt{3} \left[\frac{\omega_p^2 \omega_c}{4\gamma\omega_s}(\omega_c + k_0 V_z)\left(\frac{kk_0}{k_r^2} - 1 \right)d^2 u^2 \right]^{1/3}. \qquad (18)$$

Both axial and azimuthal mechanisms contribute to this gain; in the limit of $k \to 0$ (waveguide cutoff) the gain is entirely azimuthal. In Eq. (17) the word "threshold" stands for the onset of positive instability growth rate. In Secs. IV and V we shall use the same word in connection with the requirements for (ud) such that the free electron laser will oscillate. The latter requirement involves the losses in the oscillator cavity, and therefore the oscillator threshold for (ud) is somewhat larger than that given by Eq. (17) in practice.

As $k_r \to 0$ (removing the waveguide wall), one finds from (18) and the definitions of d and u that $\text{Im}(\delta\omega) \to 0$. The interaction assumed in this model will not occur when the electromagnetic wave is purely transverse. We have chosen to study this feature analytically by modeling the actual cylindrical waveguide wall in the experiment using the simpler parallel-plate model, which is therefore an approximation. On the other hand, McMullin and Bekefi[12] have recently considered a similar electron beam where the system is pumped by a longitudinal component, but assuming a different electron orbit and no waveguide wall. They obtain an instability at the same frequency [Eq. (2)] but with a different growth coefficient. It is very likely that both mechanisms are operative in the experiment described in the following section, because our undulator has a longitudinal component at the actual electron-beam location. Therefore, theory suggests that electromagnetic waves having frequency given by (2) and growth rate of order predicted by (18) will occur, permitting the operation of a free electron laser device according to these principles. It is clear, however, that quantitative comparisons with (18) may be questionable. Substituting the parameters of this experiment [Sec. IV] into Eq. (17) give $0.14 > 0.03$. Thus we are considerably above threshold and Eq. (18) gives the growth rate as $\text{Im}(\delta\omega) \approx 0.6 \times 10^9/\text{sec}$.

III. APPARATUS

The electron beam was obtained by field emission from a graphite cathode in a foil-less diode. A high-voltage pulse, 600–800 kV and lasting 150 nsec, is obtained from our Physics International Pulserad 220 generator. This is applied to the cathode in an evacuated diode (pressure $\lesssim 10^{-5}$–10^{-4} Torr). Electrons are emitted from the sharp corner lip of the cathode, and form a cylindrical shell beam having diameter ≈ 40 mm, thickness ≈ 1–2 mm in a drift tube having i.d. = 47 mm. About 20 kA propagate in the beam for guiding magnetic field $\gtrsim 10$ kG. Standard beam diagnostics include diode voltage, diode current, and beam current (the latter requires insertion of a Faraday cup in the beam line).

Radiation emerging from the drift tube passes through a vacuum window (polyethylene, or an aluminized z-cut quartz mirror), is filtered by a high pass ($\lambda < 4$ mm) filter, and is guided into a shielded room for spectroscopic analysis via a 2.5-cm-diam light pipe. Measurement of total power is made—after passing the radiation through two widely sepa-

rated 1-mm mesh elements—by a Schottky-barrier diode detector. Spectroscopy is done with the aid of either a Fabry–Perot interferometer (this uses two plane parallel, separated meshes, mesh constant $= 250\,\mu$) or a grating spectrometer. When doing spectroscopy, the 1-mm mesh filters are of course removed, but the 4-mm high-pass filter remains in place. Calibration of the Fabry–Perot and spectrometer was done with coherent sources (millimeter Klystrons and molecular gas lasers). Microwaves emitted from the system in the 2-cm band can be observed if the light pipe is removed and replaced with a microwave horn and waveguide leading into the shielded room.

IV. EXPERIMENTAL DATA

The experiment was done in two independent parts using different diode geometries. In each case the objective is to prepare a beam having appreciable transverse motion. In the first configuration, a cold beam is injected into a short, nearly magnetoresonant undulator, from which the electrons emerge with appreciable transverse energy.[13] In the second configuration, transverse energy is imparted to the beam at the cathode and is enhanced by field compression. Neither technique is original to this investigation.[14,15] What is new is the provision of a long undulator downstream, which established the operating frequency of the radiation and which drives the beam system (marginally stable in the absence of the long undulator) unstable.

A. Uniform beam-line geometry

A four-period, iron ring, $l = 20$-mm, nonadiabatic undulator having ripple field amplitude about 5% B_0 partly converts the parallel energy of the incoming electrons $[(\gamma - 1)mc^2]$ into a transverse component (Fig. 1), providing one operates near the magnetoresonance condition $\omega_c \approx \omega_0 = k_0 V_\parallel$. Thereby the electron energy is redistributed between the $\beta_\parallel$ and $\beta_\perp$ motion, giving the component $\gamma_\parallel$ parallel to B_0 as

$$\gamma_\parallel^2 = \gamma^2/(1 + \gamma^2\beta_\perp^2). \tag{19}$$

Analysis of x-ray data in a related experiment showed[13] that $v_\perp/v_\parallel \sim 0.5$–1.0 is possible using such an undulator. There will be no singularity in $V_\perp/c$ at magnetoresonance, owing to transit time effects of the electron in the undulator. Simula-
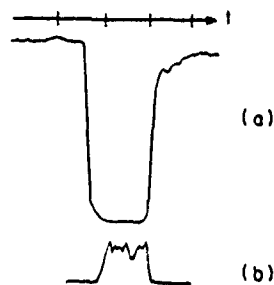
FIG. 2. (a) Diode voltage signal (600 kV), 100 nsec/div. (b) Radiation signal, $\lambda \approx 1.8$ mm using $B_w \approx 200$ G from $l_0 = 8.5$ mm undulator. $B_0 \approx 11$ kG; the four-period $l_0 = 20$-mm undulator has $B_t \approx 500$ G.

tion of the electron trajectory[x] in the four-period wiggler revealed that $0.50 < \beta_\perp < 0.75$ and that the magnetoresonance was rather broad but maximized at $B_0 \approx 10.2$ kG. Over a wide zone of B_0, $\beta_\perp > \frac{1}{2}$, which places the electron beam system either near or above threshold ($\beta_\perp \gtrsim \gamma^{-1}$) of instability.[4,6] Taking $\beta_\perp > \frac{1}{2}$, one finds $\beta_\parallel \lesssim 0.73$ for $\gamma = 2.1$.

Very close to magnetoresonance, we found substantial millimeter and microwave radiation from the beam; we estimate the power level $\gtrsim 100$ kW. If the field ripple of the 20-mm undulator is large, this radiation can be obtained over a wide range of B_0. However, at $B_w \approx 5\% B_0$, this radiation is produced over only a very narrow zone ($\lesssim 400$ G) of B_0 near magnetoresonance (10.2 kG). Away from this zone of magnetic field, the millimeter spectrum is quiet. If then a second undulator—a 60 period bifilar helical current system having $l_0 = 8.5$ mm—is energized, one can again produce short wavelength radiation (Fig. 2). The threshold B_w required of the $l_0 = 8.5$ mm undulator for this new radiation to appear was found to increase the farther one operates from the magnetoresonance.

Fabry–Perot spectroscopy of the two types of radiation shows marked differences. The radiation obtained at magnetoresonance (upon which the $l_0 = 8.5$-mm wiggler has no effect) (Fig. 3, upper), is found to be relatively broad band, although there appears to be a periodic feature in the Fabry–Perot data indicating $\lambda \approx 4$ mm (this may be caused by the high-pass filter). On the other hand, based on theory[4], broadband radiation having frequency $\omega_s \approx 2\gamma_\parallel^2\omega_c$ is expected above $\beta_\perp$ threshold, and since $\gamma \approx 2.1$ one expects here $2\gamma_\parallel^2 \approx 4$ and $\omega_c/2\pi \approx 14$ GHz, then $\omega_s/2\pi \approx 56$ GHz. This
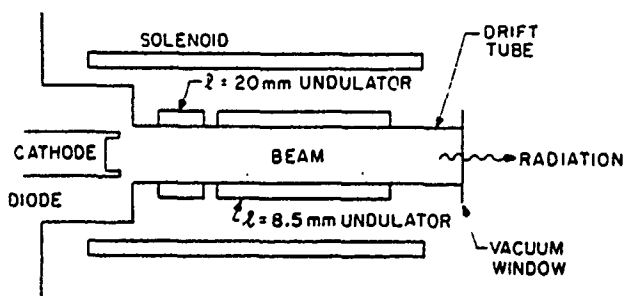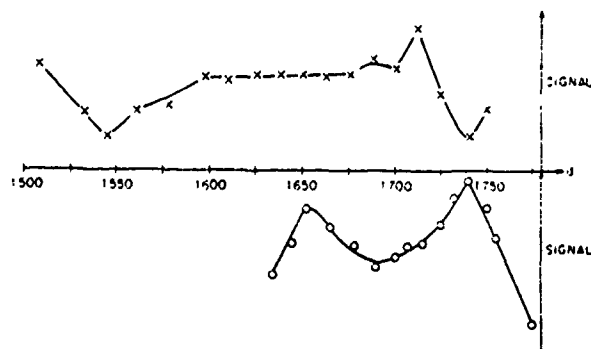
FIG. 1. Diagram of linear beam-line apparatus, using a four-section magnetoresonant ($l = 20$ mm) undulator followed by a long (50 cm) undulator. System length 100 cm, drift tube o.d. = 5.0 cm, cathode diam 4.4 cm, anode-cathode gap 25 mm.

FIG. 3. Spectrograms using the Fabry–Perot interferometer, $\gamma \approx 2.1$; $d =$ Fabry–Perot mesh plate separation in centimeters, arbitrary zero. Above: System at magnetoresonance ($B_0 = 10.2$ kG), $B_w = 0$ for $l_0 = 8.5$ mm undulator, showing $\lambda \approx 4$ mm. Below: nonmagnetoresonant case, requiring $B_w \approx 400$ G from $l_0 = 8.5$ undulator to produce signal at $B_0 \approx 11.5$ kG, showing $\lambda \approx 1.8$ mm.

radiation is probably the same as that obtained by a group at the Ecole Polytechnique[16] in an experiment which used a long magnetoresonant undulator. In Fig. 3 (lower) we examine the spectrum of the radiation which results from the $l_0 = 8.5$-mm undulator, for $B_0 \approx 11$ kG. Here $\lambda \approx 1.8$ mm and bandwidth $\Delta\lambda/\lambda \approx 7\%$; this radiation at 1.8 mm was observed using the grating spectrometer as well. Calculating ω_s from Eq. (2) and taking $\omega_0/2\pi = 26$ GHz ($\beta_\parallel = 0.73$, $l_0 = 8.5$ mm) we find $\omega_s/2\pi \approx 150$ GHz ($\lambda \approx 2$ mm); thus the new radiation frequency is controlled by the long undulator and the observed wavelength is consistent with the theory of Sec. II.

B. Field compressed beam geometry

One would like to add feedback to this convectively unstable system to implement an oscillator, however the geometry in Fig. 1 is not suitable. Addition of a partially transmitting anode mirror at the end of the drift tube and insertion of a mirror into the cathode will give a power recirculation factor[17] $\lesssim 15\%$, which is inadequate to provide steady oscillation.[2] Increasing the cathode mirror diameter so that it exceeds the drift tube i.d. will, however, cause an improvement[17] in the recirculation factor to $\approx 40\%$, thereby improving the expectations for the oscillator system.

We therefore built the new diode in the geometry shown in Fig. 4. A large graphite cathode—with a polished aluminum plate insert serving as a mirror—is placed in a zone of weak but converging magnetic field and the electrons are guided into the drift tube adiabatically along converging field lines. This magnetic geometry will enhance the conversion of the beam longitudinal energy to transverse energy. Electrons are emitted from the cathode in crossed magnetic and electric fields. We expect this configuration will provide the electron with transverse motion (at the cathode k) given by[18]:

$$\beta_{\perp k} = 3.3 \times 10^{-6} E_{\perp k}/B_{0k}, \tag{20}$$

where $E_{\perp k}$ is the electric field at the cathode surface (V/cm) perpendicular to B_{0k}, and B_{0k} is in kG. As B_0 increases downstream, $\beta_\perp$ scales as $\beta_\perp \approx \alpha^{1/2}\beta_{\perp k}$ and the beam radius scales as $R_B \approx \alpha^{-1/2}R_k$, where $\alpha \equiv B_0/B_{0k}$.
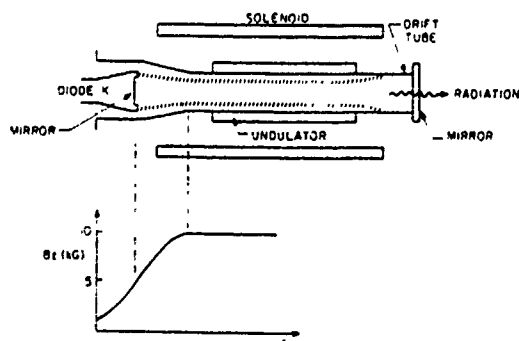

FIG. 4. Diagram of profiled beam-line system. Undulator is a bifilar helical winding, period $l_0 = 12.5$ mm, length 60 cm, tapered B_w at point of beam entry. Cathode diam 58 mm, drift tube i.d. = 47 mm, length of magnetic field taper zone 15 cm, transverse distance between cathode and anode wall 1.7 cm. Mirror at cathode is polished plane aluminum insert into graphite. Mirror at anode is z-cut quartz, having a 2 cm diam nonaluminized transmitting "window" (note reflectivity from this "window" is 50%).

Taking $E_{\perp k} \approx 400$ kV/cm, $B_{0k} = 5$ kG, $B_0 = 10$ kG, we calculate $\beta_\perp \approx 0.4$ in the drift section. Witness plates confirmed the compression of the beam to the expected diameter: $2R_k = 5.8$ cm, $2R_B = 4.0$ cm. One notable constraint is that beam equilibrium requires $\omega_p^2/\omega_{ck}^2\gamma^3 < \frac{1}{2}$, where $\omega_p^2 = 4\pi n_k e/m$. This places a lower bound on the magnetic field required at the cathode. (The Faraday cup showed that a beam current 10–20 kA propagated, and at $\omega_p/2\pi \approx 7$ GHz, $\gamma\omega_{ck}/2\pi \approx 14$ GHz.) Simulation of the electron motion in this diode geometry was done for us at the Naval Research Laboratory[19]: for $\gamma = 2.5$ it shows $\langle \beta_\parallel \rangle = 0.80$ ($\Delta\beta_\parallel \sim 0.04$) and $\langle \beta_\perp \rangle = 0.43$ ($\Delta\beta_\perp \sim 0.1$) in a thin annular beam. (The velocity spread $\Delta\beta_\parallel$ of the beam may be open to question in view of the fact that the electron emission is very localized at the sharp corner lip of the cathode. Rather cold intense electron beams have been created and observed[14] for a sufficiently strong, uniform guiding field.) The value $\beta_\parallel = 0.8$ is consistent with the cyclotron period observed on the "witness paper" (Sec. II).

In Fig. 5 we show the effect of adding an aligned anode mirror to the free electron laser system. Without the mirror, filtered radiation at the wavelength given by Eq. (2) is below the threshold of our detector, except for a transient as the beam turns on, and off [Fig. 5(c)]. Addition of the mirror causes an increase—perhaps as much as two orders of magnitude—in the power output. The large laser pulse follows an initial transient [Fig. 5(b)] at the initiation of the electron beam, after 50–100 nsec; this pulse shape varies substantially as experimental conditions are varied, but the peak power remains nearly the same. In Fig. 5(b) one notes at the termination of the flat diode voltage pulse, a sharp drop in laser power followed by a tail of radiation emitted by the empty cavity. Analysis of the latter permits a calculation[2] of the power loss per radiation bounce (10 nsec) in the resonator, which is about 50%. Microwave radiation ($2 < \lambda < 3$ cm), at approximately the level we report in Sec. IV A, appears when the millimeter free electron laser signal shows a tendency to saturate or decrease. A relatively high level of B_w at the beam was necessary ($\gtrsim 1$ kG) to drive the system unstable (viz., to produce the second peak) with the quasi-optical feedback; in this example, $l_0 = 12.5$ mm, and the V_w, arising from electron motion in the undulator, is greater than $0.1c$. Oscillation could not be obtained if the diode voltage was less than approximately 800 kV for $B_w \approx 1$ kG. The level of oscillation was sensitive to mirror alignment: tilting the cathode mirror by approximately $1.5°$ was sufficient to spoil the oscillation.

Spectroscopy (in two separate runs) was done using both the Fabry–Perot and the grating spectrometer in this example. The Fabry–Perot shows that the interferogram of the second pulse of Fig. 6 is a relatively coherent wave having $\lambda \approx 1.6$ mm and $\Delta\lambda/\lambda \approx 3\%$. Using the spectrometer, $\lambda \approx 1.4$ mm was obtained (Fig. 7). In both Figs. 6 and 7, spectral analysis of the first transient [Fig. 5(b)] showed no coherent feature. Taking $\gamma \approx 2.5$, $\beta_\perp \approx 0.4$, and $\beta_\parallel \approx 0.8$, $\omega_0/2\pi = 20$ GHz, $\omega_c/2\pi = 12$ GHz and $\omega_s = 2\gamma_\parallel^2(\omega_0 + \omega_c) \approx 2\pi \times 180$ GHz ($\lambda \approx 1.6$ mm). The resolution of the detector/spectrometer system in Fig. 7 was not as good as the Fabry–Perot system, Fig. 6. These spectra are characteristic of operation
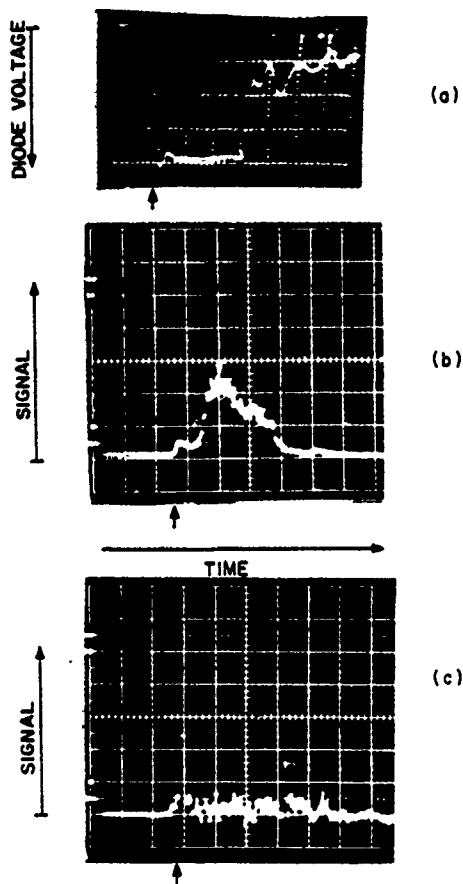
FIG. 5. (a) Diode voltage waveform, 800 kV. (b) Radiation signal, $\lambda = 1.6$ mm when both mirrors are in place and aligned: $B_0 \approx 9.5\,\text{kG}$, $B_w \approx 1.3\,\text{kG}$. (c) Radiation signal, $\lambda \approx 1.6$ mm, when anode mirror is replaced by a thin polyethylene window. Arrow locates $t = 0$ on each photograph; 50 nsec/div.

at near-threshold conditions of ripple-field pump. As the pump amplitude is increased, the spectrum broadens and harmonics can be identified; in particular the case $l = 1$, $n = 2$ was clearly seen. This effect may explain why the signal amplitude at the fundamental ($l = 1$, $n = 1$) decreases
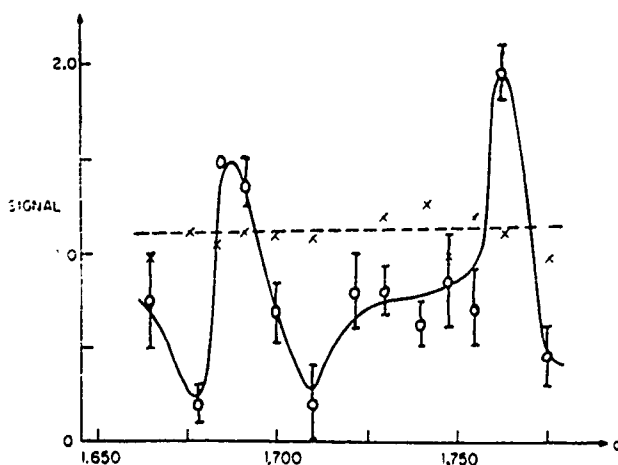

FIG. 6. Spectrogram using the Fabry–Perot: $d =$ mesh plate spacing in centimeters, arbitrary zero. Solid line—second peak, Fig. 5(b); dashed line—first peak, Fig. 5(b). $B_0 \approx 10\,\text{kG}$, $B_w \approx 1.5\,\text{kG}$, $\gamma = 2.5$, $l_0 = 12.5$ mm.
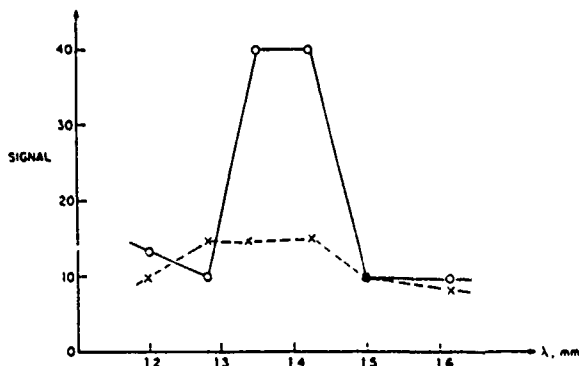

FIG. 7. Spectrogram from the grating spectrometer: conditions nearly similar to those of Fig. 6. Detector crystal uses a mirror 5 cm wide so system resolution here is 0.1 mm. The detector response is flat. Solid line—second peak, Fig. 5(b); dashed line—first peak, Fig. 5(b).

later in the pulse [Fig. 5(b)]. We have also observed that an increase of the guiding magnetic field will cause a decrease of scattered wavelength, in the magnitude indicated by Eq. (2).

V. DISCUSSION

In the two experiments just described, the beam energy and undulator period were varied, and under circumstances where a substantial $\beta_\perp$ was present, the emitted frequency from the two systems was in agreement with Eq. (2). We note this frequency is also near that expected from stimulated Raman[2] backscattering, viz.,

$$\omega_s \approx 2\gamma_\parallel^2 (\omega_0 - \omega_p/\gamma^{3/2}). \tag{21}$$

One would not, however, expect to obtain stimulated Raman backscattering in this experiment, because there is reason to believe that the parallel velocity spread of the beam is substantial (a few percent) and therefore the energy spread would be too high to permit excitation of the space charge wave. Indeed, in the oscillator configuration described in Sec. IVB, no regenerated FEL radiation was obtained in a range of diode voltage (600–750 kV) where we had previously obtained stimulated Raman-backscattering using a different configuration[2] (in that experiment the cathode magnetic field was ≈ 20 kG and the estimated $\beta_\perp$ was $\lesssim 0.07$). The frequency of the radiation we report here is also far above the backscattered radiation from the negative energy cyclotron wave[20]

$$\omega_r \approx 2\gamma_\parallel^2 (\omega_0 - \omega_c). \tag{22}$$

The result of the theoretical calculation (Sec. II) depends on the electron orbit assumed, and the appropriateness of our choice is open to question because of complications from the radial inhomogeneity of the undulator field and the beam space charge. The theory predicts an instability below the threshold calculated by Ott and Manheimer for the case of no undulator. This may explain why the system can sustain the high-frequency mode and yet remain stable against the radiation having frequency $\approx 2\gamma_\parallel^2 (\omega_c)$. From Eq. (18), we find a growth distance of the FEL radiation to be less than L, the undulator length, and therefore it is reasonable to expect to obtain this radiation in our apparatus. The cold beam theory predicts radiation at harmonics of the undula-

tor and cyclotron frequencies which we did observe. Finally, one might expect the electron beam thermal spread effect to become important when the corresponding spread of Doppler-shifted frequencies becomes comparable with the bandwidth due to finite growth rate and finite undulator length: this requires $\Delta V_\parallel / V_\parallel$ to be less than a few percent, which is compatible with the result of the diode simulation.

The power emitted is in the range 10^5–10^6 W, comparable with that obtained in our previous experiments.[1] In the steady state the power will depend on the nonlinear processes which clamp the beam signal gain per pass to the threshold value required to balance the losses.[2] However, inspection of the signal [Fig. 5(b)] shows that the system is in the transient state. The noise level of the unperturbed beam system is 1–10 kW at $\lambda \approx 1$–2 mm into a 5% bandwidth detector, measured by comparison with the output of 1.22 mm $C^{13}H_3F$ gas laser; thus, this oscillator operates approximately 20 dB above ambient beam noise. The free electron laser radiation requires about 70 nsec to develop, or about seven bounces of radiation between the mirrors in the cavity. Accordingly, as can be seen from Fig. 5(b), the net power gain per bounce is of order two. Thus the product of the exponentially growing signal by the loss per bounce (about 50%) should give this factor of two, near threshold conditions in pump amplitude. It follows that $[\mathrm{Im}(\delta\omega)]L/c \approx 1$. This permits one to solve for the factor $(V_\perp/c)(V_w/c)$ in Eq. (18); taking the experimental value $V_w/c \approx 0.1$, we obtain $V_\perp/c \approx \frac{1}{3}$, which is consistent with our diode modeling. It is interesting to observe that the amplitude of electron quiver motion required to drive this laser above threshold is several times the value of V_w/c (0.03) required in the example of the Raman free electron laser system.[1,2]

[1]D. B. McDermott, T. C. Marshall, S. P. Schlesinger, R. K. Parker, and V L. Granatstein, Phys. Rev. Lett. 41, 1368 (1978).

[2]D. S. Birkett, T. C. Marshall, S. P. Schlesinger, and D. B. McDermott, IEEE J. Quant. Electron. QE-17, 1348 (1981).

[3]T. C. Marshall, S. P. Schlesinger, and A. Grossman, Bull. Am. Phys. Soc. 26, 937 (1981); and W. A. McMullin and G. Bekefi, Bull. Am. Phys. Soc. 26, 909 (1981).

[4]E. Ott and W. M. Manheimer, IEEE Trans. Plasma Sci. PS-3, 1 (1975).

[5]J. L. Hirshfield, K. R. Chu, and S. Kainer, Appl. Phys. Lett. 33, 847 (1978).

[6]J. L. Vomvoridis and P. Sprangle, Phys. Rev. A 25, 931 (1982).

[7]S. K. Ride and W. B. Colson, Appl. Phys. 20, 41 (1979).

[8]A. Grossman and T. C. Marshall, Bull. Am. Phys. Soc. 25, 989 (1980).

[9]H. P. Freund, P. Sprangle, D. Dillenburg, E. H. da Jornada, B. Liberman and R. S. Schneider, Phys. Rev. A 24, 1965 (1981); and L. Friedland, Phys. Fluids 23, 2376 (1980).

[10]R. M. Gilgenbach, D. B. McDermott, and T. C. Marshall, Rev. Sci. Instrum. 49, 1098 (1978).

[11]K. R. Chu and J. L. Hirshfield, Phys. Fluids 21, 461 (1978).

[12]W. A. McMullin and G. Bekefi, Appl. Phys. Lett. 39, 845 (1981).

[13]S. Talmadge, T. C. Marshall, and S. P. Schlesinger, Phys. Fluids 20, 974 (1977).

[14]M. Friedman, D. A. Hammer, W. M. Manheimer, and P. Sprangle, Phys. Rev. Lett. 31, 752 (1973).

[15]M. Friedman and M. Herndon, Phys. Rev. Lett. 28, 210 (1972).

[16]K. L. Felch, L. Vallier, J. M. Buzzi, P. Drossart, H. Boehmer, H. J. Doucet, B. Etlicher, H. Lamain, and C. Rouille, IEEE J. Quant. Electron QE 17, 1354 (1981).

[17]D. S. Birkett (private communication).

[18]K. E. Kreischer, MIT Report No. PFC/RR-81-11, 179 (1981).

[19]S. C. Chen and R. H. Jackson (private communication).

[20]R. M. Gilgenbach, T. C. Marshall, and S. P. Schlesinger, Phys. Fluids 22, 971 (1979).

A Reprint from the

PROCEEDINGS

Free-Electron Generators of Coherent Radiation

26 June–1 July 1983
Rosario Resort, Orcas Island, Washington

**A Thomson-scattering experiment to determine parallel velocity
spread of an intense relativistic electron beam**

S. C. Chen, T. C. Marshall, S. P. Schlesinger
Plasma Laboratory, Columbia University, New York, New York 10027

A Thomson-scattering experiment to determine parallel velocity spread of an intense relativistic electron beam

S.C. Chen, T.C. Marshall, S.P. Schlesinger

Plasma Laboratory, Columbia University, New York City 10027

Abstract

We describe a non-interactive Thomson-Backscattering experiment to determine the parallel-energy spread of a 1 KA/cm^2, 600 KV beam. Principles of the experiment, optics, complicating factors (e.g. X-rays, background light), Diode and TEA laser performance, and preliminary single-channel scattering data are discussed. A momentum-spread of $(\Delta\gamma/\gamma)_{\shortparallel} \sim \frac{1}{2}\%$ is consistent with the data.

Introduction

In order to obtain high gain and efficiency for a Free Electron Laser (FEL) operating in the Raman regime, an intense, relativistic electron beam must be cold, that is the parallel electron momentum-spread parameter $(\Delta\gamma'/\gamma)_{\shortparallel} \stackrel{\sim}{\sim} (\omega p/2\pi c) (\lambda_0/2\gamma)$, where ω_p is $(4\pi ne^2/\gamma m)^{\frac{1}{2}}$, $\gamma = (1-V^2/c^2)^{-\frac{1}{2}}$, n is the electron density, and λ_0 is the wiggler period. For an FEL operating at $\lesssim 1$ mm wavelength, a typical required value of $(\Delta\gamma/\gamma)_n$ is in the range of 1-3%, depending on the actual distribution of electron velocities in the beam. A recent detailed calculation of signal amplification along a warm electron beam by Ibanez and Johnston[1] shows that the Raman gain falls monotonically for increasing values of $(\Delta\gamma/\gamma)_{\shortparallel}$. Very little experimental data on intense electron beam devices is available, and that relies principally on interactive diagnostics: one experiment [2] indicated that $(\Delta\gamma/\gamma) \sim 2\%$ was not unreasonable. What is clearly needed is a non-interactive diagnostic sensitive to electron-beam parallel velocity spread, with application to electron systems appropriate for the FEL.

In this paper, we describe a Thomson-Backscattering diagnostic, which is capable of resolving momentum spread $\sim 1\%$ in dense relativistic electron streams (j $\gtrsim 10^3$ A/cm^2). We review the theory, describe the apparatus, and quote some data for the first such experiment of this nature.

Theory

Thomson-scattering from a relativistic electron stream will yield the thermal spread of electron parallel velocities (in the lab frame), $(\Delta v_{\shortparallel}/c) = (1/\gamma^2) (\Delta\gamma/\gamma)_{\shortparallel}$, from the Doppler-broadened spectrum of scattered light:

$$(\Delta\lambda/\lambda) \sim 2(\Delta\gamma/\gamma)_{\shortparallel} \sim 2(1-1/\gamma) (\Delta W/W)_{\shortparallel} \tag{1}$$

where $W = (\gamma-1)mc^2$. The ratio of frequency of scattered light (ω_s) to incident light (ω_i) is given by

$$(\omega_s/\omega_i) = \frac{1+\beta}{1-\beta\cos\theta} \sim \frac{2}{1-\beta\cos\theta} \sim \frac{4\gamma_{\shortparallel}^2}{1+\gamma^2\theta^2} \tag{2}$$

where $\beta = v/c$ and θ is the angle between the electron velocity and the scattered wave-vector (we have applied this to the back-scattering direction, $\theta \sim 0$, where the incident beam of radiation is directed counter to the electron flow). Scattering into a finite solid angle, dΩ, will cause an independent spread of frequencies, ($\delta\omega_s$)

$$(\delta\omega_s/\omega_s) \sim \frac{\gamma^2}{\pi} d\Omega \tag{3}$$

and therefore, to make this source of spectral-broadening negligible (viz., $\delta\omega_s/\omega_s \lesssim \frac{1}{2}\%$) we take d$\Omega = 2\times10^{-3}$ which is roughly f/20 optics. Taking W $\sim$ 650KV, one finds $\omega_s/\omega_i = 19.2$ from eq. (2): TEA CO$_2$ laser radiation at 9.6μ would be shifted to a scattered wave-length $\lambda_s \sim \frac{1}{2}\mu$.

To calculate the differential cross section for scattering, we use formulae from Quantum Electrodynamics in the limit of $\hbar\omega/mc^2 \ll 1$, setting the $\theta \sim 0$. Then the photon

cross section, $(d\sigma/d\Omega)_p$, is given by

$$\left(\frac{d\sigma}{d\Omega}\right)_p \sim \frac{1+\beta}{1-\beta} r_o^2 \sim 4\gamma^2 r_o^2 \tag{4}$$

where $r_o = e^2/mc^2$. Since the experiment uses a photomultiplier (PMT) photon detector, the number of scattered photons (N_s) can be written in terms of the number of incident photons (N_i) as

$$(N_s/N_i) \sim 2(4\gamma^2)r_o^2 (n\ell) \, d\Omega \tag{5}$$

where the factor of two, actually $(1+\beta)$, is the photon flux compression appropriate to our geometry and ℓ is the length of the electron beam illuminated. Taking $n\ell=3\times10^{14}/cm^2$, $N_s N_i^{-1} \sim 2\times10^{-14}$. On the other hand, the energy differential cross section $(d\sigma/d\Omega)_w$ can be obtained by multiplying eq. (4) by the photon frequency upshift factor, ω_s/ω_i, together with the photon flux compression factor:

$$(d\sigma/d\Omega)_w \sim 32\gamma^4 r_o^2 \tag{6}$$

This result can also be obtained from classical theory, taking care to apply the retarded time factor correctly. [Unfortunately, an erroneous "finite-volume" effect[3] has been propagated in the literature, and has only recently been laid to rest by Kukushkin[4]; the actual effect from a finite volume of scattering electrons is very difficult to observe].

Finally, the spectrum of scattered radiation can be calculated once the electron velocity distribution is assumed. A suitable ansatz is a narrow gaussian in the beam-frame (characterised by temperature T_o), in which case Zhuravlev and Petrov[5] find

$$\left(\frac{d^2\sigma}{d\omega d\Omega}\right)_w \alpha \, e^{-mc^2/T_o} \quad , \quad T_o << mc^2 \tag{7}$$

where the Doppler half-width of the line in the laboratory frame $(\Delta\omega)_s$ is

$$\Delta\omega_s/\omega_s \sim 2\sqrt{\frac{2T_o}{mc^2}} \, \ell n2 \tag{8}$$

(The formulae of reference (5) contain a few minor errors having to do with the normalization of the velocity distribution).

Experiment

Turning now to experimental matters, we are currently using a TEA CO_2 laser oscillator and a Lumonics 922S amplifier to provide power for the incident beam (cross section $\sim 1cm^2$). The oscillator is tuned to one line near $\lambda_i = 9.6\mu$ by a diffraction-grating mirror element. The amplified output is a series of mode-locked spikes, 10-20 MW in amplitude, spaced ~ 20 nsec apart over a 100 nsec interval. The mode-locked spikes (detected with a photon-drag element) make a convenient and characteristic signature for the scattered signal. The radiation is directed through a NaCl window into the drift-tube of the accelerator via a long-focal length mirror system, oriented 1° off the electron beam axis. The scattered beam-line is also tilted about 1° from this axis to avoid picking up excessive background visible light from the diode, as well as light from the spark at the TEA beam-dump; an aperture-stop further discriminates against background light (Fig.1). The scattered beam is passed through a window in a shielded room (~ 5 M to one side of the accelerator), into a copper box [enclosed in a wall of lead 5cm thick] in which is located an RCA C31000A photomultiplier. At this point the radiation is filtered with 5000Å interference filters of variable width.

The arrangement of the diode is shown in Fig. 1. A Physics International Pulserad accelerator applies a square pulse, $\sim 650kV$, to a cold, graphite-tipped cathode immersed in a uniform magnetic field (10kG). The pulse is very flat (within 2%) and lasts about 150 nsec (Fig. 2a). Electrons are field emitted across a 2-cm gap into a graphite anode; a small fraction of the total electron current passes through an axi-centered hole (5mm dia) and propagates down a 2 cm dia. drift-tube as a cylindrical beam (this arrangement is similar to that used in the recent high-power Raman FEL experiment at NPL[6]). Optical alignment with a moveable jig and mirror is relatively easy. The up-stream-pressure in the drift tube is in the range 10^{-5} to 10^{-4} torr; the electron beam is then at least 95% un-neutralized by ions.
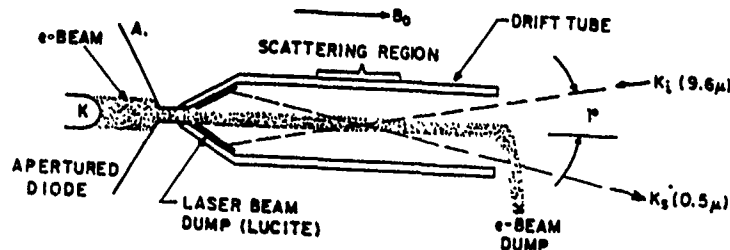
Fig.1 Experimental geometry, The anode-cathode gap is 2cm, $B_o = 10kG$, $\gamma \sim 2.3$.

As in all Thomson-scattering work, background light is a severe problem. The most serious interference arises from light emitted in the diode: the latter increases throughout the pulse, particularly at the time of gap closure ($\gtrsim 300ns$ after initiation). The stray light level during the first 50-80 nsec of the accelerator pulse is acceptably low. The TEA laser cannot be directed up the axis of the system, because of the spark that is formed at the cathode; this will change the electron beam current distribution. The TEA laser dump is a lucite wedge located upstream in the drift tube (Fig.1).

Results

An example of backscattered signal is shown in Fig.2. In Fig.2(a), one sees the synchronism between the diode voltage pulse and the TEA CO_2 laser mode-locked spikes (detected by a photon-drag monitor which intercepts a small portion of the light beam). The timing on the oscilloscope photo is adjusted so that it accurately corresponds to the laser beam intercepting the electron beam. In Fig.2(b), we display a filtered light signal ($1/2\mu$) from the PMT (the PMT signal is delayed ~ 30 nsec because of transit-time effects). A set of spikes, having the same spacing as the mode-locked pulses at 9.6μ is clearly evident, superimposed on the background signal. A careful investigation shows the diode voltage is flat to $\sim 2\%$ during this 80 nsec interval. Furthermore, changing the diode voltage by $\sim 2\%$ caused the mode-locked pulses to disappear from the PMT signal.
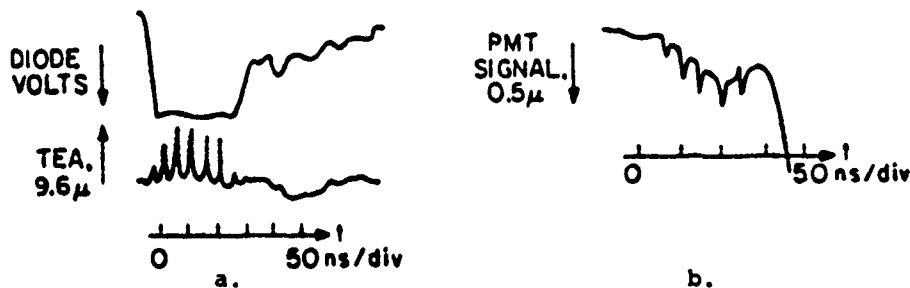

Fig.2 (a)Synchronism between the accelerator pulse (above) and
       the 9.6μ laser signal (below).
      (b)Scattered light (spikes), superimposed on background,
       for $\lambda_s = 5000Å$, detected by PMT.

The light detected by the photocell in Fig.2(b) results from incoherent back-scattering. Note the typical order of the Debye distance for this electron beam is a few hundred microns, clearly much larger than the 9.6μ laser wavelength. On the other hand we can also calculate maximum single-pass growth, with parameters taken for our experiments, using an electromagnetic pump wave (instead of a wiggler) at 9.6μ having intensity $\lesssim 10^7$ w/cm^2: using the warm-beam weak pump case [7], we find negligible power from stimulated Compton scattering.

To determine the spectrum of scattered light, from which the momentum spread is obtained, we substitute a set of wavelength filters having different filter-width in front of the photomultiplier. Averaging over many shots, we obtain the dependence of normalized, averaged power versus filter width (Fig.3). We deduce the parallel, normalized momentum spread of the beam by fitting a Gaussian spectrum to the data (use of a symmetrical trial

spectrum is justified only if the width is very narrow). To date - using 50, 100, and 200 Å width filters at 5000Å, our best estimate is that $(\delta\gamma/\gamma)_{||} \sim 1/2\%$, or $\delta v_{||}/c \sim .1\%$.

After obtaining more data, using additional filters, we shall determine the beam velocity spread when an undulator is used. A bifilar-helical winding having period $\ell_o = 17mm$ has been chosen. The objective is to induce a measureable enhancement of the beam velocity spread, to determine how the velocity spread induced by the undulator combines with that already present in the unperturbed electron beam.

Thomson back-scattering from an intense relativistic electron beam has several advantages over traditional Thomson scattering. One is the enhancement of the backscattered photon cross-section by a factor $\sim 4\gamma^2$. Another is that photons are more plentiful in an infrared source laser by another factor $\sim 4\gamma^2$. Accordingly, we are able to scatter from $\sim 10^{12}$ electrons using the comparatively low power $\sim 10MW$, an impossibility with non-relativistic electrons. Backscattering of visible photons from a very energetic electron source ($\sim 10GeV$) has been reported[8].

Finally, our preliminary report that $(\Delta W/W)_{||} \sim 1\%$ for this electron-beam system largely substantiates the claim of the NRL group to have achieved low energy-spread in their Raman FEL experiment[6]. Accordingly, one can contemplate practical, efficient Raman FEL systems in the submillimeter spectral range.

Fig. 3

References

1. L.F. Ibanez and S. Johnston, IEEE J. Quant. Electr., QE-19, 339 (1983).
2. M. Friedman, D. Hammer, W. Manheimer, P. Sprangle, Phys. Rev. Lett., 31, 752 (1973).
3. See: R.E. Pechacek and A.W. Trivelpiece, Phys. Flds., 10, 1688 (1967);
   G. Ward, R.E. Pechacek, Phys. Flds., 15, 2202 (1972);
   J. Sheffield, Plasma Phys., 14, 783 (1972;
   J.H. Williamson and M.E. Clark, J. Plasma Phys., 6, 211 (1971).
4. A.B. Kukushkin, Sov. J. Plasma Phys., 7, 63 (1981) [Engl. transl.].
5. V.A. Zhuravlev and G.D. Petrov, Sov. J. Plasma Phys., 5, 3 (1979) [Engl. transl.].
6. R.K. Parker et al., Phys. Rev. Lett., 48, 238 (1982);
   R.H. Jackson et al., IEEE J. Quant. Electr., QE-19, 346 (1983).
7. A. Hasegawa, Bell System Tech. J., 57, 3069 (1978).
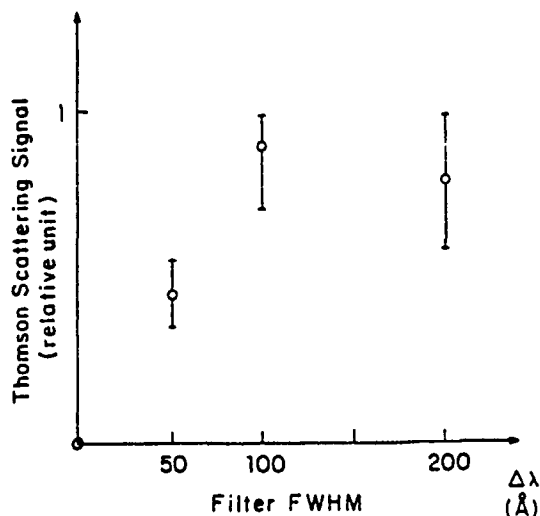8. C.K. Sinclair, et al., IEEE Trans. Nucl. Sci. 116, 1065 (1969).

Thomson Backscattering from a Relativistic Electron Beam as a Diagnostic for Parallel Velocity Spread

S. C. Chen and T. C. Marshall

Plasma Laboratory, Columbia University, New York, New York 10027
(Received 16 November 1983)

Thomson backscattering of CO_2-laser radiation is used to determine the parallel momentum spread of a 1-kA/cm^2, 700-kV magnetized electron beam, emitted from a cold cathode in an apertured diode. The beam is found to be suitable for Raman free-electron-laser applications: a normalized momentum spread of $(0.6 \pm 0.14)\%$ was obtained for the inhomogeneous broadening; it is also found that the use of an undulator will cause an increase of the broadening.

In order to obtain high gain and efficiency for a free-electron laser (FEL) operating in the Raman regime, $\omega_p L/\gamma c \gg 1$, an intense relativistic electron beam must be cold, that is the parallel component of normalized momentum spread should satisfy $(\delta\gamma/\gamma)_{\shortparallel} < (l_0/2\gamma)(\omega_p/2c)$, where $\omega_p = (4\pi n e^2/\gamma m)^{1/2}$, $\gamma = (1-v^2/c^2)^{-1/2}$, n is the electron density, and l_0, L are the undulator period and length. In the regime of long wavelength and comparatively low γ, inhomogeneous broadening caused by electron beam emittance, space charge, and gradients in the undulator field must be held to $(\delta\gamma/\gamma)_{\shortparallel} \approx (1-2)\%$ in order that FEL gain remain high.[1] However, available electron-beam data relevant to this question rely principally on interactive diagnostics. What is needed is a noninteractive diagnostic which is sensitive to the spread of electron velocities parallel to the axis of the beam. In this Letter, we describe a Thomson-backscattering diagnostic which is capable of resolving momentum spread $<1\%$ in dense relativistic electron streams. We review the theory, describe the apparatus, and quote data for the first experiment of this nature.[2] Backscattering of photons from a very energetic (10 GV) electron beam has been reported several years ago.[3]

In the laboratory frame, a thermal spread of electron parallel velocities $\delta v_{\shortparallel}/c$ is related to the spread of electron momentum or energy by $(\delta v_{\shortparallel}/c) = \gamma^{-2}(\delta\gamma/\gamma)_{\shortparallel}$; it is also related to the broadened spectrum of scattered light:

$$\delta\lambda/\lambda \approx 2(\delta\gamma/\gamma)_{\shortparallel} \approx 2(1-1/\gamma)(\delta W/W)_{\shortparallel}, \qquad (1)$$

where $W = (\gamma-1)mc^2$. The ratio of the frequency of scattered light (ω_s) to frequency of light incident upon the electron stream (ω_i) is

$$\omega_s/\omega_i \approx \frac{1+v/c}{1-(v/c)\cos\theta} \approx \frac{4\gamma_{\shortparallel}^2}{(1+\gamma^2\theta^2)}, \qquad (2)$$

where $\gamma_{\shortparallel} = (1-v_{\shortparallel}^2/c^2)^{-1/2}$ and θ is the angle between the electron velocity and the scattered wave vector (in the backscattered direction, where the scattered photons travel parallel to the electrons and the incident photons antiparallel, $\theta \approx 0$). Scattering into finite solid angle, $d\Omega$, will cause another spread of frequencies, $\delta\omega_s/\omega_s = \gamma^2 d\Omega/\pi$; to make this type of spectral broadening negligible (say $\lesssim 0.1\%$), we shall take $d\Omega \lesssim 10^{-3}$ which is roughly $f/30$ optics. If $W = 670$ kV, from Eq. (2) one finds $\omega_s/\omega_i = 19.2$: transversely-excited-atmospheric (TEA) CO_2-laser radiation at 9.6 μm would be shifted to a scattered wavelength $\lambda_s = 0.5$ μm.

To calculate the differential scattering cross section we use standard formulas from quantum electrodynamics in the limit $\hbar\omega/mc^2 \ll 1$, setting $\theta \approx 0$. The photon differential cross section, $(d\sigma/d\Omega)_p$, is given by

$$(d\sigma/d\Omega)_p \approx \left(\frac{1+v/c}{1-v/c}\right) r_0^2 \approx 4\gamma^2 r_0^2, \qquad (3)$$

where $r_0 = e^2/mc^2$. Since the experiment uses a photomultiplier (PMT) detector, the number of scattered photons (N_s) can be written in terms of the number of incident photons (N_i) as

$$N_s/N_i \approx 2(4\gamma^2)r_0^2(nl)d\Omega, \qquad (4)$$

where the factor of 2, actually $(1+v/c)$, is the photon flux compression factor appropriate to backscattering geometry, and l is the length of the electron beam illuminated. Taking $nl = 3 \times 10^{12}$ cm^{-2} yields $N_s/N_i = 3.5 \times 10^{-14}$. The energy-differential cross section can be obtained by multiplying Eq. (4) by the frequency upshift factor, from Eq. (2). This result can be obtained from classical theory, taking care to apply the retarded-time factor correctly. (Unfortunately, an erroneous "finite-volume" effect[4] has been propagated in the literature, and has only recently been laid to rest by Kukushkin[5]; the actual finite-vol-

ume effect is very difficult to observe.)

The spectrum of scattered radiation can be calculated once the electron velocity distribution is assumed. A suitable *Ansatz* is a narrow Gaussian in the beam frame (characterized by temperature T_0), in which case[6]

$$(d^2\sigma/d\omega d\Omega)_w \propto \exp(-mc^2/T_0), \quad T_0 \ll mc^2, \quad (5)$$

where the Doppler half-width of the line in the laboratory frame is $2[2T_0 \ln2/mc^2]^{1/2}$. (The formulas of Ref. 6 contain a few minor errors having to do with the normalization of the electron distribution.)

Turning now to experimental matters, we use a TEA laser oscillator and a Lumonics 922s amplifier to provide about 20 MW in a sequence of mode-locked narrow spikes, spaced over a 100-ns interval. The oscillator is tuned to one line by a diffraction grating. The mode-locked spikes make a convenient signature for identifying the scattered signal. The radiation is directed through a NaCl window into the drift tube of the accelerator via a long-focal-length optical system, oriented $\approx 1°$ off axis so that the incident light misses the cathode, and hits a beam dump (Fig. 1). The scattered beam line is also tilted $1°$ off axis to reduce visible-light pickup from the diode and the TEA beam dump. The scattered light is apertured, and passed through a window in a shielded room and into a copper box, which is enclosed in a wall of lead 5 cm thick and in which is located an RCA C31000A PMT. At this point the optical radiation is filtered with a set of $\frac{1}{2}$-μm interference filters having variable width. Background light must be kept below the saturation level of the PMT; the stray-light level, which increases throughout the accelerator pulse, is discriminated against by a high-pass filter (50 MHz) in the output circuit.

A Physics International pulse-line accelerator applies a square pulse ≈ 700 kV to a cold, graphite-tipped cathode immersed in a uniform magnetic field, $B_0 = 9.5$ kG. The pulse is very flat (within 2%) and lasts about 150 nsec (see Fig. 2). Electrons are field emitted across a 2-cm gap into a graphite anode; a small fraction of the total current passes through an axially-centered hole (5 mm diam) and propagates down a 2-cm-diam drift tube as a cylindrical beam (this arrangement is similar to one used in the recent high-power Raman FEL experiment at U. S. Naval Research Laboratories[7]). Optical alignment with a movable jig and mirror in the electron beam line is relatively easy. The upstream pressure in the drift tube is in the range 10^{-4} to 10^{-5} Torr; the electron beam is then at least 95% nonneutral.

An example of the backscattered signal is shown in Fig. 2. The lower portion of the figure shows the synchronism between the diode voltage pulse and the TEA-CO_2-laser spikes (detected by a photon drag device which monitors a portion of the beam). The timing is adjusted on the oscilloscope so that the laser beam intercepts the electrons at coincidence. The PMT signal is delayed an extra 35 ns by transit-time effects. A set of spikes, having the same spacing as the mode-locked spikes at 9.6 μm, is clearly evident on the $\frac{1}{2}$-μm channel. A change of the diode voltage by $\leq 2\%$ will cause the scattered spikes to disappear. Having calibrated the diode voltage as 700 kV, and expecting scattering for $\gamma = 2.3$ (670 kV), the difference of 30 kV is apparently due to the space-charge potential depression of the beam. From this follows the estimate of the beam electron density, 3×10^{11} cm^{-3}. Comparing the observed level of the signal with that pre-
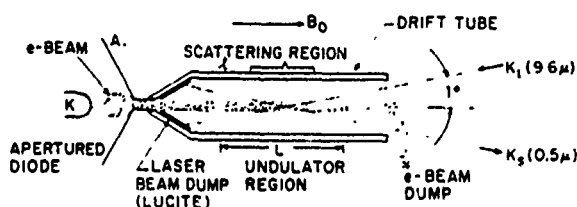

FIG. 1. Schematic of the apertured diode and beam line. Anode-cathode gap, cathode diameter, and drift tube i.d. are each 2 cm. Undulator length is 40 cm and period is 1.7 cm; the first and last three periods are tapered so that B_1 varies gradually.
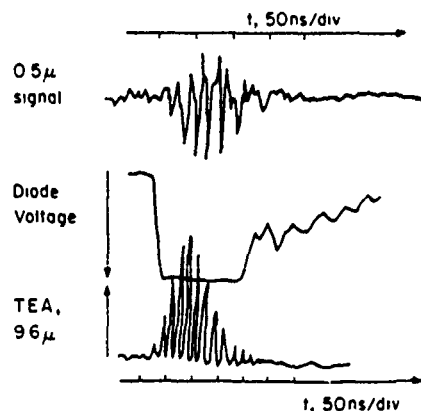

FIG. 2. (Bottom) Diode voltage (700 kV) and TEA laser signal and (top) scattered signal at $\frac{1}{2}$ μm.

dicted by Eq. (4) (including PMT gain and optical losses), we find that the scattered power is of the expected order.

The quantitative scattering data are shown in Fig. 3. The dashed line is the scattered spectrum signal which would be detected by use of a set of ideal Gaussian filters characterized by half-power width $\delta\lambda$, centered at 5000 Å, under the assumption that the electron velocity distribution is a narrow, Doppler-shifted Gaussian characterized by inhomogeneous width $(\delta\gamma/\gamma)_{\parallel}$. The data points, obtained by averaging many shots under nearly identical conditions of accelerator performance, were obtained with use of filters which did not have exactly Gaussian response functions. Each filter transmission characteristic was measured, and the data points were normalized so that each channel could be compared as a Gaussian filter. The best data fit, for zero undulator field $B_{\perp}$, gave $(\delta\gamma/\gamma)_{\parallel} = (0.6 \pm 0.14)\%$. We estimate the electron momentum spread caused by the beam space charge as $(\delta\gamma/\gamma)_{\parallel\ s.c.} = \omega_p^2 r_b^2/4c^2 \approx 0.5\%$ (r_b is the beam radius).

Next, data were taken when the bifilar helical undulator was energized. The period of the undulator is 17 mm and $B_{\perp} = 225$ or 375 G. Because of the proximity of magnetoresonance ($2\pi\gamma v_{\parallel}/l_0 = eB_0/mc$), the corresponding electron quiver velocity, given by

$$v_{\perp}/c \approx \left(\frac{eB_{\perp}l_0}{2\pi\gamma mc^2} \right) \left[\frac{eB_0l_0}{2\pi\gamma mc^2} - 1 \right]^{-1}, \qquad (6)$$
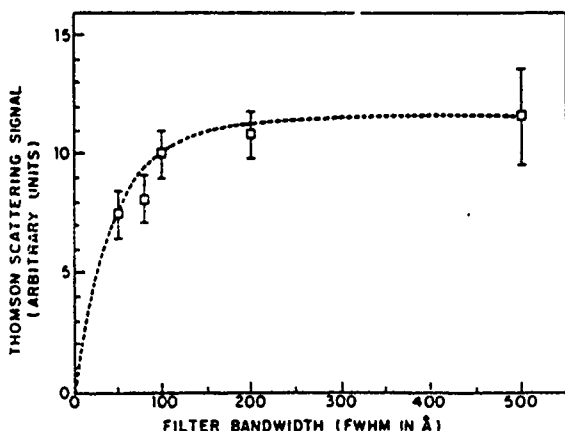
is $0.06c$ or $0.1c$. The enhancement factor in

FIG. 3. Fit of Thomson-scattering data with a calculated curve corresponding to scattering from a electron momentum spread $(\delta\gamma/\gamma)_{\parallel} = 0.6\%$ at $\gamma = 2.3$ into filters characterized by a Gaussian transmission response.

square brackets is ≈ 4. The radius of the electron spiral orbit due to the undulator is only $\approx 0.10 r_b$.

The data show that the total inhomogeneous broadening increases to 0.8% ($B_{\perp} = 225$ G) and 1.1% ($B_{\perp} = 375$ G), $\pm 0.1\%$. The additional broadening expected from the undulator is due to the parallel velocity shear which arises from the radial gradient in quiver velocity, and is an important factor in this experiment since $2\pi r_b/l_0 \approx 1$. The anticipated undulator contribution to the momentum spread is $(\delta\gamma/\gamma)_{\parallel\ und} \approx (\gamma v_{\perp}/c)^2 \delta B_{\perp}/B_{\perp}$, where $\delta B_{\perp}/B_{\perp}$ represents the systematic variation in undulator field amplitude across r_b of $\approx 20\%$. Therefore we expect the undulator to contribute an additional 0.3% or 1.0% momentum spread, respectively, for $B_{\perp} = 225$ G and $B_{\perp} = 375$ G. Combining the predicted space charge and undulator broadenings will give the experimental value that we report (within error limits) provided that these two sources of inhomogeneous broadening are added as the root-mean-square sum.

Thomson backscattering from an intense relativistic electron beam has certain advantages compared with the plasma case. One factor is the enhancement of the differential scattering cross section by $4\gamma^2$. Another is that, for comparable laser power, photons are more plentiful in the infrared source by another factor of $4\gamma^2$. There is no ion bremsstrahlung light, but diode light, x-ray background, and the large f-number requirement contribute to experimental difficulties.

Finally, our measurement of a beam energy spread $< 1\%$ is consistent with the claim of Jackson et al. to have achieved low-energy spread in their Raman FEL experiment.[7] Accordingly, one can contemplate practical, efficient Raman FEL systems in the submillimeter spectral region.

[1]L. F. Ibanez and S. Johnston, IEEE J. Quantum. Electron. 19, 339 (1983).

[2]S. C. Chen, T. C. Marshall, and S. P. Schlesinger, in Proceedings of the LASERS 1982 Conference (to be published), and in Proceedings of the 1983 Free Electron Laser Workshop (unpublished), and Bull. Am. Phys. Soc. 28, 1062 (1983); see also H. Davis and

O. Willi, Bull. Am. Phys. Soc. 28, 1040 (1983).

[3]C. K. Sinclair *et al.*, IEEE Trans. Nucl. Sci. 116, 1065 (1969).

[4]See R. E. Pechacek and A. W. Trivelpiece, Phys. Fluids 10, 1688 (1967); G. Ward and R. E. Pechacek, Phys. Fluids 15, 2202 (1972); J. Sheffield, Plasma Phys. 14, 783 (1972); J. H. Williamson and M. E. Clark, J. Plasma Phys. 6, 211 (1971).

[5]A. B. Kukushkin, Fiz. Plazmy 7, 110 (1981) [Sov. J. Plasma Phys. 7, 63 (1981)].

[6]V. A. Zhuravlev and G. D. Petrov, Fiz. Plazmy 5, 7 (1979) [Sov. J. Plasma Phys. 5, 3 (1979)].

[7]R. H. Jackson *et al.*, IEEE J. Quantum. Electron. 19, 346 (1983).

Parallel Velocity Spread Induced in a Relativistic Electron Beam by an Undulator

SHIEN-CHI CHEN AND T. C. MARSHALL

Abstract—The parallel momentum-spread of an intense relativistic electron beam (1 kA/cm^2, 700 kV), used in a Raman free-electron laser, has been determined by a Thomson backscattering experiment. Infrared radiation at 9.6 μm, provided by a CO_2 TEA laser, is backscattered by the electron beam and is observed at a wavelength of 0.5 μm. The spectral width of this scattered light is a quantitative measure of the beam energy spread or temperature. The beam itself has a fractional momentum spread, ≈ 0.6 percent. When a region of periodic, transverse helical field is imposed by an undulator, the momentum spread is found to increase, becoming ≈ 2 percent when the quiver velocity of the electrons induced by the undulator is roughly 15 percent C. The data also show how the intrinsic spread of beam combines with that induced by the undulator.
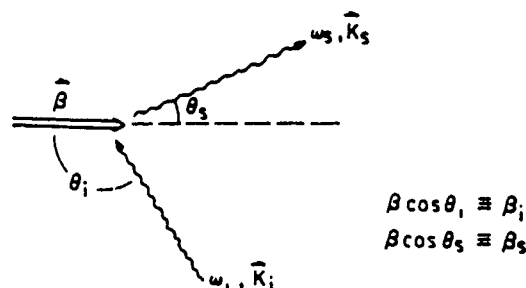
Fig. 1. Thomson scattering shown in laboratory coordinates.

$$\beta \cos\theta_i \equiv \beta_i$$
$$\beta \cos\theta_s \equiv \beta_s$$

I. INTRODUCTION

TO obtain high gain and efficiency for a free-electron laser (FEL), it is necessary that the electron beam be "cold," that is, the normalized electron axial momentum spread should be $\leq 1/N$, where N is the number of undulator periods. This means in practice that a momentum spread ≈ 0.5-2 percent is adequate; larger momentum spread will result in poor performance. Consequently, it is necessary to develop diagnostic methods to measure this important parameter in an accurate and noninteractive way, particularly in the example of intense, low energy beams used in collective, or "Raman" configurations [1]. This paper reports measurements made on such a beam using the recently reported technique of Thomson backscattering of coherent radiation from a relativistic electron beam [2]. We present details of the experimental methods and new results showing the effect of the undulator on the beam momentum-spread.

Referring to Fig. 1, the frequency of the scattered light is related to the frequency of the incident laser light (for low photon energy) by

$$\frac{\omega_r}{\omega_i} = \frac{1 - \beta \cos\theta_i}{1 - \beta \cos\theta_s} \equiv \frac{1 - \beta_i}{1 - \beta_s}. \tag{1}$$

For a particular choice of incidence angle, the frequency shift as a function of scattered angle is an ellipse. The most pronounced upshift is obtained in the $\theta_s = $

0^0 direction, by a factor roughly $4\gamma^2$. Also, at $\theta_s = 0^0$, the scattered spectrum is stable for first order variation over θ_s, which means that the half-angle of the observation cone, $d\Omega$, can be extended without introducing a significant amount of angular broadening which comprises the resolving power. For an optical system with f/30, a spectral resolution of $\delta\omega_r/\omega_r \approx 0.1$ percent is possible in the $\theta_s = 0^0$ direction. Finally, the inhomogeneous broadening from various electron velocity components within the beam is resolved most effectively in the $\theta_s = 0^0$ direction. The disadvantage in this geometry is that the entire length of electron beam is observed, viz., the spatial resolution is not high.

The calculation of the photon scattering cross section for a relativistic electron proceeds by quantum electrodynamics [3], [4]; however, certain simplifications occur. First, the photon energy is negligible compared with the rest energy; neither initial nor final spin states are observed, and an average is taken over initial and final polarizations. One then obtains the scattering probability of a "one photon-one electron" system. However, the actual situation involves streaming electrons interacting with an incident flux of photons, so in addition to multiplying by the density of electrons and the density of photons, one must also include a geometrical factor that describes the orientation of the two beams, the "flux compression factor" [5] $(1 - \beta \cdot \kappa_i)$. For the case of practical interest in laser diagnostics, where the incidence and observation beam lines are orthogonal to each other, and for the special case of our backscattering geometry, we obtain

$$\frac{d\sigma}{d\Omega} = \frac{r_0^2}{\gamma^2} \frac{(1 - \beta_i)}{(1 - \beta_s)^2}. \tag{2}$$

This shows a dramatic enhancement of interaction in the electron beam direction, and permits the application

of this technique to relativistic electron beams of comparatively low density ($\approx 10^{11}$ cm^{-3}).

A classical derivation will give the same result, except that it is the scattered energy which is calculated, and there is an additional factor of $4\gamma^2$ which accounts for the Doppler upshift. We note that "finite residence time" effects, which have been mentioned in the literature [4], [6], [7] as a possible complicating factor, have been shown to be incorrect [8]. This is also true for finite laser pulse time effects. The main requirement is that there be many wavelengths in a pulse which illuminates the electrons, in which case one may interpret the experimental data using (2).

With the incident, high power laser radiation working as an electromagnetic pump on the electron beam, the system can be regarded as a type of FEL, where the undulator is an electromagnetic wave. In the rest frame, the Debye length $(c/\omega_p)(\delta\gamma/\gamma) \approx 10^{-2}$ cm, is much longer than the Lorentz-contracted electromagnetic "undulator" period, $10\mu/2\gamma$, so the interaction is noncollective, viz., it is in the single-particle or Compton regime. The Compton gain for this situation is so low that the stimulated scattering process is negligible and only the incoherent scattered radiation is important. In other words, the bunching effects and coherent gain process associated with an FEL do not contribute to the scattered signal.

The width of the FEL spectrum is determined by the finite undulator length $(\delta\omega/\omega \approx 1/N)$, a homogeneous broadening, together with the inhomogeneous broadening from the finite temperature electron beam. The number of electromagnetic "undulator" periods is more than 10^4, so in the Thomson scattering experiment the inhomogeneous terms determine the shape of the scattered spectrum at $\frac{1}{2}$ μm, and we may use the spectral width as a measure of the parallel velocity spread. The scattered spectrum is obtained by summing contributions from all the electrons over the electron velocity distribution parallel to the beam axis, using the single-electron cross section defined by (2). The integration has been carried out for a narrow Gaussian in the rest frame by Zhuravlev and Petrov [9], obtaining a Gaussian spectrum providing the beam is cold enough; the width is

$$(\delta\omega/\omega)_{\text{inhomo}} = 4\sqrt{\frac{2T_0 \ln 2}{mc^2}} = 2\left(\frac{\delta\gamma}{\gamma}\right)_{\parallel} \qquad (3)$$

where T_0 is the rest frame beam parallel temperature, and $(\delta\gamma/\gamma)_{\parallel}$ is the fractional energy or parallel momentum spread in the lab frame. The data are interpreted under the assumption that the rest frame electron velocity distribution is Gaussian, which is open to question. However, if we assume a flat distribution with a width equal to the Gaussian, it turns out that the error we make in interpreting the data is only of the order of the experimental resolution ($\delta\gamma/\gamma \sim 0.1$ percent).

On the other hand, a "true" FEL interaction does occur between the electron beam and the magnetostatic undulator (period, 1.7 cm, amplitude, ≈ 500 G). This interaction is not observed, since with a beam energy of 700 kV, both the spontaneous and stimulated FEL radiations ($\lambda_s \approx l_0/2\gamma^2 \approx 1.7$ mm, where l_0 is the undulator period and (γ) is the relativistic factor) fall in the millimeter spectrum and they do not interfere with the diagnostic scattering channel at $\frac{1}{2}$ μm. The undulator is used in this experiment only to provide another source of inhomogeneous broadening.

II. Experimental Considerations

A. Laser and Optical Systems

The laser system consists of a "homemade" CO_2 TEA oscillator and a Lumonics 922S amplifier (see Fig. 2); the oscillator is tuned to the 9.6 $P(24)$ line of the 001–020 band by a diffraction grating acting as a mirror. An intracavity diaphragm is used in the oscillator to suppress off-axis modes. The round-trip cavity time $2 L/C$ defines the spacing between mode locked spikes of radiation, roughly 20–30 ns. The oscillator output is double-passed through the amplifier which is timed to amplify the 120 ns pulse of 9.6 μm radiation. The electron accelerator is triggered by a light signal from the oscillator spark gap. There is roughly a 50 ns jitter between the pulse of laser radiation and the electron beam pulse; however, the latter is about 150 ns wide, so there are a reasonable number of good coincidences.

The amplifier output is directed into the interaction region through a NaCl window. The high power density of the output (≈ 20 MW/cm^2) makes it necessary to place the first mirror at least 2 m away from the amplifier output window. The amplifier radiation (2×3 cm) is focused by a 5 m f.l. mirror to a 6 mm spot in the drift tube, roughly the same cross section as the electron beam. A focusing optic of $f/120$ is employed so that the radiation is scattered efficiently by the large aspect ratio electron beam. Copper mirrors are used as the last two optical components in directing the high power laser into the scattering system. The laser power is monitored by a photon drag detector, which samples about 5 percent of the total power reflected off a NaCl flat located in the optical path. Fig. 3(a) shows the coincidence of the electron beam (diode voltage monitor) and the laser pulse. The equally spaced spikes of radiation make a convenient signature for identifying the scattered optical signal.

The scattered light from the interaction volume (Fig. 4) is collected by a 103 cm f.l. mirror, corresponding to $f/30$. The collected light is focused further by a lens (f.l. 23 cm) down to a 1 mm spot where an aperture stop is used to reduce the visible light pickup from the diode and the TEA laser beam dump. After passing through this aperture, the diverging beam is focused again and directed into a shielded room through a 2.5 cm window in the wall, into a copper box, which is enclosed in a wall of lead 5 cm thick. Inside this box is an RCA C31000A photomultiplier tube inside another 3 cm lead jacket. The quantum efficiency of the photocathode is 11 percent at $\frac{1}{2}$ μm, and the current gain is $\approx 10^7$ at the 2.5 kV tube voltage. The fast anode rise time permits observation of the narrow
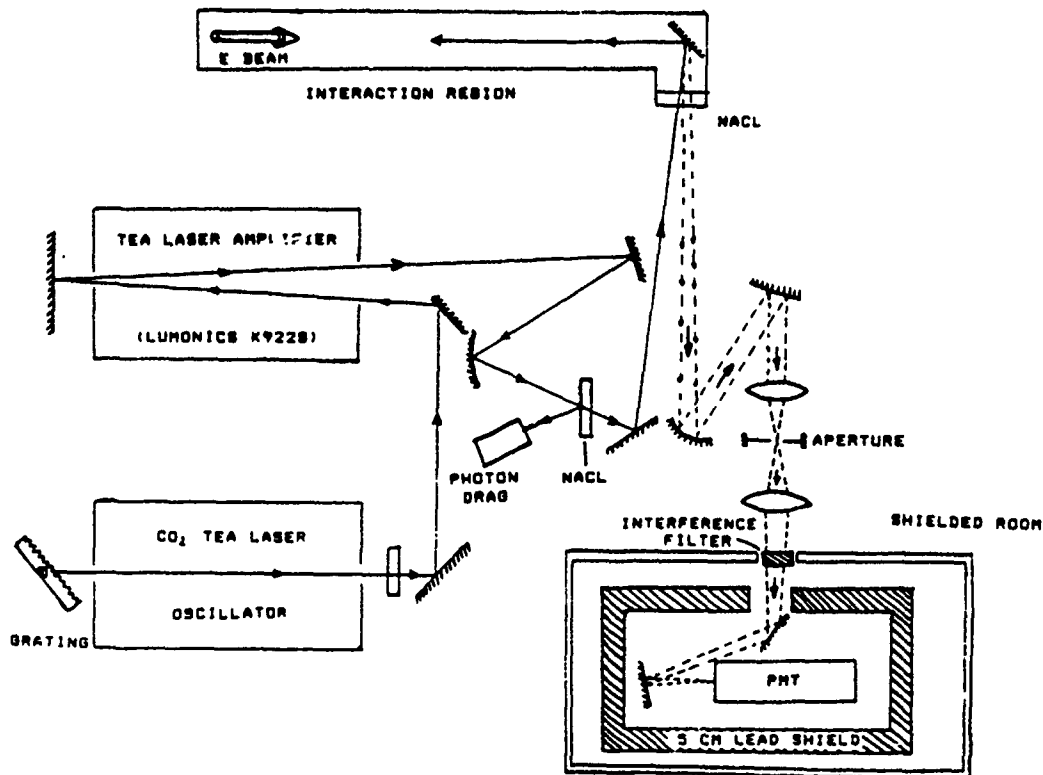
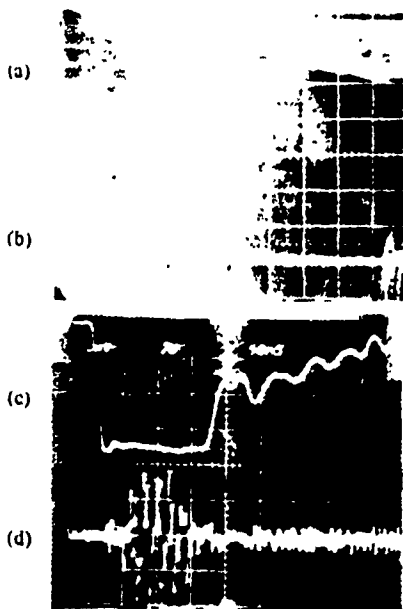Fig. 2. Layout of the laser, accelerator, beam, and detector systems.

Fig. 3. Oscilloscope photograph of typical signals. Above. each figure, diode voltage pulse. ≈ 700 kV. 50 ns/div. (a) Diode voltage. (b) TEA laser signal. photon drag detector. (c) Diode voltage [same as in part (a)]. (d) scattered light at ½ μm PMT The PMT signal is delayed 35 ns in the detector and therefore appears later in (d) compared with the photon drag signal in (b).

scattered spikes of radiation. Spectral information is obtained by filtering the scattered light with a set of narrow-band interference filters, having transmission peaks located at ½ μm, with the various bandwidths (e.g., 50, 80, 100, 250, and 500 Å).

B. Electron Beam

The accelerator is a pulse line system designed by Physics International (220G), and consists of a Marx generator, a pulse forming line, and an impedence-matching radial resistor (the latter following a self-breaking diode switch). The diode.voltage is monitored with dividing resistors, which are calibrated *in situ* against a precision electrostatic voltmeter (at reduced voltage, of course). The calibration is determined using the same circuit elements actually used, so there is no need to know the exact parameters of the circuit. Fig. 3 shows the typical diode voltage signal. Although it is ordinarily flat to ≈ 2 percent, the scattered signal spikes can be referenced to the corresponding time in the pulse, so that a sequence of scattered spikes may be correlated with the appropriate electron energy.

The radial resistor is in parallel with the vacuum diode. The function of this resistor is to match the pulse line impedance to the diode and to reduce accelerator voltage droop which is caused by diode impedence collapse. The latter can be further improved by adjusting the center conductor of the pulse line slightly off-axis; this permits the output voltage of the line to be ramped up about 4 percent during the pulse. The result is a nearly flat diode voltage signal.

The diode is shown in Fig. 4. It is adopted from a configuration used at NRL [10], specially designed to meet the cold-beam requirements set by a Raman FEL. The electrode surfaces were shaped to provide a radial electric field which balances the self-pinching effects of the azi-
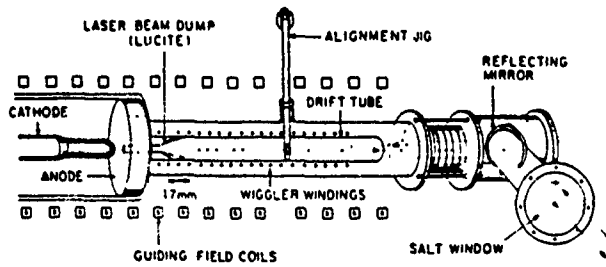
Fig. 4. Diagram of the diode, drift tube, and undulator configuration.

muthal magnetic field from the beam current. Only the central 10 percent of the beam is extracted through a 5 mm diameter aperture. The anode is a reactor graphite disk with a 15° conical concave surface and a 5 mm aperture on axis. The "cold" cathode, made from reactor graphite, is separated from the anode by a 15 mm gap; this is partly determined by the need to avoid accidental short circuits in the diode. The entire beam is immersed in a uniform guiding field of 9.5 kG. The apertured beam propagates along the axis of 71 cm long, 1.9 cm ID stainless steel drift tube. The upstream pressure in the interaction region is maintained in the range 10^{-4}–10^{-5} torr. We estimate the beam current density at ≈ 1 kA/cm^2 from the scattering data. To avoid pickup of diode light (from the cathode), and to avoid dumping the high power laser radiation at the cathode, both the incident and scattered beam lines are tilted about 1° from the axial directions. The laser beam hits a plastic beam dump concentric with the beam; this tends to reduce light emitted by the laser spark.

C. The Undulator

A current-driven bifilar helical undulator provides a right-hand, circularly-polarized magnetostatic pump field which perturbs the electron velocity in the manner appropriate to an FEL. The two coils are wound onto a grooved nylon form. The undulator is 43 cm long and contains 25 periods. A three-period transition is introduced at both ends of the undulator to provide a smooth entry of the beam into the undulator. The transverse undulator field is adjusted from 0 to 600 G by charging voltage of the capacitor bank which energizes the coils. The transverse field was measured with a multi-turn miniature pickup coil.

The magnetic field from a double-wound helical undulator is (11)

$$B_r \approx B_\perp \, (1 + \tfrac{3}{8} [2\pi r/l_0]^2 + \cdots)$$

$$\cdot \sin \, (2\pi z/l_0 + \theta_0)$$

$$B_\theta \approx B_\perp \, (1 + \tfrac{1}{8} [2\pi r/l_0]^2 + \cdots)$$

$$\cdot \cos \, (2\pi z/l_0 + \theta_0)$$

$$B_z \approx B_\perp \, (-2\pi r/l_0) (1 + \tfrac{1}{8} [2\pi r/l_0]^2 + \cdots) \quad (4)$$

$$\cdot \cos \, (2\pi z/l_0 + \theta_0)$$

using the assumption $2\pi r/l_0 < 0.8$. The radial inhomogeneity of the field causes the electrons in different orbits to be pumped to different transverse "quiver" velocities. The parallel energy spread induced by the transverse pump field gradient $\delta B_\perp / B_\perp$, averaged over the beam is

$$\left(\frac{\delta \gamma}{\gamma} \right)_{\perp,\text{und}} = (\gamma \beta_\perp)^2 \left(\frac{\delta B_\perp}{B_\perp} \right)$$

$$= \frac{\delta B_\perp}{B_\perp} \left(\frac{eB_\perp l_0}{2\pi mc^2} \right)^2 \left| \frac{eB_0 l_0}{2\pi \gamma mc^2 \beta_\parallel} - 1 \right|^{-2} \quad (5)$$

where the term in the absolute value brackets is the enhancement factor for a system operating near the magnetoresonance of the guiding field, B_0. This enhancement factor is roughly 3.5 for our choice of $\gamma = 2.3$, guiding field, and undulator period, and the representation in (5) is an approximation which is accurate to about 1 percent for our choice of parameters, taking into account a more detailed calculation of the orbit which allows for the radial variation of the undulator field across the orbit. The transverse field variation over the electron beam is about 20 percent for our parameters; this is deliberately chosen to be larger than necessary in order to bring out the inhomogeneous broadening from this element. The electron beam is injected into this tapered-entry undulator and the orbits fall into the classification of stable "type I" [12], even though we operate near magnetoresonance with $eB_0 l_0 / 2\pi \gamma mc^2 \beta_\parallel = 0.7$. Equation (5) should therefore provide an accurate estimate of the inhomogeneous broadening contribution from the undulator. The quiver velocity induced on the beam by the undulator can be as high as 0.15 c.

III. Experimental Method

Having chosen the laser wavelength of 9.6 μm, and the detector wavelength of $\tfrac{1}{2}$ μm, the Doppler upshift factor of 19.2 will determine the electron (β) and (γ) from (1): $\gamma = 2.3$ (670 kV). To detect an energy spread of $\approx$ 1–2 percent we need a resolution ≈ 0.1 percent. In comparison, the linewidth of the laser is ≈ 0.001 percent. The main constraint on the resolution comes from collecting the scattered light from a finite solid angle, $\pi (\Delta \theta_s)^2$. This will cause a spectral width $2\gamma^2 \theta_s \Delta \theta_s$ even if the electron beam is monoenergetic. If we take $f/30$ optics, the solid angle is < 0.001 and our spectral resolution will be adequate.

The signal level is proportional to the scattered photon number

$$S \propto N_s = \left(\frac{d\sigma}{d\Omega} \right) d\Omega N_e L N_{\text{inc}}. \quad (6)$$

Only the interaction length L and the incident photon number N_{inc} can be manipulated to increase the scattered power. Because of the required tilt in the optical beam

lines, a cross-beam geometry results and $L \approx 1$ cm. The power obtained from the laser amplifier is ≈ 20 MW, less than its potential because we operate using a selected monochromatic transition. Taking the electron density to be 3×10^{11} cm^{-3}, the number of scattered photons is obtained from $N_s/N_{\text{inc}} = 3 \times 10^{-15}$. As the optical efficiency is only ≈ 30 percent the scattered signal from the PMT into a 50 Ω load is only about 100 mV. Sources of interference include light emitted from the diode and X-rays; the former must not saturate the PMT and the latter must be reduced to a low level by geometry and shielding, especially because the X-ray signal appears as a random narrow spike. A narrow band optical filter is used to reject diode light and to define the spectral width of the channel. The background was such that the maximum filter width was 250–500 Å. Slowly-varying signals, principally from the diode light, were rejected by using a high pass (20 MHz) electrical filter before the oscilloscope. Combining these features, the system signal-to-noise was brought up to 5.

An optical jig was used for beam alignment, and heat-sensitive paper was used to bring the laser signal into spatial alignment with the electron beam. The incident beam path was 25-m long, and folding mirrors were used to fit this into the relatively small space available. A special sliding platform was made to isolate the optics from the accelerator, as the diode must be opened frequently for servicing (hence realignment is necessary every few shots). The scattered light signal is shown in Fig. 3(b): the spikes of the photomultiplier output appear as a bipolar signal because of the high-pass video filter. Knowing the signal delay between the incident and scattered signals (≈ 35 ns) it is possible to correlate the scattered signal spikes with the incident signal spikes and normalize the output. The spikes are a few nanoseconds wide and the voltage is constant during the scattering event. Given that the accelerator voltage is constant to within 2 percent over a 150 ns interval, it is slowly-varying to the extent of a small fraction of a percent between scattering spikes (≈ 25 ns). This permits one to find the optimum scattering voltage for centering the scattered light into the given filter, within a range of the order $\pm\frac{1}{4}$ percent; this is small compared with the energy spread and it is comparable with the resolution of the system. (Because the beam gamma is ≈ 2, it follows that an optical filter with say 1 percent bandwidth will accept a range of electron kinetic energies also ≈ 1 percent.) Although the accelerator voltage does vary slightly from shot to shot, the methodology outlined above permits one to associate a given scattering level with a fixed electron energy value; if the accelerator voltage falls outside the acceptable range or varies too much during the pulse, this defines a "bad shot."

When a finite bandwidth signal $I(\omega)$ passes through a filter with response function $T(\omega)$, the transmitted signal is

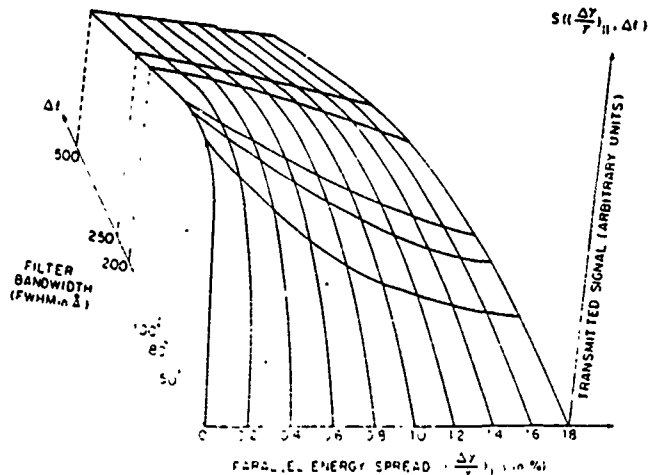$$S = \int I(\omega) \, T(\omega) \, d\omega. \qquad (7)$$

Fig. 5. Transmitted signal through an interference filter versus filter bandwidth, for several beam energy spreads (Gaussian filter shapes).

If both functions are Gaussians. with half-widths (δw) and (δf) respectively,

$$S(\delta\omega, \delta f) = IT\sqrt{\pi} \sqrt{\frac{(\delta\omega)^2 (\delta f)^2}{(\delta\omega)^2 + (\delta f)^2}}. \qquad (8)$$

In (8), $(\delta\omega)$ may be related to $(\delta\gamma/\gamma)_\parallel$. However, the filters used in the experiment did not have an ideal Gaussian shape. A grating spectrometer was set up to measure the actual transmission characteristic (the PMT response is nearly flat over the narrow spectral region defined by the filters). Using the actual filter lineshape, a response curve is generated which is somewhat more complicated in appearance than the graph of (8), shown in Fig. 5, but the data were reduced numerically according to the more complicated prescription.

IV. Results

Data are accumulated by cataloging "good" shots (about 80 of the 250 shots actually taken were "good," in which 120 spikes were used to determine the spectral widths) taken under the same alignment conditions and diode voltage with various filters in front of the detector. These signals are first normalized to the incident laser power level, whose shot-to-shot variation is about 30 percent, and these data are then fitted to the transmitted filtered signal function generated according to the methods discussed in the preceding paragraph. The curve fitting the data best yields the data point for the experimentally measured $(\delta\gamma/\gamma)$. Once the $(\delta\gamma/\gamma)$ is determined, each data point is renormalized with respect to the "ideal" filter curve, viz., Fig. 5. The result of such analysis is shown in the example Fig. 6, where we have shown the data appropriate to zero undulator field (the dotted line is a fit of $(\delta\gamma/\gamma)_\parallel = 0.6$ percent to the data). A similar curve is generated for each additional condition of undulator pump field [an example for $B_\perp = 375$ G is shown in Fig. 6(b)]. As $B_\perp$ is increased, the diode voltage is increased so as to maintain constant parallel average electron velocity.
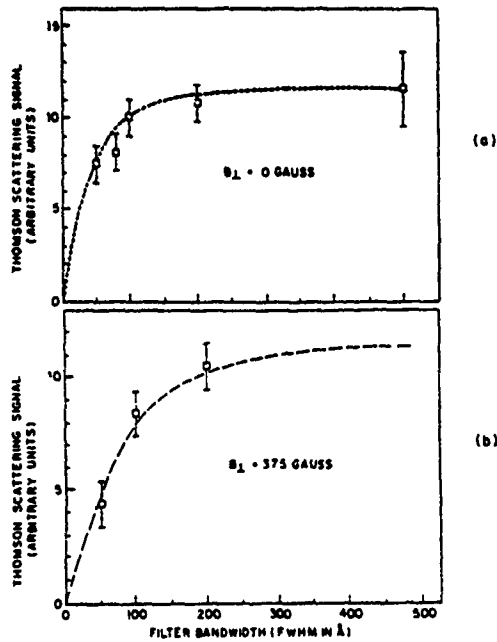
Fig. 6. (a) Scattered signal data versus filter bandwidth, for zero undulator field. The dotted line is a fit of $(\delta\gamma/\gamma)_t \approx 0.6$ percent to the data. (b) Undulator field, 375 G, line is a fit of $(\delta\gamma/\gamma)_t \approx 1.1$ percent.
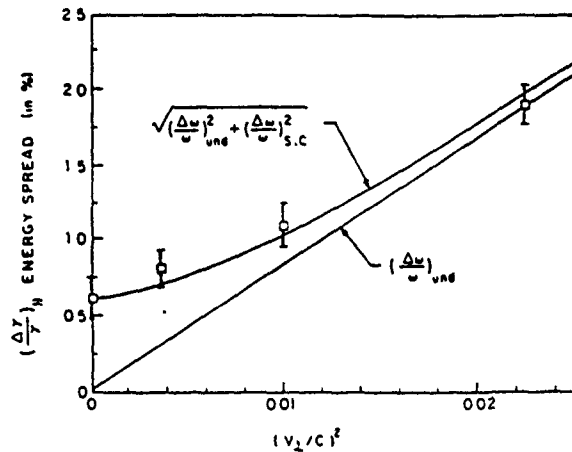

Fig. 7. Dependence of beam parallel momentum spread on the transverse "quiver" velocity induced by the undulator. The straight line is a calculation based on (5); the curved solid line is a quadratic combination of the expected undulator and beam inhomogeneous broadening terms (see Table I).

TABLE I.
SUMMARY OF THOMSON SCATTERING DATA ("MEASURED") AND ESTIMATES THE VALUE $(\delta\gamma/\gamma)$ SC IN THE "ESTIMATED" COLUMN IS OBTAINED FROM THE SPACE CHARGE INHOMOGENEOUS TERM USING ELECTRON DENSITY $= 3 \times 10^{11}$ cm^{-1}

$B_\perp$ (G)	$v_\perp/c$ QUIVER	MEASURED $(\frac{\delta\gamma}{\gamma})_t$ (TOTAL)	ESTIMATED		
			$(\frac{\delta\gamma}{\gamma})_{SC}$	$(\frac{\delta\gamma}{\gamma})_{und}$	$[(\frac{\delta\gamma}{\gamma})^2_{SC}+(\frac{\delta\gamma}{\gamma})^2_{und}]^{1/2}$
000	0 0	0 6% ± 0 14%	0 5%	0 0%	0 5%
225	0 055	0 8% ± 0 14%	0 5%	0 3%	0 77%
375	0 10	1.1% ± 0 14%	0 5%	0 8%	0 9%
525	0 15	1 9% ± 0 14%	0 5%	1 9%	2 06%

A summary of the data taken is given in Table I. The numbers in the "estimated" region of the table correspond to calculations of the inhomogeneous broadening based on the measured macroscopic parameters of the system. The broadening from the beam space charge is contained in the term denoted by "S.C." $((\delta\gamma/\gamma)_{SC} = \omega_p^2 r_b^2/4c^2) = 0.5$ percent; this number is based on the space charge electrostatic depression obtained from the drift tube geometry and measurements described later in this section. The effect of diode emittance is not measured separately, but is combined with the space charge effect when the undulator is not energized. If the emittance and space charge effects are combined quadratically (as independent sources of momentum spread), and the total spread is taken as the experimentally determined value, then we find $0 \leq (\delta\gamma/\gamma)_{\parallel,e} \leq 0.5$ percent, with a most probable value of 0.35 percent. This range of values is consistent with the range of values presented in [10], namely 0.13 percent to 0.6 percent. Thus, without the undulator, we find the Thomson scattering diagnostic is providing reasonable results for the beam momentum spread.

The inhomogeneous broadening is then observed when the undulator is energized. The estimated value in the table is based on (5), accounting for the change of gamma as $B_\perp$ is increased. In the last column, we have combined the inhomogeneous terms quadratically. The comparison between the expected inhomogeneous broadening and the measured result is best shown in Fig. 7: the latter summarizes all the data taken in this experiment. In interpreting the data, it is important to realize that the large contribution to the inhomogeneous broadening from the undulator is intentional here, as $k_0 r_b \approx 1$, and does not represent "typical" data from a well-designed FEL of this type.

The experimental results show first that an intense, relativistic electron beam obtained from a well-engineered but simple diode using a cold cathode is sufficiently "cold" for Raman FEL applications. In this example, a 50 period undulator could be used before thermal effects on the beam would cause a reduction in gain [13]. Using an electron beam with a total momentum spread of 2 percent, it should be possible to operate an FEL at wavelength as small as 100 μm with a 3 cm period undulator and beam energy of 10 MV in the high-gain Raman mode. This would require limiting the undulator amplitude and therefore restricting the gain. The limiting criterion we have used for this estimate is that the period of the plasma wave be twice the Debye distance, all referred to the electron rest frame.

The second point—one which would not have been appreciated prior to this experiment—is that the inhomogeneous broadening terms should be combined quadratically, that is, as "random error" type effects. The reason this might not have been expected is that the beam space charge causes electrons on the inside of the electron beam to have less forward energy than electrons on the outside; whereas, the undulator pumps more effectively on the outside of the beam, converting parallel motion to transverse quiver. These two effects are in opposite tendencies, which means that for an optimum undulator field there would be

expected a compensation of broadening effects and a resulting monochromatic beam. This is clearly not the result we obtain (the "optimum " $B_\perp$ would be close to the 225 G data point). The Thomson scattering diagnostic measures the $(\delta\gamma/\gamma)_\parallel$ averaged over the electron beam cross section, which is exactly what is available to the FEL. How accurately can we say the data can be fitted quadratically? The calculation of the undulator inhomogeneous broadening term is done using (5), and a source of error is the measurement of the guiding field which enters into the magnetoresonant factor. Taking a liberal estimate of 5 percent error for the experimental value of B_0, the quadratic fit to the data is still a good representation, that is, better than a linear fit.

Having measured the diode voltage at which scattering was observed, we find this is 30 kV higher than the electron energy which is necessary to cause a scattering upshift factor of 19.2 as given by (1), i.e., 670 kV. As this is statistically significant, in view of the calibration accuracy and experimental error limit (≈ 2 percent, or 15 kV), we suggest the higher value of diode voltage is necessary to inject the beam space charge into the drift tube in concentric coaxial cylindrical geometry. A simple electrostatic calculation involving the radius of the beam and the drift tube permits a determination of the electron density, $\approx 3 \times 10^{11}$ cm^{-3}. (The electron density can be used to calculate the current density and the expected inhomogeneous broadening from the space charge well.) This then can be used to estimate the absolute signal level, given certain uncertainties involving the optical system. Our conclusion is that the signal level is consistent with the $(4\gamma^2)$ factor in the differential scattering cross section. The frequency upshift factor and enhancement of cross section effect were also obtained in an experiment reported by Sinclair et al. [14], wo used a 20 GV electron beam to produce 7 GV protons from an incident ruby laser signal. However, our experiment is the first to report measurements of the actual electron energy distribution in the beam.

ACKNOWLEDGMENT

REFERENCES

[1] D. B. McDermott. T C Marshall, S. P. Schlesinger. R. K. Parker, and V. L. Granatstein. "High power free electron laser based on stimulated Raman backscattering." *Phys. Rev. Lett.*, vol. 41. pp. 1368-1371. 1978.

[2] S. C. Chen and T. C. Marshall. "Thomson backscattering from a relativistic electron Beam as a diagnostic for parallel velocity spread." *Phys. Rev. Lett.*, vol. 52. pp. 425-428. 1984.

[3] J. D. Bjorken and S. D. Drell, *Relativistic Quantum Mechanics.* New York: McGraw-Hill, 1964.

[4] R. H. Pechacek and A. W. Trivelpiece, "Electromagnetic wave scattering from a high temperature plasma," *Phys. Fluids,* vol. 10, pp. 1688-1696. 1967.

[5] A. I. Akhiezer and V. B. Berestetskii, *Quantum Electrodynamics.* New York: Wiley. 1965.

[6] J. Sheffield, "Incoherent scattering of radiation from a high temperature plasma," *Plasma Phys.*, vol. 14, pp. 783-791. 1972.

[7] J. H. Williamson, and M. E. Clarke, "Construction of electron distribution functions from laser scattering spectra," *J. Plasma Phys.*, vol. 6, pp. 211-221. 1971.

[8] A. B. Kukushkin, "Incoherent scattering of light by a finite volume of a relativistic plasma," *Sov. J. Plasma Phys.*, vol. 7, pp. 63-67, 1981.

[9] V. A. Zhuravlev and G. D. Petrov, "Scattering of radiation by a finite volume of relativistic plasma streams," *Sov. J. Plasma Phys.*, vol. 5, pp. 3-5, 1979.

[10] R. H. Jackson et al., "Design and operation of a collective millimeter-wave free-electron laser." *IEEE J. Quantum Electron.*, vol. QE-19. pp. 346-356. Mar. 1983.

[11] J. P. Blewett and R. C. Chasman. "Orbits and fields in the helical wiggler."*J. Appl. Phys.*, vol. 48. pp. 2692-2698, 1977.

[12] H. P. Freund, "Nonlinear analysis of free electron laser amplifiers with axial guide fields." *Phys. Rev.*, vol. A27. pp. 1977-1988. 1983.

[13] L. F. Ibanez and R. S. Johnston, "Finite temperature effects in free electron lasers," *IEEE J. Quantum Electron.*, vol. QE-19. pp. 339-346. Mar. 1983.

[14] C. K. Sinclair, J. J. Murray, P. R. Klein, and M. Rabin. "A polarized photon beam for the SLAC 82-inch hydrogen bubble chamber." *IEEE Trans. Nucl. Sci.*, vol. NS-16. pp. 1065-1068. 1969.

Shien-Chi Chen was born in Taipei, Taiwan, on February 23. 1956. He received the B.S. degree in physics from National Taiwan University. Taipei. Taiwan in 1978, and the M.A. and Ph.D. degrees in physics from Columbia University. New York, NY, in 1982 and 1984. respectively.

He is currently at AT&T Bell laboratories, Murray Hill. NJ. where he is engaged in research on free-electron lasers and far infrared spectroscopy.

T. C. Marshall was born in Cleveland. OH on January 29. 1935 He received the Ph.D. degree in physics from the University of Illinois. Urbana. in 1960.

He is currently a Professor of Applied Physics at Columbia University. New York. NY In addition to research in free-electron lasers, he has undertaken research in intense relativistic beam phenomena. plasma-wave scattering and instabilities. trapped-particle effects in plasmas, and the formation and heating of plasmas in high beta equilibrium.

Prof. Marshall is a Fellow of the American Physical Society

Section IX. Raman FELs and FELs with guide fields

A RAMAN FEL AT 2 mm WAVELENGTH

J. MASUD, F.G. YEE, T.C. MARSHALL and S.P. SCHLESINGER

Columbia University, New York City 10027, USA

Recent results from the Columbia Raman FEL oscillator and amplifier are summarized. About 2 MW of power at 2 mm has been obtained from a constant period undulator oscillator, which is close to the theoretical maximum. Spectral data on the oscillator linewidth (~ 1%) and dispersion are discussed, and compared with theory. Progress on the amplifier configuration, which uses the output from a NH_3 molecular laser as a coherent source, is also summarized.

1. Introduction

The nonlinear physics of the free electron laser (FEL) involves waves set up in a nearly cold electron beam when it passes through the undulator. In addition to the pump field and the growing scattered EM wave moving parallel to the electrons, there is a disturbance in the beam space charge caused by the ponderomotive force. Since a dense electron beam ($\omega_p L/\gamma c \gg 1$) may also support a space charge (or plasma) electrostatic wave, there can be an important interaction when the ponderomotive force resonates with this mode. Even when the pump is weak, exponential gain can occur; this is referred to as the "Raman" FEL. The name is drawn from Raman lasers when an intermediate energy level is involved in a stimulated scattering interaction with an optical pumping source.

In this paper we discuss initial experimentation using a simple Raman oscillator and amplifier. The purpose of the oscillator is to define initially the regions of substantial gain by observing the emission wavelength. Following this, the gain is observed in an amplifier configuration, using a CO_2 laser pumping an NH_3 gaseous laser at 140 GHz (2.14 mm).

2. Experimentation

We use a 60 cm long bifilar helical undulator, having tapered entry and exit (period: $l_0 \approx 1.45$ cm), positioned over a 5 mm diameter, ~ 100 A beam enclosed in a 6.2 mm diameter drift tube (TE11 cutoff, 27 GHz). In a previous experiment, a Thomson backscattering diagnostic showed [1] that the intrinsic parallel momentum spread was $< \frac{1}{2}\%$, and was largely dominated by the beam space charge. In this new configuration, the only important change is to reduce the diameter of the drift tube, which should improve the beam quality. In the energy range of the beam (650–750 kV), for a guiding field, B_0, of 8.8 kG, the electron orbits are stable type I, viz., $\gamma k_0 v_{\parallel} > eB_0/mc$, where $k_0 \approx 2\pi/l_0$. The guiding field causes an enhancement in the electron quiver velocity induced by the undulator, so that $v_{\perp}/c$ ~ 10% for $B_{\perp}$ ~ 500 G. The forward scatter mode is convective, and therefore will not compete with the desired backscatter (FEL) mode. The configuration of the accelerator, the FEL amplifier and its assortment of gas lasers is shown in fig. 1.

In the oscillator, the upstream reflector is just a thin annular ring concentric with the electron beam. The thickness of the ring is ~ 1.5 mm, which reflects only ~ 50% of the incident radiation (it is thin to avoid a substantial electrostatic perturbation on the beam). The downstream reflector is the quartz vacuum window with ~ 10% reflectivity. Thus the oscillator will operate only if the single pass FEL gain is very high. A pulse of radiation at ~ 2 mm is shown in fig. 2. The power at the output window was observed to be 2 MW (determined by a calibrated receiver). As a comparable amount of radiation is emitted into the diode, we compute an efficiency ~ 3%, which compares favorably with theory ($\omega_p/\gamma k_0 c$). The long start time is required because of the large cavity losses. We do not know why the FEL pulse does not last longer, but it may have something to do with the high intensity radiation which is beamed into the diode. Also shown in fig. 2 is the dependence of power radiated upon undulator pump field. The threshold for oscillation is high because the losses at each end of the cavity are very high. In the upper range of $B_{\perp}$, we leave the Raman region and enter the region of the strong pump instability. The power was measured using the radar formula and a set of attenuators which we calibrated in the FEL's own radiation, so that the crystal detector remained in its linear response zone.

Next, spectroscopy was done on the radiation emitted from the simple oscillator using a millimeter grating spectrometer. The latter was calibrated against conven-
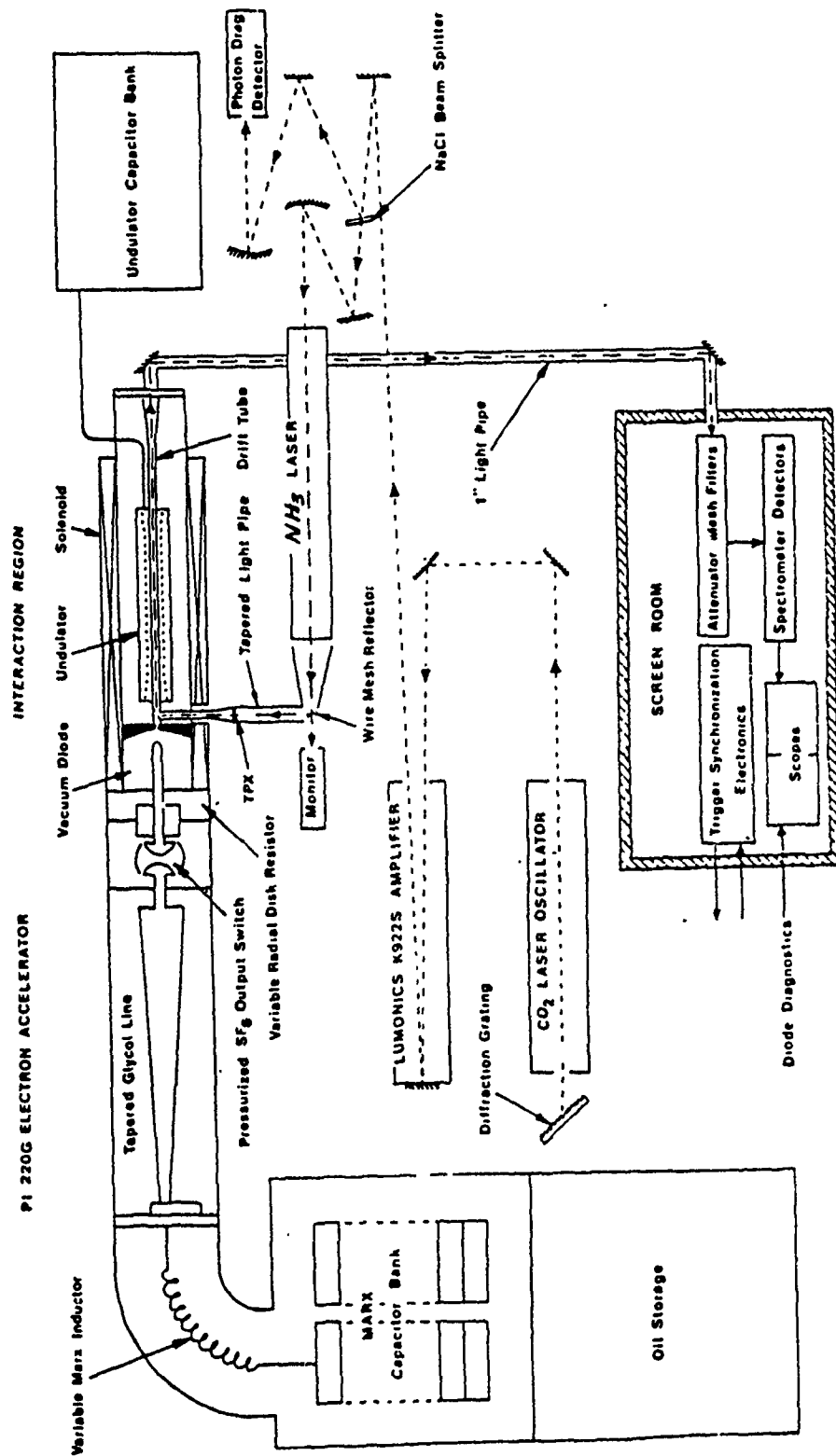
Fig. 1. Layout of the experimental hardware, consisting of accelerator, FEL, gas lasers, and diagnostics. The timing of the lasers and the accelerator pulse is crucial, <50 ns jitter permissible.
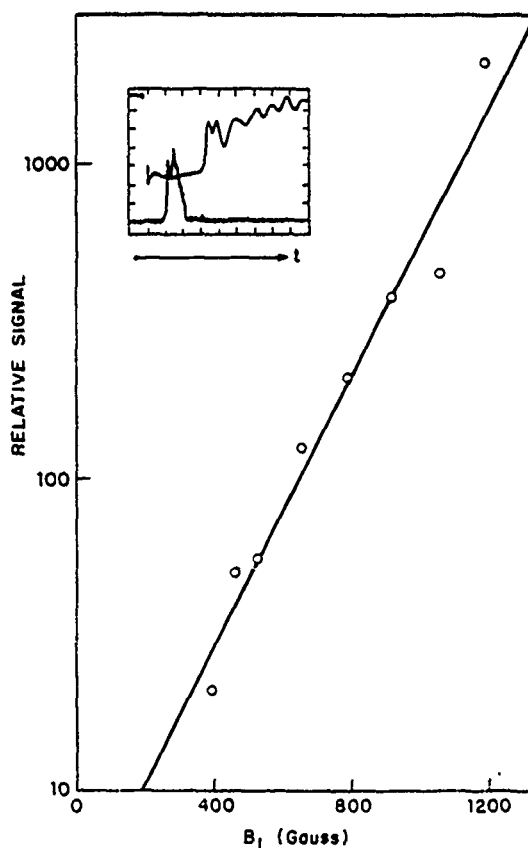
Fig. 2. Dependence of FEL oscillator power on pump field amplitude. Total power output, ~ 2 MW. Inset: diode voltage pulse (above) and radiation pulse (below) at 2 mm wavelength; time scale, 50 ns/div.
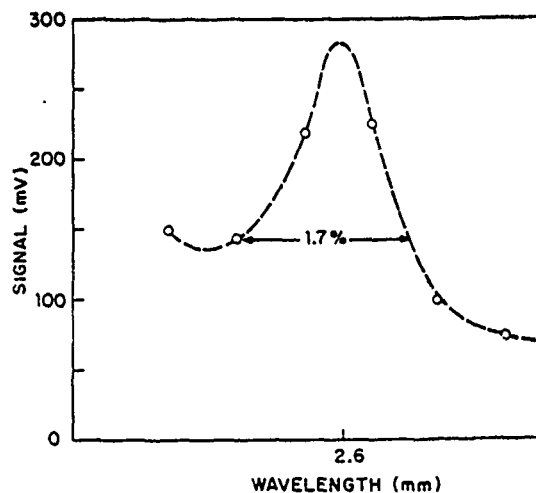

Fig. 3. FEL oscillator line profile, obtained from a grating spectrometer.

voltage). At lower energy, smaller transmitted current may result from high $V_\perp$, and this may explain the discrepancy. These results show that the amplifier should be operated at a diode voltage of ~ 750 kV.

The amplifier experiment requires a dependable high power (~ 1 kW) source of coherent signal in the millimeter region. Initial efforts utilized a 1.2 mm line emitted from isotopic methyl fluoride pumped by a CO_2 TEA laser. However, the 3D theory predicted low gain.

tional 2 and 3 mm sources. The resolving power of the instrument was ~ 100, and in fig. 3 we see a profile of the oscillator emission line. The total linewidth, 1.7%, compares favorably with the linewidth measurement of the first Raman FEL [2]. The intrinsic linewidth of the radiation is only about 1%, and is therefore less than the undulator linewidth (~ 2%). One would expect that for an oscillator the homogeneous linewidth should be smaller than $1/N$ by roughly a factor of the square root of the number of radiation bounces, which should account for the factor of two. On the other hand, the inhomogeneous line broadening is also ~ 1% [1].

In fig. 4 we show a plot of the dependence of scattered wavelength upon beam energy, in which a comparison with Freund's three-dimensional theory is indicated [3]. The agreement with the theory is good, especially at lower pump field, farther from magnetoresonance; only the point at longer wavelength falls substantially away from the prediction (the electron energy is based on the empirical determination of the diode
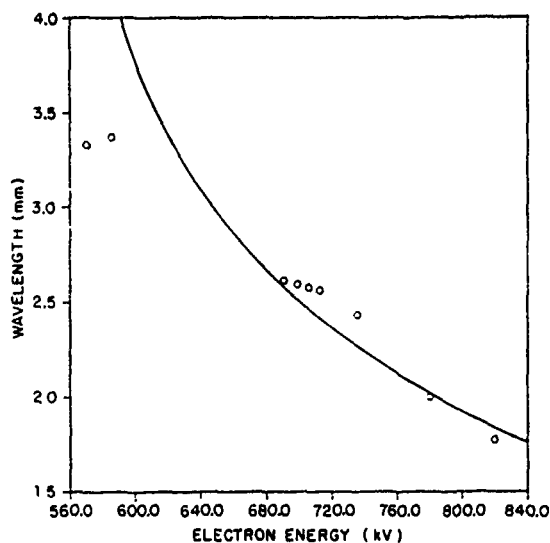

Fig. 4 FEL wavelength for different energies. The theory curve is for the following parameters: beam current 200 A, TE11 mode in drift tube, guiding field 9 kG, undulator period 1.45 cm, $B_\perp = 800$ G.
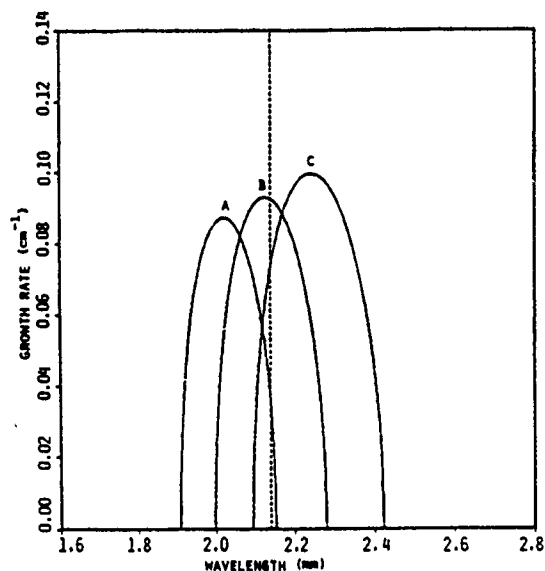
Fig. 5. Theoretical calculation for the spatial growth rate, after [3]; same conditions as fig. 4 except beam current = 100 A, A = 740 kV, B = 720 kV, C = 700 kV. The dashed line indicates the 140 GHz ammonia laser.

It was not possible to obtain reliable quantitative data using this line given the experimental limitations on guiding field and accelerator energy, because of the necessity for a short undulator period (1.1 cm). Recently, a new long wavelength (2.14 mm) ammonia laser – also CO_2 TEA pumped – has been studied [4], and this should be a more satisfactory source of signal imput for the FEL. The longer wavelength permits an increase of undulator period (1.45 cm, the same as for the oscillator described above) and $V_\perp$. Gain measurements are in progress. In fig. 5 is shown a theoretical 3D computation for the FEL gain of our apparatus in the vicinity of the NH_3 line: ~ 30 dB single-pass power gain should result.

Acknowledgement

References

[1] S.C. Chen and T.C. Marshall, IEEE J. Quantum. Electron. QE-21 (1985); Phys. Rev. Lett. 52 (1984) 425.
[2] D.B. McDermott et al., Phys. Rev. Lett. 41 (1978) 1368.
[3] H.P. Freund and A.K. Ganguly, Phys. Rev. A28 (1983) 3438.
[4] P. Woskobomikow, J.Z. Machuzak and W.J. Mulligan, IEEE J. Quantum. Electron. QE-21 (1985) 14.

Gain Measurements from Start-Up and Spectrum of a Raman Free-Electron–Laser Oscillator

J. Masud, T. C. Marshall, S. P. Schlesinger, and F. G. Yee

Columbia University, New York, New York 10027

Results from a Raman free-electron–laser oscillator producing ~ 2 MW at 2.5-mm wavelength ($\Delta\lambda/\lambda \simeq 1\%$) are reported. A novel method of extracting regenerative-gain and power-coupling-loss measurements from signal delay times is described and the experimental analysis compared with 3D theory. The first observation of long-wavelength sideband power in the Raman regime is reported at high undulator strength. Temporal behavior of the output after saturation is reached is discussed.

PACS numbers: 52.75.Ms, 42.55.Tb

In a free-electron laser (FEL), radiation present at the electron-beam entry is convectively amplified by a traveling-wave mechanism. The system will oscillate if the output signal is returned to the input by mirrors, and it should be possible to uncover the details of the FEL signal gain and saturation by analysis of time-dependent effects. In this Letter, we report such data from a Raman FEL oscillator, operating at $\lambda \simeq 2.5$ mm, using a 700-kV, 1-kA/cm^2 electron beam interacting with a constant-period ($l_0 = 1.45$ cm) undulator 50 cm in length in a 9.45-kG guiding field. Operation at 2-mm wavelength in a waveguide of 6-mm diameter requires the use of 3D theory[1] to interpret the results. These results, which compare favorably with calculations from theory, show high-power output (2 MW) and reasonable efficiency (~ 3%); in addition, the coupling loss is measured as well as the parametric dependencies of the small signal gain.

FEL oscillation in the millimeter and submillimeter range has been reported[2] and studied[3] with respect to basic power and spectroscopy measurements. Recent experiments have utilized high-quality beams (i.e., low temperature); in one,[4] high power, gain, and efficiency were achieved with use of a guiding field near "magnetoresonance" [$\gamma k_0 \beta = eB_0/mc^2$, where $k_0 = 2\pi/l_0$ is the undulator wave number, B_0 is the axial guiding field, $\gamma = (1 - \beta^2)^{-1/2}$, and $\beta = v_\parallel/c$]. The magnetoresonant effect enhances the electron quiver motion in the undulator and permits larger gain to be obtained at reduced undulator field $B_\perp$, but can lead to nonlinear effects which are not yet fully understood. More recently, extensive measurements have been made[5] on a microwave FEL operating in the Raman regime. Our study also uses a high-quality electron beam [parallel normalized momentum spread $(\delta\gamma/\gamma)_\parallel \simeq \frac{1}{2}\%$],[6] but unlike these experiments, it avoids magnetoresonance ($eB_0/\gamma mc^2 k_0 = 0.53$) by use of stable "group I" electron orbits.[7]

In the "weak pump" Raman regime, the traveling-wave signal grows exponentially along the undulator.[8] The conditions for a Raman FEL are those of high beam density, low energy [$\omega_p L/\gamma c \gg 1$, where

$\omega_p = (4\pi n e^2/\gamma m)^{1/2}$ and L is the interaction length], together with a relatively weak undulator field ($B_\perp < 1$ kG here) and, of course, adequate beam quality [$(\delta\gamma/\gamma)_\parallel < 1/N$, where N is the number of undulator periods]. The "strong pump" regime, where exponential growth continues, has also been explored experimentally.[9]

A schematic of the oscillator is shown in Fig. 1(a). A pulse-line accelerator provides a 150-nsec voltage pulse to an apertured diode. The undulator, 64.5 cm long, is a bifilar helical winding powered by a capacitor bank. The entry and exit of the undulator are zones (7.3 cm each) of adiabatically changing field, caused by variation of the winding diameter, with a 50-cm-long uniform-field region in the middle. Two mirrors, one of which is a polished annular disk (M1) and the other a quartz window (M2), provide feedback. An upper limit to their power reflectivities has been calculated to be $R_1 = 65\%$ and $R_2 = 9\%$ so that $R_1 R_2 \sim 5.9 \times 10^{-2}$. A lower value of $R_1 R_2 \sim 3.8 \times 10^{-2}$ was found to fit the data best and this was used in drawing comparisons with theory. After a certain start time, $t = t_s$, the system oscillates at high power, often as a sequence of "mode-locked" pulses spaced by the cavity bounce time, $2L_c/c$ [Fig. 1(b)].

A grating spectrometer (resolving power = 100) shows that the radiation consists of a narrow (~ 1%) line and a lower-frequency sideband dispaced from the fundamental by ~ 6% [Fig. 1(c)]. The sideband is to be expected in a system which runs to saturation,[10] and is due to particle trapping in the pondermotive potential well, but had not been previously observed in the collective regime. As the undulator field is increased, power at the sideband frequency is found to grow to levels comparable to the fundamental, whereas the latter quickly saturates above the threshold field (~ 400 G). The dependence of the wavelength upon electron energy was found to be in good agreement with the 3D calculation of the frequency of maximum growth for a TE$_{11}$ mode and tunability from 90 to 170 GHz was demonstrated.[11]

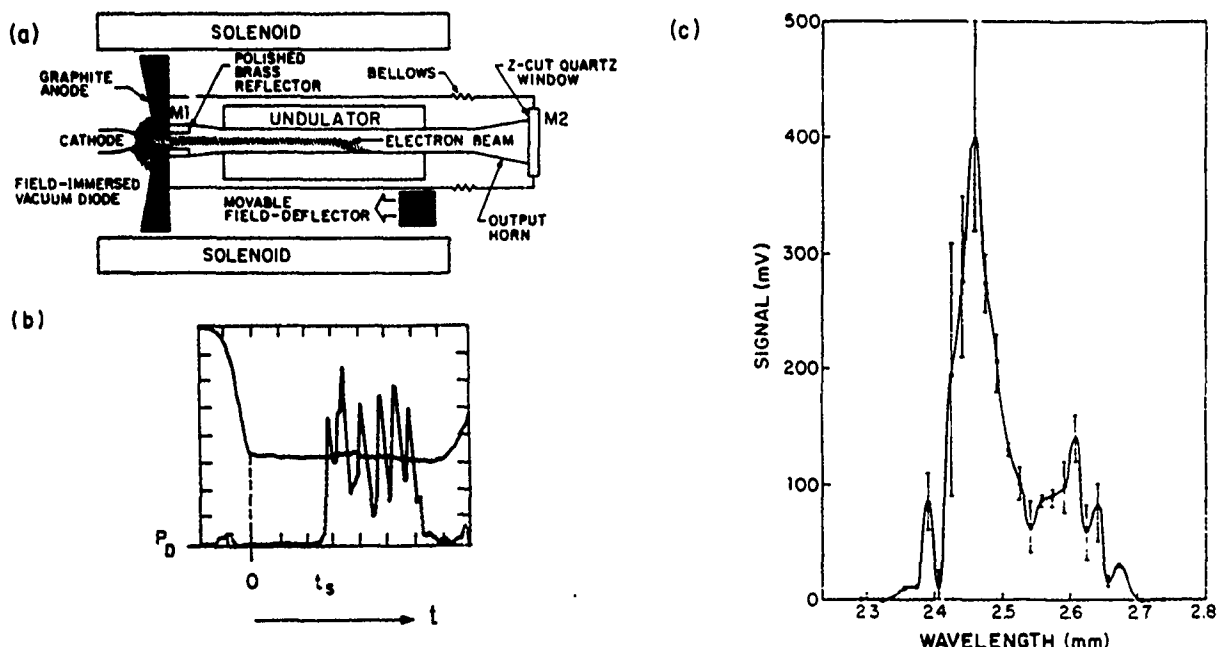A new method of obtaining radiation growth-rate

FIG. 1. (a) Oscillator schematic. (b) Typical wave forms (time scale, 20 ns/div.). Above: Diode voltage (120 kV/div.); below: FEL output, showing mode locking and "start time" t_s. (c) 2.4-mm-grating spectrometer data showing FEL spectrum at $E = 700$ kV, $B_\perp = 650$ G. The 2.45-mm and ~ 2.6-mm peaks correspond to the fundamental and sideband wavelengths, respectively. Bars indicate shot-to-shot fluctuations.

measurements and subsequently making quantitative comparisons with theory was employed on this system. It consists of observing the dependence of t_s on any of the variables which affect the FEL gain per pass: the undulator field, the electron energy, the interaction length, the guiding field, the cavity losses, or the beam current. Functional dependence on the first three of these parameters is presented here.

If the oscillator starts from noise power (P_0) and builds up to a high, but unsaturated, level (P_D) after exponentiation over n radiation bounces [Fig. 1(b)], then

$$\frac{P_D}{P_0} = \left\{ \frac{1-\alpha}{m^2} [\exp(2\Gamma L) + \exp(-2\Gamma L)] \right\}^n, \quad (1)$$

where $n = t_s/(2L_c/c)$, $t_s =$ "start time," Γ is the Raman spatial growth rate, $L = Nl_0$ is the interaction length, α is the total cavity power loss per pass and is dominated by the large mirror losses (i.e., $\alpha = 1 - R_1R_2$), and m is the number of modes between which the recycled electromagnetic power is divided at the input mirror M1. In Eq. (1), this power sharing is assumed to take place between a growing and a decaying EM wave with no coupling between the electron beam and the backward-propagating EM wave, so that the coupling loss factor is $1/m^2 = \frac{1}{4}$. In the experiment, P_D is taken to be the threshold detection level, determined by detector responsivity, transmission losses, and attenuation needed to keep signal levels

within the linear-response range of the crystal-diode detector.

In Eq. (1) the negative-exponent term inside the square brackets can be neglected for the typically large FEL gain pertinent to our system ($\Gamma L > 2$). Also, for the weak-pump Raman regime, the spatial growth rate can be written as $\Gamma L = KB_\perp$, where K is essentially independent of $B_\perp$ far from magnetoresonance.[12] Therefore Eq. (1) becomes

$$LB_\perp = \{L_c \ln(P_D/P_0)/ct_s - \ln(R_1R_2/4)/2\}/K. \quad (2)$$

Note that $LB_\perp$ is inversely proportional to t_s.

The variation of start time with the undulator field is shown in Fig. 2(a) in which the predicted linear dependence of $B_\perp$ on $1/t_s$ is evident. The vertical dashed line indicates the end of the voltage pulse by which time about 18 radiation round trips can take place in the cavity. The bars indicate uncertainties in the measurement technique and they increase as t_s becomes smaller. However, the shot-to-shot reproducibility of the data points was found to be excellent with a flat voltage pulse ($\Delta V/V < 2\%$). The spread of the points around the best-fit line increased for a more rippled voltage ($\Delta V/V \sim 5\%$), especially for small t_s. This is expected since Eq. (2) assumes that K is constant during the interval $0 < t < t_s$. Nevertheless, the intercept at $1/t_s = 0$ which yields a value for K can be unambiguously determined even with a rippled voltage run since the points were found to converge to a single value as
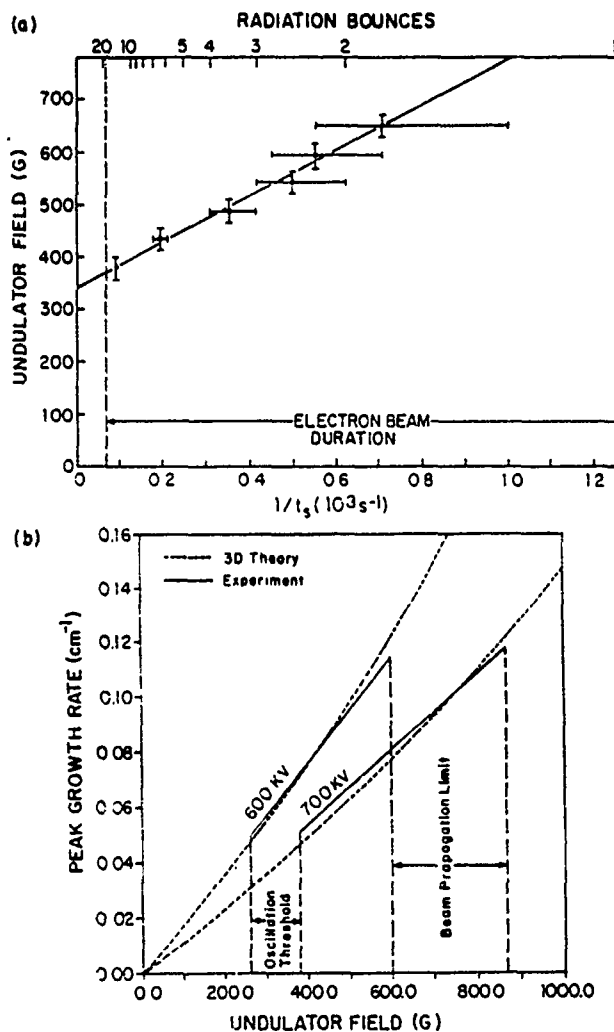
FIG. 2. (a) $1/t_s$ vs $B_\perp$ at $E = 700$ kV and $L = 50$ cm. (b) $\Gamma = KB_\perp$ (solid lines) and theoretical (dashed) curves obtained at $E = 600$ and 700 kV.

t_s increased. As far as possible, only identical flat-voltage shots were considered. The procedure can be repeated for another set of parameters and in this manner the factor K and $\Gamma = KB_\perp$ can be obtained as functions of, for instance, the electron energy. In Fig. 2(b) are shown two example of $\Gamma = KB_\perp$ gain curves obtained at two widely different diode voltages. The agreement with 3D theory[1] can be seen to be very good insofar as we are trying to fit a straight line to a curve. The experimental window is bounded, on the low-$B_\perp$ side, by the finite electron-beam duration (i.e., the gain has to be large enough for the power to build up out of noise before the end of the voltage pulse at $t = 150$ ns) and, on the high-$B_\perp$ side, by the electron transverse motion, which, when large enough, results in the electrons striking the drift-tube walls. The latter fact was verified with witness-plate and Faraday-cup measurements. In addition, these experimentally determined limits can be seen in Fig. 2(b) to corre-

spond to very nearly the same growth rates (and therefore, the same $v_\perp$) in both cases as expected: the same critical gain at the $t_s = 150$ ns oscillation threshold and the same large transverse velocity resulting in beam disruption. In the theoretical modeling, the beam is assumed to be cold, which is a good assumption in the light of previous experimental measurements.[6]

The coupling-loss factor, $1/m^2$, is important to the theoretical modeling of FEL oscillators. The number of ways in which the amplified wave energy is divided depends, for example, on the undulator strength: In the strong-pump regime, there exists a third, oscillatory solution to the FEL dispersion relation,[3] so that the coupling-loss factor becomes $\frac{1}{9}$. For single-pass amplifiers, the gain per pass must be large enough to overcome not only any signal-insertion and polarization-matching losses, but also this substantial mode-coupling loss. Despite the importance of the coupling loss for both FEL theory and experimental design, no systematic effort has yet been made to measure this factor. The good agreement between calculations and experiment in Fig. 2(b) not only confirms the 3D theory employed (which predicts only single-pass growth rates), but also strongly supports the choice of $m = 2$ made in Eq. (2).

In another approach, the undulator field was kept constant and the interaction length L was varied. This was accomplished by our moving an asymmetrical soft-iron piece along the undulator length [Fig. 1(a)] thereby deflecting the guiding field and with it the electron beam to the drift-tube wall. One example of the resulting L vs $1/t_s$ plot is shown in Fig. 3(a) where the linear dependence predicted by Eq. (2) is clearly seen. The flattening at $L = 50$ cm corresponds to the end of the uniform undulator. By use of the theoretical growth-rate value for these parameters, the expected $1/t_s = 0$ intercept, L_0, can be calculated from Eq. (2) with $R_1R_2/4$ replaced by R_1R_2/m^2 for different m. Once more, agreement with $m = 2$ is excellent. As with Fig. 2(a), the standard deviation in the data points was much less than the error bars would indicate.

The interaction length and the undulator field can also be simultaneously adjusted for the FEL output power to reach P_D at $t \sim 150$ ns, the end of the voltage pulse. This allows a rapid determination of L_0 at different pump strengths, but is approximate in that $1/t_s \neq 0$ as required [the discrepancy can be seen in Fig. 3(a) to be not large]. The experimental data [Fig. 3(b)] are seen to track the $m = 2$ curve quite well, given the approximate nature of the measurement technique and shot-to-shot variations (these are single-shot measurements). Agreement is even better for the $B_\perp = 430$ and 650 G points (circled) which were evaluated at the correct $1/t_s = 0$ intercept. This
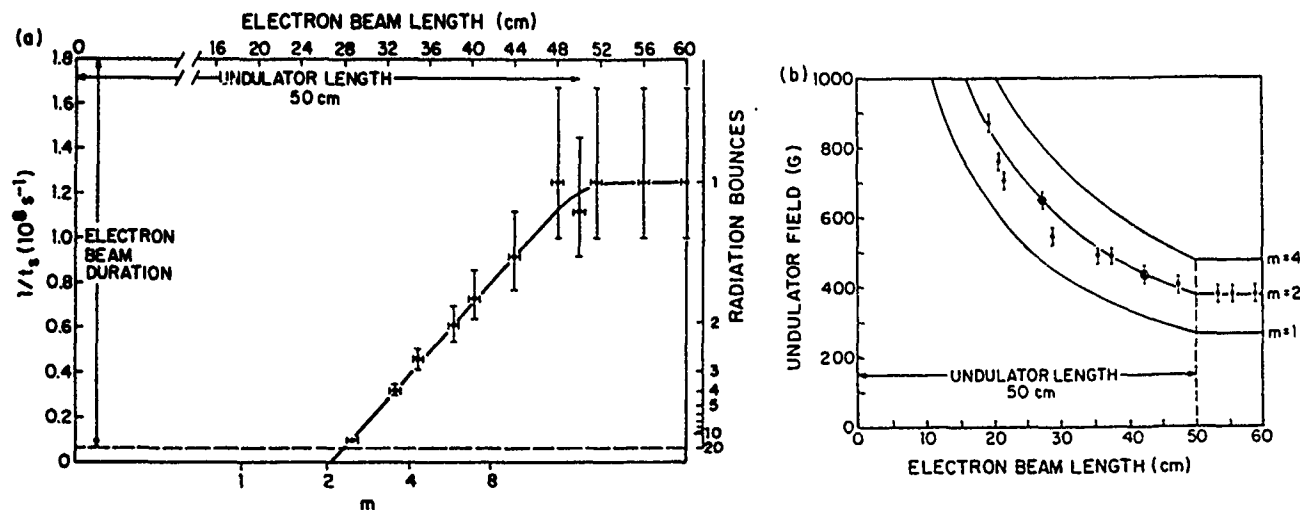
FIG. 3. (a) $1/t_s$ vs L at $E = 700$ kV and $B_\perp = 650$ G. (b) L_0 vs $B_\perp$ at $E = 700$ kV and $t_s = 150$ ns (dots) and $t_s = \infty$ (circled).

suggests that for operation at $B_\perp < 1$ kG we remain within the weak-pump collective regime.

Two additional points about the temporal evolution of the FEL power deserve mention. First, the FEL output does not persist for the entire duration of the voltage pulse but lasts typically ~ 50–60 ns and usually falls off in the < 5-ns decay time of the cavity. The exact shutoff mechanism is not yet understood, but we believe that the high power radiated into the diode and/or the parasitic nature of the off-resonance sideband instability may be responsible. Second, even at high gain when the start time is short, the signal does not build up again during the remainder of the voltage pulse after the initial disruption. The reason for this behavior was found to be the initial noise level, P_0, needed for power to increase to P_D in $t < 150$ ns. This threshold noise level—found to be $\simeq 10$–100 W from the slopes of Figs. 2(a) and 3(a), Eq. (2), and the estimated value of P_D—is about 10^6 times greater than that available as spontaneous undulator emission even at high $B_\perp$. The source of this high background level, we believe, is the beam noise present at the abrupt accelerator voltage turnon at $t = 0$. A 100-W noise level would correspond to an electron density perturbation of only $\simeq 0.02\%$ via the pondermotive force. This explains the absence of late-time FEL signal after the ini-

tial oscillation has died away and the beam is quiet.

The authors wish to acknowledge the cooperation of H. P. Freund and A. K. Ganguly in making available their 3D code. This work was supported by the U.S. Office of Naval Research Grant No. N0014-79C-0769.

[1]H. P. Freund and A. K. Ganguly, Phys. Rev. A 28, 3438 (1983).

[2]D. B. McDermott et al., Phys. Rev. Lett 41, 1368 (1978).

[3]D. S. Birkett et al., IEEE J. Quantum Electron. 17, 1348 (1981).

[4]S. H. Gold et al., Phys. Fluids 26, 2683 (1983).

[5]J. Fajans et al., Phys. Fluids 28, 1995 (1985).

[6]S. C. Chen and T. C. Marshall, Phys. Rev. Lett. 52, 425 (1984).

[7]L. Friedland, Phys. Fluids 23, 2376 (1980).

[8]T. C. Marshall, Free Electron Lasers (Macmillan, New York, 1985), p. 78.

[9]T. J. Orzechwoski et al., Phys. Rev. Lett. 54, 889 (1985).

[10]R. A. Freedman and W. B. Colson, Opt Commun. 46, 37 (1983).

[11]J. Masud et al., in Proceedings of the Seventh International Conference on Free Electron Lasers, Tahoe City, California, 1985 (to be published).

[12]H. P. Freund, Phys. Rev. A 27, 1977 (1983).

Regenerative Gain in a Raman Free-Electron Laser Oscillator

J. Masud

T.C. Marshall

S.P. Schlesinger

F.G. Yee

Regenerative Gain in a Raman Free-Electron Laser Oscillator

J. MASUD, T. C. MARSHALL. S. P. SCHLESINGER, AND F. G. YEE

Abstract—A parametric study of gain in a millimeter-wave Raman free-electron laser oscillator and comparisons to linear theory are carried out. The intense (1 kA/cm^2), relativistic (600–800 keV), cold [($\delta\gamma/\gamma$)$_\parallel$ < 1 percent] electron beam employed is guided by a 9.45 kG magnetic field through a 1.45 cm period, 49.5 cm long uniform undulator. Operation at < 1 kG pump field results in a < 10 percent electron quiver velocity ($v_\perp/v_\parallel$) velocity. The laser power output has been measured at ~ 3 MW corresponding to an efficiency of 4 percent, and tunability in the 90–170 GHz range has been achieved with a narrow linewidth ($\Delta\lambda/\lambda \leq 1$ percent). Using a new technique, linear small-signal growth rates have been unfolded from the oscillator startup delays. Excellent agreement is found with three-dimensional small-signal calculations for both the spatial growth rate and the resonance frequency. One-dimensional theory was found to predict shorter wavelength laser output than that observed.

I. INTRODUCTION

A novel method of extracting free-electron laser growth rates from the regenerative gain in an oscillator [1] is described. The method is based on the time lag between the onset of the interaction and the rise of the laser output level to a predetermined small, but detectable, level. We report data obtained from a Raman FEL oscillator producing several megawatts of millimeter wave radiation with a narrow (≤ 1 percent) linewidth from a 49.5 cm long bifilar undulator of 1.45 cm period. A pulse-line accelerator provides the intense (1 kA/cm^2) electron beam of 150 ns duration which is long enough to produce amplification over approximately 19 radiation passes in the 1.2 m long Fabry–Perot resonator. The voltage stability of the accelerator pulse is an important factor in obtaining good data using this method.

The small-signal linear growth rates of up to 115 dB/m magnitude obtained from the startup delays were examined over a wide range of parameters and compared to the results of a three-dimensional calculation [2] with very good agreement. It was found that one-dimensional theory is inadequate for describing our FEL experiment which uses a short period undulator field and a small diameter waveguide. We also report measurements of the coupling loss factor appropriate to the Raman traveling-wave FEL interaction.

Previously, direct measurements of the gain in a mildly relativistic Raman FEL amplifier have been reported [3]

in the microwave region. Such a method is possible where the single-pass gain is high and the injection losses of an external signal do not pose a problem (i.e., microwave wavelengths). The high intrinsic gain can additionally limit operation to relatively weak undulator fields in order to prevent self-oscillation. At shorter wavelengths, especially in the submillimeter wave regime, the lower growth rates can seriously constrain quantitative measurements in an amplifier mode [4], and the lack of suitable high-power signal sources is another obstacle. The evaluation of the growth rate from the startup time, on the other hand, can, in principle, be applied to a free-electron laser oscillator operating in any regime as long as the start of the interaction can be established and experimental conditions remain relatively stable since the oscillation start time can be controlled independently of the growth rate by adjusting the cavity quality factor. In a tunable oscillator, the frequency dependence of the gain can also be studied. A similar approach adopted at NRL [5] suffered from the lack of a well-defined beam current turn-on on the accelerator. An earlier attempt to study the time dependence of the FEL gain function found qualitative agreement with a simple 1D model [6].

II. EXPERIMENTAL SETUP

The oscillator configuration is shown in Fig. 1. The 600–800 keV electron beam is generated by a Physics International 220G pulse-line accelerator with a 150 ns duration. Electrons are collimated into a 2.5 mm radius solid cylindrical beam by an aperture on the anode axis which provides a good filling factor (~ 65 percent) in the 6.16 mm inner diameter drift tube. A 9.45 kG axial field employed to guide the beam through the interaction region allows operation well removed from "magnetoresonance" [$eB_\parallel/\gamma m_e c = k_0 v_\parallel$ where $k_0 = 2\pi/\lambda_0$. λ_0 is the undulator period, e and m_e are the electronic charge and mass, respectively. $B_\parallel$ is the axial field. $\gamma = (1 - v_\parallel^2/c^2)^{-1/2}$, $v_\parallel$ is the electron axial velocity] at $B_\parallel = 16$ kG. This enables operation with Group I stable electron orbits [7]. The normalized parallel momentum spread of the electron beam was found experimentally to be ~ 1/2 percent [8], thereby satisfying the Raman cold beam criterion of ($\delta\gamma/\gamma$)$_\parallel$ < 1/N = 3 percent where N is the number of undulator periods.

The FEL interaction length could be varied by dumping the electrons to the drift tube wall at any position along
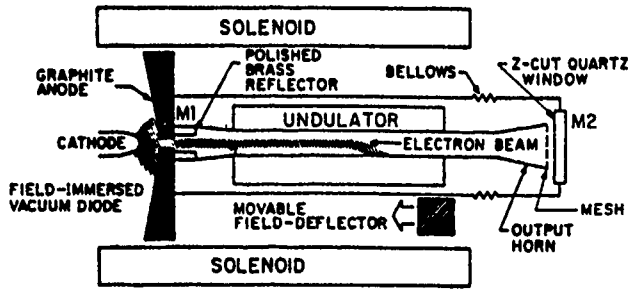
Fig. 1. Schematic of free-electron laser oscillator.

Fig. 2. Output mirror ($M2$) characteristics. (a) 6 86 mm thick crystalline quartz plate. (b) Woven wire mesh (#1) with periodicity g = 1.6 mm and width $2a$ = 0.28 mm and strip-mesh (#2) with g = 1016 μm and $2a$ = 400 μm.
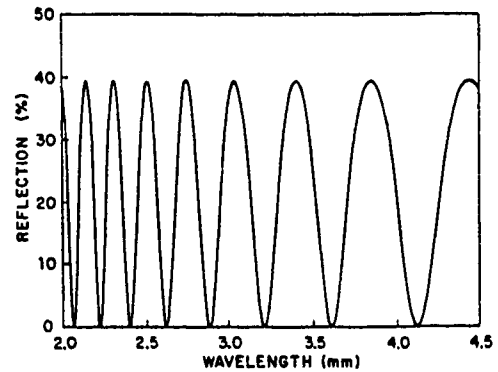
its length by deflecting the guiding field with an iron piece. Witness plate shots revealed that the beam remained well defined until its impact with the wall so that the beam length could be accurately controlled to within ±1 cm.

Beam transport measurements were made for all the parameter values of interest in the experiment to enable an accurate comparison to predicted laser performance. Faraday cup measurements showed a decrease in the amount of beam current transmitted through the system length due to the proximity of the drift tube wall as the electron quiver velocity is increased either by raising the undulator field at constant electron energy or by decreasing the energy at a fixed undulator strength. The decline in the beam current is initially gradual for $v_\perp / v_\parallel < 0.11$, after which it abruptly falls to zero as $v_\perp / v_\parallel$ is increased to 0.15.
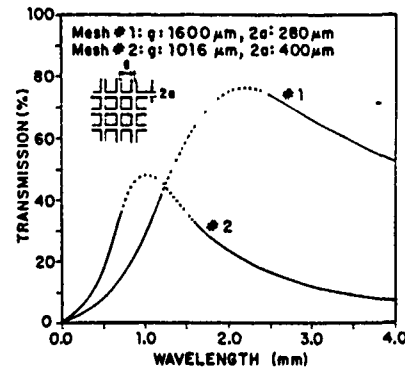
The bifilar helical undulator has a constant-amplitude length of 49.5 cm with a 1.45 cm periodicity and 7.3 cm adiabatic entrance and exit taper regions. The drift tube flares out at either end and is terminated at the laser mirrors; an annular polished brass step ($M1$) with an approximately 65 percent reflectivity at the upstream end immediately following the anode and partially transmitting flat reflectors at the downstream end ($M2$). The downstream reflectors consisted, alternatively, of metallic meshes and a crystalline quartz plate. This allowed the reflectivity there to be changed from about 5 to 82 percent, enabling direct control of the feedback and the laser startup time. Mirror transmission characteristics are obtained using standard analytical treatment, and the results are shown in Fig. 2 for the different types used. The oscillations in the quartz plate reflectivity are caused by interference from its two reflecting surfaces. These calculations have been verified using a CW test source [9]. The laser radiation, after considerable attenuation, is picked up by a crystal detector placed ~2.5 m in front of the output window.

III. Oscillator Output Characteristics

When the undulator field is raised above a certain threshold level (300–400 G), coherent output from the FEL at millimeter wavelengths is observed [10]. The linewidth of the radiation corresponding to the upper FEL intersection, as measured with a grating spectrometer [11] (resolving power < 100), is about 1 percent, significantly narrower than the superradiant emission width of about 10 percent [12]. The FEL spectra were obtained in the multiple-shot mode, and slight shot-to-shot fluctuations in the diode voltage could not be completely factored out, resulting in a broadening of the observed linewidth so that the actual laser output would correspond to $\Delta\lambda / \lambda < 1$ percent. The output rapidly grows to megawatt levels as the undulator field is increased further. At a particular high undulator field value (650–900 G), the power abruptly falls to zero. The lower and upper bounds on the transverse magnetic field between which oscillation occurs depend on the operating parameters of the laser, and in particular, they are found to correspond to a threshold growth depending on resonator losses and a nearly complete disruption of electron beam transport as mentioned above, respectively.

Typical FEL oscillographs are shown in Fig. 3. The diode voltage pulse (as well as the electron beam current) rise time is very short (< 10 ns) and its top remains flat (<2 percent) for 150 ns. After a certain delay t_s determined by the FEL gain and resonator losses, the system begins to oscillate, with the power increasing within one cavity roundtrip time τ (=8 ns) to saturated levels where $\tau = 2L_c / c$ and L_c is the distance between the mirrors $M1$ and $M2$. Occasionally, "mode-locked" spikes spaced 8 ns apart are also observed. The FEL power persists for <60 ns regardless of the start time and then decays with the characteristic 1–3 ns decay time of the cavity.
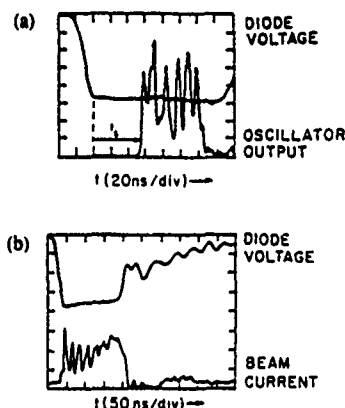
The reason for the premature turnoff of the FEL pulse

Fig. 3. Typical FEL oscillator oscilloscope traces. Upper trace: diode voltage (120 kV/div.); lower trace: (a) FEL output, showing mode locking and "start time" t_s; (b) electron beam current (100 A/div.). The rapid oscillation on the beam current signal is an electrical transient relating to the grounding of the Faraday cup; the transient varies even on identical shots and is not seen in the total beam voltage or diode current signals; therefore, it does not correspond to an actual fluctuation in beam current.

is not fully understood, but it appears to be unrelated to the dynamics of the electron beam generation as all portions in time of the beam can be made to support oscillation. A possible explanation is arcing inside the cavity due to the high electromagnetic power levels, and a possible location would be the small hole in the upstream metal mirror $M1$ through which the electron beam passes or near the end of the solenoid where plasma is created by the electrons dumped to the drift tube wall. Open-shutter photography at the downstream mirror did not reveal any flashing at that position.

Coupling of the electron synchrotron oscillations to the saturated optical field has been predicted to produce undesirable sidebands in the FEL power spectrum [13]. Such sideband power has been recorded in our experiment at the high undulator field strengths required for saturation. A method for controlling the sideband frequency shift independently of the laser output at the fundamental frequency by means of reducing the electron pulse slippage was also successfully demonstrated [14].

IV. POWER AND EFFICIENCY

The total power output of the FEL is measured with a calibrated crystal detector mounted 2.42 m directly in front of the laser output window. The power distribution was found to be isotropic with respect to the polarization angle of a wire grid placed in the path of the radiation, as would be expected of circularly polarized radiation amplified by the right-hand circularly polarized undulator. Standard radar formulas were used to calculate the radiation patterns of the laser output and detector receiver antennas, giving a saturated power level of ~3 MW. This number has been independently confirmed by calorimetric measurements. The scaling of the total power with the undulator field is shown in Fig. 4(a) for the case of a 700 keV beam and a 9.45 kG guiding magnetic field. Although the exponential trend indicates that the saturated
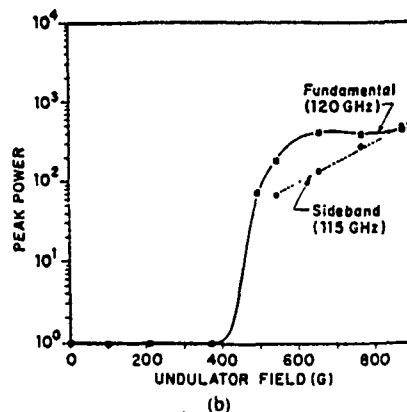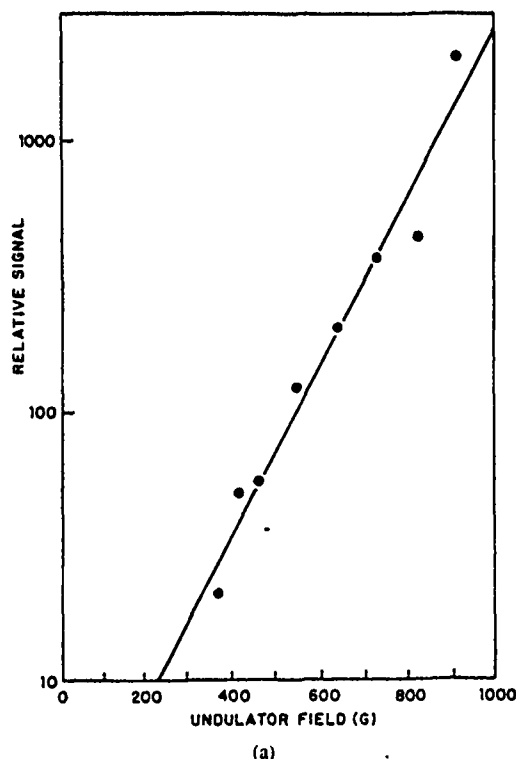

(a)

(b)

Fig 4 FEL power output as a function of the undulator strength with λ_0 = 1 451 cm. E = 700 keV. and $B_\perp$ = 9 45 kG. Maximum radiated power ~3 MW. (a) Total power. (b) Output at fundamental and sideband frequencies, as recorded by a diode detector, in mV. Attenuation (~ −60 dB) is provided by spatial separation of transmitter and receiver (−31 dB), together with a calibrated attenuator.

power level increases with the undulator field, it should be remembered that the signal has not been spectrally resolved. Spectroscopy revealed that not all the power occurs at the fundamental FEL frequency, and that above 650 G, the fundamental saturates in intensity and there is a strong tendency for powerful sidebands to develop as the undulator field is raised further, which accounts for the persisting exponential trend [Fig. 4(b)]. As much as half of the total FEL output is observed to appear in the lower frequency sideband at $B_\perp$ = 870 G.

The electronic efficiency η of the uniform undulator free-electron laser, defined as the power extracted as electromagnetic energy relative to the initial power of the electron beam, prior to the onset of the sidebands, is found

to be 4 percent. The theoretical maximum efficiency η_m given by [15]

$$\eta_m = \frac{\omega_p}{\gamma k_0 c} \qquad (1)$$

where ω_p is the invariant plasma frequency, which has been estimated from the beam current measurements to be 1.94×10^{10} rad/s for $\gamma = 2.4$, predicts $\eta_m = 6$ percent as the upper limit, so that observed efficiency is close to the saturated maximum governed by electron trapping in the ponderomotive potential wells. It is also in excellent agreement with the results of a nonlinear simulation which included the effects of finite beam emittance carried out for the Columbia FEL parameters [16].

V. FREQUENCY TUNING

The tunability of the fundamental FEL wavelength was demonstrated by varying the electron energy. In Fig. 5 are plotted the results of observing the upper FEL output frequency as a function of the diode voltage using the grating spectrometer with a 650 G undulator field. The data points correspond to operation from 90 to 170 GHz when γ is changed from 2.1 to 2.6. Oscillation at wavelengths corresponding to minima in the quartz mirror reflectivity (Fig. 2) were not observed due to reduced feedback. The agreement with the results of the 3D code for a TE$_{11}$ mode, which is the only waveguide mode which couples to the beam space charge line for the conditions of the experiment, is very good. Also shown in the figure is the calculated resonant frequency using a one-dimensional model [17], which is found to predict shorter wavelengths than those observed. This is because in the short-period undulator ($k_0 r \approx 1$), the radial variation of the undulator fields is not negligible. Off-axis electrons therefore experience a stronger net undulator field, which enhances their transverse motion at the expense of the resonant frequency. A transition to reduced beam current transmission through the interaction region at low electron energies occurs in the range 620–660 keV and accounts for the break in the theory curves for which constant beam current was assumed.

In addition to the "FEL" radiation at ~ 2.5 mm, the oscillator also produced tens of kilowatts at ~ 8 mm. This results from the "lower intersection" of the beam line with the TE$_{11}$ waveguide mode. Since $v_{\parallel}/\lambda_0$ is less than the waveguide cutoff frequency, the microwave branch is also a convective instability. For the small-signal studies which follow, we expect no interaction between the microwave and millimeter wave branches. The microwave radiation can be eliminated by replacing the upstream reflector with a "Bragg" (tuned) reflector.

VI. FEL GAIN MEASUREMENT FROM STARTUP

Taking advantage of the delay of the onset of the oscillator power relative to the diode voltage, a new method [1], [5] of determining the free-electron laser growth rate has been devised. This makes possible a parametric study
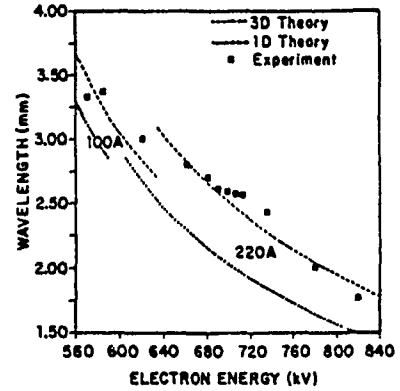

Fig. 5. Free-electron laser free-space wavelength measured with a grating spectrometer as a function of electron energy with $\lambda_0 = 1.45$ cm, $B_\perp = 650$ G, and $B_\parallel = 9.45$ kG. The curves correspond to one- and three-dimensional calculations of the wavelength of peak growth for the TE$_{11}$ mode.

of the FEL instability and comparison to linear (small-signal) theory.

Fig. 6 shows in schematic form the time evolution of the electromagnetic power stored in the cavity. When the FEL gain per pass is made to exceed the total roundtrip power losses, oscillation sets in [Fig. 6(a)]. However, by controlling the gain and/or losses, the time t_s it takes for the power to build up from the initial cavity noise level P_0 to reach a particular reference power level P_d can be varied over several bounce periods τ as shown by the dashed line in Fig. 6(b). Fig. 6(c) illustrates the variation of the power of a slice of the electromagnetic pulse trapped inside the resonator. Starting at the upstream end at the background noise level P_0, the power first grows with the net growth rate Γ' over the length L of the undulator where $\Gamma' = \Gamma - \alpha_d/2$ and Γ is the FEL small-signal growth rate and α_d is the power absorption per unit length in the drift tube. Upon exiting the undulator, the power level droops due to further attenuation in the waveguide before it reaches the downstream mirror $M2$. Here a fraction T_2 is lost due to transmission through the mirror and the rest is reflected back, suffering drift tube losses over the entire cavity length L_c as there is no amplification of a backward-traveling wave in an FEL. Once at the upstream mirror $M1$, another fraction T_1 is radiated out, and of the remaining energy, only $1/m^2$ couples back into the growing EM mode where m is the total number of modes present in the system. Thus, the net laser roundtrip power gain G can be only slightly above the oscillation threshold of unity, even though the undulator power gain $e^{2\Gamma' t}$ may be substantially greater. The process bootstraps, with the signal level starting for the next pass at GP_0 instead of P_0, resulting in exponentiating power over many bounces until the power saturates at some high level and the FEL growth rate falters.

Thus, the free-electron laser spatial growth rate Γ can be unfolded from experimental studies of the variation of the start time as either the cavity losses represented by T_1 and T_2 or the factors influencing the laser gain, such as the undulator strength $B_\perp$, interaction length L, axial field
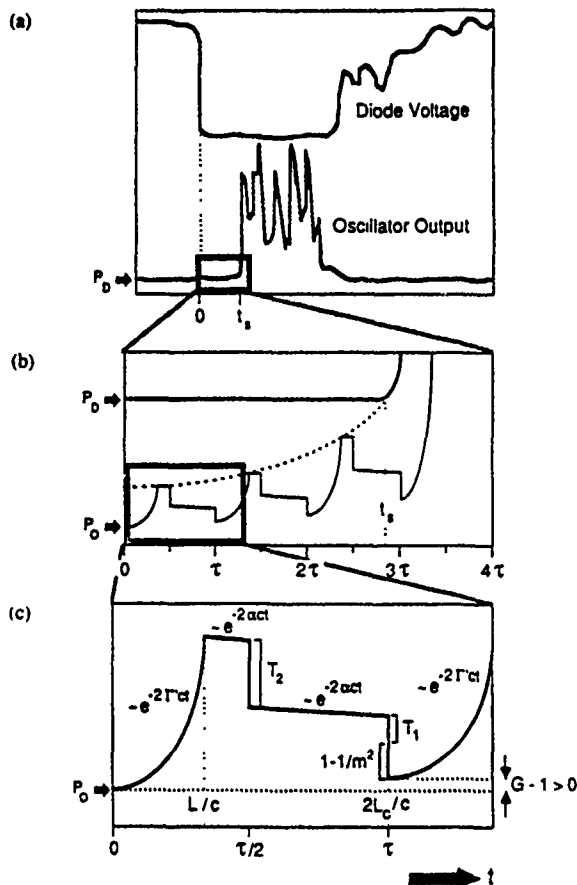
Fig. 6. Evolution of an optical pulse inside the FEL resonator

Fig. 7 Observed dependence of FEL output start time and amplitude on undulator field. In each oscillograph, the upper trace is the diode voltage and the lower trace is the oscillator pulse. (a) $B_\perp = 390$ G. (b) $B_\perp = 430$ G (c) $B_\perp = 600$ G.

B_{ij}, beam current I_b, or the electron energy γ, are changed. In the experiment, the reference cavity power level P_d is chosen to be that which results in a laser output corresponding to the threshold level of the detection system as determined by the detector responsivity, free space attenuation, and any additional attenuation used in front of the detector. Henceforth, in describing the oscillator output, the term "threshold" will be used in this sense of the detection threshold rather than the lower oscillation threshold, unless specified otherwise.

Fig. 7 illustrates the effect of gradually increasing the undulator field on the observed start time and amplitude of the FEL output. As $B_\perp$ is raised above the threshold level, the FEL signal first appears at the end of the voltage pulse and then proceeds to occur at earlier times, finally starting after one bounce time of 8 ns at high undulator strengths before beam disruption ensues.

Writing G_i as the net power gain (including distributed losses) per pass of the ith axial electromagnetic mode, the total regenerative power gain over n bounces in the cavity G_n to reach the threshold power level P_d is

$$G_n = \frac{P_d}{P_0} = \left[\frac{1 - \alpha_c}{m^2} \sum_{i=1}^{\infty} G_i\right]^n \qquad (2)$$

where α_c is the total lumped cavity power loss factor. The distributed loss is caused by the waveguide attenuation, while the lumped losses include mirror transmission and
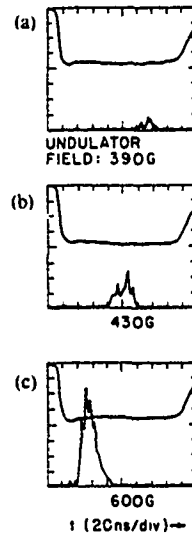
diffraction. Diffraction occurs at the downstream end of the cavity due to the geometry of the mirror mounts used, and is therefore different for the particular mirror used at $M1$. These losses are calculated using standard Gaussian wave propagation analysis and are found to be ~ 70 percent for the quartz mirror and ~ 0 percent for the mesh mirrors [9]. In the weak pump Raman regime [15]. $m = 2$, representing the exponential growing mode and its conjugate decaying mode, so that

$$\frac{P_d}{P_0} = \left\{\frac{1 - \alpha_c}{4} \left[\exp\left(2\Gamma L - 2\alpha_d L_c\right)\right.\right.$$

$$\left.\left. + \exp\left(-2\Gamma L - 2\alpha_d L_c\right)\right]\right\}^n \qquad (3)$$

where L is the interaction length. Combining all the loss terms together, taking logarithms, and writing $n = t_s/\tau = ct_s/2L_c$, (2) becomes

$$\Gamma L = \frac{L_c}{ct_s} \ln\left(P_d/P_0\right) - \frac{1}{2} \ln\left[R_1 R_2(1 - A)(1 - D)/4\right]$$

$$(4)$$

where R_1 and R_2 are the power reflection coefficients of the laser mirrors, A is the roundtrip waveguide attenuation loss ($A = 1 - e^{-2\alpha_d L}$), and D is the diffraction loss determined by the cavity configuration. In (4), the contribution of the decaying mode to the total cavity power level represented by the second term in (3) has been neglected since for operation above threshold, it is less than 2 percent when compared to the growing mode. Also ignored is the superradiant amplifier mode of operation of the laser (corresponding to $n = 0$), as the single-pass amplification is assumed to be small compared to the power detection threshold in the experiment. Further simplification occurs when the waveguide loss term is combined with the up-

stream mirror reflectivity since both of these depend on the overall system design and remain unchanged. Similarly, the diffraction loss occurs at the position of the downstream mirror and can therefore be combined with its reflectivity. Therefore,

$$\Gamma L = \frac{L_c}{ct_s} \ln{(P_d/P_0)} - \frac{1}{2} \ln{(RR'/4)} \qquad (5)$$

where $R' = R_1(1 - A) = R_1 e^{-2\alpha_d L}$ and $R = R_2(1 - D)$ can be considered the *net* reflectivities of the two mirrors. Calculated values for the loss factors give $A = 0.45$, $D = 0$ and 0.72 for the meshes and the quartz mirror, respectively, and $R_1 = 65$ percent at the typical 2.5 mm operating wavelength of the FEL; the value of R_2 (~ 5–82 percent) is obtained according to Fig. 2.

The inverse linear dependence of the start time t_s on the single pass growth factor ΓL (5) can be exploited to obtain an indirect measure of the free-electron laser instability growth rate Γ. It should be noted that the effect of uncertainties in the cavity loss estimates is mitigated by the appearance of R and R' inside the logarithm in (5). Since the threshold level P_d is chosen to be substantially lower than the saturated power level, the experimental method results in a measurement of the linear small-signal growth rate, regardless of whether the laser is driven to saturation or not.

A. Gain as a Function of Undulator Strength

In 1D free-electron laser theory, the small-signal growth rate Γ is directly proportional to the undulator field $B_\perp$; in 3D theory, the proportionality is not exactly linear, but approximates one for moderate quiver velocities [18]. Assuming $\Gamma = KB_\perp$ where

$$K = \frac{e}{2m_e c^2}\left[\frac{\gamma_\parallel \omega_p}{\gamma c k_0}\right]^{1/2} \qquad (6)$$

is a constant, (5) can be rewritten in the form

$$B_\perp = \frac{1}{K}\left[\frac{L_c}{Lct_s}\ln{(P_d/P_0)} - \frac{1}{2}\ln{(RR'/4)}\right]. \qquad (7)$$

According to (7), the start time should be inversely proportional to the applied undulator strength.

Experimental plots of $B_\perp$ versus $1/t_s$ are shown in Fig. 8. The horizontal error bars indicate the ± 4 ns uncertainty in reading off the start time from the oscilloscope photographs. Since both the diode voltage and electron beam current turn on is very rapid and well defined [Fig. 3(b)], any systematic errors in the determination of t_s are assumed to be negligible. The vertical dashed line indicates the end of the diode voltage pulse at $t_s = 150$ ns which corresponds to about 19 radiation bounces in the cavity.

A constant growth rate is assumed in (7) in the interval $t = 0$ to t_s as the power builds up and is therefore valid for a very flat diode voltage pulse. Fig. 8 shows the results from both a constant voltage ($\Delta V/V \leq 2$ percent) run and one where the diode voltage had a ~ 5 percent
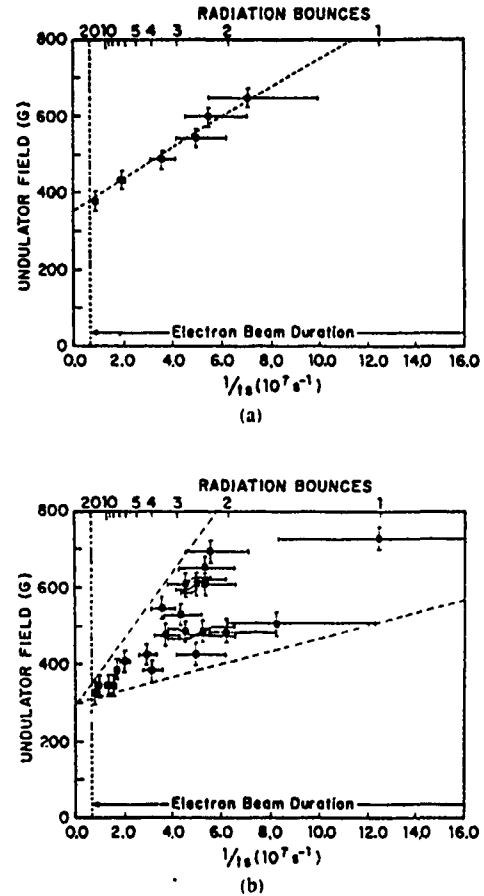
Fig. 8. Plot of $1/t_s$ versus $B_\perp$ using the quartz output mirror, with $\lambda_0 = 1.451$ cm, $L = 49.5$ cm, and $B_\perp = 9.45$ kG. The vertical dashed line indicates the end of the diode voltage pulse at $t = 150$ ns. (a) Diode voltage, $E = 700$ keV with $\Delta E/E \leq 2$ percent. (b) $E = 600$ keV with $\Delta E/E \approx 5$ percent.

undulation, using the quartz window as the output mirror. The expected linear dependence of $1/t_s$ on $B_\perp$ is very evident in Fig. 8(a), and the standard deviation of the data points as found by repeating each measurement several times is much less than the errors bars shown. The scatter of the data is much greater for the case of a rippled diode voltage and increases for short t_s (high $B_\perp$). The free-electron laser spatial growth rate for threshold oscillation can be found from the intercept on the $B_\perp$ axis which, according to (7), is $|\ln(RR'/4)/2K|$, and knowing R and R', the proportionality constant K, and hence Γ, can be found. The determination of the growth rate from the intercept somewhat relaxes the constraint on the variation of the electron energy, since even for the rippled diode voltage run, the data points are seen to converge to an unambiguous value at large t_s [Fig. 8(b)]. It is important, however, that the variation of the voltage, if any, be of the form of an oscillation about some mean value and not a monotonic change.

Examples of the $\Gamma = KB_\perp$ curves obtained in this manner are shown in Fig. 9 for two different electron energies. Good agreement is obtained with the calculated growth rates for the TE_{11} mode. The experimental win-
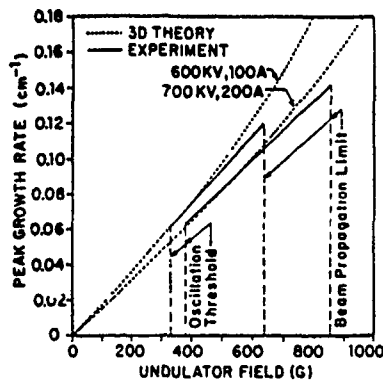
Fig. 9. Peak free-electron laser growth rate versus undulator field. The solid lines are the experimentally determined $\Gamma = KB_\perp$ curves for $E = 600$ and 700 keV. The dashed lines are obtained from a three-dimensional calculation for the TE_{11} mode. Group I electron orbits; $\lambda_u = 1.451$ cm. $B_\perp = 9.45$ kG.

dow is bounded by the usual oscillation (detection) threshold and beam disruption limits. The lower threshold in both cases is found to correspond to $\Gamma = 0.06$ cm^{-1} and the upper cutoff occurs when the beam current falls below 100 A and is probably expedited by thermalization of the electron beam at high undulator fields. In the theoretical treatment, the beam is assumed to be initially monoenergetic, which is found from previous experimental measurements [8] to be a good approximation even at moderately high undulator fields.

B. Gain as a Function of Interaction Length and Coupling Loss

The gain measurement technique described in the previous section in reality applies at only the threshold $B_\perp$ value where the intercept in Fig. 8 is measured. At different undulator fields, the growth rate has been extrapolated using the $\Gamma \approx KB_\perp$ approximation, and the discrepancy caused by this can be judged from Fig. 9. An extension to the method of measuring the FEL growth rate which is not limited by any scaling approximation is to vary the interaction length and the undulator strength simultaneously so as to always obtain oscillation at the threshold level (or any other subsaturation reference power level). This does not result in a measurement of the electric field growth rate only at the threshold value, since the growth rate can be varied over a wide range as long as the interaction length is also adjusted to keep the *net power gain* at the detection threshold.

From (5), it is seen that the start time varies as $1/L$ provided the growth rate (or $B_\perp$) is the same. In the experiment, the interaction length L is varied by the use of the field deflector (Fig. 1) with which the length of the electron beam inside the undulator can be changed to within ± 1 cm. An example of the observed variation of $1/t_s$ with the interaction length is plotted in Fig. 10 where the linear dependence is again obvious. The interaction length has been defined as the region of uniform $B_\perp$ through which the electrons pass; the end taper lengths have been ignored as the field rapidly falls below the os-

cillation threshold value there. The flattening of the curve at $L \approx 50$ cm represents the physical end of the undulator, i.e., moving the deflector beyond that point does not increase the length of the interaction region. As with Fig. 8(a), the scatter of the data points is negligible for constant electron energy shots.

If the substitution $m = 2$ is not made in (2), the expected intercept L_{th} on the $1/t_s = 0$ axis can be calculated from

$$L_{th} = -\frac{1}{2\Gamma} \ln \left[\frac{RR'}{m^2} \right] \qquad (8)$$

where Γ is the theoretical single-pass growth rate independent of m. Different m would correspond to the different number of convective modes between which the recycled electromagnetic power is shared in the traveling-wave system. In our analysis, we have assumed only one with a purely growing amplitude, but there can be a number of additional modes with oscillatory or decaying propagation factors. Thus, the available power is divided up according to the number of modes present, and the factor m^2 represents the coupling loss which reduces the overall amplification in the FEL. The predicted intercepts for $m = 1, 2, 4$, and 8 are also shown in Fig. 10 from which the data are seen to conform to $m = 2$ assumed earlier. This is consistent with theory in the case of the weak pump Raman regime which is the operating regime of the experiment.

That the electromagnetic waves are launched with an equal magnitude at the outset for each of the different possible modes is a result of including the boundary conditions in the traveling-wave analysis of the FEL. Therefore, the coupling loss phenomenon is an important test of the theoretical model where it is equal to the number of solutions of the dispersion relation. In addition, it is important in the practical design of both free-electron laser oscillators and external signal amplifiers where the net system gain is reduced by the $1/m^2$ factor. No systematic effort of uncovering the experimental coupling loss factor had previously been undertaken. In this experiment, although the growth rate and the coupling loss are not independently determined, their mutual agreement with theory is excellent.

As a further test of the relevant coupling loss parameter, the threshold undulator field at different interaction lengths was determined. This is equivalent to observing the inverse relationship between the growth rate Γ and the interaction length L at constant start time t_s in (5). The choice of the reference start time is arbitrary, and $t_s = \infty$ corresponding to the threshold where the oscillation condition ($G = 1$) is satisfied is taken for convenience since the ratio P_d/P_0 in (5) is then not required. In obtaining the data, $t_s = 150$ ns, corresponding to the oscillator output reaching the detection threshold at the end of the diode voltage pulse. was substituted for $1/t_s = 0$, contributing a negligible error. The data are plotted in Fig. 11 and the different theoretical curves relevant to different coupling
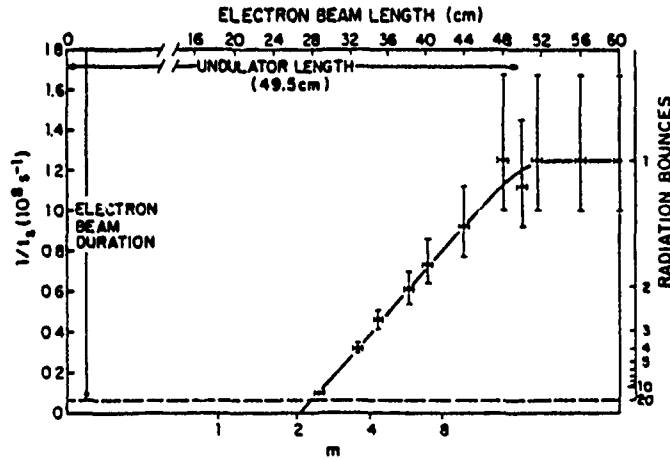
Fig. 10. Plot of $1/t_s$ versus interaction length L using the quartz output mirror, with $E = 700$ keV, $B_\perp = 650$ G, $B_* = 9.45$ kG, and $\lambda_0 = 1.451$ cm. The lower horizontal axis indicates the $t_s = \infty$ intercepts calculated for the same parameters with the 3D code for different coupling coefficient m.
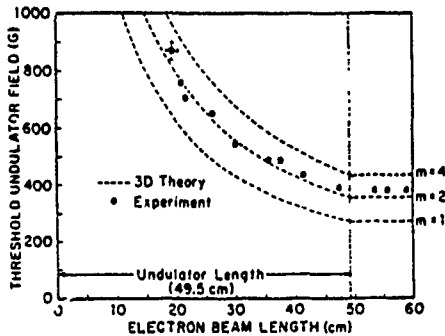

Fig. 11. Threshold undulator field as a function of interaction length L using the quartz output mirror, with $E = 700$ keV, $B_s = 9.45$ kG, and $\lambda_0 = 1.451$ cm. The theory curves correspond to different coupling coefficient m.
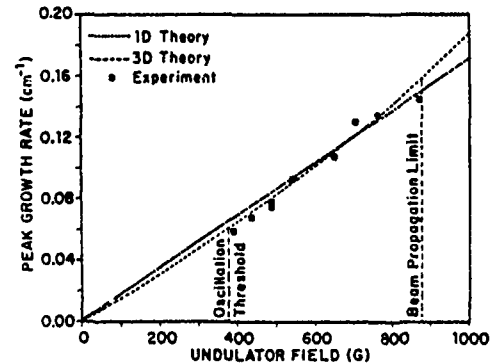
Fig. 12. Experimental and calculated free-electron laser linear growth rate versus undulator field for $E = 700$ keV, $B_s = 9.45$ kG, and $\lambda_0 = 1.451$ cm. The theory curves are for the TE_{11} mode.

losses are also shown for comparison. The experimental results agree well with the $m = 2$ curve even at the highest undulator fields possible, indicating that we remain in the weak pump regime. The transition to the strong pump regime is accompanied by the appearance of a third oscillatory mode so that the coupling loss factor should increase to 9.

As mentioned earlier, the FEL growth rate at different undulator field values can be obtained directly by compensating for the effect on the power gain by appropriately changing the interaction length. Once L_{th} at different $B_\perp$ has been determined, $\Gamma(B_\perp)$ can be obtained from (8). Fig. 12 illustrates the experimentally obtained growth rates using this method, as well as the one- and three-dimensional calculation for the same parameters. The experimental points track the theory curves well, and although the distinction between the two curves may not be readily observable, the agreement seems to be better for the three-dimensional case, especially for conditions near threshold where the data are more reproducible. The measurements are less reliable near the beam propagation limit

due to deteriorating electron transport at high undulator fields.

C. Gain as a Function of Mirror Reflectivity

In (2), P_d is the cavity power level which results in the smallest detectable signal at the position of the detector. This factor depends on the output coupling of the laser, the attenuator chain in front of the detector, and the detector sensitivity itself. To make this dependence more transparent, we write P_d in terms of P'_d, the actual minimum amount of power striking the detector element which will give a measurable output where

$$P'_d = P_d T_2 T_a T_f \tag{9}$$

and T_2 is the transmittivity of the laser output mirror, T_a is the transmission through the attenuator, and T_f is the free space transmission into the detector receiver antenna. Neglecting absorption in the mirror $M2$, $T_2 = 1 - R_2$. The attenuation needed to reduce the laser output to levels within the linear response range of the detector T_a is -17.7 dB. The free space propagation factor T_f can be

calculated using the standard radar formula

$$T_f = \left[\frac{\lambda}{4\pi r}\right]^2 G_1 G_2 \qquad (10)$$

w   e G_1 = 28.5 dB and G_2 = 22.0 dB are the power gain factors for the laser output and the detector receiver horns, respectively, and r = 2.42 m is the distance between them. For a 2.5 mm wavelength, (10) gives T_f = −31.2 dB.

Substituting (9) back into (4) or (5), we get

$$\Gamma = \frac{1}{L}\frac{L_c}{ct_s} \ln\left[\frac{P'_d}{P_0(1 - R_2)T_a T_f}\right]$$

$$- \frac{1}{2}\ln\left[\frac{R' R_2(1 - D)}{4}\right] \qquad (11)$$

which explicitly brings out the dependence on the laser output mirror reflectivity R_2. Since both P'_d and P_0 are constants representing the detector responsivity and the initial cavity noise level which should not vary greatly from shot to shot, the functional dependence of the start time on the output mirror reflectivity can be studied.

The three different output mirrors used in the experiment had net reflectivities (including diffraction losses) at the operating wavelength of approximately 5, 35, and 82 percent, respectively [9], making possible relatively large changes in the laser resonator quality factor to be studied. In Fig. 13(a) and (b), the inverse start time versus the undulator field with two metal mesh mirrors used at the downstream end is shown. The dashed curve is not the best fit straight line, but the theoretical determination of t_s from (11) and the 3D code, with the cavity losses calculated as mentioned earlier and the ratio P'_d/P_0 found from the slopes of the experimental plots (Fig. 13). Also shown [Fig. 13(c)] for comparison is the case of the quartz mirror and the corresponding theory curve. Excellent agreement is found between the observed and the calculated start times in all three cases with widely different net reflectivities.

A variation of R_2 manifests itself in a change in both the t_s = ∞ intercept and the slopes of the plots in Fig. 13. This is because of the appearance of R_2 in both terms of the right-hand side in (11) where the first term describes the power transmitted through the output window of the laser and the second governs the buildup of power inside the resonator. The effect is evident in Fig. 13; as $R = R_2(1 - D)$ increases from ~5 percent for the quartz to ~82 percent for mesh 2, the intercept decreases, indicating the decreasing undulator strength needed to build up power to the threshold level inside the cavity because of the enhanced feedback. At the same time, the slopes of the curves increase as the smaller fraction of the cavity power transmitted to the detector through the mirror affects the time required to reach the detection level. For the meshes, the two opposing effects are seen to balance each other at $B_\perp$ = 600 G, with the mirror reflectivity dominating at lower $B_\perp$ and its transmissivity important at high fields.
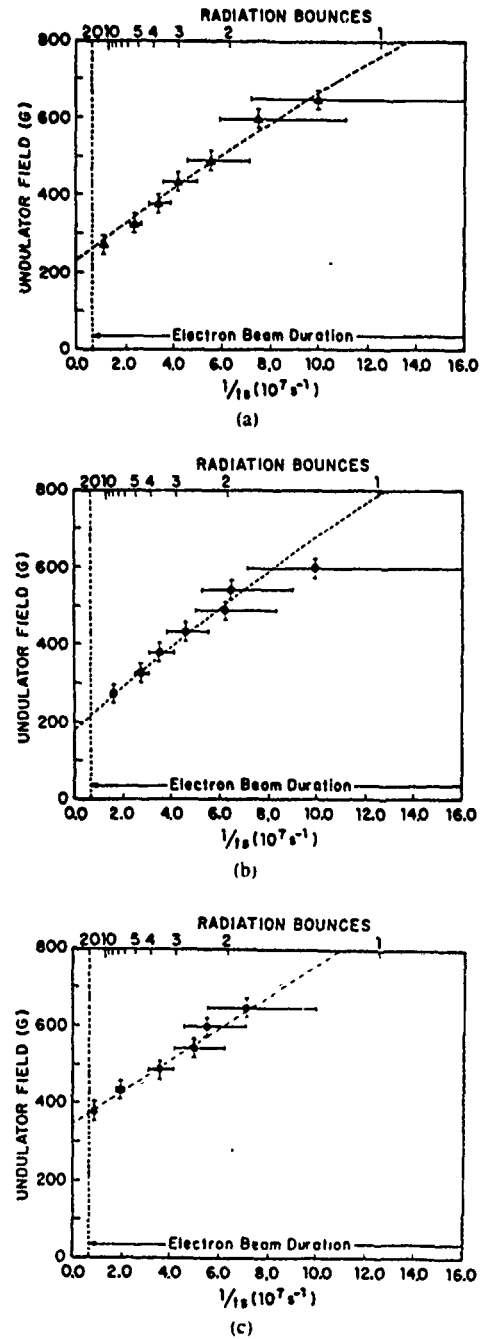

Fig. 13 $1/t_s$ versus $B_\perp$ with different output mirrors and E = 700 keV, B = 9.45 kG. and λ_0 = 1.451 cm and output mirror (a) mesh 1. (b) mesh 2. and (c) quartz. The dashed lines are obtained from a 3D calculation with the ratio P'_d/P_0 in (11) determined from the average slope of the experimental plots and m = 2.

The effect of the downstream mirror reflectivity on the oscillator start time is illustrated in Fig. 14. The theory curves are derived in the same manner as in Fig. 13. The output mirror reflectivity includes the diffraction loss there, which is nonzero only in the case of the quartz mirror. The three different mirrors provide a means to study the effect of low, moderate, and high net reflectivities. The experimental start times at each given undulator field are found from the least squares straight line fit to the data in Fig. 13. The slight variation in the free-electron laser
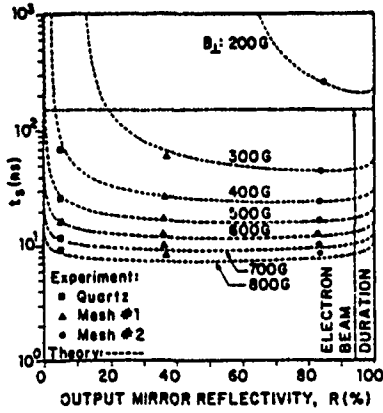
Fig. 14. Dependence of the oscillator output start time t_s on downstream mirror reflectivity R at different undulator field strengths $B_\perp$. The dashed theory curves are calculated in the same manner as in Fig. 12. The experimental points are obtained from the best fit straight line to the data in Fig. 12.

fundamental frequency with undulator strength, as found from the 3D code, accounts for a small change in the calculated reflectivities of the mirrors and is visible in the figure. The singularities in the theory curves at $R = 0$ and 100 percent are a consequence of zero feedback and output coupling respectively. If $R = 100$ percent, no amount of power is transmitted out to the detector, and t_s is therefore infinite. On the other hand, if $R = 0$, then there does, in principle, exist a threshold gain Γ_t below which $t_s = \infty$, but above which the single-pass ($n = 0$) growth of the background noise is sufficient to overcome external attenuation and give a measurable signal at the detector. This threshold is easily calculated from (11) to be $\Gamma_t = [\ln(P'_d/P_0 T_j T_a)]/2L$ and is found to be ~ 0.1 cm^{-1} for $L = 50$ cm and P'_d/P_0 obtained experimentally (see next section). From Figs. 9 or 12, this corresponds to $B_\perp \approx 650$ G for a 700 keV beam. Thus, for the $B_\perp = 700$ and 800 G curves in Fig. 14, the singularity at $R = 0$ does not really exist. This, however, does not affect the comparison to the experimental data.

The excellent agreement over a large variation in undulator field and cavity configurations confirms the model on which the previous time-dependent measurements were based: the three-dimensional amplifier theory [2], the regenerative gain formula including the coupling loss factor (4), and the calculated cavity losses.

D. Cavity Noise Level

The slope of the $B_\perp$ versus $1/t_s$ curves in Fig. 13 is

$$\frac{\Delta B_\perp}{\Delta(1/t_s)} = \frac{L_c}{cLK} \ln\left[\frac{P'_d}{P_0(1 - R_2)T_a T_f}\right]. \quad (12)$$

The approximate constant $K = \Gamma/B_\perp$ (6) can be obtained from the 3D code. Therefore, given R_2, T_a, and T_f, the ratio P'_d/P_0 can be determined for the three different mirrors employed. With the known detector sensitivity, the initial cavity noise level P_0 is thus found to be 10–100 W. This level is high, about 10^6 times the power available as spontaneous undulator emission even at high $B_\perp$, which

can be calculated from classical electrodynamics [19]. However, at the abrupt turn on of the diode voltage pulse at $t_s = 0$, the background noise level is expected to be high because of beam current noise. A 100 W effective noise level would correspond to an electron density perturbation of $\delta n \approx 0.02$ percent only via the ponderomotive force which is low even for the high-quality beam employed.

Laser startup from the transient beam noise also explains the lack of a second FEL pulse after the first one has been quenched. For high undulator field shots where the initial start time is very short, the FEL oscillation ends within 60–70 ns, leaving a comparable amount of time for the cavity power to exponentiate again before the diode voltage falls. However, such secondary pulses are not observed. The beam noise initially present decays out of the cavity in the characteristic time

$$\tau_c = \frac{\lambda Q}{2\pi c} \quad (13)$$

where the cavity Q varies from 700–2000 depending on the kind of mirrors used. Thus, the high noise level is available only in the first ~ 3 ns of the voltage pulse and drives the laser oscillation to high output levels. At the end of the FEL pulse, the beam noise is no longer present, and the spontaneous noise level is too low with the given growth rates and cavity Q for the laser power to build up to the detectable level P_d within the time remaining in the diode voltage pulse.

VII. CONCLUSIONS

In summary, quantitative measurements of the radiation characteristics of the Columbia Raman free-electron laser oscillator have been made. These include spectral analysis of the laser output and a direct measure of the FEL instability growth rate and coupling loss factor obtained from the temporal dependence of the oscillation start time on various factors influencing the net laser roundtrip gain.

In the experiment, a 600–800 keV, 1 kA/cm^2 cold electron beam drives a 50 cm uniform bifilar undulator having a 1.45 cm periodicity to produce multimegawatt radiation output in the TE$_{11}$ mode at 90–170 GHz frequency with a 4 percent efficiency. Narrow linewidth (≤ 1 percent) was observed prior to the onset of sidebands in the saturated spectrum. By focusing on subsaturation power levels, single-pass linear growth rates can be obtained from startup measurements and compared to existing theory. We report excellent frequency and growth rate agreement with the three-dimensional theory of [2] over the entire parameter space experimentally studied and a verification of the weak pump Raman regime coupling loss factor. Although similar growth rates are predicted by earlier one-dimensional analyses, the laser frequency predicted by 1D theory is significantly higher than that measured. The 3D theory was found to correctly account for the lowering of the FEL frequency caused by the finite radial variation of the short-period undulator field.

REFERENCES

[1] J. Masud, T. C. Marshall, S. P. Schlesinger, and F. G. Yee, "Gain measurement from start-up and spectrum of a Raman free-electron-laser oscillator," *Phys. Rev. Lett.*, vol. 56, pp. 1567-1570, 1986.

[2] H. P. Freund and A. K. Ganguly, "Three-dimensional theory of the free-electron laser in the collective regime," *Phys. Rev. A*, vol. 28, pp. 3438-3449, 1983.

[3] J. Fajans, G. Bekefi, Y. Z. Yin, and B. Lax, "Microwave studies of a tunable free-electron laser in combined axial and wiggler magnetic fields," *Phys. Fluids*, vol. 28, pp. 1995-2006, 1985.

[4] J. Masud, T. C. Marshall, and S. P. Schlesinger, "A Raman FEL amplifier at 1.22 mm," *Bull. Amer. Phys. Soc.*, vol. 29, p. 1341, 1984.

[5] J. Mathew and J. A. Pasour, "High-gain, long-pulse free-electron-laser oscillator," *Phys. Rev. Lett.*, vol. 56, pp. 1805-1808, 1986.

[6] D. S. Birkett, T. C. Marshall, S. P. Schlesinger, and D. B. McDermott, "A submillimeter free-electron laser experiment," *IEEE J. Quantum Electron.*, vol. QE-17, pp. 1348-1353, 1981.

[7] L. Friedland, "Electron beam dynamics in combined guide and pump magnetic fields for free electron laser applications," *Phys. Fluids*, vol. 23, pp. 2376-2382, 1980.

[8] S. C. Chen and T. C. Marshall, "Parallel velocity spread induced in a relativistic electron beam by an undulator," *IEEE J. Quantum Electron.*, vol. QE-21, pp. 924-930, 1985.

[9] J. Masud, "Regenerative gain and sideband instability in a Raman free electron laser," Plasma Phys. Lab., Columbia Univ., New York, NY, Rep. 106, 1986.

[10] J. Masud, F. G. Yee, T. C. Marshall, and S. P. Schlesinger, "A Raman REL at 2 mm wavelength," in *Proc. 7th Int. Conf. Free Electron Lasers, Lake Tahoe, CA; Nucl. Instrum. Methods Phys. Res.*, vol. A250, pp 342-345, 1986.

[11] J. A. Pasour and S. P. Schlesinger, "Multichannel grating spectrometer for millimeter waves," *Rev. Sci. Instrum.*, vol. 48, pp. 1355-1356, 1977.

[12] R. M. Gilgenbach, T. C. Marshall, and S. P. Schlesinger, "Spectral properties of stimulated Raman radiation from an intense relativistic electron beam," *Phys. Fluids*, vol. 22, pp 971-977, 1979.

[13] N. M. Kroll and M. N. Rosenbluth, "Sideband instabilities in trapped particle free electron lasers," in *Physics of Quantum Electronics, Vol 7*. Reading, MA. Addison-Wesley, 1980, 147-174.

[14] J Masud, T C Marshall, S. P. Schlesinger, F G Yee, W M. Fawley, E. T. Scharlemann, S S. Yu, A. M Sessler, and E. J. Sternbach, "Control of sideband instability in a millimeter wave free electron laser," *Phys. Rev. Lett.*, vol. 58, p. 763, 1987.

[15] T. C. Marshall, *Free-Electron Lasers*. New York: Macmillan, 1985.

[16] H. P. Freund, private communication, 1986.

[17] A. Gover and P. Sprangle, "A unified theory of magnetic bremsstrahlung, electrostatic bremsstrahlung Compton-Raman scattering, and Cerenkov-Smith-Purcell free-electron lasers," *IEEE J. Quantum Electron.*, vol. QE-17, pp. 1196-1215, 1981.

[18] H P. Freund, P. Sprangle, D. Dillenburg, E. H. da Jornada, R. S. Schneider, and B. Liberman, "Collective effects on the operation of free-electron lasers with an axial guide field," *Phys Rev. A*, vol 26, pp. 2004-2015, 1982.

[19] J. D. Jackson, *Classical Electrodynamics*. New York: Wiley, 1975, p. 278.

J. Masud, photograph and biography not available at the time of publication.

T. C. Marshall was born in Cleveland, OH, on January 29, 1935 He received the Ph D degree in physics from the University of Illinois, Urbana, in 1960.

He is currently a Professor of Applied Physics at Columbia University, New York. In addition to research in free-electron lasers, he has undertaken research in intense relativistic beam phenomena, plasma-wave scattering and instabilities, trapped-particle effects in plasmas, and the formation and heating of plasmas in high beta equilibrium.

Prof. Marshall is a Fellow of the American Physical Society.

S. P. Schlesinger, photograph and biography not available at the time of publication.

F. G. Yee, photograph and biography not available at the time of publication.

POWER AND SIDEBAND STUDIES OF A RAMAN FEL

F.G. YEE, J. MASUD, T.C. MARSHALL and S.P. SCHLESINGER

Columbia University, New York City, NY 10027, USA

Power and spectral measurements are reported from the Columbia Raman Free Electron Laser experiment. High power pulsed radiation (4 MW, 100 ns) is obtained at wavelength ~ 2 mm, using a 750 kV electron beam with high current density and very small (< $\frac{1}{2}$%) momentum spread. We show the development of high power sidebands as the undulator pump field is increased, and discuss a mechanism for control of the sideband wavelength. The FEL, configured as an oscillator, has been operated with both constant and variable period undulators.

The sideband instability in free electron lasers is driven by the coupling of the synchrotron motion of the trapped electrons to the strong optical field. The beat wave produced by the fundamental and the incipient noise at the sideband frequency can resonate with the synchrotron motion, leading to an energy exchange which feeds the sideband wave and the synchrotron oscillation at the expense of the carrier. This is also referred to as a Raman effect, and for the longer wavelength (Stokes) case, an electron absorbs a laser photon and moves to a higher oscillation level in the ponderomotive potential well, emitting a photon at lower frequency. This can lead to electron detrapping and a disruption of the FEL mechanism. For the anti-Stokes case, a short wavelength sideband is produced, but there is no enhancement of detrapping. In this paper we report on some spectral measurements of sidebands, obtained in a Raman FEL oscillator operating at high power (~ 10 MW/cm^2) at millimeter wavelength. We also show how the sidebands "enhance" the efficiency of the device, and report on some initial findings obtained when the constant-period undulator is replaced by a slightly-tapered version (using identical geometry and beam conditions).

The configuration is the same as reported in a recent study of regenerative gain in this FEL [1]. The electron beam energy is ~ 750 kV with current density ~ 1 kA/cm^2 in a 5 mm diameter beam. The beam is guided in a 6 mm diameter drift tube, which also serves as a waveguide in which the FEL radiation propagates as a TE$_{11}$ mode. Feedback is provided by an annular metallic mirror located upstream, and a quartz plate reflector located downstream. The undulators were bifilar helical windings on a phenolic tube mounted on the drift tube; the windings were 60–70 cm long, and fields ($B_\perp$) up to 1 kG were produced on-axis when the winding period (l_0) was ~ 1.5 cm. A guiding field (B_0 ~ 10 kG) is used to extract the cold electron beam through an apertured

anode. The wavelength is tunable over the range of 1.7–3.5 mm [2]. After a "start time" of ~ 50 ns, the FEL radiation pulse builds up to saturation level in roughly one pass (~ 10 ns) in the resonator, and is sustained at high (~ 4 MW) level. The spectroscopic studies which we report on here were done when the power first reached saturation level. It was observed that when the undulator was operated at high field, the sideband amplitude increased almost simultaneously with the carrier.

The first result we discuss shows spectra obtained with a 1.45 cm undulator. The first, fig. 1, shows a well-defined, narrow fundamental (or "carrier") at 2.45 mm, together with an incipient long-wavelength sideband at 2.60 mm. The linewidth of the fundamental, taking into account the spectrometer resolving power (< 100), is roughly 1%; it may be even narrower, as data was averaged on a shot-to-shot basis and small fluctuation in the accelerator voltage would yield additional
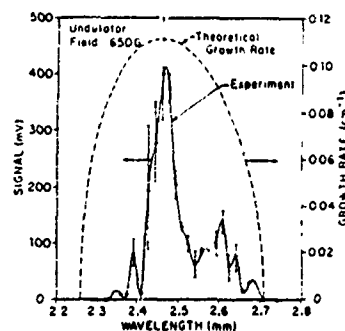

Fig. 1. Spectrum obtained with a grating spectrometer, 700 kV beam, B_0 = 9.45 kG, undulator period = 1.45 cm, with an undulator field at 650 G. The solid lines are generated from the data with a spline interpolation and the bars indicate maximum shot-to-shot fluctuation. The dashed curves are the appropriate single-pass linear growth rates from the 3D code.

observed line width. However, even at 1%, the line is much narrower than the spectrum of unstable wavelengths which can regenerate in the optical resonator: the dotted line shows a theoretical growth spectrum, of which a growth rate > 0.06 cm^{-1} is necessary for net regeneration; thus the spontaneous line width is ~ 15%. The fundamental is positioned near the maximum of the computed growth spectrum [3]. The laser resonator will therefore support excitation of many axial modes, but only one transverse mode (the TE$_{11}$) is excited. As the pump field is increased, well defined upper and lower sidebands appear, and at high pump field, the long wavelength sideband has become comparable in intensity with the fundamental (fig. 2). (The vertical scale is calibrated in different units in each diagram.) The sideband shift is about 6%, with the longer wavelength sideband dominant.

In fig. 3 we show how the power in the FEL carrier and the long wavelength sideband depends on undulator pump field. Beyond the threshold pump field, the carrier power saturates, whereas the intensity in the sideband grows exponentially in intensity. At the strongest pump field, it was found that the sideband power was comparable to the fundamental. The efficiency of the FEL, based upon the intensity of only the fundamental line (e.g. fig. 1) is ~ 4%, which is in fair agreement with a theoretical result computed in the cold-beam limit [6].

The frequency shift of the sidebands is given approximately by the following [4]:

$$\frac{\Delta\omega}{\omega} \approx \frac{N_{s,v}}{N} \frac{1 - V_{\parallel}/c}{1 - v_{\parallel}/v_g}.$$

where N is the number of undulator periods (~ 30), $N_{s,v}$ is the number of synchrotron periods in the system (~ 1), $v_{\parallel}$ is the electron axial speed, and v_g is the group velocity of the EM waves in the waveguide. Taking $v_{\parallel}/v_g = 0.93$, the observed sideband displacement, 6%,
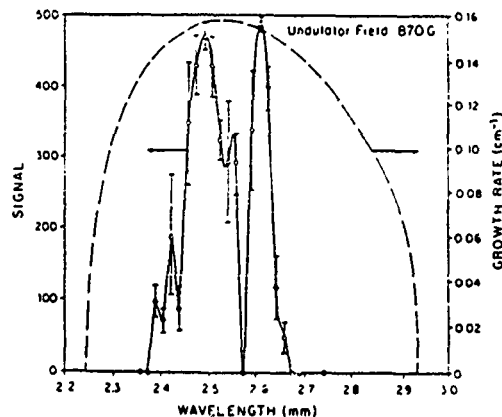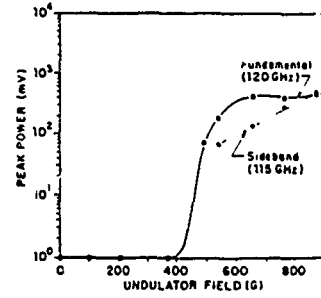

Fig. 3. Peak FEL output power at the carrier and sideband frequencies as a function of the undulator strength.

is in good agreement with this formula ($N_{s,v} \sim 2N\sqrt{a_s a_\omega} \sim 1$, and can be estimated from the power output of the FEL). This formula also predicts that it is possible to displace the sideband further from the fundamental by taking the limit $v_g \to v_{\parallel}$; this eliminates the "slippage". Indeed, by increasing the undulator period and fundamental wavelength, we have shown that the sideband displacement can be increased to ~ 30% [4]. Under those circumstances, the sideband wavelength fell outside the spectrum of unstable FEL modes, demonstrating that the sideband is parasitic and does not require a linear gain mechanism to persist. This result is shown in fig. 4.

The power of the FEL radiations was determined using a calorimeter located in the vacuum system outside the optical resonator. The calorimeter is fabricated from maycor (a machineable glass), in the form of a thin-walled cone. Thermistors attached to the cone deliver a signal which unbalances a bridge circuit. The maycor has virtually a 100% absorption for millimeter
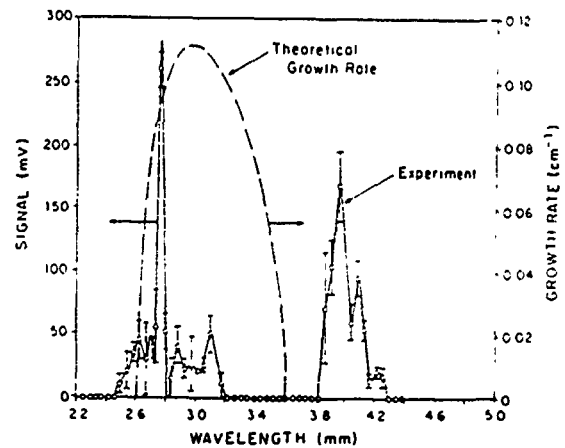

Fig. 2. Same as fig. 1, but with an undulator field of 870 G.

Fig. 4. Spectrum of the FEL with a constant period undulator (1.85 cm) for $B_0 = 7.3$ kG, $B_\perp = 700$ G, and $V = 780$ kV, showing sideband displacement to 4 mm when the carrier is shifted to 2.7 mm.

II. HIGH GAIN EXPERIMENTS

waves, determined on a test-bench setup. The calorimeter will respond to signals with intensity in the 10 mJ level. The FEL power was split so that a portion could be monitored by a detector.

Next, we report some preliminary observations of power emitted from a tapered undulator. This was designed with a 1D code [5], and consists of a section ~ 30 cm in length with constant period (1.45 cm) followed by a section ~ 30 cm in length with a gradually decreasing period. The period was decreased roughly 10%. The first section therefore provides the high small-signal gain needed for regeneration in the oscillator, while the tapered section is used to maintain resonance of the fundamental radiation with the electron energy; a modest enhancement of efficiency was expected (the limitation is due to the fixed length of the guiding field solenoid, ~ 1 m). The tapered undulator FEL oscillator was otherwise identical to the constant period device.

A conspicuous feature of the tapered-undulator oscillator was that the system would sustain oscillation much better than the constant period undulator device. This may be due to the broader gain-resonance which we associate with the tapered undulator. Improvements were noted in the pulse length especially as the beam was permitted to traverse the full extent of the tapered zone. Measurements show that the tapered undulator FEL is producing power comparable with the constant period FEL, but the *total* power output now shows a saturation at high pump field (unlike fig. 3); sideband power appears to be less significant.

Acknowledgement

References

[1] J. Masud, T.C. Marshall, S.P. Schlesinger and F.G. Yee, Phys. Rev. Lett. 56 (1986) 1567.

[2] J. Masud, F.G. Yee, T.C. Marshall and S.P. Schlesinger, Nucl. Instr. and Meth. A250 (1986) 342.

[3] H.P. Freund and A.K. Ganguly, Phys. Rev. A28 (1983) 3438.

[4] J. Masud et al., Sideband Control in a Millimeter Wave FEL, Phys. Rev. Lett 58 (1987) 763.

[5] F.G. Yee and T.C. Marshall, IEEE Trans. Plasma Sci. PS-13 (1985) 480.

[6] H.P. Freund, private communication.

Sideband Control in a Millimeter-Wave Free-Electron Laser

J. Masud, T. C. Marshall, S. P. Schlesinger, and F. G. Yee

Columbia University, New York, New York 10027

W. M. Fawley, E. T. Scharlemann, and S. S. Yu

Lawrence Livermore National Laboratory, Livermore, California 94550

and

A. M. Sessler and E. J. Sternbach

Lawrence Berkeley Laboratory, Berkeley, California 94720

(Received 30 June 1986)

The frequency offset of the sideband instability in a free-electron laser (FEL) should depend on $(1 - v_\shortparallel/v_g)^{-1}$, where $v_\shortparallel$ is the average longitudinal velocity of the electrons and v_g is the group velocity of the electromagnetic waves. We have tested the $v_\shortparallel/v_g$ dependence of the sideband shift in a 2-mm, Raman-regime FEL oscillator. A change of $v_\shortparallel/v_g$ from 0.93 to 0.98, accomplished by an increase in the undulator period, resulted in the measured sideband shift increasing from 6% to 40%, in approximate agreement with theory.

Free-electron lasers (FEL's), especially in the microwave (3 cm–1 mm) range, have been demonstrated to be prodigious sources of power. Microwave FEL experiments at Columbia University,[1] Massachusetts Institute of Technology,[2] the Naval Research Laboratory,[3,4] and Lawrence Livermore National Laboratory and Lawrence Berkeley Laboratory[5,6] have reported peak output powers ranging from 2 MW to 1 GW. Only a few studies have been made of the spectral quality of this power, sometimes initiated from noise, and sometimes as an amplification of an input signal.

Many applications of microwave FEL's require a signal with a well-defined frequency; i.e., considerable temporal coherence. The sideband instability threatens this coherence, and is a subject of much FEL work, both experimental[1,7] and theoretical.[8]

The physical origin of the sideband instability is the slippage between the light pulse and the electron pulse in an FEL. The slippage is customarily considered to occur because the light travels at c, while the electrons travel at some $v_\shortparallel < c$. The slippage couples different longitudinal slices of the electron beam, and can lead to growing modulations in the light intensity, coupled to synchrotron oscillations of electrons in buckets.

A microwave FEL must operate in a waveguide because the wavelength of the electromagnetic radiation is long and diffraction is very strong. But a waveguide provides the possibility of controlling the *group* velocity of the radiation, or the velocity at which modulations propagate. It is perfectly possible to arrange for the microwave group velocity to equal the parallel electron velocity. In that circumstance, the slippage vanishes, modulations of the radiation do not propagate forward with respect to the electron pulse, and, in principle, the

sideband instability should be completely stabilized.[9]

For a waveguide we may write

$$\omega^2/c^2 = k^2 + k_\perp^2, \qquad (1)$$

where $k_\perp$ is the transverse wave number. The group velocity is

$$v_g \equiv d\omega/dk = kc^2/\omega = c[1 + k_\perp^2/k^2]^{-1/2}. \qquad (2)$$

For large γ, the parallel velocity of the electrons is

$$v_\shortparallel = c[1 - (1 + \gamma^2\beta_\perp^2)/2\gamma^2], \qquad (3)$$

where $\beta_\perp$ is the normalized transverse velocity of the electrons due to the wiggler magnetic field $B_\perp$ and longitudinal guide field B_z, if any. Equating v_g and $v_\shortparallel$ we obtain the condition for sideband suppression:

$$\gamma \simeq (1 + \gamma^2\beta_\perp^2)^{1/2}(k/k_\perp). \qquad (4)$$

It is easy to estimate the frequency, in the laboratory, of the sideband as a function of $v_\shortparallel$ and v_g. In the Compton regime, the sidebands approximately satisfy the relation

$$[(k \pm \Delta k) + k_w]z - (\omega \pm \Delta\omega)t \simeq k_{\text{synch}}z, \qquad (5)$$

where

$$k_{\text{synch}}^2 = \frac{2}{\gamma^2}\left(\frac{eE_s}{mc^2}\right)\left(\frac{eB_\perp}{mc^2}\right) \quad \text{(cgs units)}. \qquad (6)$$

Here $\Delta\omega$ and Δk are the shift from the fundamental of the sideband frequency and wave number, respectively, k_w is the wiggler wave number, E_s is the signal electric field strength, and k_{synch} is the wave number of the synchrotron oscillations of electrons in the ponderomotive

potential or buckets. Writing $z = v_\parallel t$, using the resonance condition for the FEL

$$\omega = (k + k_w) v_\parallel, \qquad (7)$$

and recognizing that $\Delta\omega = v_g \Delta k$, one finds that

$$\Delta\omega \simeq k_{synch} c/(1 - v_\parallel/v_g). \qquad (8)$$

Equation (8) has been derived for the Compton regime, but the result $\Delta\omega \propto (1 - v_\parallel/v_g)^{-1}$ is very general, and is rigorously valid (following directly from the Manley-Rowe relations) in both the Compton and the Raman regimes, as long as $\Delta\omega/\omega$ is small. When $\Delta\omega$ becomes a significant fraction of ω, the scaling is approximate. It is Eq. (8) which we study experimentally. As v_g approaches $v_\parallel$ the sideband frequencies should get further from the main frequency.

The equations that describe sideband growth [10,11] are modifications of the standard, time-independent FEL equations, [12,13] with derivatives with respect to longitudinal distance z replaced by convective derivatives corresponding to the particle motion (in the $2N$-particle equations, where $v_\parallel$ enters) and to the propagation of signal modulations (in the field equations, where v_g enters). The solution of these coupled equations demonstrates that the peak growth rate of the sideband instability is *independent* of $v_\parallel/v_g$. This conclusion cannot be valid as $v_\parallel \rightarrow v_g$ because Eq. (8) predicts that the lower sideband moves beyond waveguide cutoff; this must have a significant effect upon the sideband growth rate. The difficulty arises because the modified FEL equations, with convective derivatives, consider a slowly varying amplitude and phase of the central frequency with fixed group velocity. This approximation is not adequate to describe sidebands which are far removed (in $\Delta\omega/\omega$ or in $\Delta k/k$) from the central frequency.

The experiment was done with the Columbia University free-electron laser, and the reader is referred to Ref. 1 for further experimental details and a schematic of the laser. An electron beam was extracted from an apertured, cold-cathode diode immersed in a strong (7-10 kG) magnetic field. A typical value of accelerator voltage was ~700 kV, and a beam current ~200 A was injected down the axis of a 6-mm-diam drift tube which also serves as a cylindrical waveguide. The undulator was a bifilar helical winding energized by a small capacitor bank timed with the accelerator pulse. The undulator consisted of a uniform section 50 cm in length between two zones (7.3 cm each) of adiabatically changing field. Two mirrors were used for feedback; the upstream mirror was a polished annular disk with reflectivity equal to 65% and the output mirror was a surface of a quartz window, with net reflectivity ~5-10%. After a certain start time, the FEL oscillates at a power level ~2-4 MW (determined calorimetrically). The spectrum was observed with a grating spectrometer (resolving power equal to 100) [14] when the power reached saturation. To

obtain each spectrum, roughly 100 shots must be taken under circumstances of constant and reproducible accelerator voltage (2% variation was acceptable), and data at each wavelength were averaged. To speed the data acquisition, two calibrated Schottky-barrier diode detectors were used in the spectrometer.

The range of wavelength studied was ~2-4 mm. The laser operates in the regime of stimulated Raman backscattering, as the beam current density is high (~1 kA/cm^2) and the pump field is "weak" ($B_\perp$ ~600-800 G); the quiver velocity of the electrons, with the guiding field taken into account, is about 10% of the speed of light. The electron orbits are "stable type I." A 3D theory [15] has been used to predict successfully not only the wavelength of the radiation but also the small-signal coefficient of exponential signal growth (~0.1 cm^{-1}). The EM wave in the drift tube is propagated in the TE$_{11}$ mode, appreciably above the cutoff wavelength of 1 cm.

A study of the time-dependent power at the wavelength of the FEL fundamental and its sideband showed the following features. After an interval of a few radiation bounce times ($2L_c/c$ ~10 nsec each), the power was observed to grow to detectable levels: This defines the start time of the device. Roughly one bounce time later the fundamental saturates, and fluctuates in strength at megawatt levels. This is followed, usually within one bounce time, by the appearance of a strong sideband signal. This indicates that the sideband growth rate is comparable to the growth rate of the FEL signal.

The experiment was done in two stages, with the use
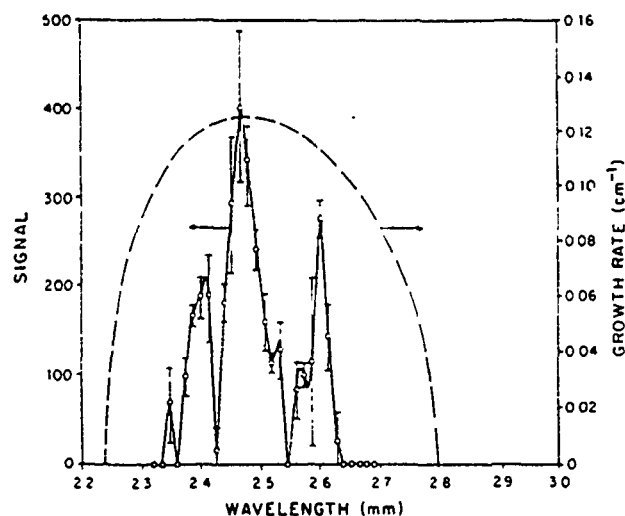

FIG. 1   Spectrum of FEL radiation, obtained under the following conditions: $V = 700$ kV; $B = 760$ G, $I = 200$ A, $\lambda_w = 1.45$ cm. The theory curve (dashed line) is the small-signal growth rate calculated according to Ref. 15. The solid line is drawn through the data points with a spline fit. The spectrum is obtained under conditions of saturated power. Guiding field $= 9.5$ kG.

of different undulators. These were identical in all respects, except that the period (λ_w) in one case was 1.45 cm (corresponding to the experimental situation of Ref. 1) while the other undulator had a period of 1.85 cm. In Fig. 1 we show a spectrum obtained with the $\lambda_w = 1.45$-cm undulator [another spectrum, at weaker $B_\perp$, is shown as Fig. 1(c) in Ref. 1]. In Fig. 1 the spectrum shows both upper and lower sidebands; at stronger pump field, the long-wavelength sideband grows to a power level comparable with that of the fundamental. The linewidth of the fundamental, under conditions where the sideband power is not large,[1] is about 1%. On the other hand, the width of the linear growth spectrum is theoretically found to be $\sim 5-10\%$, and so appreciable line narrowing has occurred from the quasioptical resonator $(Q \sim 1000)$. From Eq. (8), the fractional sideband shift is proportional to the ratio N_{synch}/N, where N, the number of undulator periods, is 35. The synchrotron period, L_{synch}, defines $N_{synch} = L/L_{synch}$, where L is the undulator length. The synchrotron period can be calculated once the power level in the resonator is known; this gives $N_{synch} \sim 1$. With $V = 700$ kV, at the given $B_\perp$, $v_\eta/c = 0.90$ and we compute $v_\eta/v_g = 0.93$ from the waveguide properties; the predicted (Eq. 8) sideband shift is 6%, in good agreement with the measured value.

The experiment was then "repeated" at $V = 780$ kV, with the same hardware, but with the 1.45-cm period undulator replaced by the 1.85-cm undulator. This has the effect of increasing the fundamental wavelength in which case the ratio v_η/v_g becomes a very important factor in increasing the sideband shift. In order to keep the Group I orbits away from magnetoresonance, we reduced the guiding field from 9.5 to 7.3 kG. In Fig. 2 the spectrum clearly shows the FEL line at 2.75 mm and the lower sideband at 4 mm; the most striking feature is the

increase of the sideband shift to $\sim 40\%$ (the upper sideband fell outside the range of the spectrometer grating). Computing $v_\eta/c = 0.91$, noting that now $N = 27$, and taking $N_{synch} = 1$ (the laser power is nearly the same), we find, from Eq. (8), $v_\eta/v_g = 0.98$. As the cutoff wavelength has not changed, we can calculate what FEL wavelength would be required to give this group velocity: the result is 3 mm, which is close to the actual FEL fundamental. The spectrum of Fig. 2 shows a dramatic increase of the sideband shift due to a small change in group velocity, in accord with the result in Eq. (8).

Calculations of the small-signal growth rate have been made for the conditions appropriate for Figs. 1 and 2, with the use of a 3D theory[15]; these are shown as dotted lines in the figures (the peak growth rate is kept about the same). It is interesting to note that the sideband falls outside the zone of unstable growth for the FEL in the case of the 1.85-cm undulator. Although the effect of the guiding field is accounted for in the small-signal theory, it is not accounted for by the theory in this paper, nor has it been used in the waveguide calculations. The waveguide is filled with electrons through which a right-handed circularly polarized EM wave is propagated, but the effect of the guiding field on the group velocity is negligible because the invariant plasma frequency $[ne^2/\pi\gamma m]^{1/2}$ is ~ 2 GHz and the cyclotron frequency $eB_z/2\pi\gamma mc$ is ~ 9 GHz, whereas the wave frequency is 75-100 GHz.
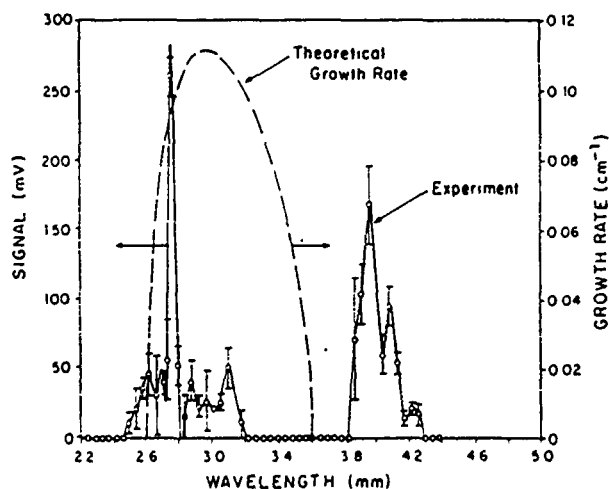
FIG. 2. Data obtained for the same FEL as in Fig. 1, but under the following conditions: $V = 780$ kV, $B = 690$ G, $\lambda_w = 1.85$ cm, and guiding field $= 7.3$ kG.

[1]J. Masud, T. C. Marshall, S. P. Schlesinger, and F. G. Yee, Phys. Rev. Lett. 56, 1567 (1986).

[2]J. Fajans, G. Bekefi, Y. Z. Yin, and B. Lax, Phys. Rev. Lett. 53, 246 (1984).

[3]J. A. Pasour, R. F. Lucy, and C. A. Kapetanakos, Phys. Rev. Lett. 53, 1728 (1984).

[4]S. M. Gold et al., in Free Electron Generators of Coherent Radiation, edited by C. A. Brau, S. F. Jacobs, M. O. Scully, SPIE Proceedings Vol. 453 (SPIE, Bellingham, Washington, 1984) p. 350.

[5]T. J. Orzechowski et al., Phys. Rev. Lett. 54, 889 (1985).

[6]T. J. Orzechowski et al., Phys. Rev. Lett. 57, 2172 (1986).

[7]R. W. Warren, B. E. Newman, J. C. Goldstein, IEEE J.

Quant. Electron. **21**, 882 (1985).

[8]N. M. Kroll and M. N. Rosenbluth, in *Physics and Quantum Electronics* (Addison-Wesley, Reading, MA, 1980), Vol. 7, p. 147.

[9]W. M. Fawley, E. T. Scharlemann, A. M. Sessler, and E. J. Sternbach, Lawrence Berkeley Laboratory Internal Note No. TBA 30, 1986 (unpublished).

[10]M. N. Rosenbluth, H. V. Wong, and B. N. Moore. in Ref. 4, p. 25.

[11]N. S. Ginzburg and M. I. Petelin, Int. J. Electron. **59**, 291 (1985).

[12]N. M. Kroll, P. L. Morton and M. N. Rosenbluth, in Ref. 8, p. 81.

[13]A. Szöke, V. K. Neil, and D. Prosnitz, in Ref. 8, p. 175.

[14]J. A. Pasour, S. P. Schlesinger, Rev. Sci. Instrum. **48**, 1355 (1977).

[15]H. P. Freund and A. K. Ganguly, Phys. Rev. A **28**, 3438 (1983).

Design of an Efficiency-Enhanced Raman FEL Oscillator

F. G. YEE AND THOMAS C. MARSHALL

Abstract—The paper reports numerical calculations appropriate for the design of an "efficiency-enhanced" Raman free electron laser (FEL) oscillator. A helical undulator is used which consists of a constant period section followed by a section where the period is decreased roughly 10 percent. Simulation of the FEL is done by following the radiation dynamics in both the small- and large-signal regimes, using the "generalized pendulum equation" with self-consistent radiation field. It is found that the efficiency of the oscillator may be enhanced from ≈8 (no taper) to ≈15 percent (with taper). The configuration of an experimental oscillator is described; this device should produce ≈25 MW at a wavelength ≈1.8 mm using an 800-kV electron beam.

I. INTRODUCTION

THEORETICAL studies indicate (see [1], which contains a survey of theoretical and experimental information, together with references) that the efficiency of a Raman free electron laser (FEL) can be enhanced by properly "tapering" the undulator amplitude and/or period; under optimized conditions, efficiency of order 25 percent or more can be obtained. Already, a series of experiments at LANL and Boeing/Math Sciences [1] has shown that the efficiency of a Compton FEL may be improved by roughly a factor of ten using these techniques. However, very little consideration has been devoted to proving this concept in the case of Raman, or space-charge dominated, FEL's, particularly in the oscillator configuration. Using pulse-line technology, with an 800-kV 200-A beam, we shall show that a Raman FEL should produce roughly 25 MW at a wavelength ≈2 mm. Since the level of radiation inside the resonator is substantially higher, this opens the possibility of studying a "two-stage" FEL in the collective regime, where the millimeter radiation is backscattered from the cold portion of the electron beam upstream from the undulator, regenerates inside the resonator, and appears in the lab at wavelength λ, ≈ $l_0/8 \gamma_{11}^4$ ≈ 0.1 mm. In what follows, we discuss the numerical solution [2] of the tapered undulator problem in one dimension, appropriate to the design of the "first-stage" high-power oscillator [3]. The results show that the efficiency of a Raman FEL oscillator can be improved by roughly a factor of two using a variable-period undulator, even in a very short (≈70 cm) system using a short-pulse electron accelerator (≈100 ns).

As an actual experiment is planned, we begin by summarizing the constraints under which it must be operated. For the electron beam, the electron γ ≈ 2.5, with current density ≈ 1 kA/cm². We have demonstrated in previous experimentation, using this beam, that the electron momentum spread is ≈0.6 percent in the absence of the undulator [4], and that substantial (10 dB) gain may be obtained at ≈ 1 mm [5]. As the high-current density beam requires a guiding magnetic field, the space available for the undulator is only ≈70 cm, and the quiver velocity induced on the beam by the electrons should be in the range ≤0.1–0.15 c so that the momentum spread induced by the undulator remains small [4]. The pulse length of the accelerator is 150 ns, so this defines the time span over which the oscillation must build up from noise, saturate, and interact with the "tapered" undulator. We shall choose an undulator period $l_0 = 1.7$ cm, which will stimulate radiation at a wavelength $l_0/2\gamma_{11}^2$ ≈ 1.8 mm. The configuration of the planned laser (shown later in Fig. 3) will be discussed in Section IV.

After giving appreciable energy to the laser signal field, the electrons in an FEL are slowed down and fall out of resonance with the ponderomotive potential well. Among the possible efficiency enhancement schemes, two are studied: 1) slowing the well by decreasing the period of the undulator magnet, so the phase velocity is decreased to synchronize with the electrons; and 2) compensating for the loss of parallel (axial) energy by decreasing the amount of pumping, that is, decreasing the undulator field amplitude along the beam direction. The latter decreases the path length traveled by an electron so as to maintain the resonance frequency constant along the system. These methods may be combined.

In the design, one strives initially for adequate small-signal gain, say > 10 dB per pass, so that the spontaneous radiation will grow from noise in a few passes through the Fabry–Perot resonator and the growth on each pass will substantially exceed the mirror and diffraction losses (at millimeter wavelength, these could be as high as 90 percent). If the net power gain is G, and there are M passes, the output will grow to

$$P(M)/P(0) \approx M + e^{GM}. \tag{1}$$

The magnitude of the signal vector potential at saturation (end of the small-signal regime) is

$$A_{sat} \approx \frac{\gamma}{2} \sqrt{\gamma_{11}^5 (\omega_p/k_0 c)^3} \cdot (mc^2/e) \tag{2}$$

which is ≈ 10 statvolts in CGS units, where m and e are the electron mass and charge, and c is the speed of light. We find typically that about 35 cm of the undulator is enough to provide a growth to saturation in perhaps eight bounces of the radiation, providing the undulator amplitude is high (roughly 2 kG in the absence of a guiding field, so that the electron quiver velocity is at least 0.1 c). In the regime of small-signal growth, the tapered region is not effective. Enhancement of efficiency is dependent on large-signal gain in the tapered end region of the undulator in the last pass or two of the radiation. The design of this region provides a trade-off between the small-signal gain and the large-signal efficiency enhancement.

It is important to understand that in the oscillator one cannot assume that the intial signal is known at the undulator entry. Thus one endeavors to optimize the oscillator performance in such a way that it remains satisfactory over a wide range of initial signal amplitudes. The theory requires a value of signal specified at the input, and it calculates the growth in a single passage along the undulator. If the initial signal is sufficiently small, the signal grows exponentially at the resonance wavelength; large signals involve trapping of electrons in potential troughs and exhibit saturation and periodic variation of amplitude.

II. THEORY

The design is based on a one-dimensional numerical model of the generalized pendulum equation (2):

$$d^2\psi/dz^2 = -\left(\frac{e}{\gamma mc^2}\right) 2k_s k_0 A_w A_s \sin \psi$$

$$+ \frac{2\omega_p^2}{\gamma c^2 \gamma_{11}^2} [\langle \cos \psi \rangle \sin \omega - \langle \sin \psi \rangle \cos \psi]$$

$$\cdot + \frac{dk_s}{dz} - \frac{1}{4}\left(\frac{e}{\gamma mc^2}\right)^2 \frac{\omega_s}{c}\frac{d}{dz} A_w^2 + \frac{dk_0}{dz} \quad (3)$$

where ψ is the phase and ω_p is the plasma frequency, together with the self-consistent signal wave equations, approximated in the limit of slowly growing amplitude on the scale of the wavelength:

$$(\omega_r/c - k) A_s(z) = \frac{\omega_p^2}{2c^2}\frac{v_{11}}{\omega_r}\left[A_w \left\langle\frac{\cos \psi}{\gamma}\right\rangle \right]$$

$$\sqrt{...}\frac{d}{dz}(A_s\sqrt{k}) = \frac{\omega_p^2}{2c^2}\frac{v_{11}}{c}\left[A_w \left\langle\frac{\sin \psi}{\gamma}\right\rangle \right] \Bigg\} \quad (4)$$

where A_s, A_w = vector potential of signal wave and undulator, $k_0 = 2\pi/l_0$, $k = (d\phi/dz + \omega_s/c)$, ϕ = optical phase, and $k_s = 2\pi/\lambda_s$. The first term on the left of (3) is the conventional pendulum term, while the second accounts for the effects of high space-charge density. The latter must be included when the density of electrons exceeds

$$n > k_0^2\gamma^3 A_w A_s/4\pi mc^2 = \frac{B_\perp E_s\gamma}{8\pi mc^2}. \quad (5)$$

The third and fourth terms account for the change of optical phase ϕ and the undulator amplitude variation, while the last involves the change of undulator period. As initial conditions, we choose l_0, γ, k_s, the system parameters. A finite number of electrons ($i = 1, 2, \cdots, n$) with initial phases $\psi_i(0)$ are evenly distributed between $-\pi$ and $+\pi$, to simulate the random phase of the electron ensemble without any special injection preparation; in addition, these electrons will also have different energies within a range $(\delta\gamma/\gamma)_{11}$, in order to simulate the typical beam momentum spread to be expected (≈ 1 percent). Parameters to be optimized are A_w, the length of untapered section L, the period $l_0(z)$, the initial signal amplitude $A_1^{(0)}$, and the frequency mismatch at injection $\Delta\omega/\omega$. To prescribe in a proper way, the electron energy must be known at every position by solving (2)

$$\frac{d\gamma}{dz} = -2\gamma k_0 \left(\frac{e}{mc^2}\right) A_w A_s \sin \psi - \frac{eE_s}{mc^2}. \quad (6)$$

In solving for the electron energy using (6), the interaction with the space-charge field may be neglected, as the electrostatic energy in the space-charge fluctuations is smaller [6] than the energy of the electromagnetic wave by a factor ≥ 10. In the small-signal limit, (3) reduces to the small-signal Raman or Compton gain result. We assume the electron beam is nearly cold, that is, the axial momentum of all electrons is nearly the same, which is satisfactory providing the momentum spread is negligible compared with the ponderomotive amplitude

$$(\delta\gamma/\gamma)_{11} \leq \frac{e}{mc^2}\sqrt{A_w A_s} \quad (7)$$

in which event the electrons can easily be trapped in the "buckets" of the ponderomotive wave potential.

In optimizing the undulator period profile, we use a "resonant electron approximation"

$$\frac{d\gamma_r}{dz} = \frac{-k_s(z) A_s(z) A_w \sin \psi_r}{\gamma_r} \cdot \left(\frac{e}{mc^2}\right)^2 \quad (8)$$

and

$$\frac{d\psi_r}{dz} = 0 = k_0(z) - \frac{k_s}{(1 + \beta_{11}) \gamma_{11}^2\beta_{11}}\left\{1 + \left(\frac{eA_w}{mc^2}\right)^2\right.$$

$$- 2\left(\frac{e}{mc^2}\right)^2 A_w A_s(z) \cos \psi_r$$

$$\left. + \left(\frac{e}{mc^2}\right)^2 A_s^2(z)\right\}. \quad (9)$$

Equations (8) and (9), which neglect space charge, are useful in choosing a first approximation to the optimum $k_0(z)$. The actual calculation, however, uses (3), (4), and (6).

III. RESULTS OF THE CALCULATION

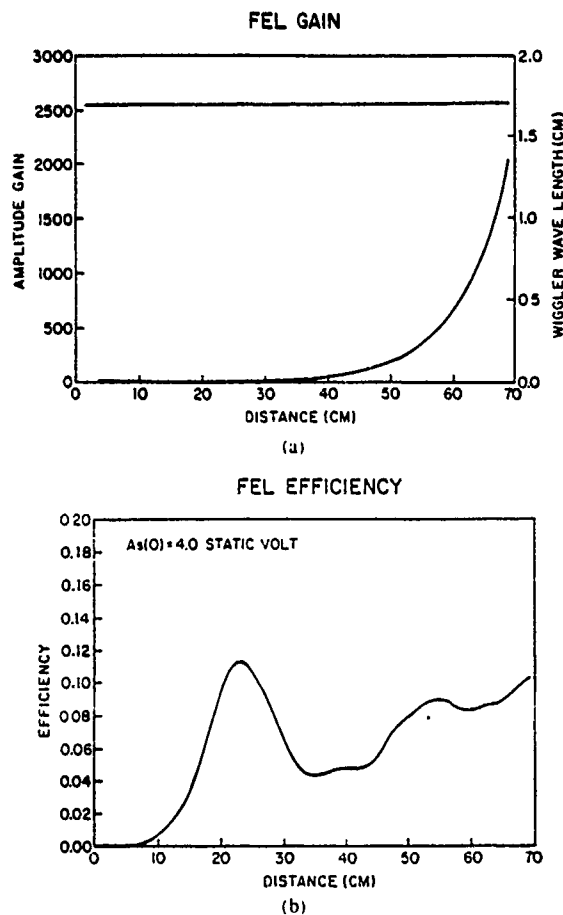The following parameters were chosen: pumping magnetic field = 2.0 kG (see next section for the discussion

Fig. 1. Signal growth and saturation in a Raman FEL having an undulator (or "wiggler") with constant helical pitch. (a) Small-signal growth, constant undulator period above. (b) Saturation and synchrotron oscillations at high-signal power.

Fig. 2. Signal growth and saturation in a Raman FEL having an undulator with programed pitch (1.7 cm for the first 20 cm, linear taper to 1.4 cm over the remaining 50 cm, same electron beam conditions). (a) Small-signal growth, variable undulator pitch above. (b) Saturation and synchrotron oscillations at large-signal power (the different curves show the effect of variation of the large-signal amplitude).

pertaining to the guiding field effect, which is the actual situation experimentally); $(\delta\gamma/\gamma)_{11} = 1$ percent; optimized resonant phase $\psi_r = 10°$; and $\gamma(0) = 2.425$. The undulator is helical and drives a right-handed circularly polarized electromagnetic wave.

Fig. 1 shows the result for the case of an undulator having constant amplitude and period. Fig. 1(a) is the growth of a small-amplitude test signal along the undulator. Fig. 1(b) shows what happens when the initial signal is large (in this example, 4.0 statvolt): synchrotron oscillations are apparent. If the beam were cold, the synchrotron oscillation would be even more pronounced. As the input "large" signal to the oscillator is not known—it depends on growth during several radiation bounces in the small-signal regime, and therefore depends on unspecific initial conditions—we might anticipate that on the average the output efficiency of the oscillator might be roughly 8 percent.

For the tapered undulator example, we have found that a suitable choice consists of a leading uniform period section, 20 cm long (which produces adequate small-signal gain), followed by a 30-cm tapered period section (which promotes enhanced efficiency). Fig. 2(a) shows the period profile (above), and the small-signal power gain in this section is about 26 dB. Fig. 2(b) shows the efficiency for
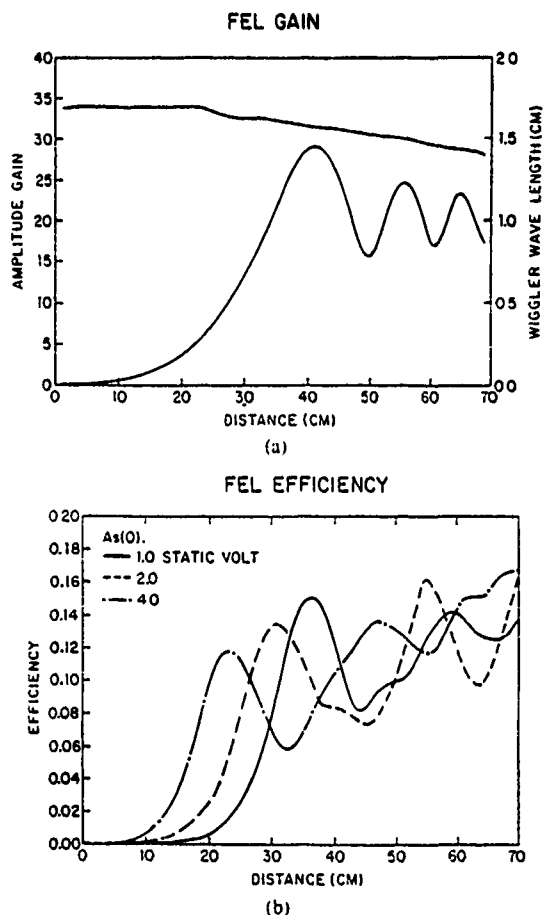
three different values of "large" signal: 1.0, 2.0, and 4.0 statvolts at the input of the oscillator. After one pass, the typical output signal shows an efficiency which is of order 15 percent, that is, roughly a factor of two enhancement over the untapered period simulation. Thus, in an actual experimental situation, a modest tapering of the undulator period should cause a marked improvement in the power obtained from the oscillator. Furthermore, at the end of the undulator the power extracted is not particularly sensitive to the signal level present at the input on the last pass; for this reason we believe that our calculation should satisfactorily model operation as an oscillator.

The calculations have been done in one dimension, taking unity filling factor. We have found that better results were obtained by changing the undulator period rather than the amplitude.

IV. EXPERIMENTAL CONFIGURATION

The electron beam will be cylindrical, with diameter about 5 mm, and is obtained from an aperture in a field-emission diode; a similar beam in a 1.9-cm-diameter drift tube was found to have an intrinsic parallel momentum
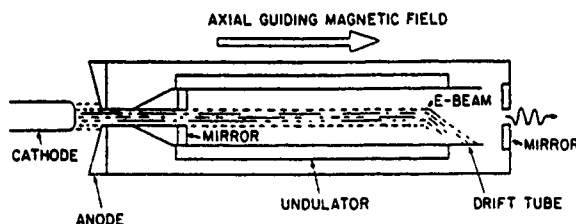
Fig. 3. Proposed experimental configuration. The mirror on the upstream side is a high-dielectric constant disk mounted on a low-dielectric constant wedge.

spread of 0.5 percent from the combined effects of emittance and space charge [4]. The undulator will be a bifilar helix, machined with a variable pitch by a numerically controlled lathe. A transverse magnetic field on axis ≈ 600 G is readily produced by a capacitor-bank discharge through the winding. Although the numerical work did not include a guiding magnetic field. this is necessary to contain the space-charge forces of the beam in an equilibrium. If we require that the quiver velocity in the experimental situation be the same as that found necessary in the simulation, the guiding field B_0 permits one to operate the laser with smaller pump magnetic-field amplitude. A large quiver velocity is obtained as the undulator is operated near "magnetoresonance," viz.. $eB_0/\gamma k_0 mc^2 \beta_{11} = 0.7$; this is given by

$$v_\perp/v_{11} = \frac{eB_\perp/mc}{(eB_0/mc - \gamma k_0 v_{11})} \qquad (10)$$

where $B_\perp$ is the undulator field. It is expected that stable "type I" orbits [7] will result in this undulator. As the period of the undulator is decreased, the quiver velocity will be reduced from two effects: 1) moving farther from magnetoresonance, and 2) reduction of $B_\perp$ owing to the increasing ratio of the coil winding radius to the period. All these effects combine to reinforce the original taper, that is, they combine to maintain the resonant energy. However, in the simulation, only the period is allowed to change. Therefore the actual change in undulator period required is less than that introduced into the theoretical model.

Power will be recirculated in a multimode resonator between two mirrors (Fig. 3 shows the laser configuration anticipated). The end mirror, having a coupling hole, is to be fitted into a larger pipe; thus off-axis resonant modes

will suffer high diffraction and will not be regenerated. At the upstream end of the system, we use a dielectric mirror, fitted onto a wedge having low-dielectric factor. An appreciable fraction of the radiation will be reflected from the high-dielectric constant interface $(K \sim 15)$, and this may be reinforced still more by choosing the thickness of the mirror slab to be half-wavelength. The advantage of this scheme is that the dielectric mirror does not perturb the radial electrostatic geometry of the beam and the drift tube: then the electron beam momentum spread will remain adequately low, as in the original design.

Fig. 2(a) shows that the small-signal single-pass power gain is ≈ 500 (≥ 1 dB/cm). Assuming 90-percent power loss in the feedback system (i.e., $P_{out}/P_{in} = 50$), and that noise power ≤ 1 W is present at the input, then from $P(M)/P(0) = 10^8$ and (1), we find five optical bounces (30 ns) are required to reach saturation. This is far less than the accelerator pulse length (150 ns).

Spectral measurements, particularly bandwidth, will be made initially with a Fabry–Perot external interferometer. We expect the FEL system to exhibit a primarily homogeneously broadened line, and therefore appreciable line narrowing should result (unlike the original [8] Raman FEL, where the gain was influenced by inhomogeneous broadening effects). Power measurements will be made using a calorimeter cone fabricated of "Macor," a machineable glass with high absorption at millimeter wavelength. Operation of the actual laser should be possible in 1986.

REFERENCES

[1] T. C. Marshall. *Free Electron Lasers.* New York. Macmillan. 1985
[2] P. Sprangle and C M Tang. "A laser beat-wave electron accelerator." *IEEE Trans. Nucl. Sci.*, vol. NS-28. pp. 3346-3348. 1981.
[3] F. G. Yee and T. C. Marshall. "A tapered-undulator Raman oscillator." *Bull. Amer. Phys. Soc.*, vol. 29. p. 1342. 1984.
[4] S. C. Chen and T C Marshall. "Thomson backscattering from a relativistic electron beam as a diagnostic for parallel velocity spread." *Phys. Rev. Lett.*, vol. 52. pp 425-428. 1984
[5] J. Masud. T C Marshall. and S P. Schlesinger. "A Raman-FEL amplifier at 1.22 mm." *Bull Amer Phys Soc.*, vol 29 p 1341. 1984
[6] T. Kwan. J. M. Dawson, and A. T Lin. "Free electron laser." *Phys Fluids.*, vol. 20 pp. 581-588. 1977.
[7] H. P. Freund. "Nonlinear analysis of free electron laser amplifiers with axial guide fields." *Phys Rev.*, vol. A27. pp 1977-1988. 1983
[8] D. B. McDermott. T C Marshall. S P Schlesinger. R. K Parker. and V. L. Granatstein. "High power free-electron laser based on stimulated Raman backscattering." *Phys Rev Lett.*, vol 41. pp. 1368-1371. 1978

Efficiency and Sideband Observations of a Raman FEL Oscillator with a Tapered Undulator

F. G. Yee

T. C. Marshall

S. P. Schlesinger

Efficiency and Sideband Observations of a Raman FEL Oscillator with a Tapered Undulator

F. G. YEE, T. C. MARSHALL, AND S. P. SCHLESINGER, LIFE FELLOW, IEEE

Abstract—Power and spectral measurements are reported from the Columbia Raman free-electron laser (FEL) oscillator experiment. High-power radiation pulses (~ 12 MW, 100 ns) are generated at a wavelength of ~2.5 mm, using a 750-kV electron beam injected into a helical undulator; the latter is made up of a constant-period (1.45 cm) section 40 cm long followed by an equal length of tapered undulator. The period is decreased by 7.6 percent in such a way that the on-axis field remains constant. We find that the taper allows an increase in total power efficiency from ~4 to ~12 percent. Most noteworthy is that the tapered undulator reduces the sideband radiation compared with a constant-period undulator FEL which was studied in the same configuration. The power was measured calorimetrically and compared with the results of a 1-D Raman code. The reduction of sideband power observed in the experiment was consistent with computational results obtained with a 2-D sideband code.

VARIOUS studies, both theoretical [1], [2] and experimental [3], [4] have shown that the efficiency of a free-electron laser (FEL) may be improved through the use of an undulator designed with a varying period. Experimentation of an FEL amplifier operating in the regime of "strong-pump" collective effects [5] shows that experimental data can be satisfactorily interpreted numerically. Results from Compton oscillators also indicate that efficiency is improved using a tapered-period undulator [6], [7]. In this paper, we report data obtained from a Raman oscillator which has been operated with an undulator having a constant as well as a variable period. In each case, we study the spectrum of the radiation emitted, which shows in the first example a well-developed set of sidebands, but in the second instance the sidebands are much reduced

The oscillator configuration (Fig. 1(a)) is the same as reported in a recent study of regenerative gain in this FEL [8]. The electron beam energy is ≈750 kV, obtained from a pulse-line accelerator which produces a voltage pulse lasting about 150 ns with <2 percent voltage fluctuation. The electron beam, emitted from a cold graphite cathode immersed in a 1-T magnetic field, is apertured to 5-mm diameter and propagates in a cylindrical drift tube (waveguide) of 6.3-mm diameter. FEL radiation is produced and propagated as a TE_{11} mode of this waveguide [8]. The power gain is large (≈ 10–20 dB/pass), and the electron motion induced by the undulator is in the range $v_\perp/c \approx$ 0.1. Feedback is provided by a pair of reflectors; a reflectivity ≈50 percent is adequate since the Raman gain of the device is high. After a "start time" ≈30 ns, the radiation builds up to saturation level (Fig. 1(b)). The spectroscopic studies were done when the power was in the saturation regime.

When designing the tapered undulator [9], a trade-off must be made between having adequate gain for short start time, and the efficiency enhancement. The latter is ideally done using an undulator several synchrotron periods in length. The publication cited [9] describes a 1-D simulation using a cold beam in a Raman FEL interaction as an amplifier, comparing constant- and variable-period undulators. The variable-period undulator actually used was a "hybrid" composed of a section with constant period followed by a section where the period was decreased in a linear way over several periods. Thus, the experiment is an "unoptimized" tapered-undulator device from the efficiency point of view. Also, unlike an amplifier, the oscillator will reach saturation after several radiation passes, and so it is not possible to predict the efficiency on any given shot; in fact, the output pulse power showed appreciable variability, and the data we report represent an average based on several shots. This variability can be understood by consulting [9, fig. 2(b)]. Oscillator simulations have been reported [10], but the tapered undulator used in that calculation was not a hybrid.

We have extended the calculation reported in [9] by incorporating a finite parallel momentum spread into the model. No important decrease in gain or efficiency was observed using the simple numerical model until the parallel normalized momentum spread was increased to the 2–4-percent range; this is substantially larger than the actual momentum spread we expect to encounter in this experiment [11]. The cold-beam simulations show that, given the restrictions on the total undulator length of our apparatus, we should expect the efficiency of the tapered undulator FEL to be roughly a factor of 2 better than the same FEL with constant-period undulator; that is, we expect roughly 12 percent of the electron beam kinetic energy to be converted into radiation.

The undulators used in the experiment have period of 1.45 cm and are wound as bifilar helices, about 80 cm in length, on a phenolic form located over the drift tube; a pulse current synchronized to the accelerator provided the
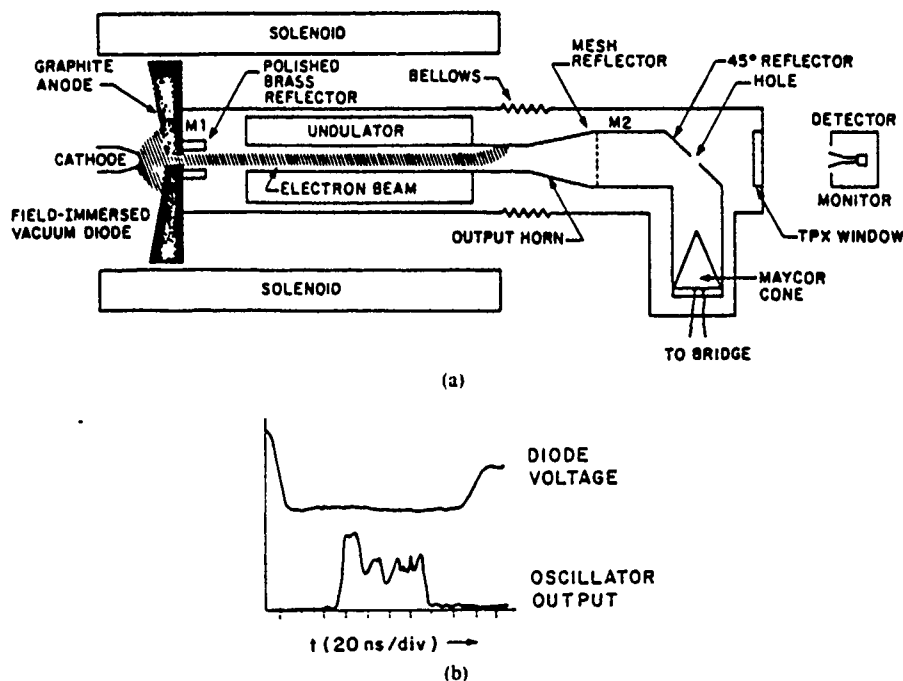
Fig. 1 (a) A schematic of the oscillator, showing the calorimeter in place.
(b) Typical output pulse of the tapered-undulator FEL showing a 40-ns
"start time" followed by saturation; diode voltage negative-going pulse
above; 20 ns/div

field. The hybrid-undulator tapered section was 40 cm in length over which the period was decreased by 7.6 percent. The undulator winding groove was cut on a computer-controlled lathe such that the winding depth increased as the period decreased, so that the field produced on axis remained approximately constant. Each undulator was provided with an "adiabatic entry" zone where the groove winding depth increased over several periods (≈ 9 cm) so that the helical magnetic field slowly increased as the electron spiraled into the undulator.

The first experiment consisted of a power measurement. This was done by two methods: 1) a calibrated diode detector located some distance beyond the FEL horn antenna, using a calibrated attenuator and the "radar formula" to relate the detected signal to the power radiated, and 2) a calorimeter attached to the FEL output. The calorimeter consisted of a thin cone of "macor" (machinable glass) to which ten thermistors were bonded; the signal was obtained from the output of a bridge circuit. The cone was incorporated into the FEL vacuum chamber, and was shielded from X rays and diode debris by locating it beyond a 90° bend in the light pipe; a small portion of the signal was allowed to escape through the 90° beam splitter and was monitored by a diode detector located nearby. This is also shown in Fig. 1(a). The response of the bridge circuit permitted the detection of energy as low as 10 mJ. The power follows from the observation of the signal duration. The values we quote here take into account power radiated upstream through a partially transmitting mirror (35 percent) and the downstream power that was detected.

Above the threshold magnetic field required for oscillation (500 G), the power radiated by the variable-taper undulator did not change as the undulator pump field was increased to 1 kG; furthermore, the power output was insensitive to changes in beam energy in the 600–800-kV range. The average efficiency for these parameters was found to be 12 percent, in good agreement with the simulation [9]. There was, however, a large variability in power obtained from one shot to another, possibly due to small changes in system performance during start-up. The case of the constant period is very different. The total power increased with increasing pump field, but the cause for the increase is due to a strong sideband: the signal strength of carrier does not increase further with an increase in pump field. The "hybrid" undulator, however, produces appreciably less sideband radiation. Therefore, since the numerical simulations do not account for the sideband radiation, we compare only values of the total power in each case. It was found that the efficiency of the constant period undulator was 4 percent, whereas the efficiency of the "hybrid" was 12 percent. We believe this demonstrates successful operation of the hybrid undulators in the FEL oscillator, given the limitations on the system length (simulations suggest that the efficiency of the hybrid would continue to increase providing the tapered zone could be lengthened). The power output (several megawatts in each case) was not sensitive to the downstream mirror reflectivity, but we did not attempt to construct a resonator with a very high Q because the losses from the upstream reflector are always high because of the beam-entry aperture. The power inside the resonator was
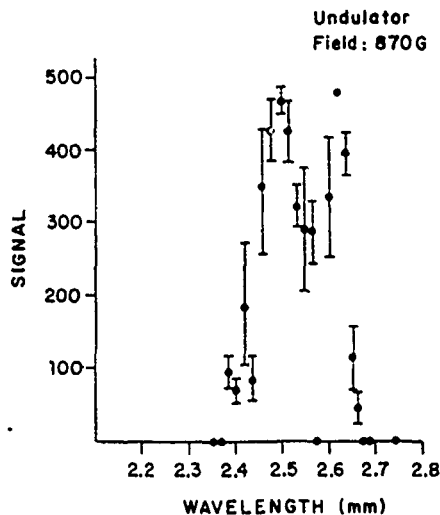
Fig. 2. Power spectrum from the constant-period Raman FEL oscillator.

of the correct magnitude to cause trapping and efficiency enhancement according to the simulation [9], viz., the vector potential of the FEL radiation was ≈ 1 statV.

Next we compare the spectrum of the radiated power for the constant-period undulator and the hybrid. Fig. 2 shows the spectrum of the constant period undulator [12] and Fig. 3 shows the spectrum of the hybrid, taken under the same conditions of beam energy, current, undulator field, etc. Fig. 2 shows a powerful long-wavelength sideband, comparable in intensity to the carrier, whereas Fig. 3(a) shows considerably less sideband radiation. Data were taken using a calibrated grating spectrometer, assembling approximately 100 shots per spectrum and then discarding shots having nonreproducible features. The resolving power of the grating was ≈ 100 (instrumental line width $\approx. 1$ percent). The data reported in Fig. 3 are obtained under conditions of saturated power, when the power (see Fig. 1(b)) reaches maximum after the initial exponential buildup. However, the general features of the spectrum remain unchanged throughout the remainder of the pulse, as shown by Fig. 3(b) and (c). Experimentation with the sideband (constant-period undulator) has shown that the sideband radiation is parasitic in nature and appears nearly simultaneously with the saturated carrier power [8].

To interpret the sideband results, simulations are done using a numerical model of the 1-D electron equations with space-charge effect and a 2-D electromagnetic wave equation which uses the slowly growing amplitude approximation [13]. The wave equation is solved in a cylindrical pipe using a TE boundary condition, the 2-D fields are then coupled to the 1-D particle motion with the electrons arranged in layers. The division of the electron beam into radial laminae is justified, since the radius of the electron's helical orbit is considerably less than the electron beam radius. Three wavelengths are followed, corresponding to the carrier (at maximum gain) together with an upper and lower sideband which are separated from the carrier by the experimentally observed amount. Fig. 4
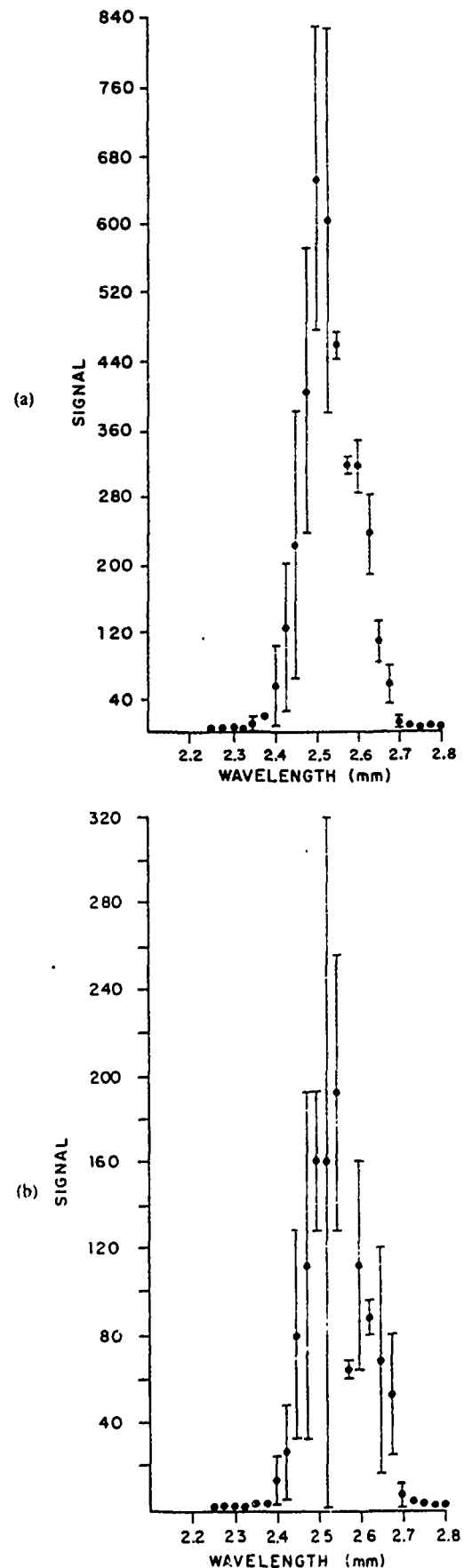

Fig. 3. Power spectrum from the variable-period Raman FEL oscillator. The spectrum is observed at (a) $t = 0$, (b) $t = 10$ ns (one cavity bounce time), and (c) $t = 30$ ns after onset of saturation
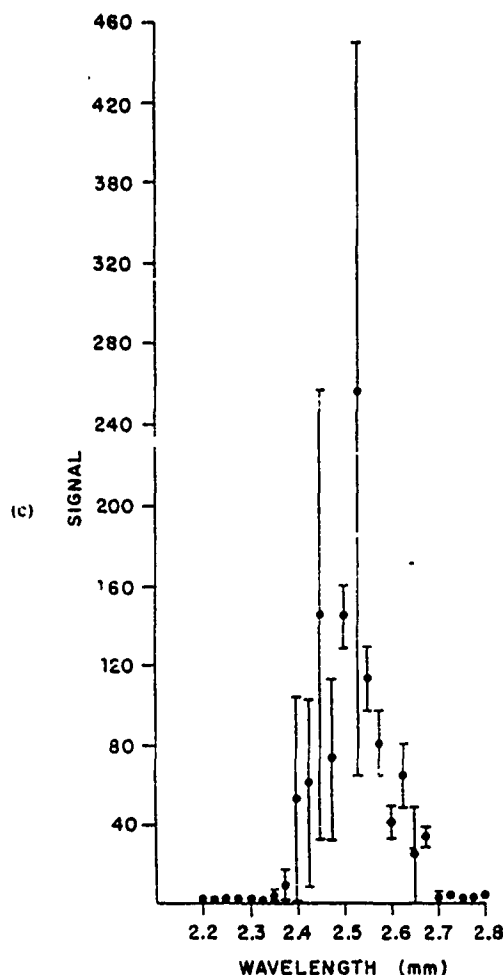
(c)

Fig. 3. *(Continued)*

Fig. 4. Numerical simulation of the carrier and sideband growth: same parameters taken as in the experiment: thin line—carrier. heavy line—short-wavelength sideband; dash-dot line—long-wavelength sideband (a) Constant-period undulator. (b) Tapered- (10-percent) period undulator. Abscissa is measured in normalized undulator length. The ordinate axis scale for the sidebands is 1/50 the scale of the carrier

shows two cases, for constant-undulator period (Fig. 4(a)) and a 10-percent tapered undulator (Fig. 4(b)), with the tapered-undulator section preceded by a constant-period section as in the experiment. The fields are followed for three cycles through the undulator, taking a 90-percent loss of power in the feedback. The simulation shows that the long-wavelength sideband is reduced in amplitude to a level comparable with the short-wavelength sideband due to taper. The computed efficiency (total radiation) from this code is slightly lower than the efficiency computed with the 1-D code with no sideband (8 and 4 percent, tapered and untapered, versus 12 and 6 percent, respectively). As can be seen from Fig. 4, the growth rate of the sidebands is comparable to the carrier; however, the initial amplitude of the sideband compared to the carrier is not known (it was arbitrarily set at 2 percent of the carrier amplitude in the simulation). Therefore, the ratio of the carrier to sideband amplitude after one pass cannot be compared with the experimental data in this simulation. The simulation does, however, appear to correctly predict the trend toward sideband reduction when the taper is imposed.

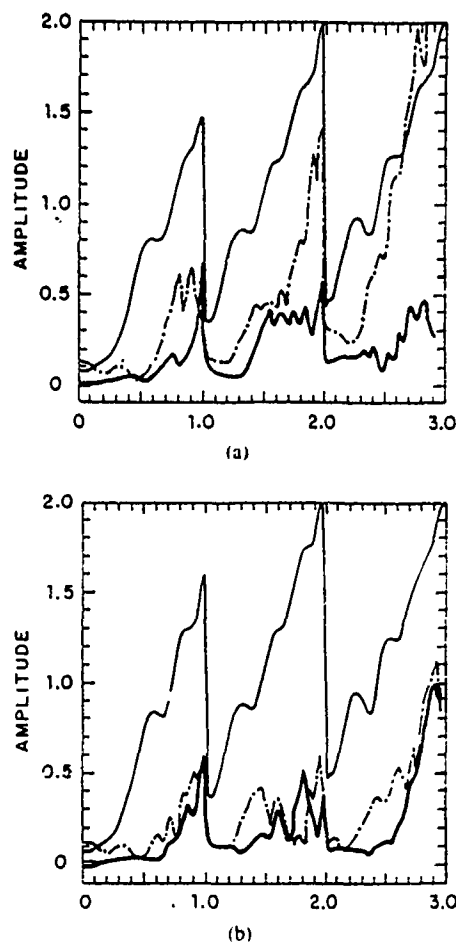One conclusion from this experiment has to do with sideband control. When the sideband growth is very rapid, as it is here, the sideband cannot be controlled effectively by manipulation of the resonator reflectivity: in any event, such a technique would compromise the desirable feature of FEL tunability. One method of control [14] is to change the group velocity of the EM waves so that the sidebands are well removed from the carrier. In this work we found that a small "taper" of the undulator period will reduce the sideband power, perhaps by "detuning" the synchrotron oscillation. As expected, the use of an undulator with a tapered period caused a substantial improvement in the efficiency of the laser.

REFERENCES

[1] N. M. Kroll, P. Morton, and M. N. Rosenbluth. "Free electron lasers with variable parameter wigglers." *IEEE J Quantum Electron.*, vol. QE-17, pp. 1436-1468, 1981

[2] P Sprangle, C. M. Tang. and W M Manheimer. "Nonlinear formulation and efficiency enhancement of free electron lasers." *Phys Rev. Lett.*, vol. 43, pp. 1932-1936, 1979.

[3] R. W. Warren *et al.*, "Results of the Los Alamos FEL experiments." *IEEE J. Quantum Electron.*, vol. QE-19, pp 391-401, 1983

[4] W M. Grossman *et al.*, "Demonstration of large electron beam energy extraction by a tapered wiggler Fu ." *Appl Phys. Lett.*, vol. 43 pp. 745-747, 1983.

[5] T. J. Orzechowski *et al.*, "High efficiency extraction of microwave

radiation from a tapered-wiggler FEL," *Phys. Rev. Lett.*, vol. 57, pp. 2172-2176, 1986.

[6] R. Warren *et al.*, "Recent lasing results with the Los Alamos FEL," *Nucl. Instrum. Methods*, vol. A259, pp. 8-12, 1987.

[7] J. A. Edighoffer *et al.*, "Variable wiggler free-electron laser oscillator," *Phys. Rev. Lett.*, vol. 52, pp. 344-347, 1984.

[8] J. Masud, T. C. Marshall, and S. P. Schlesinger, "Regenerative gain in a Raman FEL oscillator," *IEEE J. Quantum Electron.*, vol. QE-23, pp. 1594-1604, 1987.

[9] F. G. Yee and T. C. Marshall, "Design of an efficiency-enhanced Raman FEL oscillator," *IEEE Trans. Plasma Sci.*, vol. PS-13, pp. 480-483, 1985.

[10] W. P. Marable, C. M. Tang, and P. Sprangle, "Tapered wiggler analysis of a high gain FEL oscillator," *Nucl. Instrum. Methods*, vol. A259, pp. 210-218, 1987.

[11] S. C. Chen and T. C. Marshall, "Thomson backscattering from a relativistic electron beam as a diagnostic for parallel velocity spread," *Phys. Rev. Lett.*, vol. 52, pp. 425-428, 1984.

[12] F. G. Yee. J. Masud, T. C. Marshall, and S. P. Schlesinger, "Power and sideband studies of a Raman FEL," *Nucl. Instrum. Methods*, vol. A259, pp. 104-106, 1987.

[13] S. Y. Cai, A. Bhattacharjee, and T. C Marshall, "Optical guiding in a Raman FEL," *IEEE J. Quantum Electron.*, vol. QE-23, pp. 1651-1656, 1987.

[14] J. Masud *et al.*, "Sideband control in millimeter wave FEL," *Phys. Rev. Lett.*, vol. 58, pp. 763-766, 1987.

Optical Guiding in a Raman Free-Electron Laser

S.Y. Cai

A. Bhattacharjee

T.C. Marshall

Optical Guiding in a Raman Free-Electron Laser

S. Y. CAI, A. BHATTACHARJEE, AND T. C. MARSHALL

Abstract—A theoretical and computational study of optical guiding in a Raman free-electron laser (of wavelength $\approx$ 2 mm) is given. A set of basic dynamical equations is given, including the effects of space-charge and two-dimensional diffraction, both with and without a waveguide. The results from a computer code based on these equations are reported, showing optical guiding. An experiment is proposed in the Columbia free-electron laser to measure optical guiding.

I. INTRODUCTION

IN a free-electron laser (FEL), the electron beam is not only the source of energy for the radiation field, but also constitutes a medium which, under certain conditions, can distort the wavefront and reduce the phase velocity of the radiation. The modified index of refraction can then lead to a focusing effect which overcomes the diffractive spreading of the optical beam. This effect, known as optical guiding [1], [2]. has been recently studied in the high-gain Compton regime, and shown to yield guided optical beams over many Rayleigh ranges [3]–[5]. However, there is to date no experimental demonstration of this important effect.

In this paper we study optical guiding in a Raman FEL. in which it is essential to include the effects of space charge. One of our objectives is to define the parameters for an experimental demonstration of optical guiding in the Columbia FEL device [6]. We observe that Raman FEL's typically use waveguides to confine the radiation, which explains why there has been no need to develop optical guiding methodology for such devices. However, the natural effectiveness of optical guiding leads to the interesting possibility that waveguide structures may be dispensable in long wavelength FEL's operating in the amplifier mode.

The plan of this paper is as follows. In Section II, we give a general formulation of FEL equations in two dimensions (2-D) including the effects of space charge and diffraction of the optical beam. In Section III. we present numerical results from a 2-D computer code which integrates the complete set of equations given in Section II, and follows the evolution of a Gaussian optical beam through the exponential gain regime into saturation in the absence of external waveguides. In particular, we show the effect of varying the current density on optical guiding. In Section IV, we calculate optical guiding in a waveguide environment by representing the optical wave in a

set of TE modes. We conclude in Section V with a summary of the main results of our work.

II. GENERAL FORMULATION

We use cylindrical polar coordinates (r, θ, z), with the axis of the undulator aligned with the z-axis. We assume that the system is axisymmetric $(\partial/\partial\theta = 0)$. For a helical undulator, the vector potential is

$$\vec{A}_w(\vec{r}) = -\frac{mc^2}{e} a_w(z) \left[\hat{x} \cos k_w z + \hat{y} \sin k_w z\right]. \quad (1)$$

The vector potential of the time-dependent radiation field is

$$\vec{A}_s(\vec{r}, t) = \frac{mc^2}{e} a_s(r, z, t)$$
$$\cdot \left[\hat{x} \cos \left\{k_s z - \omega t + \phi(r, z, t)\right\}\right.$$
$$\left. - \hat{y} \sin \left\{k_s z - \omega t + \phi(r, z, t)\right\}\right]. \quad (2)$$

where ϕ is the phase shift of the radiation. In (1) and (2). m is the rest mass of the electron and e is its charge: k_w, k_s are the wave numbers of the undulator and radiation fields, and $\omega = ck_s$ is the frequency of the radiation field. Assuming that $|\partial a_s/\partial t| \ll |\omega_s a_s|$. $|\partial \phi/\partial t| \ll |\omega_s|$ and $a_s \ll a_w$. the single-particle equations are [7], [8]

$$\frac{d\gamma_j}{dz} = -\frac{k_s a_w a_s}{\gamma_j} \sin \Psi_j + \frac{2\omega_p^2}{k_s c^2}$$
$$\cdot \left[\langle \cos \Psi \rangle \sin \Psi_j - \langle \sin \Psi \rangle \cos \Psi_j\right]. \quad (3)$$

and

$$\frac{d\Psi_j}{dz} = k_s + k_w - k_s / \left[1 - (1 + a_w^2 - 2a_s a_w \right.$$
$$\left. \cdot \cos \Psi_j)/\gamma_j^2\right]^{1/2} + \frac{\partial \phi}{\partial z}. \quad (4)$$

where $\Psi_j = (k_w + k_s)z_j - \omega t + \phi$ is the relative phase of the jth electron with respect to the radiation field and $\gamma_j mc^2$, its energy: n_0 is the electron density and $\omega_p = (4\pi n_0 e^2/m)^{1/2}$ is the plasma frequency. The angular brackets denote an ensemble average over all electrons. Equations (3) and (4) are essentially equivalent to those derived recently from a Hamiltonian formulation [9], [10]. The interaction between the radiation and electrons is

governed by Maxwell's equation

$$\left(\nabla^2 - \frac{1}{c^2}\frac{\partial^2}{\partial t^2}\right)\vec{A}_s = -\frac{4\pi}{c}\vec{J}_\perp, \qquad (5)$$

where $\vec{J}_\perp(\vec{r}, t)$ is the transverse current, and $\vec{A}_s$ is given by (2). In most cases of interest. $u = a_s e^{i\phi}$ varies slowly along z; therefore, we keep only first derivatives and drop all second derivatives with respect to z. Then. (5) reduces to

$$2ik_s\frac{\partial u}{\partial z} + \nabla_\perp^2 u$$

$$= -\frac{\omega_p^2 a_w}{c^2}\left\langle\frac{\exp\left[-i(\Psi - \phi)\right]}{\gamma}\right\rangle. \qquad (6)$$

In (6). the term $\nabla_\perp^2 u$ describes the effect of diffraction of the optical beam. Equations (3), (4), and (6) constitute a self-consistent set of equations for the evolution of the electrons and the radiation field. The equations of [3] are recovered if we drop the second term on the right-hand side in (3), describing the effect of space charge. Equation (6) neglects slippage between the electrons and the radiation, and, therefore, does not include the effect of the sideband instability.

III. 2-D Nonlinear Numerical Simulation

A 2-D computer code has been developed to integrate (3), (4), and (6). In this code, 300 test electrons are uniformly distributed in Ψ_0 between 0 and 2π at each of 24 radial positions dividing the beam radius. At $z = 0$, as sketched in Fig. 1. the electron beam is assumed to have a cylindrically symmetric step function in density, and the optical beam is assumed to be Gaussian. The parameters of the simulation are listed in Table I. column 1. A guiding magnetic field of $B_0 = 10$ kG in the actual experiment is omitted in the theory, except that its effect is included in the calculation of the electron quiver velocity ($v_\perp/c)_{rms}$ in the undulator.

Fig. 2 is a plot of the optical beam radius along the undulator in the linear (exponential gain) regime compared to the case when the beam diffracts in free space. The optical beam associated with the Raman FEL is confined approximately in a constant radius of 0.75 cm centered on the electron beam. Fig. 3 shows the corresponding optical field amplitude distribution in (r, z) space.

It has been suggested [3] that a bunched electron beam may be treated as if it were an optical fiber with a constant refractive index n and a well-defined edge. The one-dimensional theory predicts the complex refractive index to be

$$\text{Re } n = 1 + \frac{1}{k_s}\frac{d\phi}{dz}, \qquad (7)$$

$$\text{Im } n = -\frac{1}{k_s a_s}\frac{da_s}{dz}. \qquad (8)$$

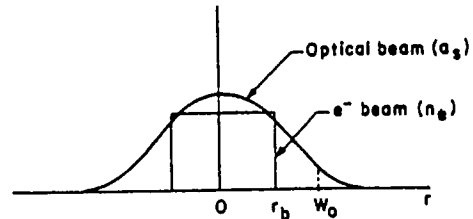
Fig. 1. Radial profiles of the input optical beam amplitude and electron beam density at $z = 0$.

TABLE I
PARAMETERS IN USE

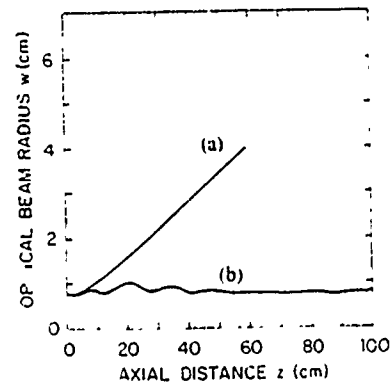|	1 Without Waveguides	2 With Waveguides
Undulator period (ℓ_0)	1.7 cm	1.7 cm
$\gamma(v_\perp/c)_{rms}$	0.175	0.3
Input optical power	(0.4, 277) KW/cm^2	2.8 KW/cm^2
Wavelength (λ_s)	1.56 mm	1.57 mm
Optical beam waist (W_0)	0.75 mm	—
Electron beam radius (r_0)	4 mm	3 mm
Current density (J)	1000 A/cm^2	2000 A/cm^2
Electron energy (γ_0)	2.57–2.64	2.5
Waveguide radius (R)	—	1.2 cm
Initial optical mode	Gaussian	TE$_{11}$

Fig. 2. The optical beam radius along the undulator in the Raman FEL operating in the exponential gain regime (b) compared to the diffraction of the same input optical beam in a free space (a).
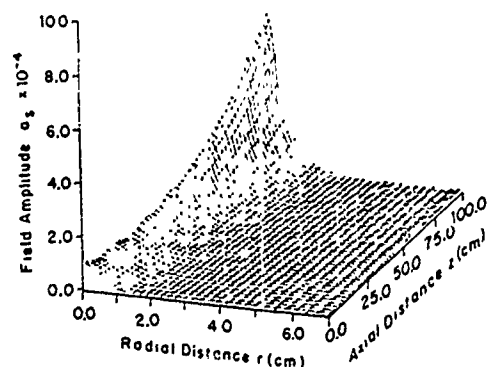

Fig. 3. A 3-D plot of the optical field amplitude distribution in the exponential regime.
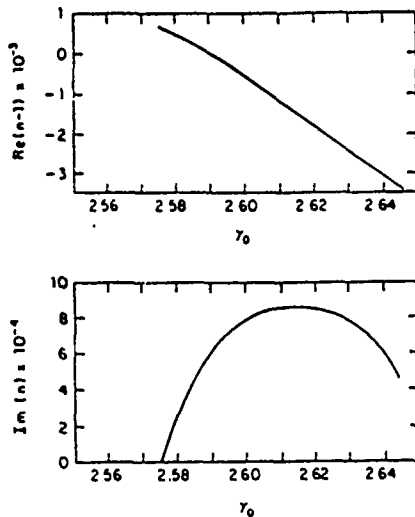
Fig. 4. The real part and imaginary part of the index of refraction as functions of input electron energy γ_0 calculated from the 2-D simulations. The resonant energy is at $\gamma_r = 2.6$. The parameters of Table I are used with small input optical signal so that the FEL operates in the exponential gain regime.

In the small signal (exponential gain) regime, we use (7) and (8) to calculate the complex index of refraction from the (averaged) numerical values of $k_s^{-1} \, d\phi/dz$ and $(k_s a_s)^{-1} \, da_s/dz$, computed at $r = 0$. Fig. 4 gives Re n and Im n as functions of the initial electron energy. We note that at maximum gain Re $n < 1$. This is different from the high-gain Compton FEL without space charge, where maximum gain is obtained exactly at Re $n = 1$. The shift from Re $n = 1$ at maximum gain in a Raman FEL is due to the effect of space charge, and is known to occur in high-gain Compton FEL's as well if space-charge effects are taken into account [10], [11]. Due to this shift, it is not possible to enhance both gain and optical guiding indefinitely by increasing the current density. Instead, there is a maximum current density for optimal guiding and gain.

At saturation, plots for the optical beam radius and the field amplitude are given, respectively, in Figs. 5 and 6. We see in Fig. 6 that a part of the beam escapes from the strict confines of the guided beam, and the appealing analogy to an optical fiber with a well-defined edge and constant refractive index [3] becomes somewhat questionable at this stage. The reason for this behavior is that at saturation, the electrons are trapped in the ponderomotive potential, and the consequent oscillatory motion leads to negative values of $\langle \cos \Psi / \gamma \rangle$. This, in turn, results in Re $n < 1$, and a diverging optical beam. The loss of optical power from the guided beam may be irreversible under such conditions. A possible remedy is to taper the undulator in a manner which will keep $\langle \cos \Psi / \gamma \rangle$ positive.

In Fig. 7, we show optical guiding of a beam in a Raman FEL with the parameters of Table I, column 1, except that the current density is reduced to $J = 100 \, \text{A/cm}^2$. The beam radius is seen to increase to approximately 1 cm.
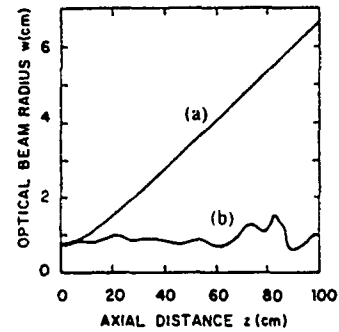

Fig. 5. The optical beam radius along the undulator in the Raman FEL operating in the saturation regime (b) compared to the diffraction of the same input optical beam in free space (a).
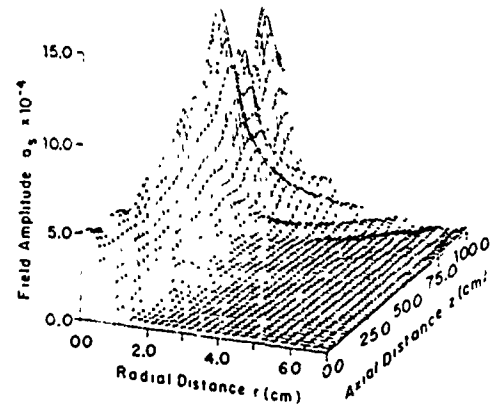

Fig. 6 A 3-D plot of the optical field amplitude distribution in the saturation regime.
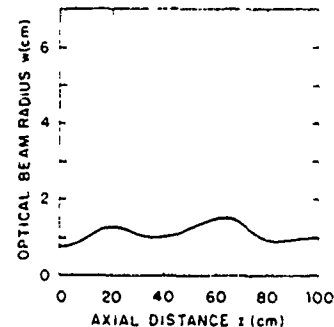

Fig. 7 The optical beam radius along the undulator in the Raman FEL operating in the exponential regime with current density reduced to 100 A/cm²

IV. OPTICAL GUIDING IN A WAVEGUIDE CONFIGURATION

In this section, we calculate optical guiding in a waveguide configuration for the parameters given in Table I, column 2. The radius of the waveguide (R) is taken to be appreciably larger than the radius of the electron beam (r_b), permitting several waveguide modes to interact with the electron beam via the FEL mechanism. The purpose of the calculation is to establish that a test of optical guiding can be undertaken in a typical Raman FEL producing radiation of wavelength ~ 2 mm.

Before we present details of our calculation, we give a qualitative overview. We consider the small-signal (exponential gain) regime. Experiments [12] have reported accurate measurements of the threshold undulator field required to cause regeneration in an FEL oscillator. The coefficient of exponential growth depends on the beam filling factor (for constant field amplitude throughout the waveguide, this would be $r_b^2/R^2 = 0.06$ for the case chosen). Should optical guiding occur, we expect that the filling factor would show appreciable enhancement, as the waves are more tightly bound to the electron beam. An enhanced filling factor, in a resonator with fixed losses, will cause a reduction in the undulator field needed to initiate oscillation. We report below calculations which not only show optical guiding, but which also demonstrate enhancement of the filling factor. As a boundary condition, we take the optical wave input to the electron beam at the beginning of the undulator to be the dominant TE_{11} mode of the cylindrical waveguide. Two cases are compared, having comparable growth rate: a case where optical guiding occurs, and one where it does not. The only parameter distinguishing the two cases is a slight change of wavelength.

In the presence of a waveguide, (6) needs to be replaced by an appropriate wave equation. The starting point of the analysis is the Maxwell's equation for a TE wave, given by

$$\left(\nabla^2 - \frac{1}{c^2} \frac{\partial^2}{\partial t^2} \right) B_{1z}(\vec{r}, t) = -\frac{4\pi}{c} (\nabla \times \vec{J})_z, \quad (9)$$

where B_{1z} is the z-component of the time-dependent magnetic field associated with the radiation. B_{1z} is represented as

$$B_{1z}(\vec{r}, t) = \frac{mc^2}{e} \sum_{\ell,m} C_{\ell m}(z) J_\ell(K_{\ell m} r) e^{i\ell\theta}$$

$$\cdot \exp[i(k_{\ell m} z - \omega t)], \quad (10)$$

where J_ℓ is the Bessel function of order ℓ, and $K_{\ell m}$ and $k_{\ell m}$ are subject to the conditions

$$\frac{d}{dr} J_\ell(K_{\ell m} r)\big|_{r=R} = 0, \quad (11)$$

and

$$K_{\ell m}^2 + k_{\ell m}^2 = \frac{\omega^2}{c^2}. \quad (12)$$

The amplitudes $C_{\ell m}(z)$ are slowly varying along z and are generally complex. Neglecting terms involving the second derivative of $C_{\ell m}(z)$, (9) becomes

$$\sum_{\ell,m} 2k_{\ell m} \frac{dC_{\ell m}(z)}{dz} J_\ell(K_{\ell m} r) \exp[i(\ell\theta + k_{\ell m} z)]$$

$$= -\frac{\omega_p^2 a_w}{c^2} \exp[i(\theta + k_s z)]$$

$$\cdot \left[\frac{\partial}{\partial r} \left\langle \frac{\exp[-i(\Psi_j - \phi)]}{\gamma_j} \right\rangle \right.$$

$$\left. - \left\langle \frac{\exp[-i(\Psi_j - \phi)]}{\gamma_j} \right\rangle \delta(r - r_b) \right] \quad (13)$$

where the δ function arises from the assumed step-function form for the electron beam density shown in Fig. 1. We assume that the term $\langle \exp[-i(\Psi_j - \phi)]/\gamma_j \rangle$ is independent of θ and neglect any poloidal asymmetry of the beam, which means that the only surviving terms in (13) are those with $\ell = 1$. We let $C_{\ell m}(z) = C_m(z) \delta_{\ell, 1}$, and drop all subscripts ℓ. We finally obtain

$$\frac{dC_m}{dz} = \frac{\omega_p^2 a_w}{c^2} \frac{K_m^3 \exp[i(k_s - k_m)z]}{k_m(K_m^2 R^2 - 1)[J_1(K_m R)]^2}$$

$$\cdot \int_0^{r_b} dr r J_0(K_m r) \left\langle \frac{\exp[-i(\Psi_j - \phi)]}{\gamma_j} \right\rangle \quad (14)$$

and

$$a_s \exp(i\phi) = \frac{i}{2k_s} \sum_m C_m \frac{k_m}{K_m} J_0(K_m r) \exp[i(k_m - k_s)z]. \quad (15)$$

Equations (14) and (15) are coupled with (3) and (4) to form a complete set of equations. In our model, the current density in (9) is purely transverse and does not excite TM modes.

We note that (12) allows only a finite number of modes to propagate in a waveguide for a given wavelength. For the parameters listed in Table I, column 2, the maximum number of propagating modes is 15. These parameters correspond to a value of Re n slightly greater than unity.

The numerical simulation is performed in the exponential gain regime; the total energy is conserved within the limits of computational accuracy. At input, the optical wave is assumed to be a TE_{11} mode.

Fig. 8(a) shows a plot of the filling factor along z, defined as

$$\int_0^{r_b} dr r a_s^2(r) \bigg/ \int_0^R dr r a_s^2(r).$$

Fig. 9(a) is the corresponding optical field distribution for a computation with 15 coupled modes. Note the radiation grows much more rapidly on the axis of the waveguide than at the wall. Next, for the sake of comparison, we artificially decouple the 15 modes by following the evolution of each mode as if the other modes do not exist, and then take the sum of the outputs for each mode; the results are shown in Figs. 8(b) and 9(b). We find that the filling factor is higher for case (a) than for case (b), implying that more optical power is confined in the central region for case (a) than for case (b). This demonstrates that mode-coupling effects play a crucial role in refractive
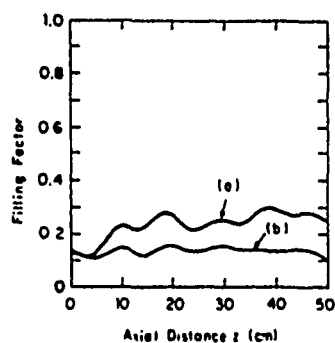
Fig. 8. The filling factors for (a) 15 coupled TE waveguide modes and (b) 15 uncoupled TE waveguide modes in a Raman FEL operating in the exponential gain regime at $k_s = 40$ cm^{-1}, which corresponds to Re (n) > 1.

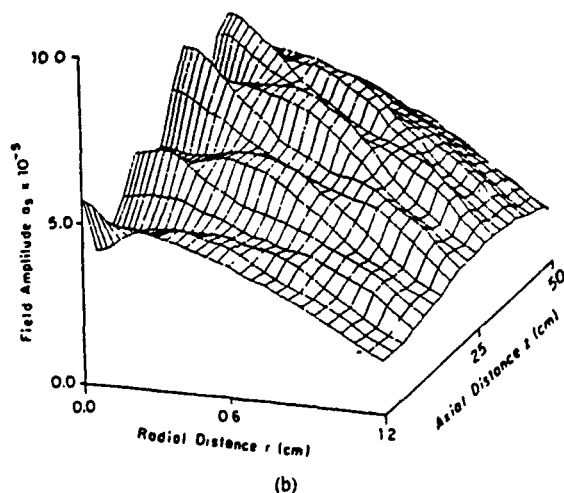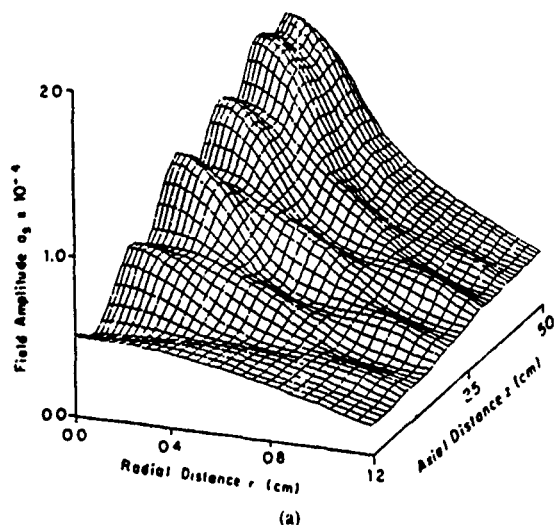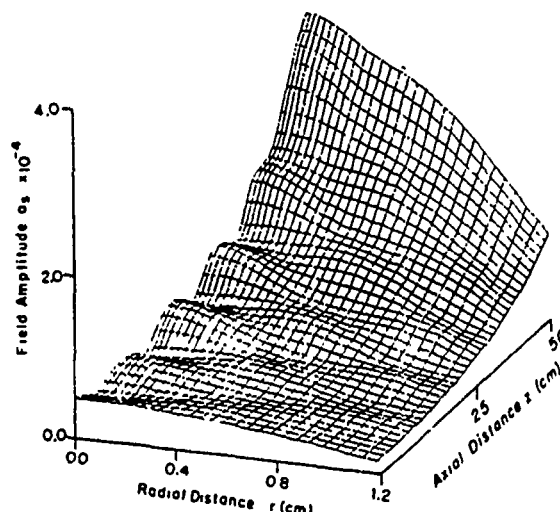Fig. 10. The optical field amplitude distribution in a Raman FEL operating in the exponential gain regime with 14 coupled TE waveguide modes. $k_s = 38$ cm^{-1}, which corresponds to Re (n) < 1 and maximum FEL gain.

gain is high, and the field distribution is almost that of a growing TE$_{11}$ mode. Mode interference accounts for the periodic variation of amplitude along the z-axis.

In Fig. 10, we show the field distribution for the same parameters as Fig. 9(a) except k_s is taken to be 38.0 cm^{-1}, corresponding to peak gain. Compared to the case of Fig. 9(a), the optical guiding is poorer. This illustrates the point that due to the effect of space charge, optimal refractive guiding requires that the input electron energy be offset from the energy corresponding to peak gain.

(a)

(b)

Fig. 9. The optical field amplitude distributions calculated from the same simulations as those shown in Fig. 8. (a) Simulation with 15 coupled TE waveguide modes. (b) Simulation with 15 uncoupled TE waveguide modes.

guiding, which is important when the characteristic gain length is much larger than the Rayleigh range (= 11 cm). We note that when the modes are decoupled, the loss of optical confinement occurs despite the fact that the FEL

V. CONCLUSION

We have examined the feasibility of optical guiding in a Raman FEL, taking parameters appropriate for the device at Columbia University in particular. Optical guiding is seen to occur in both the exponential gain and saturation regimes. The effect of a waveguide structure on guiding is studied. It is found that coupling between the propagating modes plays a crucial role in determining the effectiveness of refractive guiding in a waveguide environment.

REFERENCES

[1] W. M. Kroll. P. L. Morton, and M. N. Rosenbluth. "Free-electron lasers with variable parameter wigglers." IEEE J Quantum Electron., vol. QE-17, pp. 1436–1468, 1981.
[2] C.-M. Tang and P. Sprangle. "The three-dimensional non-linear theory of the free-electron-laser amplifier," in Free Electron Generators of Coherent Radiation, Physics of Quantum Electronics 9. Reading, MA: Addison-Wesley, 1982, p. 627.
[3] E. T. Scharlemann, A. M. Sessler, and J. M. Wurtele. "Optical guiding in a free-electron laser." Phys. Rev. Lett., vol. 54, pp. 1925–1928, 1985.
[4] G. T. Moore., "High-gain and large-diffraction regimes of the FEL." Nuclear Instruments and Methods in Physics Research A250, pp. 381–388, 1986.
[5] P Sprangle. A. Ting, and C. M. Tang, to be published.
[6] S. Y. Cai, A. Bhattacharjee, and T. C. Marshall. "Feasibility of optical guiding in a Raman free electron laser," Bull. Amer. Phys. Soc., vol. 31, p. 1538, 1986.

[7] C. M. Tang and P. Sprangle. "Nonlinear analysis of the free-electron laser utilizing a linear wiggler field," *J. Appl. Phys.*, vol. 52, pp. 3148-3153, 1981.

[8] D. Prosnitz, A. Szoke, and V. K. Neil. "High-gain, free-electron laser amplifiers: Design considerations and simulation," *Phys. Rev.*, vol. A24, pp. 1436-1451, 1981.

[9] I. Gjaja and A. Bhattacharjee. "Start-up from noise and high-gain regime of the free electron laser: A Hamiltonian formulation," *Opt. Comm'n.*, vol. 58, pp. 201-205, 1986.

[10] ——, "Start-up from noise and high-gain regime of the free electron laser: A Hamiltonian formulation, Part II," *Opt. Commun.* 1987.

[11] J. B. Murphy, C. Pellegrini, and R. Bonifacio. "Collective instability of a free electron laser including space charge and harmonics," *Opt. Commun.*, vol. 53, pp. 197-202, 1985.

[12] J. Masud, T. C. Marshall, S. P. Schlesinger, and F. G. Yee. "Gain measurements from start-up and spectrum of a Raman FEL oscillator," *Phys. Rev. Lett.*, vol. 56, pp. 1567-1570, 1986.

S. Y. Cai, photograph and biography not available at the time of publication.

A. Bhattacharjee, photograph and biography not available at the time of publication.

T. C. Marshall, for a photograph and biography, see this issue. p. 1604.

Observations of Optical Guiding in a Raman Free-Electron Laser

A. Bhattacharjee, S. Y. Cai, S. P. Chang, J. W. Dodd, and T. C. Marshall

Department of Applied Physics, Columbia University, New York, New York 10027

(Received 28 October 1987)

Evidence for optical guiding of 1.7-mm-wavelength radiation along an electron beam in a Raman free-electron laser is obtained experimentally and compared with numerical simulations. Optical guiding is manifest as the interference effect of several waveguide modes; this is observed beyond the point of electron-beam termination. The experiment operates in the regime of exponential signal gain and appreciable electron-beam space charge.

PACS numbers: 42.55.Tb

In the free-electron laser (FEL) the electron beam not only is the source of energy for the growing electromagnetic (EM) field, but can, in addition, distort the wave front and alter the phase velocity of the radiation; this leads to a focusing effect known as optical guiding, which offsets the diffractive spreading of the optical beam. Optical guiding has been studied theoretically in the FEL Compton regime[1-5] and has been shown to yield guiding over many Rayleigh ranges.

Recently, we have presented calculations[6] that indicate optical guiding should occur in the Raman regime (conditions of appreciable electron-beam space charge, "weak" undulator field, and "long" wavelength[7]). These calculations account for the presence of an overmoded waveguide, customarily used in order to contain the EM radiation as well as to provide a stable equilibrium geometry for the electron beam. However, the waveguide is not necessary for the containment of the EM fields when optical guiding occurs. Recent experiments[8] at MIT have found that the mechanisms promoting optical guiding do indeed occur. However, because only the dominant waveguide mode propagates in the MIT FEL, the FEL mechanisms which support optical guiding do not sustain a truly guided wave but rather modify the profile of the radiation intensity near the electron beam[9]; in addition, there are subtleties introduced into their experiment because the electrostatic waves are important.[10] The FEL experiment at Los Alamos National Laboratory has revealed[11] a "bending" effect of the radiation contained in the optical resonator. La Sala, Deacon, and Madey have also recently reported on optical guiding influenced by gain guiding effects.[12]

In this Letter we report experimental results, compared in detail with numerical computations, which are consistent with refractive optical guiding effects as they occur in a Raman FEL experiment at Columbia University. In contrast to the MIT experiment, the shorter wavelength in our apparatus permits the excitation of several waveguide TE modes which interfere and permit a truly optically guided beam to form. The interference pattern, which is observed in both the numerical simulations and the experiment, is evidence of optical guiding.

The numerical study, with the 2D FEL and self-consistent electromagnetic equations appropriate for modeling of our system,[6] describes an electron-beam filament ($r_b = 2$ mm) on the axis of an overmoded cylindrical waveguide ($R = 9$ mm). Other parameters are electron-beam energy 800 kV, current density 2000 A/cm^2, normalized undulator vector potential $a_w = eB_\perp/k_0mc^2 > 0.3$, helical undulator period $2\pi/k_0 = 17$ mm, and FEL radiation wavelength 1.7 mm. The theory includes the effects of space charge, appropriate to the Raman FEL. The FEL device is operated as a self-amplifier of noise, which grows exponentially to a point of near saturation at the end of the undulator (50 cm) where the optical-guiding effect is observed.

The computations use the Hamiltonian equations for electron dynamics and Maxwell's equation for the normalized vector potential of the radiation field a_s, driven by the transverse source currents which excite the TE modes of the waveguide. These equations are described in detail in Ref. 6. Note that the FEL mode couples to the waveguide via the dispersion relation which predicts the excitation of only a few waveguide modes; however, additional modes can be excited by mode coupling caused by the nonlinearities in the single-particle equations. The higher-order modes are excited at the FEL frequency, but their axial wave numbers differ because of the waveguide dispersion. In Fig. 1(a) is shown an example of optical guiding in a waveguide where ten higher-order modes are excited: Note that the field amplitude grows more rapidly on axis than off axis. Guiding enhances the power gain and growth rate, because the "filling factor" is enhanced. We find that the inclusion of "evanescent" waveguide modes in the calculation results in no change in these results. For computations we assume that the source field at the undulator entry ($z = 0$) is a TE$_{11}$ mode. Although the values of the field amplitude in Fig. 1(a) are consistent with the experimental situation, we remark that as long as the experiment is operated in the exponential gain regime, the field profile at $z = 50$ cm and the guiding achieved there are not sensitive to the choice of $a_s(0)$, because the system is several e-folding lengths long.
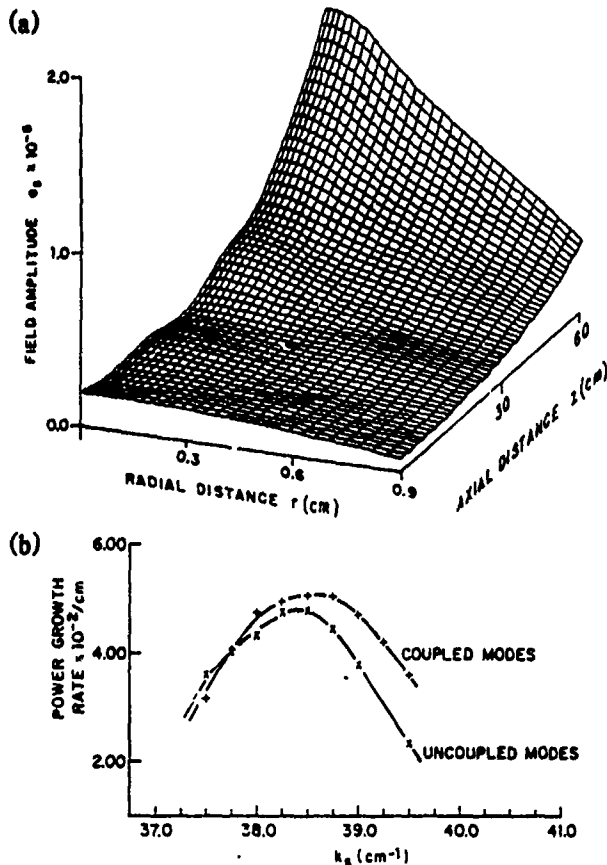
(a)

(b)

FIG. 1. (a) The exponential growth of 1.7-mm-wavelength optically guided waves on an electron beam in a cylindrical waveguide (drift tube) described in the text. The ordinate is the normalized magnetic vector potential of the FEL radiation and the axial distance is measured along the axis of the beam and undulator. (b) The growth-rate spectrum of the Raman FEL, showing the computed guiding case ("coupled modes") and the unguided case ("uncoupled modes"). The parameters are the same as in the paper, except that the electron-beam radius is 3 mm and the waveguide radius is 12 mm; this accounts for the difference in wavelength. "Antiguiding" occurs for $k < 37.8 \text{ cm}^{-1}$.

In Fig. 1(b) is shown the effect of optical guiding on the growth rate, for slightly different parameters than Fig. 1(a). The guiding can be "turned off" by our calcu-

lating the interaction of the electrons with each TE mode independently and then superimposing the solutions. Note that guiding has less effect on growth for wave numbers less than that of the gain maximum (this asymmetry is a consequence of the space charge). This effect at longer wavelengths can be described as "antiguiding": What happens in this range of wavelengths is that the phase behaves as $d\phi/dz < 0$ rather than $d\phi/dz > 0$. The effect on the wave profile is that of flattening rather than a peaking, and this contributes to a reduction of filling factor and a slight reduction of growth rate. In the experimental study which follows, the FEL is operated in the mode of amplifier of noise, and therefore the signal observed at the end of the undulator has the wavelength corresponding to maximum gain (for which guiding occurs).

The experimental apparatus is shown in Fig. 2. The diode, generation of the electron beam, and apparatus have been already described in detail elsewhere.[13] The electron beam is abruptly terminated by a polyethylene "witness plate," which permits the 1.7-mm radiation to pass. The intensity profile within the drift tube is examined with use of a "waveguide probe," which consists of a 2-mm-diam cylindrical waveguide fitted with a plastic horn antenna.[14] The local fields in the drift tube launch a guided wave on the dielectric material of the horn, which conveys the radiation into the small waveguide and thence to a Schottky-barrier detector following a high-pass ($\lambda < 2$ mm) filter. The characteristic far-field pattern of the probe is a narrow forward-directed lobe having a 3-dB half width $\gtrsim 10°$, with side lobes down by $\simeq 15$ dB. Prior to measurements of the guiding, the spectrum of the FEL radiation was examined to establish that the correct wavelength was being generated and detected. Also, it was verified that the FEL radiation was growing exponentially along the undulator up to the point of electron-beam termination. The waveguide probe has no effect on the electron-beam equilibrium, and the FEL radiation passes beyond it and diffracts out the open end of the drift tube. The witness plate, 6 mm thick, must be replaced roughly every six shots; this requires a sturdy mechanical jig for the probe so that it can return to its initial position. The experiment uses a
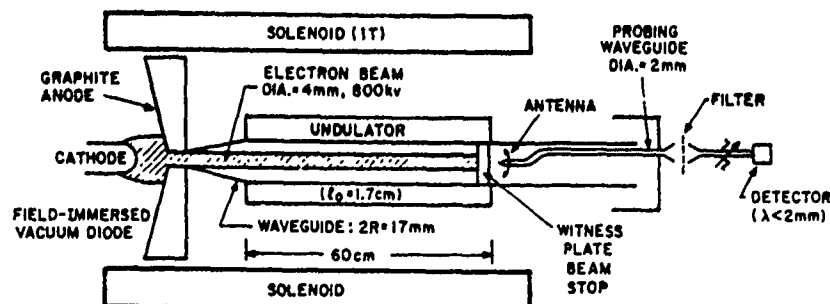

FIG. 2. Schematic of the FEL apparatus. The diode, containing a cold cathode, is attached to a pulse-line accelerator. The waveguide probe diagnostic is located behind the "witness plate," which is at the end of a 50-cm-long undulator.
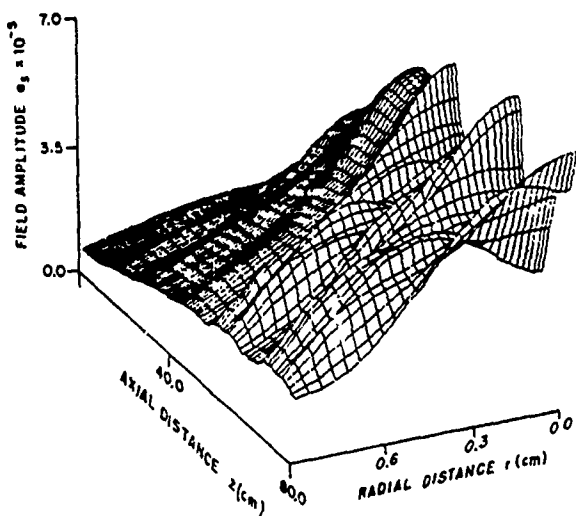
FIG. 3. A view of the computed optically guided radiation shown in Fig. 1(a) when the electron beam is terminated at $z = 50$ cm and the EM waves proceed down the empty waveguide. If the modes are decoupled, the intensity would be nearly constant beyond the termination point.

constant magnetic field (≈ 1 T) for electron-beam guiding and focusing. As the FEL frequency is far above the electron gyrofrequency, the only physical effect of the guiding field is to enhance the electron quiver motion in the undulator. We model the guiding-field effect in the theory with use of an undulator magnetic vector potential which will produce the level of quiver motion obtained in the experiment.

In Fig. 3 is shown a computation for the radiation

propagating beyond the witness-plate termination [same conditions as Fig. 1(a)]. One should note a characteristic "sloshing" of the radiation in the waveguide, resulting in periodic maxima along the z axis and off-axis local minima correlating with minima on axis. This is caused by the interference of the several modes responsible for the optical guiding; these modes, having different radial and axial wave numbers, account for the complex radiation pattern beyond the witness plate. (If the modes are artificially decoupled, in which event there can be no guiding, the radiation is dominated by the TE_{11} mode and no such interference pattern results.) The periodicity along the axis depends on the waveguide modes; that is, it is determined by the waveguide size and the operating frequency. The location of the first and subsequent minima does, however, depend on whether there is guiding or "antiguiding"; our calculations show that in the latter case, the positions of the maxima and minima fall on the respective minima and maxima of Fig. 3.

The data are assembled from >100 shots, selected for nearly identical diode voltage, and are presented in Figs. 4(a)–4(c). The intensity variation along the z axis agrees satisfactorily with the guiding (at gain-maximum) theory. However, if the undulator field is reduced by $\frac{2}{3}$, no such periodicity of intensity along the axis is observed, in agreement with the numerical simulation which predicts virtually no guiding under these conditions. The radial profiles of the intensity at the axial intensity minimum [Fig. 4(b)] and maximum [Fig. 4(c)] also show the expected qualitative features. In Fig. 4(c) is also plotted the TE_{11} intensity distribution for comparison with the prediction of the optical-guiding intensity profile; in this case the intercepts of the theory curves are
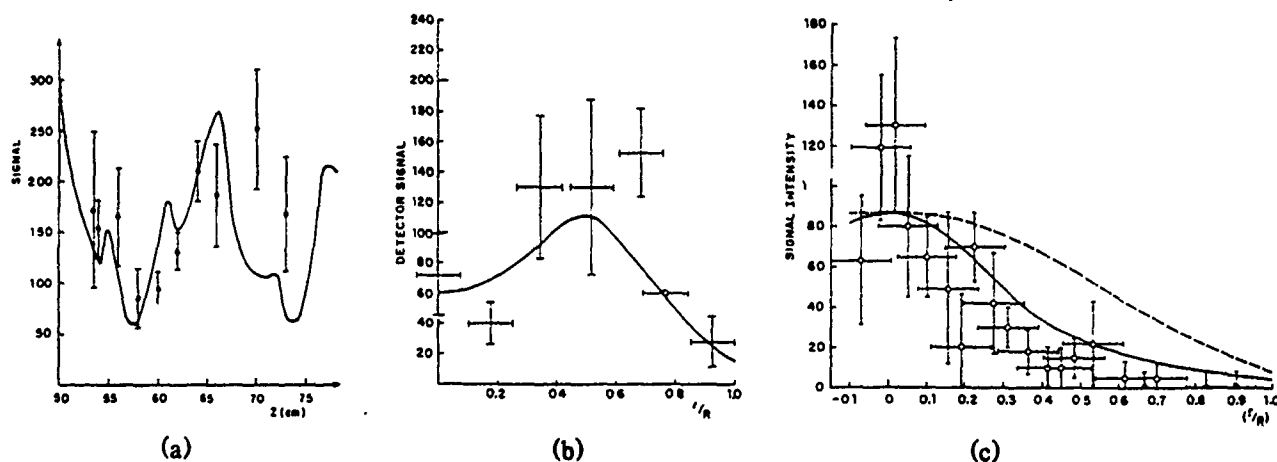

(a)   (b)   (c)

FIG. 4. Experimental data (points) compared with theory (solid or dashed lines) from Fig. 3; the experimental data are the detector signal in millivolts, while the theory scale is arbitrary intensity units. (a) Dependence of intensity along the z axis behind the termination point ($z = 50$ cm) of the electron beam. The axial location of the data points is inexact to the extent ≈ 1 cm because of the finite length of the waveguide probe. (b) Radial dependence of intensity at $z = 58$ cm and (c) $z = 65$ cm. The dashed line in (c) is a plot of the TE_{11} mode intensity which is expected if no optical guiding occurred, and both theory curves are normalized to the same point to fall within the range of the data at $r = 0$. The radial resolution of the probe is ≈ 1 mm.

both normalized to the data at $r = 0$.

The results shown in Fig. 4 only establish that the intensity is peaked at the point of beam termination, $z = 50$ cm, in accord with theoretical prediction. We have also repeated the axial intensity measurements with the beam stop at $z = 42$ cm; it was found that the data essentially reproduce Fig. 4(a). This establishes that the intensity maximum has remained centered on the electron beam in the interaction region, which is consistent with the result obtained from the optical guiding simulation [e.g., Fig. 1(a)].

---

[1]W. M. Kroll, P. L. Morton, and M. N. Rosenbluth, IEEE J. Quantum Electron. 17, 1436 (1981).

[2]C.-M. Tang and P. Sprangle, in *Physics of Quantum Electronics: Free Electron Generators of Coherent Radiation*, edited by S. F. Jacobs and M. Sargent (Addison-Wesley, Reading, MA, 1982), Vol. 9, p. 627.

[3]G. T. Moore, Opt. Commun. 52, 46 (1984).

[4]E. T. Scharlemann, A. M. Sessler, and J. M. Wurtele, Phys. Rev. Lett. 54, 1925 (1985).

[5]P. Sprangle, A. Ting, and C.-M. Tang, Phys. Rev. Lett. 59, 202 (1987).

[6]S. Y. Cai, A. Bhattacharjee, and T. C. Marshall, IEEE J. Quantum Electron. 23, 1651 (1987).

[7]P. Sprangle, R. A. Smith, and V. L. Granatstein, Infrared Millimeter Waves 1, 274 (1979).

[8]J. Fajans, J. S. Wurtele, G. Bekefi, D. S. Knowles, and K. Xu, Phys. Rev. Lett. 57, 579 (1986).

[9]F. Hartemann, K. Xu, G. Bekefi, J. S. Wurtele, and J. Fajans, Phys. Rev. Lett. 59, 1177 (1987).

[10]J. S. Wurtele and J. Fajans, unpublished.

[11]R. W. Warren and B. D. McVey, Nucl. Instrum. Methods Phys. Res., Sect. A 259, 154 (1987).

[12]J. E. LaSala, D. A. G. Deacon, and J. M. J. Madey, Phys. Rev. Lett. 59, 2047 (1987).

[13]S. C. Chen and T. C. Marshall, IEEE J. Quantum Electron. 21, 924 (1985).

[14]M. A. Heald and C. W. Wharton, *Plasma Diagnostics with Microwaves* (Wiley, New York, 1965), p. 334.